LUND UNIVERSITY

Perpendicular to grain fracture analysis of wooden structural elements - Models and applications

Danielsson, Henrik

2013

Link to publication

Citation for published version (APA):
Danielsson, H. (2013). *Perpendicular to grain fracture analysis of wooden structural elements - Models and applications*. [Doctoral Thesis (compilation), Structural Mechanics].

Total number of authors:
1

General rights
Unless other specific re-use rights are stated the following general rights apply:
Copyright and moral rights for the publications made accessible in the public portal are retained by the authors and/or other copyright owners and it is a condition of accessing publications that users recognise and abide by the legal requirements associated with these rights.
- Users may download and print one copy of any publication from the public portal for the purpose of private study or research.
- You may not further distribute the material or use it for any profit-making activity or commercial gain
- You may freely distribute the URL identifying the publication in the public portal

Read more about Creative commons licenses: https://creativecommons.org/licenses/

Take down policy
If you believe that this document breaches copyright please contact us providing details, and we will remove access to the work immediately and investigate your claim.

LUND UNIVERSITY

PO Box 117
221 00 Lund
+46 46-222 00 00

LUND
UNIVERSITY

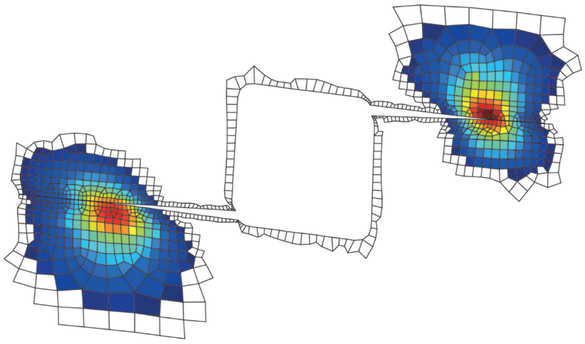

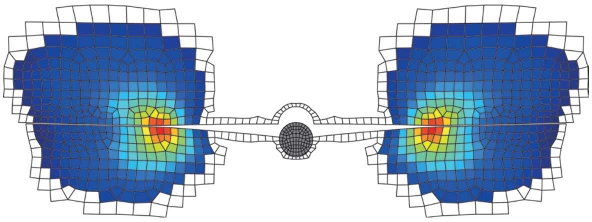

PERPENDICULAR TO GRAIN FRACTURE ANALYSIS OF WOODEN STRUCTURAL ELEMENTS
Models and Applications

HENRIK DANIELSSON

Structural
Mechanics

Doctoral Thesis

Department of Construction Sciences
Structural Mechanics

ISRN LUTVDG/TVSM--13/1024--SE (1-181)
ISBN 978-91-7473-475-1 ISSN 0281-6679

PERPENDICULAR TO GRAIN FRACTURE ANALYSIS OF WOODEN STRUCTURAL ELEMENTS
Models and Applications

Doctoral Thesis by

HENRIK DANIELSSON

Copyright © Henrik Danielsson, 2013.
Printed by Media-Tryck LU, Lund, Sweden, April 2013 *(Pl)*.

For information, address:
Division of Structural Mechanics, LTH, Lund University, Box 118, SE-221 00 Lund, Sweden.
Homepage: http://www.byggmek.lth.se

Acknowledgments

The work presented in this thesis has been carried out at the Division of Structural Mechanics at Lund University. The financial support from Formas through grant 24.3/2003-0711 for the project *Calculation models for fracture perpendicular to grain in wooden structural elements and joints* is gratefully acknowledged.

I would first and foremost like to thank my supervisor Per Johan Gustafsson. I am very grateful for his inspiring and skillful guidance, his encouragement and support and for his ability to always find time for discussions. Many of the conceptual ideas being central to the work presented in this thesis further originate from him.

I would furthermore like to thank the rest of the staff at the Division of Structural Mechanics for their good company and for creating a pleasant and inspiring atmosphere. Special thanks also to Kent Persson for discussions on wood mechanics and modeling, to Ola Dahlblom for reading and commenting manuscripts and to Bo Zadig for helping me with printing and graphics. I would also like to thank Håkan Hansson for assisting me in many types of practical matters during my time as a PhD-student and for his quite direct approach when pushing me to finish this thesis.

Several people outside the Division of Structural Mechanics have further been important for the work presented in this thesis. I would in particular like to thank Erik Serrano at Linnaeus University for his support and for discussions on wood fracture modeling and Arne Emilsson at Limträteknik AB for interesting discussions on timber engineering.

Last but not least: Special thanks to Maria for being understanding, supportive and patient with me during the course of this work. Thanks also to Lukas and Meja, not for being patient, but for keeping my days busy and bringing lots of joy to my life.

Lund, April 2013
Henrik Danielsson

Abstract

This thesis concerns experimental and theoretical work regarding perpendicular to grain fracture in wooden structural elements. The experimental part concerns strength tests of glulam beams with a hole. The theoretical parts concern development of two models for strength and fracture analysis, both based on fracture mechanics approaches, and their application to analysis of beams with a hole and dowel-type connections loaded perpendicular to grain.

The experimental tests of glulam beams with a hole include investigations of influence of beam size, bending moment to shear force ratio and hole placement with respect to beam height. A strong influence of beam size on the nominal strength was found, increasing the beam height and length dimensions by a factor of 3.5 gave about 35% reduction in mean nominal strength. Eccentric hole placement with respect to beam height gave about 5-15% reduction in beam strength compared to tests of holes with centric placement.

A 2D probabilistic fracture mechanics method for strength analysis is further presented. This method is based on a combination of Weibull theory and a mean stress method, which is a generalization of Linear elastic fracture mechanics. Combining these two methods means that strength predictions are governed by both material strength and fracture energy and also that the stochastic nature of the material properties is taken into account. The method was applied to strength analysis of glulam beams with a hole. Based on comparison to results of experimental tests, the method appears to have fairly good ability to predict beam strength for large and medium-sized beams but overestimates the capacity of small beams.

A 3D cohesive zone model is further presented, formulated using theory of plasticity and accounting for orthotropic material behavior. The material model is applied to a predefined potential crack plane, within which a fracture process zone may initiate and evolve. The Tsai-Wu criterion is used as criterion for initiation of softening, meaning that all six stress components are allowed to influence the local softening behavior and hence also the global response. The material softening performance after the instant of softening initiation is governed by the three out-of-fracture-plane stress and deformation components, corresponding to crack opening and crack shear slip in two directions. The highly nonlinear global response, often including snap-back, is solved in an incremental-iterative fashion using either a Newton-Raphson method or an arc-length type of path following method. The cohesive zone model was used for fracture analysis of beams with a hole and symmetrically and asymmetrically loaded dowel-connections. Results relating to structural element global strength and fracture course, including the 2D extension of the fracture process zone, are presented. Results of numerical analyses are compared to results of experimental tests, showing overall good agreement both in terms of global strength and general characteristics of the fracture course.

Keywords: fracture mechanics, cohesive zone modeling, Weibull theory, wood, glulam, orthotropy, heterogeneity, hole, dowel, asymmetric loading

Populärvetenskaplig sammanfattning

Trä är ett konstruktionsmaterial med många positiva egenskaper, både avseende mekaniska och tekniska egenskaper och avseende det som ibland kallas *mjuka* egenskaper. Trä har generellt hög styrka i förhållande till sin vikt, det är ett naturligt förnybart material och det anses av många vara estetiskt tilltalande. Jämfört med andra vanliga konstruktionsmaterial som stål och betong har trä en rad unika och komplexa egenskaper. Bland annat är träs styrka och styvhet mycket olika i olika riktningar. Vid belastning i fiberriktningen är trä mycket starkt, men förhållandevis mycket svagt vid belastning tvärs fiberriktningen. Dragbelastning tvärs fiberriktningen, *tvärdragbelastning*, kan leda till tvärdrag- eller uppfläkningsbrott med initiering och propagering av en spricka med ett snabbt och sprött brottförlopp som resultat.

Tvärdragbelastning är en förhållandevis vanlig orsak till skador och kollaps av träkonstruktioner. En kollaps av en stor konstruktion, som exempelvis en idrottshall eller en bro, får alltid stora ekonomiska konsekvenser och kan även få allvarliga konsekvenser i form av personskador. Uppförande av en konstruktion föregås av dimensionering, vilket förenklat kan beskrivas som val av konstruktionssystem samt val av storlek och form på ingående konstruktionselement. Vanligtvis innefattar detta beräkningar för att säkerställa att konstruktionen med hög sannolikhet klarar av de laster den förväntas utsättas för. Vid dimensionering av träkonstruktioner är tvärdragbelastning av speciellt intresse, både med anledning av att trä är svagt vid denna typ av belastning och även för att motsvarande brottlaster är svåra att prediktera.

Syftet med arbetet som presenteras i denna avhandling är att öka kunskapen om träs beteende vid dragbelastning tvärs fiberriktningen, uppkomsten av tvärdragbrott samt hur brottlaster kan predikteras. Förhoppningen är att sådan kunskap i förlängningen ska kunna leda till säkrare, bättre och även billigare träkonstruktioner.

Arbetet som presenteras i denna avhandling består av en experimentell del och teoretiska delar. Den experimentella delen består av laboratorieprovningar av bärförmågan för limträbalkar med hål, som är ett typiskt exempel på ett konstruktionselement där risken för tvärdragbrott är stor. De teoretiska delarna innefattar utveckling av matematiska beräkningsmodeller och deras implementering för numeriska datorberäkningar samt användning av dessa modeller. Två olika modeller har utvecklats, en 2D modell för linjär analys och en mer avancerad 3D modell för olinjär analys inklusive simulering av det gradvisa brottförloppet från sprickinitiering till sprickpropagering. För att verifiera att modellerna ger användbara resultat jämförs dessa med resultat från experimentella tester avseende bärförmåga och brottbeteende. För den olinjära 3D modellen erhölls överlag god överensstämmelse mellan beräkningar och experimentella tester medan den linjära 2D modellen visade något sämre överensstämmelse. Modellerna har använts för analys av olika konstruktionselement där bärförmågan vanligtvis begränsas av tvärdragbrott, med fokus på balkar med hål och en typ av dymlingsförband. Dessa beräkningar ger möjlighet att undersöka brottbeteendet och hur detta påverkas av parametrar relaterade till belastning, geometri och materialegenskaper. Konkreta slutsatser inkluderar hur olika geometri- och lastparametrar påverkar brottförlopp och predikterad bärförmåga för de analyserade konstruktionselementen.

Contents

I Introduction and overview of present work 1

1 Introduction 3
1.1 General remarks 3
1.2 Problem statement 4
1.3 Aim of research 4
1.4 Research approach and limitations 5
1.5 Structure of thesis 6

2 Background 7
2.1 Material modeling and properties 7
2.1.1 Structural scales of wood 7
2.1.2 Linear elasticity and stiffness properties 9
2.1.3 Failure criteria and strength properties 12
2.1.4 Perpendicular to grain fracture properties 15
2.2 Global strength and fracture analysis methods 19
2.2.1 Conventional stress analysis 20
2.2.2 Weibull weakest link theory 20
2.2.3 Linear elastic fracture mechanics 24
2.2.4 Generalized Linear elastic fracture mechanics 28
2.2.5 Nonlinear fracture mechanics 30
2.3 Design in codes of practice 33
2.3.1 Beams with a hole 33
2.3.2 Dowel connections loaded perpendicular to grain 37

3 Overview of present work 39
3.1 Strength tests of glulam beams with a hole 39
3.2 A probabilistic fracture mechanics method 40
3.3 A cohesive zone model based on plasticity theory 44

4 Conclusions 49
4.1 Strength of glulam beams with a hole 49
4.2 Fracture analysis models and applications 50
4.3 Proposals for future work 51

Bibliography 53

II Attachment

Path following solution approaches and integration of constitutive relations for a 3D wood cohesive zone model
Henrik Danielsson
Report TVSM-7160, Division of Structural Mechanics, Lund University, 2013.

III Appended Papers

Paper A
Strength tests of glulam beams with quadratic holes – Test report
Henrik Danielsson
Report TVSM-7153, Division of Structural Mechanics, Lund University, 2008.

Paper B
Strength of glulam beams with holes – Tests of quadratic holes and literature test result compilation
Henrik Danielsson and Per Johan Gustafsson
CIB-W18/41-12-4, St Andrews, Canada, 2008.

Paper C
A probabilistic fracture mechanics method for strength analysis of glulam beams with holes
Henrik Danielsson and Per Johan Gustafsson
European Journal of Wood and Wood Products 69:407-419, 2011.

Paper D
A three dimensional plasticity model for perpendicular to grain cohesive fracture in wood
Henrik Danielsson and Per Johan Gustafsson
Engineering Fracture Mechanics 98:137-152, 2013.

Paper E
Fracture analysis of glulam beams with a hole using a 3D cohesive zone model
Henrik Danielsson and Per Johan Gustafsson
Submitted for publication

Paper F
Fracture analysis of perpendicular to grain loaded dowel-type connections using a 3D cohesive zone model
Henrik Danielsson and Per Johan Gustafsson
Submitted for publication

Part I

Introduction and overview of present work

1 Introduction

1.1 General remarks

Wood is a structural material with many appealing properties. The material has in general a high strength to weight ratio, it is a renewable resource and it is also by many considered to be esthetically appealing. Compared to other commonly used structural materials such as steel and concrete, wood do however possess some unique and complex properties. One important example is the anisotropy, with strength and stiffness properties being very much different for different orientations of the load. Wood is in general strong and stiff when loaded parallel to grain, but relatively weak when loaded perpendicular to grain. The most troublesome modes of loading are commonly tension perpendicular to grain and shear. Excessive loading in these modes causes perpendicular to grain fracture and cracking along grain which may occur in a very brittle manner without much prior warning by for example excessive deformations.

Due to the strongly anisotropic strength properties, an aim in design should be to avoid or at least limit loading in weak directions of the material. There are however a number of technical solutions, which may be desirable for engineering or architectural reasons, that induce a state of stress giving risk for perpendicular to grain fracture. Some examples are given in Figures 1.1 and 1.2. Perpendicular to grain fracture is in general complicated to predict and there appears to be a lack of knowledge regarding its modeling. This is in timber design codes of practice reflected by absence of design criteria, or presence of questionable design criteria, for structural elements exposed to perpendicular to grain tension and shear.

Perpendicular to grain fracture is a relatively common type of damage for timber structures, see e.g. [35], [37] and [38]. Structural damage and collapse may be very costly, both in terms of pure economic costs and also in terms of human injuries or fatalities. Safe and reliable structural design is hence of great importance. This is closely related to knowledge about material and structural behavior and its modeling. Proper design is further dependent on this knowledge being incorporated into design codes and in the extension also how this knowledge is dealt with in practical design and during construction. The theme of the research presented in this thesis is the development of knowledge regarding perpendicular to grain fracture in terms of material and structural behavior and its modeling.

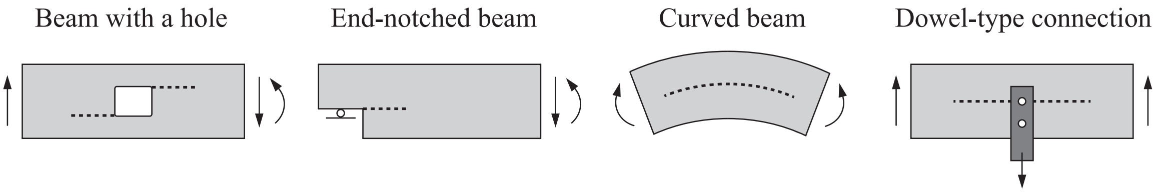

Figure 1.1: Examples of structural elements with risk for perpendicular to grain fracture.

Figure 1.2: Ideon Science Park in Lund (top left, top right, bottom left) and indoor swimming pool in Västerås (bottom right, with permission from Martinssons Trä AB).

1.2 Problem statement

Perpendicular to grain fracture, caused by perpendicular to grain tensile stress and shear stress, is a major concern in timber engineering and a relatively common cause for structural damage. This is partly due to lack of knowledge and shortcomings in contemporary methods for wood fracture modeling and prediction of strength of wooden structural elements exposed to perpendicular to grain tension and shear.

1.3 Aim of research

In a wide perspective, the aim of the research presented in this thesis is to contribute to better timber and glulam structures. In a more confined sense, the aim is to develop fracture mechanics calculation methods suitable for general fracture simulation and strength prediction for applications where fracture perpendicular to grain is of importance.

A vehicle in such development is examples of applications which give the possibility to test, calibrate and verify calculation methods. In this context are two sub-aims defined: investigation of strength and fracture performance of beams with a hole and investigation of wood fracture at symmetrically and asymmetrically loaded dowels.

1.4 Research approach and limitations

The work presented in this thesis consists of an experimental part and a theoretical part including model development and applications. The experimental part concerns glulam beams with a hole. The theoretical part includes development of two models for strength analysis with respect to perpendicular to grain fracture in wood. The applications relate to beams with a hole and dowel-type connections loaded perpendicular to grain.

Literature studies concerning experimental tests and methods for strength analysis with respect to perpendicular to grain fracture was carried out, focusing on the considered applications of beams with a hole and dowel-type connections. Although much research effort has been but into these areas, a need for increased knowledge regarding strength, modeling and design with respect to perpendicular to grain fracture was identified.

Based on identified needs for experimental investigations, laboratory short term strength tests of glulam beams with a hole have been carried out within the work presented here. The test program concerns investigations of design parameters of importance in practical design, including parameters which appear not to have been tested before.

Within the theoretical work, two different models for global strength and fracture analysis with respect to perpendicular to grain fracture were developed. Both models are based on fracture mechanics approaches and have been implemented for FE-analysis. Testing and verification of the models were carried out by means of comparison of results from numerical calculations and results of experimental tests, including tests carried out within the work presented here and tests found in the literature. The testing and verification of models was focused on analysis of beams with a hole and dowel connections loaded perpendicular to grain. The models have further been used for numerical parameter studies relating to influence of different parameters assumed to be of importance for the global strength of the considered applications. Based on these analyses, and assuming the strength analysis models to yield reliable and accurate results, practically relevant conclusions regarding the perpendicular to grain fracture performance of the considered structural elements have been drawn. Results of experimental tests and numerical analyses were also compared to strength predictions according to design criteria found in codes of practice, in order to evaluate their reliability and strength predicting capabilities.

The general character of the considered strength analysis models allows for application to a wide variety of wooden structural elements where perpendicular to grain fracture is of importance. The presented models are however hardly suitable in a conventional practical design context and their usefulness is hence most likely limited to research activities and possibly to special practical engineering cases. Such cases may include analysis of specific structural elements where simplified approaches, such as the ones commonly found in design codes and handbooks, are assumed to be insufficient.

The work presented in this thesis is further subjected to the following general limitations:

- only short term quasi-static loading is considered
- climate effects such as moisture and temperature are not considered
- wood material is in modeling regarded as continuous, orthotropic with homogeneous or heterogeneous orientation of material directions, with deterministic or stochastic properties, and linear elastic outside the fracture process zone
- glue-lines in glulam and LVL are not explicitly considered in modeling
- small strains are assumed and geometrically nonlinear effects are disregarded in modeling

1.5 Structure of thesis

The thesis is divided into three parts with the following contents:

Part I of the thesis is divided into four chapters, including this one. General background regarding wood material modeling, material properties and global strength and fracture analysis methods regarding perpendicular to grain fracture, including code design methods, are presented in Chapter 2. An overview of the present work is given in Chapter 3, in the form of summaries of the work relating to experimental testing and perpendicular to grain fracture modeling and applications presented in the appended papers. Conclusions drawn from the present work and proposals for future work are finally given in Chapter 4.

Part II concerns the numerical implementation used for the cohesive zone model presented in Paper D and used in Papers E and F. The nonlinear finite element formulation, solution approaches for the global equations of equilibrium and integration of incremental constitutive relations are considered.

Part III of the thesis holds the six appended papers. Papers A and B deal with experimental tests of glulam beams with a hole. In Paper C is a probabilistic fracture mechanics method presented and applied to strength analysis of glulam beams with a hole. In Paper D is a 3D cohesive zone model presented, derived within the framework of theory of plasticity. This cohesive zone model is applied to analysis of beams with a hole in Paper E and to analysis of dowel-type connections loaded perpendicular to grain in Paper F.

2 Background

2.1 Material modeling and properties

2.1.1 Structural scales of wood

Wood is a natural, heterogeneous and cellular material. The mechanical behavior is complex and affected by for example duration of load, moisture content and temperature. The characteristics of the material may be described and modeled as a continuous media at different scales, ranging from the components of the cells walls to massive structural members. These scales may be differentiated into the *macro scale*, the *meso scale* and the *micro scales*. A brief presentation of characteristic features and modeling aspects on these scales is given below. The presentation concerns softwoods and is based on [15], [27] and [55] where specific references are not given. The material modeling approaches used within the work presented in this thesis relate to 2D and 3D representation on the macro scale.

Macro scale

Mechanical behavior and properties may on the macro scale be characterized using distinction between three orthogonal directions as depicted in Figure 2.1: the longitudinal L, the radial R and the tangential T direction. The R- and T-directions are defined from the growth ring orientation and the L-direction is defined as being aligned with the direction of the wood fibers, i.e. in the direction of the grain. The L-direction is however not necessarily fully aligned with the longitudinal direction of the tree stem, due to possible log taper and spiral growth [69]. The macro scale is the level of representation commonly used for 2D and 3D stress and fracture analysis of wood. 3D continuum representation commonly involves rectilinear or cylindrical orthotropy. Wood is for 2D plane strain or plane stress analysis in the LR- and LT-planes commonly modeled as a homogeneous and transversely isotropic material while RT-plane analysis may involve consideration of the circular growth ring pattern.

Natural imperfections such as knots, growth ring irregularities, resin pockets and other defects develop in the tree during the growth process. The term *clear wood* refers to material volumes free from defects having major influence on the mechanical behavior. Wooden elements of common structural size do however in general contain such defects. Explicit modeling of gross defects such as knots is feasible although such an approach is not utilized within the work presented here. Wood do further in general display considerable variation in mechanical properties between species, between different logs of the same species and within a single log. This variability, which may be random or structured, can in modeling be accounted for by use of probabilistic approaches such as Weibull theory or so called Monte Carlo simulations.

Within the theoretical work presented in this thesis, considerations of stochastic variability of material properties according to Weibull theory are included in the probabilistic fracture mechanics method presented in Paper C. This approach is based on linear elastic plane stress analysis considering a transversely isotropic material model with homogeneous orientation of material principal directions. For the 3D cohesive zone model considered in Papers D, E and F is a deterministic approach used meaning that the material properties are assumed to be known for all points. This model accounts for heterogeneous orientation of material principal directions using cylindrical orthotropy.

Meso scale

The meso scale is here referred to as the scale of the growth rings. The structure of wood on the meso scale is closely related to the growing process of the tree. The radial growth takes place in the so called cambium which is located just inside the bark. During one growth season, a new growth ring is formed which consists of earlywood and latewood. The earlywood is formed during the first part of the growth season and latewood during the later part. Compared to the earlywood, the latewood has a darker color and also thicker cell walls and higher density [69]. Other features present on the meso scale are resin canals and rays. The resin canals are tubular spaces containing resin and are oriented mainly in the longitudinal direction. The rays extend in the radial direction and are in the living tree used for transportation of nutrients. Mechanical modeling on the meso scale may use a heterogeneous continuum representation with different properties for earlywood and latewood respectively. Such an approach have for example been used for RT-plane analysis of fracture [63] and global stiffness [64]. Meso scale modeling is not further considered within the work presented in this thesis.

Micro scales

The micro scales are here referred to as all scales below the meso scale, i.e. the cell structure, the cells and the cell components. The cells are hollow, tube-like structures with the longitudinal axis approximately parallel to the tree stem longitudinal axis. An example of cell structure within one growth ring is found in Figure 2.1. The clear wood mechanical properties are governed by the mechanical characteristics on the micro scale, i.e. by the cell structure and the properties of the cell wall components. Wood micro scale modeling approaches and homogenization techniques are for example considered in [52], [53] and [69] and reviews of approaches are found in [50] and [62]. The material behavior and properties on the micro scale is not explicitly considered within the work presented in this thesis.

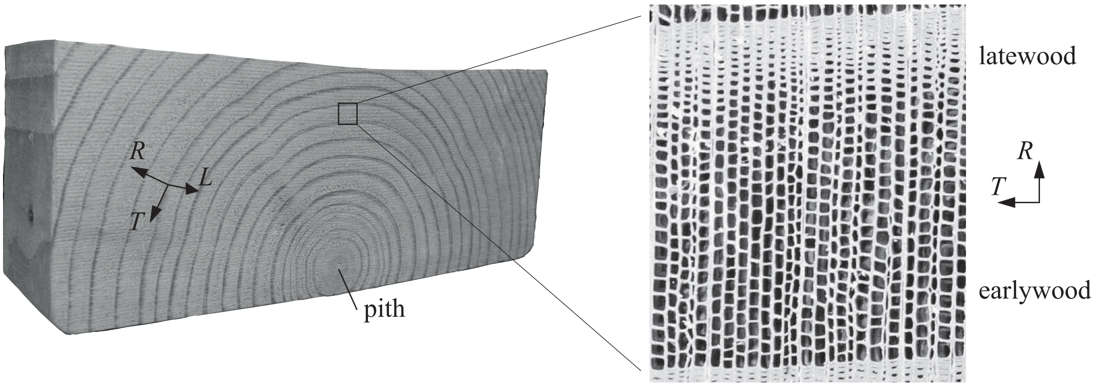

Figure 2.1: Growth ring pattern and cellular pattern for one growth ring of Norway spruce.

2.1.2 Linear elasticity and stiffness properties

For 3D continuum representation on the macro scale – assuming small strains and considering orthotropy with material principal directions defined by the longitudinal L, radial R and tangential T directions – may the linear elastic response be expressed by Hooke's generalized law as

$$\bar{\boldsymbol{\sigma}} = \bar{\mathbf{D}}\bar{\boldsymbol{\varepsilon}}^e \tag{2.1}$$

where $\bar{\boldsymbol{\varepsilon}}^e$ is the elastic strain vector which in the case of plastic strains $\bar{\boldsymbol{\varepsilon}}^p$ are taken as $\bar{\boldsymbol{\varepsilon}}^e = \bar{\boldsymbol{\varepsilon}} - \bar{\boldsymbol{\varepsilon}}^p$. The total strain vector $\bar{\boldsymbol{\varepsilon}}$ and the stress vector $\bar{\boldsymbol{\sigma}}$ are in the material directions LRT given by

$$\bar{\boldsymbol{\varepsilon}} = \begin{bmatrix} \varepsilon_{LL} & \varepsilon_{RR} & \varepsilon_{TT} & \gamma_{LR} & \gamma_{LT} & \gamma_{RT} \end{bmatrix}^T \tag{2.2}$$

$$\bar{\boldsymbol{\sigma}} = \begin{bmatrix} \sigma_{LL} & \sigma_{RR} & \sigma_{TT} & \tau_{LR} & \tau_{LT} & \tau_{RT} \end{bmatrix}^T \tag{2.3}$$

The material stiffness matrix $\bar{\mathbf{D}}$ in material directions is defined according to [15]

$$\bar{\mathbf{D}} = \bar{\mathbf{C}}^{-1} \tag{2.4}$$

$$\bar{\mathbf{C}} = \begin{bmatrix} \frac{1}{E_L} & -\frac{\nu_{RL}}{E_R} & -\frac{\nu_{TL}}{E_T} & 0 & 0 & 0 \\ -\frac{\nu_{LR}}{E_L} & \frac{1}{E_R} & -\frac{\nu_{TR}}{E_T} & 0 & 0 & 0 \\ -\frac{\nu_{LT}}{E_L} & -\frac{\nu_{RT}}{E_R} & \frac{1}{E_T} & 0 & 0 & 0 \\ 0 & 0 & 0 & \frac{1}{G_{LR}} & 0 & 0 \\ 0 & 0 & 0 & 0 & \frac{1}{G_{LT}} & 0 \\ 0 & 0 & 0 & 0 & 0 & \frac{1}{G_{RT}} \end{bmatrix} \tag{2.5}$$

where E_i, G_{ij} and ν_{ij} denote the three moduli of elasticity, the three moduli of shear and the six Poisson's ratios for which the following relations hold

$$\frac{\nu_{RL}}{E_R} = \frac{\nu_{LR}}{E_L}\,, \qquad \frac{\nu_{TL}}{E_T} = \frac{\nu_{LT}}{E_L}\,, \qquad \frac{\nu_{TR}}{E_T} = \frac{\nu_{RT}}{E_R} \tag{2.6}$$

Hooke's law may also be expressed in global directions xyz according to

$$\boldsymbol{\sigma} = \mathbf{D}\boldsymbol{\varepsilon}^e = \mathbf{D}(\boldsymbol{\varepsilon} - \boldsymbol{\varepsilon}^p) \tag{2.7}$$

$$\boldsymbol{\varepsilon} = \begin{bmatrix} \varepsilon_{xx} & \varepsilon_{yy} & \varepsilon_{zz} & \gamma_{xy} & \gamma_{xz} & \gamma_{yz} \end{bmatrix}^T \tag{2.8}$$

$$\boldsymbol{\sigma} = \begin{bmatrix} \sigma_{xx} & \sigma_{yy} & \sigma_{zz} & \tau_{xy} & \tau_{xz} & \tau_{yz} \end{bmatrix}^T \tag{2.9}$$

where the strain $\boldsymbol{\varepsilon}$, the stress $\boldsymbol{\sigma}$ and the stiffness matrix $\mathbf{D}$ are expressed in global directions. Transformation between local and global directions can be made using a transformation matrix defined by the direction cosines between the respective coordinate axes [15].

Comprehensive compilations of elastic parameters for various wood species taken from test reports are for example presented in [27], [46] and [55]. Some typical values for softwood species Spruce and Pine found in the literature are given in Table 2.1. Parameters presented by Berbom Dahl [14] are based on a recent and substantial test program using small clear wood specimens of Norway spruce (*Picea Abies*) with mean density 398 kg/m^3 and moisture content 12%. Mean stiffness values for some material strength classes of structural timber according to EN 338:2009 [30] and of glulam according to EN 1194:1999 [31] are also given in Table 2.1.

Table 2.1: Stiffness parameters in MPa and Poisson's ratios for softwoods found in literature.

Species / Class	ref	E_L	E_R	E_T	G_{LR}	G_{LT}	G_{RT}	ν_{LR}	ν_{RL}	ν_{LT}	ν_{TL}	ν_{RT}	ν_{TR}
Norway spruce	[14]	9 040	790	340	640	580	30	0.50	0.11	0.66	0.06	0.84	0.34
Spruce	[19]	10 700	710	430	500	620	23	0.38	0.03	0.51	0.03	0.51	0.31
Spruce	[46]	13 500	890	480	500	700	30		0.03	0.54			0.60
Scots pine	[65]	11 000	1000	500		680	70	0.46	0.03	0.44	0.02	0.61	0.31
Timber, C16	[30]	8 000	270	270	500	500							
Timber, C24	[30]	11 000	370	370	690	690							
Timber, C40	[30]	14 000	470	470	880	880							
Glulam, GL 24h	[31]	11 600	390	390	720	720							
Glulam, GL 32h	[31]	13 700	460	460	850	850							
Glulam, GL 36h	[31]	14 700	490	490	910	910							

The parallel to grain stiffness E_L is far greater than the two perpendicular to grain stiffnesses. The two perpendicular to grain stiffnesses E_R and E_T are of similar magnitude, although E_R in general is greater than E_T. Another characteristic property of softwoods is the very low rolling shear stiffness G_{RT}. Due to the large difference between longitudinal stiffness and radial- and tangential stiffnesses respectively, material models for timber engineering applications are often simplified by assuming a transversely isotropic behavior and hence distinguishing between only two material directions: the parallel to grain direction and the perpendicular to grain direction. This simplification is implicitly included in 2D *LR*- and *LT*-plane stress and fracture analyses. 3D analyses are often simplified by assuming homogeneous material principal directions and the typically cylindrical growth ring pattern is hence ignored.

The orthotropy within the *RT*-plane may however be of importance for perpendicular to grain strength and stiffness, i.e. in relation to deformation of cross ties and dowel joints and also for fracture mechanics strength analyses. For a plane state of stress in the *RT*-plane according to Figure 2.2, the stiffness E_y for uniaxial loading in the y-direction is given by [45]

$$\sigma_{yy} = E_y \varepsilon_{yy} \quad \text{where} \quad E_y = \left(\sin^4\alpha \, \frac{1}{E_R} + \cos^2\alpha \, \sin^2\alpha \left(\frac{1}{G_{RT}} - \frac{2\nu_{RT}}{E_T} \right) + \cos^4\alpha \frac{1}{E_T} \right)^{-1} \tag{2.10}$$

which is valid for a material point and also for a homogeneously loaded finite volume with homogeneous orientation of material directions. The influence of α on the stiffness according to Equation (2.10) is depicted in Figure 2.3a) based on stiffness parameter ratios $E_R/E_T = 2.32$, $G_{RT}/E_T = 0.088$ and $\nu_{RT} = 0.84$ reported in [14]. The low stiffness value at $\alpha = 45°$, being only 33% of the tangential stiffness and 14% of the radial stiffness, is mostly due to the low rolling shear stiffness G_{RT}.

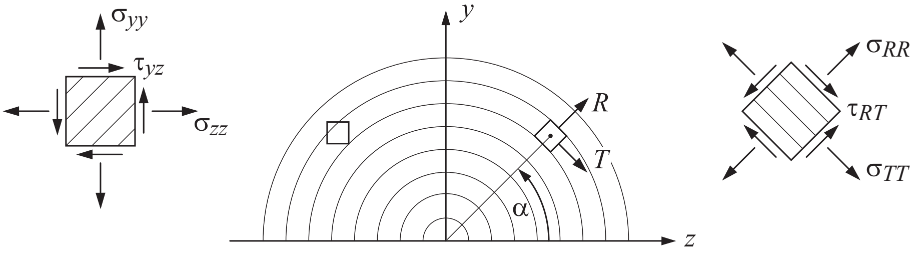

Figure 2.2: Illustration of local and global stress components in the plane perpendicular to grain.

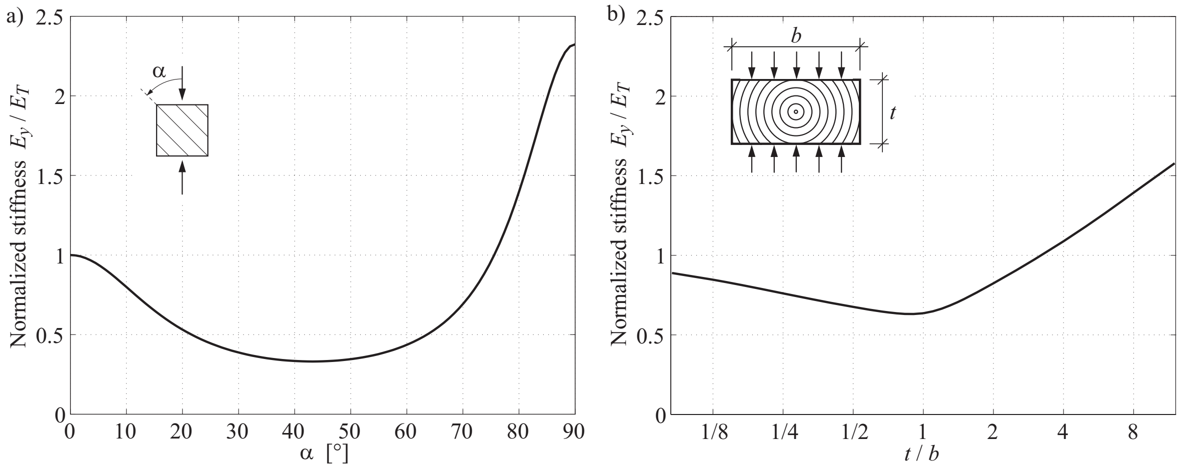

Figure 2.3: Influence of orientation of material directions on stiffness for a material point (a) and on global stiffness for a board [45] (b).

The orientation of material directions within a timber board or glulam cross section of common structural size is in general not homogeneous, but varies due the cylindrical shape of the growth rings. Numerical studies of the global stiffness of rectangular wood cross sections as affected by their size, shape and growth ring pattern are presented in [45]. The influence of cross section shape found from FE-analysis of a board with a specific growth ring pattern is given in Figure 2.3b).

Due to the strongly orthotropic stiffness properties in the RT-plane, the stress distribution within a glulam cross section or a board loaded perpendicular to grain may be very heterogeneous also for the case of a uniformly distributed external stress. Linear elastic stress distributions σ_{yy} are presented in Figure 2.4 for two glulam cross sections with slightly different lamella growth ring patterns. The maximum value of σ_{yy} is for both cross sections more than twice the uniformly distributed external stress σ_0. Studies of the linear elastic stress distribution within glulam cross sections containing several lamellas are presented in [4] and [10], considering various different lamella growth ring patterns. Ratios between the externally applied stress and maximum perpendicular to grain tensile stress of 2-4 are reported.

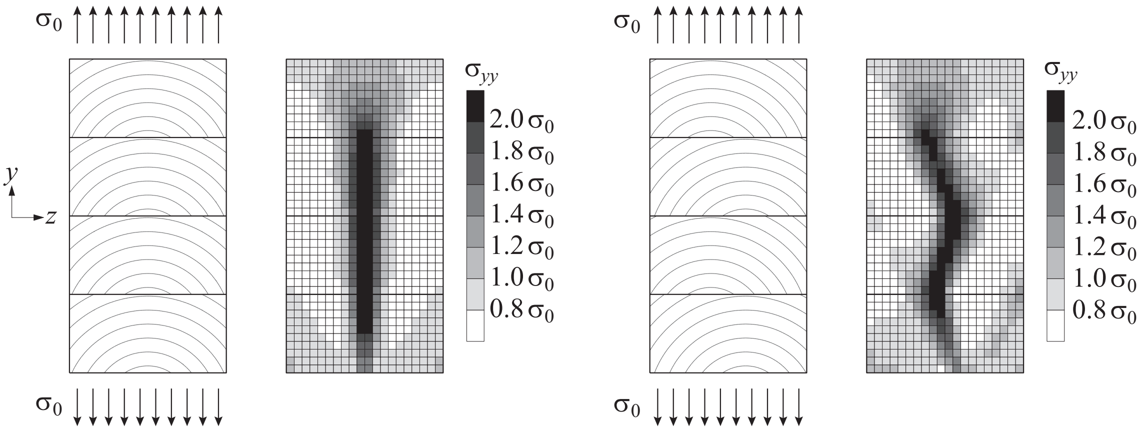

Figure 2.4: Stress distributions σ_{yy} at a uniformly applied stress σ_0.

The RT-plane orthotropy may be of great importance also for the case of compressive loading. Experimental tests and stress analysis of glulam cross sections loaded in compression are presented in [20]. The tests revealed a failure mode with cracks spreading in the direction of the load, i.e. in the cross section height direction. Linear elastic stress analysis of the cross sections forwarded local tension stress in the direction perpendicular to the applied load of about 40% of nominal compressive stress.

2.1.3 Failure criteria and strength properties

The strength and the failure types are for wood very different for different modes of loading. The material may for moderate loading be considered to respond linearly elastic while different types of material nonlinearities are present beyond limits of proportionality. These nonlinearities are manifested in different ways for different types of loading. Schematic illustrations of the material behavior for uniaxial loading parallel and perpendicular to grain are given in Figure 2.5. Limits of proportionality, i.e. the limit between what can be considered as a linear and a nonlinear stress vs. strain response respectively, are in the figure illustrated by dots. For compression parallel or perpendicular to grain, the response may be characterized as elasto-plastic in the sense that stiffness decreases at increasing strain and irrecoverable deformations occur at excessive loading. The underlying mechanisms are however profoundly different from the ones present in metal plasticity [86]. The behavior in tension is commonly much more brittle.

Failure is in practical timber engineering often assessed by linear elastic stress analysis and the use of a stress based failure criterion. Such an approach enables convenient and relatively simple assessment of the strength of loaded elements, by assuming that the capacity of the considered element drops to zero once the failure criterion is fulfilled. Since stress redistribution effects and other material nonlinear effects are disregarded, strength predictions for structural elements showing high stress gradients will in general be unreliable.

There are numerous suggestions for wood failure criteria in the literature, among which a few are briefly reviewed below. The failure criteria are here expressed using a representation considering material principal directions LRT. The notation used for the uniaxial normal strengths is f_{Li}, f_{Ri} and f_{Ti} where index i represents tension ($i = t$) or compression ($i = c$). All strengths are defined by positive numbers, i.e. a material which is assumed to fail at a compressive stress $\sigma = -5$ MPa has the compressive strength $f_c = 5$ MPa. The shear strengths are independent of sign of the shear stress and denoted f_{LR}, f_{LT} and f_{RT}.

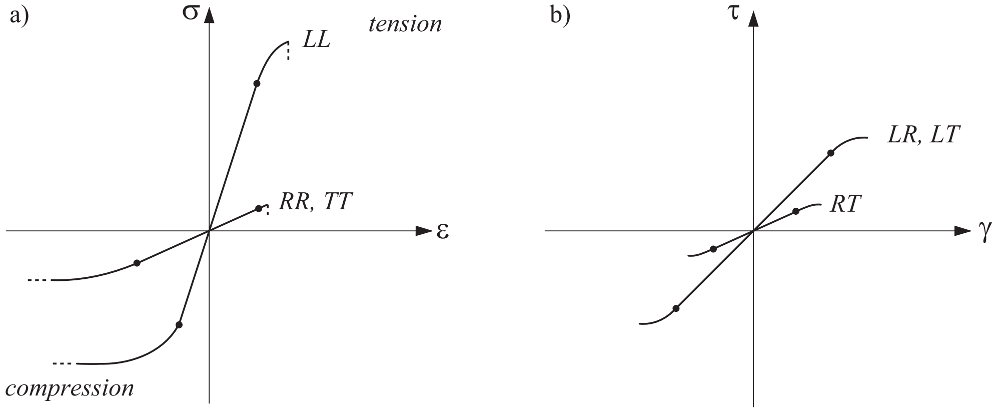

Figure 2.5: Schematic illustrations of wood behavior in tension/compression (a) and shear (b).

Failure criteria may also be used as base for modeling nonlinear material behavior, i.e. as criteria for initiation of hardening or softening using theory of plasticity or theories related to nonlinear fracture mechanics or damage mechanics.

Maximum stress criterion

A common failure criterion, used for both uniaxial and multiaxial stress states, is the maximum stress criterion where each stress component is considered separately. Maximum stress criterion for a 3D stress state may formally be expressed as

$$\max\left\{\frac{|\sigma_{LL}|}{f_{Li}}, \frac{|\sigma_{RR}|}{f_{Ri}}, \frac{|\sigma_{TT}|}{f_{Ti}}, \frac{|\tau_{LR}|}{f_{LR}}, \frac{|\tau_{LT}|}{f_{LT}}, \frac{|\tau_{RT}|}{f_{RT}}\right\} - 1 = 0 \tag{2.11}$$

where the strengths with respect to normal stress in the three material directions may have different values with respect to compression ($i = c$) and tension ($i = t$).

Norris criteria

Commonly used criteria for wood are the ones proposed by Norris [67]. For 3D applications and considering possible failure in the three principal planes of the material, one of Norris' criteria may be expressed as

$$\max\left\{\begin{array}{l} \left(\frac{\sigma_{LL}}{f_{Li}}\right)^2 + \left(\frac{\sigma_{RR}}{f_{Ri}}\right)^2 + \left(\frac{\tau_{LR}}{f_{LR}}\right)^2 - \frac{\sigma_{LL}}{f_{Li}}\frac{\sigma_{RR}}{f_{Ri}} \\ \left(\frac{\sigma_{LL}}{f_{Li}}\right)^2 + \left(\frac{\sigma_{TT}}{f_{Ti}}\right)^2 + \left(\frac{\tau_{LT}}{f_{LT}}\right)^2 - \frac{\sigma_{LL}}{f_{Li}}\frac{\sigma_{TT}}{f_{Ti}} \\ \left(\frac{\sigma_{RR}}{f_{Ri}}\right)^2 + \left(\frac{\sigma_{TT}}{f_{Ti}}\right)^2 + \left(\frac{\tau_{RT}}{f_{RT}}\right)^2 - \frac{\sigma_{RR}}{f_{Ri}}\frac{\sigma_{TT}}{f_{Ti}} \end{array}\right\} - 1 = 0 \tag{2.12}$$

which must be applied in a piecewise manner if the tensile strengths f_{Lt}, f_{Rt} and f_{Tt} are different from the corresponding compressive strengths f_{Lc}, f_{Rc} and f_{Tc}. Each of the three equations represents a closed surface in the respective stress spaces. These surfaces do however have discontinuous slopes if the tensile and compressive strengths in the respective material directions differ.

Norris also suggested a simplified version of the above given criterion for the case of plane stress. For plane stress within a plane parallel and perpendicular to grain, the criterion reads

$$\left(\frac{\sigma_{LL}}{f_{Li}}\right)^2 + \left(\frac{\sigma_{PP}}{f_{Pi}}\right)^2 + \left(\frac{\tau_{LP}}{f_{LP}}\right)^2 - 1 = 0 \tag{2.13}$$

where index P here denotes the perpendicular to grain direction.

Tsai-Wu criterion

The Tsai-Wu criterion [89] is often proposed as a suitable failure criterion for wood. It includes orthotropic strength properties and also allows different tensile and compressive strengths in the three material principal directions. The Tsai-Wu failure criterion can be expressed in matrix format according to

$$\bar{\boldsymbol{\sigma}}^T\bar{\mathbf{q}} + \bar{\boldsymbol{\sigma}}^T\bar{\mathbf{P}}\bar{\boldsymbol{\sigma}} - 1 = 0 \tag{2.14}$$

where $\bar{\boldsymbol{\sigma}}$ is defined in Equation (2.3). The Tsai-Wu matrices $\bar{\mathbf{q}}$ and $\bar{\mathbf{P}}$ are given by

$$\bar{\mathbf{q}} = \begin{bmatrix} F_{LL} \\ F_{RR} \\ F_{TT} \\ 0 \\ 0 \\ 0 \end{bmatrix} \quad \text{and} \quad \bar{\mathbf{P}} = \begin{bmatrix} F_{LLLL} & F_{LLRR} & F_{LLTT} & 0 & 0 & 0 \\ F_{LLRR} & F_{RRRR} & F_{RRTT} & 0 & 0 & 0 \\ F_{LLTT} & F_{RRTT} & F_{TTTT} & 0 & 0 & 0 \\ 0 & 0 & 0 & F_{LRLR} & 0 & 0 \\ 0 & 0 & 0 & 0 & F_{LTLT} & 0 \\ 0 & 0 & 0 & 0 & 0 & F_{RTRT} \end{bmatrix} \tag{2.15}$$

where the nine components F_{ii}, F_{iiii} and F_{ijij} are defined by the uniaxial tensile strengths f_{it}, the uniaxial compressive strengths f_{ic} and the shear strengths f_{ij} according to

$$\begin{aligned} F_{ii} &= 1/f_{it} - 1/f_{ic} && i = L, R, T \\ F_{iiii} &= 1/(f_{it} f_{ic}) && i = L, R, T \\ F_{ijij} &= 1/f_{ij}^2 && i, j = L, R, T \quad (i \neq j) \end{aligned} \tag{2.16}$$

The three remaining components F_{iijj} $(i \neq j)$, usually denoted *strength interaction coefficients* or *coupling coefficients*, relate to interaction of normal stress components and must be determined from uniaxial off-axis tests or biaxial tests. The strength interaction coefficients must satisfy

$$F_{iiii} F_{jjjj} - F_{ijij} \geq 0 \qquad i, j = L, R, T \quad (i \neq j) \tag{2.17}$$

in order for the surface defined by Equation (2.14) to intersect all stress axes and to form a closed surface in the stress space. This inequality is for example satisfied for $F_{ijij} = 0$, since F_{iiii} and F_{jjjj} are always positive.

Strength properties

The strength parameters used for description of the material and for strength analysis are in general different when considering structural sized elements in a timber engineering design context and when considering clear wood volumes free from defects. Natural defects, such as knots, may be of great importance for the strength properties. For tension or bending of a structural sized beam with grain direction essentially parallel to the beam axis, knots will in general reduce the strength since locally (around the knot) the grain direction deviates from the beam axis and perpendicular to grain stress is hence introduced. For applications with tensile stress perpendicular to the nominal direction of the grain, knots may instead act as reinforcement and hence increase strength [44].

Timber engineering design according to codes and handbooks is in general based on characteristic (5^{th} percentile) strength values. These values are determined from direct tests performed in a standardized way or alternatively determined based on relations to other material properties which are determined by tests. The specimen size is usually such that the tested material contains defects such as knots and grain deviation which are also present in the actual structural elements. These strength properties may hence be thought of as being defined on the element level rather than on the material point level [88]. For research purposes, material strength properties are also tested using clear wood specimens. A compilation of wood strength values for softwoods of different species is given in Table 2.2, based on results of comprehensive experimental studies by Berbom Dahl [14], Eberhardsteiner [29] and Hemmer [47]. For comparison, characteristic strength values for some material strength classes of structural timber according to EN 338:2009 [30] and of glulam according to EN 1194:1999 [31] are also given.

The strength values presented by Berbom Dahl [14] represent tests of clear wood specimens of Norway spruce (*Picea Abies*) with mean density 398 kg/m^3 and mean moisture content 12%.

Table 2.2: Material strength properties in MPa for softwoods.

Species	ref.	f_{Lt}	f_{Lc}	f_{Rt}	f_{Rc}	f_{Tt}	f_{Tc}	f_{LR}	f_{LT}	f_{RT}
Norway spruce	[14]	63	29	4.9	3.6	2.8	3.8	6.1	4.4	1.6
Spruce	[29]	75	50	4.9	7.0			8.6		
Silver fir	[47]	56	43			3.7	5.6		9.9	
Timber, C16	[30]	10	17	0.4	2.2	0.4	2.2	3.2	3.2	
Timber, C24	[30]	14	21	0.4	2.5	0.4	2.5	4.0	4.0	
Timber, C40	[30]	24	26	0.4	2.9	0.4	2.9	4.0	4.0	
Glulam, GL 24h	[31]	16.5	24	0.4	2.7	0.4	2.7	2.7	2.7	
Glulam, GL 32h	[31]	22.5	29	0.5	3.3	0.5	3.3	3.8	3.8	
Glulam, GL 36h	[31]	26	31	0.6	3.6	0.6	3.6	4.3	4.3	

For the tensile tests, the response was relatively linear almost all the way to maximum load and the failure mode was brittle. Higher degree of nonlinearity was found for the compressive tests, where especially the compression tests in the R- and T-directions showed high ductility. The shear strength tests were conducted using small, butterfly-like specimens and the so called Arcan shear test method.

Results presented by Eberhardsteiner [29] relate to some 750 tests of Spruce clear wood specimens loaded uniaxially and biaxially in the LR-plane. The material tested had a mean moisture content of 12% and density within the range 277-631 kg/m^3. Tests presented by Hemmer [47] relate to European silver fir (*Abies alba*) with a mean density of 442 kg/m^3. The tests were performed using hollow cylindrical specimens loaded by internal and external pressure, normal force and torsion. The strength values from [29] and [47] given in Table 2.2 were determined by fitting Tsai-Wu failure surfaces to experimentally found strength values.

An important aspect when it comes to wood strength properties is size effects, manifested as decreasing nominal strength for increasing stressed volume. This effect is well known for perpendicular to grain tensile loading, see i.e. [3] and [44] for compilations of strength tests of specimens of different sizes. The compilation in [3] concerns uniaxial tensile tests and comprises 20 test series with a minimum of 10 individual tests within each series. The test series represent specimen volumes within the range 0.027-30 dm^3 and reported mean strengths vary between approximately 3 MPa for the smallest specimens and approximately 0.65 MPa for the largest specimens. Expressing the influence of specimen volume Ω on the strength f_t according to $f_t \propto \Omega^{-1/m}$, the value $m = 4.8$ was found to conform well to the volume influence found from the experimental tests.

2.1.4 Perpendicular to grain fracture properties

The *fracture energy* is a fundamental property for global strength and fracture analysis using approaches within the framework of fracture mechanics. Within Nonlinear fracture mechanics (NLFM), as defined in Section 2.2.5, the fracture energy is denoted G_f and is the work of fracture and defined as the energy dissipated within a fracture process zone during its gradual development from formation to creation of a unit area of traction-free crack [44]. Within Linear elastic fracture mechanics (LEFM), see Section 2.2.3, is a closely related quantity denoted the *critical energy release rate* G_c used. This quantity is defined as the energy required to propagate an initial and sharp crack by a unit area, the energy being dissipated at the tip of the crack as it propagates.

The two energy quantities G_c and G_f are hence very closely related but not strictly identically defined [5]. The quantity G_c is commonly determined from the experimentally found load at which a sharp existing crack propagates. The quantity G_f is instead determined from the work required to bring a specimen, with or without a notch, to complete fracture by a stable test run in displacement control and evaluated from the load vs. displacement curve. The two quantities G_c and G_f are theoretically equal for an ideally elastic material behavior outside the fracture process zone [5] and the term *fracture energy* is often used to refer also to G_c.

The energy required for crack propagation in anisotropic materials is in general dependent on the orientation of the crack plane and the mode of loading. The orthotropic nature of wood gives three possible principal crack plane orientations aligned in the three principal planes of the material, defined by the normal to the crack plane being in the L-, R- or T-direction respectively.

Within LEFM, distinction is also made based on the direction of crack propagation and hence six possible principal crack plane orientation and propagation systems may be identified. These are illustrated in Figure 2.6, where the first index denotes the normal to the crack plane and the second index denotes the direction of crack propagation. Three types of relative displacements are conceivable, referred to as modes of deformation or modes of loading. These modes are illustrated in Figure 2.7, where mode I represents cracking due to pure tension perpendicular to the crack plane while mode II and mode III represent crack propagation due to in-plane shear and transverse shear respectively.

Within NFLM, distinction between different directions of crack propagation is not made. This means that the crack systems defined in Figure 2.6 are distinguished only by their respective crack plane orientation, having normal in the L-, R- or T-direction respectively. Explicit distinction is further not made between the LEFM modes of deformation II and III. Distinction between modes of deformation may within NLFM be viewed as being only between crack opening deformation (mode I) and crack shear slip deformation (mode II). The mode II crack shear slip deformation is however related to shear stress in two orthogonal directions. Taking the case of a crack plane with normal in the R-direction as an example; the mode I crack opening deformation is then related to the normal stress σ_{RR} while the two mode II crack shear slip deformations are related to the shear stress components τ_{LR} and τ_{RT} respectively.

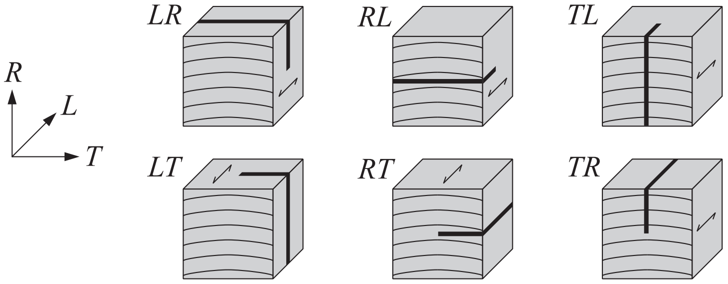

Figure 2.6: Crack plane orientation and propagation systems relative to LRT directions.

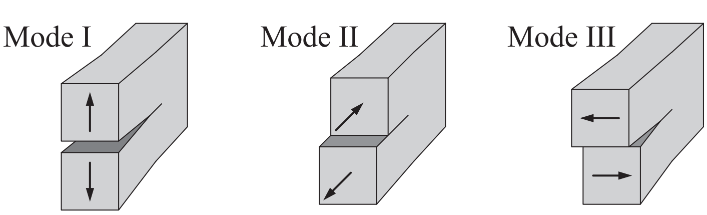

Figure 2.7: Modes of deformation I, II and III.

a) Single edge notched beam (SENB) - mode I

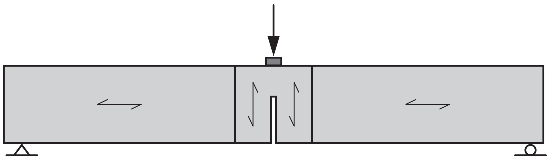

b) Small-scale notched specimen - mode I and II

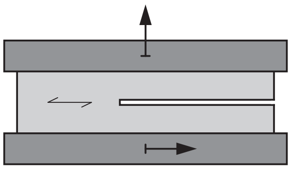

c) Double cantilever beam (DCB) - mode I

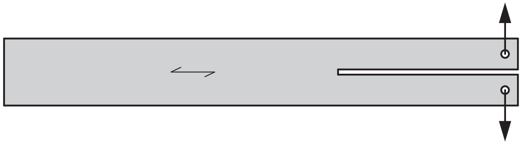

d) Compact Tension (CT) - mode I

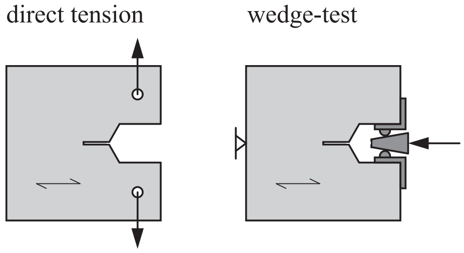

e) Tapered end notched flexure (TENF) - mode II

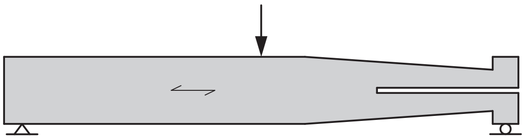

Figure 2.8: Test setups used for experimental determination of fracture energy G_f.

Examples of test setups used for experimental determination of fracture properties are presented in Figure 2.8 and a compilation of test results is given in Table 2.3. The orientation of the fracture surface is in the table given by the direction of the normal to the fracture surface. The orientation of material directions are for the mode II test results such that the crack planes were exposed to longitudinal shear, i.e. τ_{RL} for crack plane orientation R and τ_{TL} for crack plane orientation T. For NLFM, not only fracture energy but also material strength values are of importance for characterization of fracture performance and such values are hence also included in the compilation. Material stiffness properties, see Table 2.1, are further of importance in relation to both NLFM and LEFM.

The single edge notched beam (SENB) test setup in Figure 2.8a) has been widely used to determine mode I fracture energy of wood. The setup and specimen is designed to yield a stable descending branch of the load vs. deflection response allowing for evaluation of G_f as the work done by the midpoint force and the dead weight of the beam, divided by the fractured area.

A compilation of results using the SENB test setup is presented in [57]. The compilation includes fracture planes oriented with normal direction in the R-direction, in the T-direction and in intermediate directions. No significant influence of growth ring orientation was found for the mode I perpendicular to grain fracture energy. From the compilation of test results, it was concluded that a relation between density ρ and fracture energy according to $G_f = -162 + 1.07\rho$ was representative for European softwood species, with ρ in kg/m^3 and G_f in J/m^2. The reported test results for densities in the range 350-500 kg/m^3 appear however to be relatively evenly scattered between 200-400 J/m^2, irrespective of the density of the tested material. An influence of SENB specimen size on G_f is reported, with test values increasing by about 15-20% for an increase in specimen total height by a factor 2 from 40 to 80 mm and from 80 to 160 mm respectively for a constant specimen width of 45 mm.

Experimental tests of SENB specimens made of Spruce with mean density 457 kg/m^3 are further presented in [2]. The fracture planes where oriented such that the material was loaded in the R-direction. Specimen total heights in the range 10-320 mm were used while the specimen

Table 2.3: Fracture properties for Spruce and Pine found in the literature with density ρ in kg/m^3, moisture content u in %, fracture energy G_f in J/m^2 and material strength f in MPa.

Mode I				orientation R		orientation T		orientation at 45°	
Species	ref.	ρ	u	$G_{f,RR}$	f_{Rt}	$G_{f,TT}$	f_{Tt}	$G_{f,45t}$	f_{45t}
Scots pine	[17]	450	8	450	5.3	550	4.1	475	5.3
Scots pine	[17]	470	10	445	5.0	500	4.2	515	5.3
Scots pine	[17]	470	13	535	4.5	460	4.0	595	4.5
Scots pine	[17]	460	26	515	4.1				
Scots pine	[42]	467	15	294^*	4.0^*				
Scots pine	[92]	570	11					475	4.8
Spruce	[2]	475		280					
Norway spruce	[36]			180		230			
Norway spruce	[71]	479	12	337		213			
Norway spruce	[73]	463	13			298	3.3		
Norway spruce	[87]		14			283	2.9		

Mode II				orientation R		orientation T		orientation at 45°	
Species	ref.	ρ	u	$G_{f,RL}$	f_{LR}	$G_{f,TL}$	f_{LT}	$G_{f,45v}$	f_{45v}
Scots pine	[17]	460	13	815	11				
Scots pine	[92]	570	11					1120	11
Norway spruce	[36]			680					
Norway spruce	[73]	463	13			965	8.4		
Norway spruce	[87]		14			1240	9.8		
Norway spruce	[94]		12			877			

* = Crack plane orientation not explicitly distinguished within RT-plane

width was consistently 44 mm. The influence of density within the range of about 420 to 480 kg/m^3 was found to correspond to $G_f = 0.62\rho$. In contrast to the results reported in [57], no influence of specimen height was found. This agrees with results presented in [23], showing no influence of specimen height for SENB tests of European softwoods loaded in the T-direction considering beam width 45 mm and total beam heights of 45, 67 and 100 mm respectively.

Small-scale notched specimens, as illustrated in Figure 2.8b), have been used for testing in pure mode I and II loading and also for mixed mode loading. Using a small enough specimen and a testing machine that is sufficiently stiff, a stable performance is obtained and the entire load vs. displacement curve, including the descending branch, may hence be recorded. Results in terms of not only fracture energy but also material strength and characteristics of the stress vs. deformation performance of the fracture process zone are obtained. Information regarding the shape of the softening curve is of interest for fracture modeling using NLFM.

Approximate ranges of stress vs. displacement curves are depicted in Figure 2.9a) and results in terms of fracture energy as affected by the mixed mode ratio are given in Figure 2.9b) for experimental tests of Norway spruce [87] and Scots pine [92]. The orientation of the fracture planes were such that crack opening occurred in the T-direction for the Norway spruce material tested and at an angle of approximately 45° to the R- and T-directions for the Scots pine material. The direction of shear stress was in both cases in the material L-direction. The loading was applied in a displacement controlled manner, using a constant mixed mode ratio α between horizontal u_x and vertical u_y displacements for the respective individual tests.

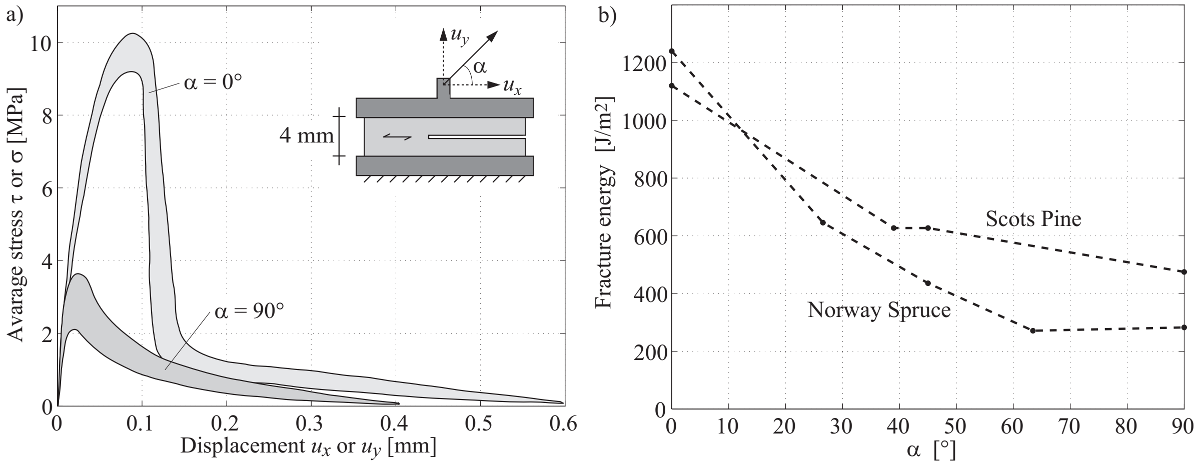

Figure 2.9: Approximate range of stress vs. displacement curves for pure mode I ($\alpha = 90°$) and mode II ($\alpha = 0°$) loading of Norway spruce [87] (a) and fracture energy for mixed mode loading of Norway spruce [87] and Scots pine [92] (b).

2.2 Global strength and fracture analysis methods

There are several available approaches for global strength and fracture analysis which are based on partly different assumptions regarding material behavior and ways of failure prediction. A variety of approaches are presented in Table 2.4, categorized based on their basic assumptions regarding material behavior in terms of material strength f_t and fracture energy G_f. These material parameters may, based on either explicit or implicit assumptions, take any value between zero and infinity including all intermediate finite values.

This categorization can also be seen from the perspective of whether an *ideally brittle* material behavior is assumed or not. Material brittleness may be described by the intrinsic material length property denoted the *characteristic length* and defined as $l_{ch} = EG_f/f_t^2$, where E is a measure of stiffness, which is often used in relation to cohesive zone modeling [48]. The absolute size of the fracture process zone at maximum load is for such modeling approaches related to, and for the case of a large crack in a large body commonly proportional to, the characteristic length l_{ch}. In this context does ideally brittle refer to a fracture process zone which at the start of crack propagation is small or even zero. Using this definition, an ideally brittle behavior ($l_{ch} = 0$) is obtained for $G_f = 0$ or $f_t = \infty$. Material models assuming nonzero size of the fracture process zone ($l_{ch} > 0$) may be referred to as being *quasi-brittle* or having *fracture ductility.*

The above given definition of a brittle material behavior refer to characteristics of the material only. Whether the response and global fracture course for nonlinear analysis of an actual structural element will be brittle or not do further also depend on the geometry and size of the considered element and on the loading situation.

For assumptions relating to finite values of material properties, distinction can further be made based on whether these properties are assumed to be *deterministic* or *stochastic.* Using an deterministic approach means that the material properties are assumed to be known for all points while a stochastic approach means that the natural heterogeneity of the material properties are taken into account by some probabilistic approach. Commonly used approaches include Weibull theory and Monte Carlo simulations, the latter typically involving a large number of individual analyses with input parameters sampled from statistical distributions.

Table 2.4: A categorization of rational strength analysis approaches.

		Material strength			
		$f_t = 0$	$f_t =$ finite *deterministic*	$f_t =$ finite *stochastic*	$f_t = \infty$
Fracture energy	$G_f = 0$	-	Conventional Stress Analysis	Weibull Weakest Link Theory	-
	$G_f =$ finite *deterministic*	-	Generalized Linear Elastic and Nonlinear Fracture Mechanics	Probabilistic Gen LE and Nonlinear Fracture Mechanics	Linear Elastic Fracture Mechanics
	$G_f =$ finite *stochastic*	-	Probabilistic Gen LE and Nonlinear Fracture Mechanics	Probabilistic Gen LE and Nonlinear Fracture Mechanics	Probabilistic Linear Elastic Fracture Mechanics
	$G_f = \infty$	-	Ideally Plastic Analysis	Probabilistic Ideally Plastic Analysis	-

Within the work presented in this thesis are two different approaches for fracture analysis considered. A probabilistic approach based on Weibull theory and a generalization of Linear elastic fracture mechanics is presented in Paper C and a Nonlinear fracture mechanics approach (a cohesive zone model) is considered in Papers D, E and F. The relevant background concerning these approaches is presented in the following sections. Reviews regarding perpendicular to grain strength and fracture analysis approaches are further found in for example in [43], [56], [83].

2.2.1 Conventional stress analysis

By *conventional stress analysis* is here meant an approach based on linear elastic stress analysis accompanied with a stress based failure criterion considering the stress state in the most stressed point, see Section 2.1.3. For strength analysis of structural elements with concentrated perpendicular to grain tensile stress and shear stress, conventional stress analysis is in general of little use. Such an approach is further of no use for the case of a sharp crack or notch giving rise to a stress singularity, since the stress at the tip of the crack theoretically is infinite.

2.2.2 Weibull weakest link theory

The Weibull weakest link theory [90] enables a probabilistically based approach to strength analysis. This means that the probability of failure at a certain state of stress for a certain volume of a material can be determined from knowledge of the magnitude and the scatter of the strength of the material. The basic assumption in Weibull weakest link theory is that the material is ideally brittle in the sense that global failure occurs when the strength of the weakest link is reached. The material is further assumed to be stochastically homogeneous, meaning that the strength properties are stochastic but all material points are however equal with respect to statistical probability distribution of the strength properties. The global strength is according to Weibull theory influenced by the size of the stress body and by the heterogeneity of the stress distribution.

Size dependencies are commonly present for wooden structural elements where global strength is governed by perpendicular to grain tensile stress. Considering the heterogeneity in material properties and the apparent brittleness for perpendicular to grain failures, Weibull theory has attained significant interest within timber engineering research. For example are the Eurocode 5 [32] design approaches for double tapered, curved and pitched cambered beams based on such considerations. The Eurcode 5 design equations for double tapered beams are reviewed and compared to 2D linear elastic FE-analysis in [22]. Weibull theory has further been applied to analysis of glulam beams with circular holes in [6], [7] and [51]. A design proposal for beams with circular holes has been proposed based on these analyses [8], see Section 2.3.1. A general drawback of Weibull theory is however that it cannot be applied to strength analysis of structural elements with a stress singularity caused for instance by a crack or a notch [42].

Basic Weibull theory

The theory can be derived considering a system of links loaded in tension and a general body loaded in tension according to Figure 2.10. Considering the system of n links coupled in series and loaded by a tensile stress σ, the probability of global survival S is

$$S = S_1 S_2 S_3 ... S_n = e^{\ln S_1 + \ln S_2 + \ln S_3 + ... + \ln S_n} = e^{\sum_{i=1}^{n} \ln S_i} \tag{2.18}$$

where S_i is the survival probability for link i, which is a function of the stress σ_i. It should be noted that the stress σ_i may be different for different links although the simple illustration in Figure 2.10 suggests equal stress in all links. Assuming statistically equal properties for all links, the survival probability S_i can for all links be expressed as a function $g = g(\sigma_i)$ according to

$$S_i = e^{-g(\sigma_i)} \qquad \text{or} \qquad \ln S_i = -g(\sigma_i) \tag{2.19}$$

where $g(\sigma_i)$ is a monotonically increasing function, referred to as the *material function*, that defines the strength properties of the link. The global failure probability F of a chain with n links is then found to be

$$F = 1 - S = 1 - e^{\sum_{i=1}^{n} -g(\sigma_i)} \tag{2.20}$$

Moving from a chain with n links to a body or material volume Ω made up of $n = \Omega/\Delta\Omega$ smaller volumes $\Delta\Omega$ and then letting $\Delta\Omega \to \mathrm{d}\Omega$, the probability of global failure is found to be

$$F = 1 - e^{-\int_{\Omega} g(\sigma)\ \mathrm{d}\Omega} \tag{2.21}$$

There are two suggestions for the material function $g(\sigma)$ stated in [90] and [91] respectively

$$\text{2-parameter model:} \qquad g(\sigma) = (\sigma/\sigma_0)^m \tag{2.22}$$

$$\text{3-parameter model:} \qquad g(\sigma) = \begin{cases} [(\sigma - \sigma_u)/\sigma_0]^m & \text{for } \sigma \geq \sigma_u \\ 0 & \text{for } \sigma < \sigma_u \end{cases} \tag{2.23}$$

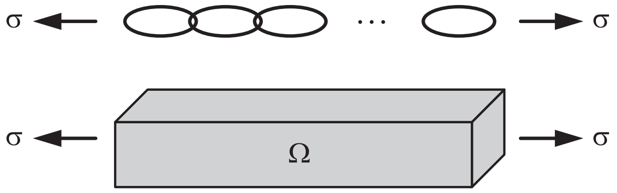

Figure 2.10: System of n serial coupled links and volume Ω loaded in tension.

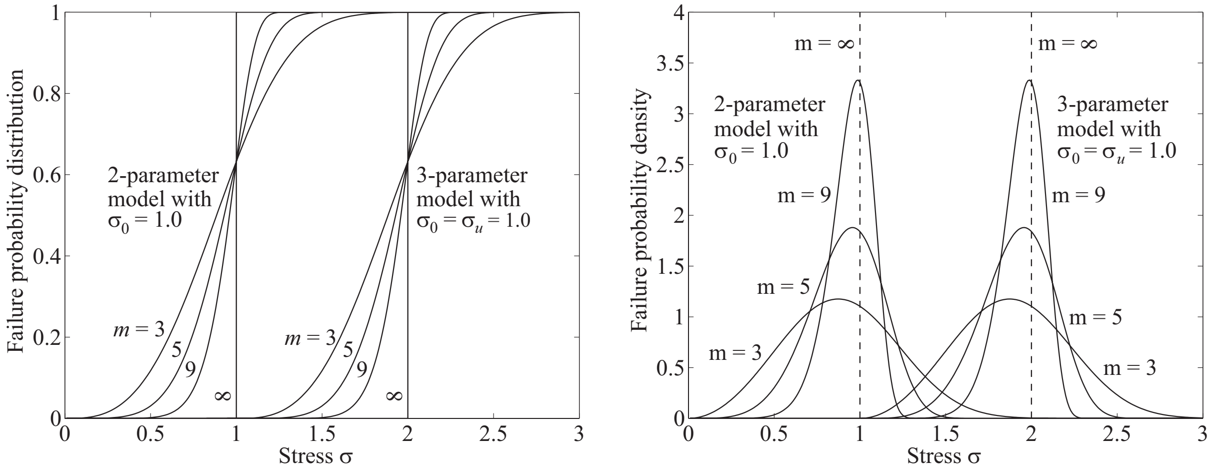

Figure 2.11: Failure probability distribution ($F = 1 - e^{-g(\sigma)}$) and density functions.

where σ is the stress in the body. The scale parameter σ_0, the location parameter σ_u and shape parameter m relate to the magnitude and scatter in the strength of the material. The failure probability distribution and density functions for a stress σ in a unit volume $\mathrm{d}\Omega$ are illustrated in Figure 2.11 for the 2- and 3-parameter models for different values of the shape parameter m.

Volume and stress distribution effects

The influence of volume and heterogeneity in stress distribution can be investigated by assuming equal probability of failure for bodies of different volume and/or with different stress distributions. According to Equation (2.21), the condition for equal probability of failure for body 1 with stress σ_1 and body 2 with stress σ_2 is

$$\int_{\Omega_1} g(\sigma_1)\ \mathrm{d}\Omega \quad = \quad \int_{\Omega_2} g(\sigma_2)\ \mathrm{d}\Omega \tag{2.24}$$

which for the 2-parameter model according to Equation (2.22) gives

$$\int_{\Omega_1} \left(\frac{\sigma_1(x,y,z)}{\sigma_0}\right)^m \mathrm{d}\Omega \quad = \quad \int_{\Omega_2} \left(\frac{\sigma_2(x,y,z)}{\sigma_0}\right)^m \mathrm{d}\Omega \tag{2.25}$$

The volume and stress distribution effects can be established by considering the different cases concerning volume and stress distribution according to Figure 2.12. The reference case is a body of volume Ω_{ref} exposed to a homogeneous stress distribution of magnitude σ_{ref}. Case A is a body of volume Ω exposed to a homogeneous stress distribution of magnitude σ_A. The general case reflects a body of volume Ω exposed to a heterogeneous stress distribution $\sigma(x,y,z) = \sigma_{max}\lambda(x,y,z)$ where σ_{max} denotes the stress magnitude in the most stressed point and where $0 \leq \lambda(x,y,z) \leq 1$. Consider now a large number of nominally equal bodies and describing the mean strengths related to the three cases by the mean values of the stress in the most stressed point (σ_{ref}, σ_A and σ_{max}) at failure. These mean strengths are denoted f_{ref}, f_A and f for the reference case, case A and the general case respectively. The influence of volume and heterogeneity in stress distribution on the mean strength can then be derived by assuming equal probability of failure according to Equation (2.25) for two of the cases in Figure 2.12.

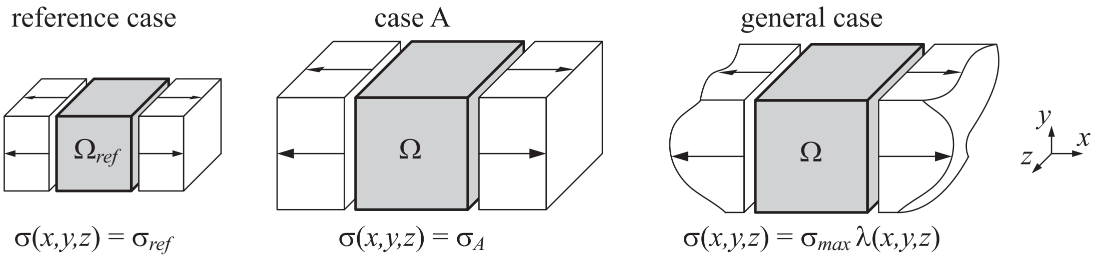
reference case
case A
general case
Ω_{ref}
Ω
Ω
y
x
z
$\sigma(x,y,z) = \sigma_{ref}$
$\sigma(x,y,z) = \sigma_A$
$\sigma(x,y,z) = \sigma_{max}\,\lambda(x,y,z)$

Figure 2.12: Considered cases for illustration of volume and stress distribution effects.

The influence of stressed volume on the strength is found by comparing the reference case and case A which both have a homogeneous stress distribution but different volumes. The influence of the volume on the strength is found to be

$$f_A = f_{ref} \left(\frac{\Omega}{\Omega_{ref}} \right)^{-1/m} \tag{2.26}$$

which shows that the theory predicts decreasing strength with increasing volume.

The influence of stress distribution heterogeneity is found by comparing case A and the general case which both have a stressed volume Ω but with different stress distributions. The influence of the heterogeneity in the stress distribution is found to be

$$f = f_A \left(\frac{1}{\Omega} \int_{\Omega} \lambda^m(x,y,z)\ \mathrm{d}\Omega \right)^{-1/m} \tag{2.27}$$

which shows that the theory predicts increasing strength for increasing heterogeneity in stress distribution since $\lambda(x,y,z) \leq 1$.

The combined influence of volume and stress distribution heterogeneity on the strength is found by comparing the reference case and the general case or inserting Equation (2.26) in Equation (2.27). The combined influence is hence found to be

$$f = f_{ref} \left(\frac{\Omega}{\Omega_{ref}} \right)^{-1/m} \left(\frac{1}{\Omega} \int_{\Omega} \lambda^m(x,y,z)\ \mathrm{d}\Omega \right)^{-1/m} \tag{2.28}$$

A convenient way of comparing the probability of failure between structural elements with different stress distribution is the so called the Weibull stress (or equivalent Weibull stress or effective Weibull stress). The Weibull stress is a fictive homogeneous stress in the volume Ω that yields the same probability of failure as the actual heterogeneous state of stress for the volume Ω considered and defined according to

$$\sigma_{wei} = \left(\frac{1}{\Omega} \int_{\Omega} \sigma^m(x,y,z)\ \mathrm{d}\Omega \right)^{1/m} \tag{2.29}$$

The level of heterogeneity in the stress distribution is often expressed by the distribution factor k_{dis} which is defined as the ratio between the maximum stress in the body σ_{max} and the Weibull stress σ_{wei} according to

$$k_{dis} = \frac{\sigma_{max}}{\sigma_{wei}} = \left(\frac{1}{\Omega} \int_{\Omega} \lambda^m(x,y,z)\ \mathrm{d}\Omega \right)^{-1/m} \tag{2.30}$$

where $k_{dis} = 1$ for a homogeneous stress distribution and $k_{dis} > 1$ for all other distributions. The distribution factor k_{dis} can be identified as the last parts of Equations (2.27) and (2.28).

Interpretations of the material function

Using the expression for the Weibull stress σ_{wei} according to Equation (2.29) and the distribution factor k_{dis} according to Equation (2.30) in Equation (2.28) for the mean strength f, the following expression can be obtained

$$\frac{\sigma_{max}}{f} = \left(\frac{1}{\Omega_{ref}} \int_{\Omega} \left(\frac{\sigma(x,y,z)}{f_{ref}} \right)^m \mathrm{d}\Omega \right)^{1/m} \tag{2.31}$$

where σ_{max} is the maximum stress in the body of volume Ω and f is the mean value of σ_{max} (for a large number of nominally equal bodies) at the instant of failure. Furthermore is f_{ref} the mean strength valid for a homogeneous stress distribution in the volume Ω_{ref}.

The ratio σ_{max}/f can be interpreted as a *global effective dimensionless stress parameter* α_{global} and $\sigma(x,y,z)/f_{ref}$ as an *effective dimensionless stress field* $\alpha(x,y,z)$ defined in the volume Ω. The expression can then be rewritten as

$$\alpha_{global} = \left(\frac{1}{\Omega_{ref}} \int_{\Omega} \alpha^m(x,y,z)\ \mathrm{d}\Omega \right)^{1/m} \tag{2.32}$$

where the value of α_{global} for the effective dimensionless stress field $\alpha(x,y,z)$ in the volume Ω corresponds to equal probability of failure as for the constant value of $\alpha(x,y,z) = \alpha_{global}$ for a homogeneous stress in the volume Ω_{ref}. Since f_{ref} is here defined as the mean strength of the reference volume Ω_{ref}, $\alpha_{global} = 1.0$ will for the volume Ω give the mean failure value of σ_{max}. The effective dimensionless stress field $\alpha(x,y,z)$ may for a multiaxial stress state also be chosen to consider several stress components and may for example be based on a failure criterion such as the ones presented in Section 2.1.3.

2.2.3 Linear elastic fracture mechanics

Linear elastic fracture mechanics (LEFM) deals with analysis of cracks and propagation of cracks and originates from the work of Griffith [39]. LEFM is based on the assumption of an ideally linear elastic material behavior and the existence of a sharp crack or notch. A consequence of the assumed material behavior is that the stresses at the tip of a crack theoretically approach infinity, see Figure 2.13. This is however accepted in LEFM as long as the fracture process zone, the zone where the material behaves nonlinearly and where the actual debonding occur, is small compared to the length of the crack and compared to the distance to boundaries, loads and supports. The fracture process zone nonlinearities are disregarded and an ideally brittle material behavior with infinitely small size of the fracture process zone and infinite material strength is assumed.

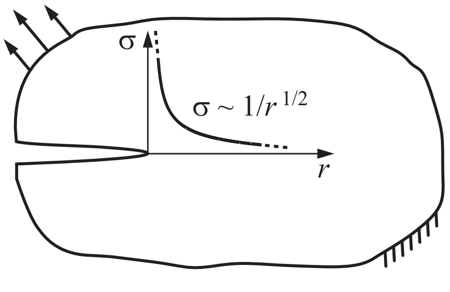

Figure 2.13: Linear elastic stress distribution at the tip of a crack.

A requirement for LEFM to yield accurate results for practical application to real materials is that the size of the actual fracture process zone is small compared to relevant dimensions of the considered body [66]. If this requirement is fulfilled, then the size of the fracture process zone and the material performance within this zone are governed only by the material properties, the mode of loading and for anisotropic materials by the orientation of the crack plane [5]. The size or geometry of the considered body do under such circumstances not influence the material performance within the fracture process zone and crack propagation is then referred to as being *autonomous* or *self-similar*.

LEFM cannot be used to determine where and when one can expect a crack in a stressed body to arise but it can be used for analysis of whether an existing crack will propagate or not. Crack propagation analysis can be carried out by considering the energy balance of the system, by considering the so called stress intensity factors or by other similar methods.

LEFM have in several studies been applied to analysis of timber and glulam beams with holes, see e.g. [5], [9], [74], [75] and [87]. LEFM-based design criteria, although expressed as conventional stress or force based failure criteria, are present in Eurocode 5 [32]. The design criterion for end-notched beams is based on work presented in [41]. Design approaches based on an analogy to end-notched beams have been and still are used in relation to design of beams with a hole. Such an approach was included in a previous draft version of Eurocode 5 [33] and is currently found in other European design codes and handbooks, see Section 2.3.1. A LEFM-based criterion is further present in Eurocode 5 for design of dowel-type connections loaded perpendicular to grain, see Section 2.3.2.

Energy balance approach

Crack propagation analysis may be carried out by consideration of the energy balance and how a virtual extension of a crack will affect the energy of the system. According to Griffith [39] is the condition for crack propagation that the potential energy of the considered system must be reduced or unchanged during propagation. Crack propagation criterion may be expressed using the concept of the *energy release rate* G and the *critical energy release rate* G_c. The energy release rate G is defined as the decrease in potential energy Π at an infinitely small increase in crack area A according to [86]

$$G = -\frac{\partial \Pi}{\partial A} = -\frac{\partial}{\partial A}\left(U_e + U_P\right) \tag{2.33}$$

where U_e and U_P are the elastic strain energy and the potential energy of the loads respectively, the latter being equal to the negative work of the loads. The value of the energy release rate G depends on the geometry of the structure, the geometry of the crack, the boundary conditions, the applied loads and the stiffness properties of the material. The crack propagation criterion may then be expressed as

$$G = G_c \tag{2.34}$$

where the critical energy release rate G_c is a material property parameter which describes the resistance to cracking. G may be interpreted as the energy available to grow a crack a unit area and G_c may be interpreted as the energy required to grow a crack a unit area.

There are three possible crack propagation scenarios; stable, semi-stable and unstable crack growth. Unstable crack growth corresponds to the common case of increasing G with increasing crack area. It is however also possible that G decreases with increasing crack area and if the value of G falls below G_c, the crack propagation will stop and the crack growth is termed stable. Semi-stable crack growth corresponds to constant G with increasing crack area.

The value of the critical energy release rate G_c do in general depend on the mode of deformation and may for anisotropic materials like wood also depend on the orientation of the crack, see Figures 2.6 and 2.7. The strain energy release rate can be separated into the three modes of deformation and the total strain energy release rate are for mixed mode conditions given by $G = G_I + G_{II} + G_{III}$ [5].

Stress intensity factor approach

Another approach for crack propagation analysis is to consider the stress field in the vicinity of the tip of the crack, see Figure 2.14. This stress field can for a large crack in a large body be solved analytically using the so called Airy's stress function. Considering a state of plane stress in an isotropic material, the solutions for mode I and II loading are given by [66]

$$\text{Mode I} \quad \begin{cases} \sigma_{xx} = \dfrac{K_I}{\sqrt{2\pi r}} \cos\dfrac{\theta}{2}\left(1 - \sin\dfrac{\theta}{2}\sin\dfrac{3\theta}{2}\right) + \sigma_{xx0} + O(\sqrt{r}) \\ \sigma_{yy} = \dfrac{K_I}{\sqrt{2\pi r}} \cos\dfrac{\theta}{2}\left(1 + \sin\dfrac{\theta}{2}\sin\dfrac{3\theta}{2}\right) + O(\sqrt{r}) \\ \tau_{xy} = \dfrac{K_I}{\sqrt{2\pi r}} \cos\dfrac{\theta}{2}\sin\dfrac{\theta}{2}\cos\dfrac{3\theta}{2} + O(\sqrt{r}) \end{cases} \tag{2.35}$$

$$\text{Mode II} \quad \begin{cases} \sigma_{xx} = \dfrac{-K_{II}}{\sqrt{2\pi r}} \sin\dfrac{\theta}{2}\left(2 + \cos\dfrac{\theta}{2}\cos\dfrac{3\theta}{2}\right) + O(\sqrt{r}) \\ \sigma_{yy} = \dfrac{K_{II}}{\sqrt{2\pi r}} \sin\dfrac{\theta}{2}\cos\dfrac{\theta}{2}\cos\dfrac{3\theta}{2} + O(\sqrt{r}) \\ \tau_{xy} = \dfrac{K_{II}}{\sqrt{2\pi r}} \cos\dfrac{\theta}{2}\left(1 - \sin\dfrac{\theta}{2}\sin\dfrac{3\theta}{2}\right) + O(\sqrt{r}) \end{cases} \tag{2.36}$$

where $O(\sqrt{r})$ represents higher order terms and where K_I and K_{II} are the mode I and mode II *stress intensity factors* respectively. The stress is singular of type $1/\sqrt{r}$, but no equilibrium relations are violated by the infinite stress since the resulting force on any finite surface is still finite [66]. The above given expressions are for $\theta = 0$ also valid for an orthotropic material with a crack oriented along one of the material principal directions, although the general solutions are affected also by the ratios of elastic constants [58].

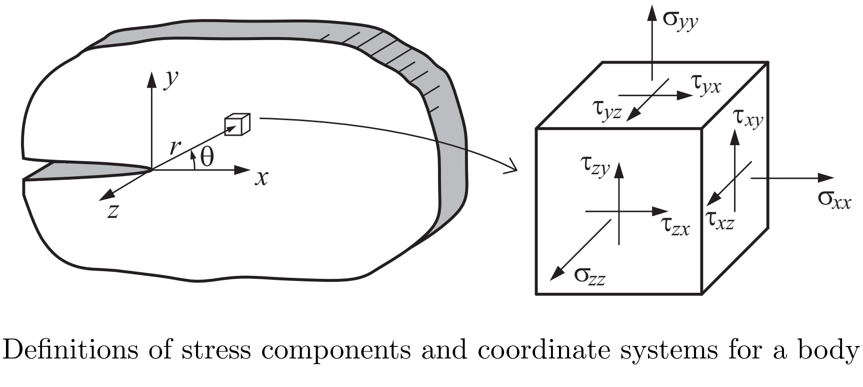

Figure 2.14: Definitions of stress components and coordinate systems for a body with a crack.

Close to the crack tip, the first term of these series become dominating and the stress intensity factors are hence sufficient to describe the stress state. The stress intensity factors in modes I, II and III are defined as [5]

$$K_I = \lim_{r \to 0} \sigma_{yy}(r)\sqrt{2\pi r} \qquad \text{for } \theta = 0 \tag{2.37}$$

$$K_{II} = \lim_{r \to 0} \tau_{xy}(r)\sqrt{2\pi r} \qquad \text{for } \theta = 0 \tag{2.38}$$

$$K_{III} = \lim_{r \to 0} \tau_{yz}(r)\sqrt{2\pi r} \qquad \text{for } \theta = 0 \tag{2.39}$$

The specific values of the stress intensity factors are governed by the geometry of the structure, the geometry of the crack, the boundary conditions and the applied load. Due to the linear elastic assumption, stresses and thereby also the stress intensity factors are proportional to the applied load. Crack propagation criteria are formulated as a comparison of the stress intensity factor K and the *critical stress intensity* K_c (also known as the *fracture toughness*) and can in general terms be expressed as $K = K_c$. For mixed mode loading, some interaction relationship is commonly adopted.

Relation between energy release rates and stress intensity factors

The energy release rate approach and the stress intensity factor approach both represent conventional LEFM approaches and should yield identical results in practical analysis. The relationships between G and K for mode I and II loading of an orthotropic material considering a plane state of stress and a fracture plane which is oriented parallel to the direction of grain (here the x-direction) are given by [68]

$$K_I = \sqrt{E_I G_I} \qquad \text{where} \qquad E_I = \sqrt{\frac{2E_x E_y}{\sqrt{\dfrac{E_x}{E_y}} + \dfrac{E_x}{2G_{xy}} - \nu_{yx}\dfrac{E_x}{E_y}}} \tag{2.40}$$

$$K_{II} = \sqrt{E_{II} G_{II}} \qquad \text{where} \qquad E_{II} = \sqrt{\frac{2E_x^2}{\sqrt{\dfrac{E_x}{E_y}} + \dfrac{E_x}{2G_{xy}} - \nu_{yx}\dfrac{E_x}{E_y}}} \tag{2.41}$$

where E_x is the modulus of elasticity parallel to grain, E_y is the modulus of elasticity perpendicular to grain, G_{xy} is the shear modulus and ν_{yx} is Poisson's ratio defined as $\nu_{yx} = -\varepsilon_x/\varepsilon_y$ for uniaxial loading in the y-direction.

Restrictions of LEFM applicability

For cases where the size of the fracture process zone is non-negligible compared to the size of the body or the length of the crack, monotonically increasing loading may lead to premature failure by unstable crack propagation before the fracture process zone is fully developed. The fracture energy is then not fully activated and application of conventional LEFM approaches will for such cases hence yield unconservative predictions of the crack propagation load [5]. This may in a LEFM framework be dealt with by letting the material property G_c in the crack propagation criterion according to Equation (2.34) be replaced by R, where R denotes some function that describes how the crack resistance varies with the length of the fracture process or the length of the crack, see e.g. [5] and [86].

2.2.4 Generalized Linear elastic fracture mechanics

The theory concerning LEFM suffers from one obvious limitation: it is based on the assumption of an existing crack or sharp notch giving rise to a square root stress singularity. Conventional stress analysis with a stress based failure criterion is on the other hand not applicable when such a singularity is present. The LEFM-theory can however be modified, or *generalized*, in order to overcome this limitation and make it valid for a general case, with or without a stress singularity. Two different methods, the *initial crack method* and the *mean stress method*, are presented in [5] and considered also in [43] and [83]. Here is only the mean stress method considered.

The basic idea of the mean stress method is to consider not the stress state in a point of the material, but instead the mean stresses acting across a *potential fracture area.* These stresses, which have finite values also for the case of presence of a stress singularity, are then used in a conventional stress based failure criterion. The size of the potential fracture area is derived in such a way that the method will give the same strength prediction for a body in a homogeneous state of stress as the conventional stress based failure criterion used and also give the same strength prediction as LEFM for a large body with a square root stress singularity. The mean stress method has been applied to analysis of end-notched beams and beams with a hole [5] and dowel connections [85].

The following section is based on assumptions of a body in a plane state of stress, a fracture plane which coincides with the direction of grain (x-direction) and mixed mode I and II loading. Two basic criteria need to be chosen, a conventional stress based failure criterion and a LEFM crack propagation criterion. The stress based failure criterion is here chosen similar to the criterion of Norris [67] according to Equation (2.13), however disregarding the parallel to grain stress component yielding

$$\left(\frac{\sigma}{f_\sigma}\right)^2 + \left(\frac{\tau}{f_\tau}\right)^2 = 1.0 \tag{2.42}$$

where σ, τ, f_σ and f_τ are the perpendicular to grain tensile stress, the shear stress and the corresponding strength values respectively. The notation used here is somewhat inconsistent with what is generally used within the thesis, but consistent with the notation used in Paper C. The LEFM crack propagation criterion is chosen according to the criterion of Wu [93]

$$\frac{K_I}{K_{Ic}} + \left(\frac{K_{II}}{K_{IIc}}\right)^2 = 1.0 \tag{2.43}$$

where K_I and K_{II} are the mode I and mode II stress intensity factors and K_{Ic} and K_{IIc} are the corresponding fracture toughnesses. Considering now the mean stresses acting across a potential fracture area instead of the stress state in a point, the stress failure criterion is then

$$\left(\frac{\bar{\sigma}}{f_\sigma}\right)^2 + \left(\frac{\bar{\tau}}{f_\tau}\right)^2 = 1.0 \tag{2.44}$$

where $\bar{\sigma}$ and $\bar{\tau}$ are the mean values of the perpendicular to grain tensile stress σ and the shear stress τ in the potential fracture area. Using Equations (2.35) and (2.36), the stresses in front of a crack tip can be expressed as

$$\sigma(x) = \frac{K_I}{\sqrt{2\pi x}} + ... \tag{2.45}$$

$$\tau(x) = \frac{K_{II}}{\sqrt{2\pi x}} + ... \tag{2.46}$$

where the first term in these series are dominating for small values of x.

The size of the potential fracture area is given by the width of the plane stress body and a length a_{ms} in the grain direction. Assuming a small length a_{ms} compared to other dimensions in the body, the mean stresses in a potential fracture area starting from the tip of a crack can be expressed as

$$\bar{\sigma} \;=\; \frac{1}{a_{ms}}\int_0^{a_{ms}} \sigma(x)\;\mathrm{d}x \;=\; \sqrt{\frac{2K_I^2}{\pi a_{ms}}} \tag{2.47}$$

$$\bar{\tau} \;=\; \frac{1}{a_{ms}}\int_0^{a_{ms}} \tau(x)\;\mathrm{d}x \;=\; \sqrt{\frac{2K_{II}^2}{\pi a_{ms}}} \tag{2.48}$$

The length a_{ms} is derived by inserting the above given expressions for the mean stresses $\bar{\sigma}$ and $\bar{\tau}$ into Equation (2.44) and using Equations (2.40), (2.41) and (2.43). By introducing the mixed mode ratio $k = K_{II}/K_I = \bar{\tau}/\bar{\sigma}$, the length a_{ms} is then found to be

$$a_{ms} = \frac{2}{\pi}\frac{E_I G_{Ic}}{f_\sigma^2}\frac{E_x}{E_y}\left(\frac{G_{IIc}}{G_{Ic}}\right)^2 \frac{1}{4k^4}\left(\sqrt{1+4k^2\sqrt{\frac{E_y}{E_x}}\frac{G_{Ic}}{G_{IIc}}}-1\right)^2\left(1+k^2\frac{f_\sigma^2}{f_\tau^2}\right) \tag{2.49}$$

and depends hence on material properties (stiffness, fracture energy, shear- and perpendicular to grain tensile strengths) and also the mixed mode ratio k. Determining the length a_{ms} is hence an iterative process where an initial guess of the mixed mode ratio k is needed. Simplified expressions are obtained for pure mode I or pure mode II loading according to

$$a_{ms} \;=\; \frac{2}{\pi}\frac{E_I G_{Ic}}{f_\sigma^2} \qquad \text{for pure mode I, } k = 0 \tag{2.50}$$

$$a_{ms} \;=\; \frac{2}{\pi}\frac{E_{II} G_{IIc}}{f_\tau^2} \qquad \text{for pure mode II, } k \to \infty \tag{2.51}$$

As mentioned above, the strength prediction given by the mean stress method derived here will correspond to the strength prediction given by the conventional stress based failure criterion for a body in homogeneous stress and also to the LEFM crack propagation criterion for a large crack in a large body. Moving from the extreme of a body in homogeneous stress towards an increasing stress gradient, the influence on the strength prediction of the size, stiffness and fracture energy of the body increases whereas the influence of the material strength parameters decreases. One can in general expect the mean stress method to give accurate strength predictions only if the length a_{ms} is reasonably small as compared to relevant dimensions of the considered body. For material parameters used in Paper C is $a_{ms} = 21$ mm and 44 mm for pure mode I and mode II loading respectively.

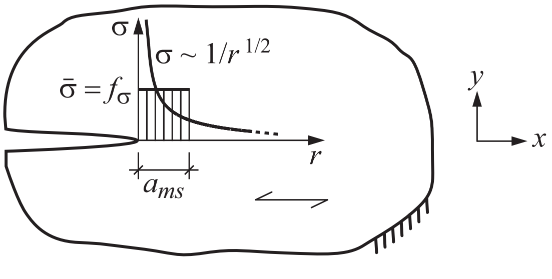

Figure 2.15: Fracture relevant mean stress for a body with a crack.

2.2.5 Nonlinear fracture mechanics

Linear elastic fracture mechanics suffers from some drawbacks which limit the feasibility and usefulness for application to wood. The applicability of LEFM is limited by the prerequisite of a crack or notch giving rise to a square root singularity. Applicability may further also be limited by the size of the considered body, since the size of the fracture process zone needs to be small compared to other relevant dimensions in order for LEFM to yield accurate results. These issues may be considered in approximate manners using generalizations of conventional LEFM such R-curves or the mean stress method discussed above. Both these issues may however also be treated using *Nonlinear fracture mechanics* (NLFM). By NLFM is here meant an approach where the nonlinear behavior in the fracture process zone is quantified and described by a constitutive relation.

Nonlinear fracture mechanics approaches, in the sense defined above, originate from the work by Barenblatt [12], Dugdale [28] and Hillerborg et al. [48]. The approach presented by Hillerborg was originally called the *fictitious crack model*, but is later more frequently referred to as the *cohesive crack model* or the *cohesive zone model* (CZM).

The basic concept of cohesive zone modeling is to describe the material performance using two constitutive relations; a conventional stress vs. strain relation for the bulk material and a stress vs. deformation relation for the fracture softening material performance within the fracture process zone. The concept can be described by considering a stable uniaxial tensile test run in displacement control as illustrated in Figure 2.16a). The test specimen and setup is assumed to be such that the complete response can be recorded, including the descending branch all the way to zero stress and complete fracture.

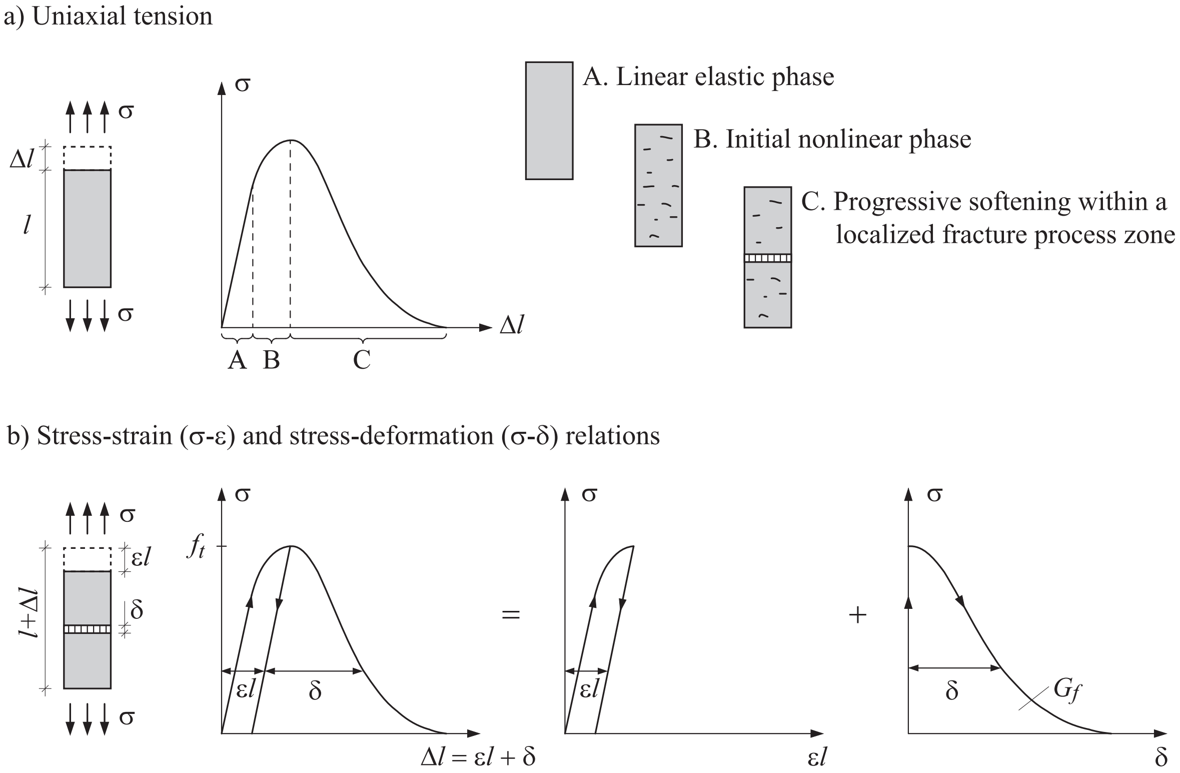
a) Uniaxial tension
σ
Δl
l
σ
σ
Δl
A
B
C
A. Linear elastic phase
B. Initial nonlinear phase
C. Progressive softening within a localized fracture process zone
b) Stress-strain (σ-ε) and stress-deformation (σ-δ) relations
σ
εl
δ
l+Δl
σ
σ
f_t
εl
δ
Δl = εl + δ
=
σ
εl
εl
+
σ
δ
G_f
δ

Figure 2.16: Stable uniaxial tensile test (a) and constitutive relations σ-ε and σ-δ (b).

The nonlinear response depicted in Figure 2.16a) can be divided into three phases [92]. The response is linear elastic during the initial phase (A). As loading is increase and the stress approaches the material strength, the material might behave in a nonlinear fashion (B). The possible nonlinearity may be due to nonlinear elastic or plastic straining or due to micro cracking and damage. At peak stress, a fracture process zone is formed within which a localized strain softening performance is initialized. As the prescribed displacement increases, the deformation of the fracture process zone will gradually increase and the stress transferring capacity will diminish (C). The material outside the fracture process zone will be elastically unloaded during the phase of progressive softening within the fracture process zone.

The response of the uniaxial test illustrated in Figure 2.16a) may be explained and modeled using the NLFM concept of the cohesive zone model [48]. Such an approach includes the use of two constitutive relations: a conventional stress-strain (σ-ε) relation for the bulk material and a stress-deformation (σ-δ) relation for the softening behavior within the fracture process zone. The total elongation of the bar Δl may be divided into a contribution from deformation due to uniform straining of the bulk material εl and a contribution due to deformation within the fracture process zone δ, as depicted in Figure 2.16b). The two constitutive relations σ-ε and σ-δ may be identified as illustrated in the figure, here assuming zero pre peak-load nonlinear elastic straining. A schematic illustration of the stress distribution at a crack according to LEFM and according to the concept of cohesive zone modeling is given in Figure 2.17.

The σ-δ relation describes the softening performance of the material and is within cohesive zone modeling assumed to be a material property. The area beneath the σ-δ curve is the work of fracture or the fracture energy G_f, i.e. the energy required to create a unit area of traction-free crack. Cohesive zone modeling hence involves material parameters relating to material strength, fracture energy and also the shape of the softening curve. These material parameters may be determine from experimental testing, see Section 2.1.4.

The concept of cohesive zone modeling was first introduced for fracture analysis of concrete but the general character makes it useful also for modeling of fracture in other materials [49], i.e. rock, adhesives and wood. Cohesive zone models are commonly implemented in a finite element environment using special purpose interface elements or nonlinear springs connecting nodes on opposite sides of a crack plane of zero initial thickness. Due to the strongly orthotropic properties of wood, cracking do in general occur in the direction of grain, irrespective of the state of stress. This means that if the location of crack initiation is known, the entire crack path may for modeling purposes be assumed to be known with reasonable accuracy. The stress state along the crack path may however be complex and do in the general case consist of all six stress components.

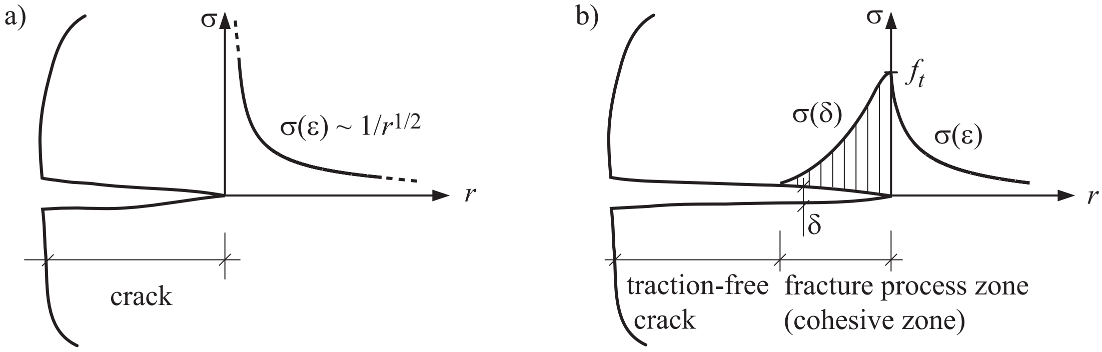

Figure 2.17: Stress distribution according to LEFM (a) and CZM (b).

Numerous CZM approaches of varying complexity have been used for perpendicular to grain fracture analyses of wood, wood products such as glulam and LVL and wood-adhesive bonds. Early applications are for example found in [40] and [16], where linear and piece-wise linear softening relationships were used for mode I wood fracture analyses. Further development led to considerations also to a shear stress component within the fracture process zone and 2D mixed mode analysis. Examples of mixed mode fracture analysis using bilinear softening functions are found in [92] for wood and glue-line fracture and in [52] for wood fracture. Furthermore are examples of 2D and 3D mixed mode fracture analysis of wood-adhesive bonds, considering piece-wise linear softening functions, found in [80], [81] and [82].

More recent contributions to wood fracture modeling include the 3D cohesive zone model presented in [77]. The considered material model is based on an interface element approach and the material performance is describe by a stress vs. deformation relation, considering components in the interface normal direction and in the two shear directions. Anisotropic material properties are taken into account by allowing different values for material strength and fracture energy for deformation in the opening direction and in the two shear directions respectively. The interface response, including both initial elastic response and post-peak stress softening response, is described using a continuous nonlinear function expressed in scalar quantities of the relevant stress and deformation components. The considered material model has been applied to analysis of a DCB specimen and end-notched beams [77], a SENB specimen, a TENF specimen and beams with a hole [78] and dowel connections [72]. It appears as homogeneous orientation of material principal directions have been used for all these analyses.

Closely related to the interface element approach for cohesive zone modeling, for wood applications commonly utilizing a predefined crack path, is the crack band model introduced by Bažant and Oh [13] for mode I cracking of concrete. The softening performance is modeled as a blunt smeared crack band and the crack opening deformation is assumed to be evenly distributed across the crack band width. By relating the crack band width to the finite element size, the stress vs. deformation relation may be converted to an equivalent stress vs. strain relation describing the softening performance. An advantage in favor of the crack band model is that the crack path does not need to be predefined and that the mesh does not need to be altered during the course of an analysis. To arrive at mesh independent results, where no crack path is favored over another, a uniform mesh of square elements is in [13] suggested to be used.

Strain softening models for perpendicular to grain tension and shear have also been derived within the framework of plasticity theory. For example is a multi-surface plasticity model for plane stress analysis presented in [59]. Yield surfaces are based on the Tsai-Wu criterion [89] and the model includes plastic hardening in compression perpendicular to grain and strain softening in tension perpendicular to grain. A single-surface plasticity model, also based on the Tsai-Wu criterion and also including strain softening in tension perpendicular to grain, is presented in [60]. This single-surface plasticity model is in [34] used for 2D analysis of beams with a hole. A 3D multi-surface plasticity model, including strain softening in tension perpendicular to grain, and accounting also for influence of moisture content on material properties is presented in [76], using the material model presented in [59] as starting point. The above mentioned plasticity based strain softening models use an approach which can be referred to as a smeared crack or crack band approach in the sense that the softening performance is not restricted to a predefined potential crack path.

Cohesive zone models are also available in commercial FE-software such as ABAQUS [1], commonly using conventional interface element approaches considering stress vs. deformation relations in the crack opening direction and in the two crack shear slip directions. An example of application is found in [79], where fracture analyses of dowel connections are presented.

2.3 Design in codes of practice

2.3.1 Beams with a hole

Looking at design recommendations for glulam beams with holes in European timber engineering design codes and handbooks over the last decades, it can be seen that the issue has been treated in many different ways. The theoretical backgrounds on which the recommendations are based show fundamental differences and there are also major discrepancies between the strength estimations according to the different codes as well as between tests and estimations according to codes. Finding a simple, general and reliable method for design of glulam beams with holes seems to be a difficult task, which is reflected by the fact that the contemporary version of Eurocode 5 [32] does not state any design criterion for beams with a hole.

Design criteria according to the Swedish Glulam handbook [18], the German National Annex to Eurocode 5 [26] and according to a design proposal presented by Aicher, Höfflin and Reinhardt [8] are briefly reviewed below. Design code regulations concerning hole size and placement according in Table 2.5 and Figure 2.18 apply. The design criteria considered here all relate to unreinforced beams. Beams with holes may be reinforced, for example using internal reinforcement such as glued-in rods or external reinforcement such as glued-on plywood or LVL.

Table 2.5: Regulations concerning hole size, shape and placement.

Code	l_a	l_v	l_z	h_u and h_l	a	b or ϕ	r
Glulam handbook	-	-	$\geq 1.0H$	$\geq 0.4H - 0.5b$	$\leq 3b$	$\leq 0.50H$	≥ 25 mm
DIN EN 1995-1-1/NA	$\geq 0.5H$	$\geq H$	$\geq 1.5H^*$	$\geq 0.35H$	$\leq 0.4H$	$\leq 0.15H$	≥ 15 mm
DIN 1052:2004	$\geq 0.5H$	$\geq H$	$\geq 1.0H^*$	$\geq 0.25H$	$\leq 1.0H$	$\leq 0.40H$	≥ 15 mm

* = or at least 300 mm

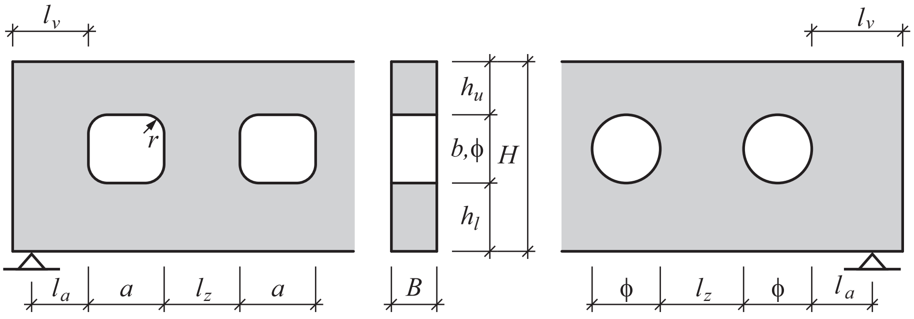

Figure 2.18: Geometry parameters for code design of beams with a hole.

Swedish Glulam handbook

The Swedish Glulam handbook (*Limträhandbok*) [18] is not an official code but rather a tool for recommendations concerning design of glulam structures. It is currently in the process of being rewritten and a new version is expected during 2013. In the present version, there are two methods suggested for design of glulam beams with holes; an empirically based method (not further considered here) and a method based on estimations by means of an analogy with design of end-notched beams. The latter method was also included in a previous draft version of Eurocode 5 [33], but is not included in the contemporary version. Design of beams with holes is treated in a similar fashion in the Swiss design code SIA 265:2012 [84].

The end-notched beam analogy method is based on the assumption that the stress distribution in the vicinity of a hole resembles that around the notch of an end-notched beam. The design approach for end-notched beams may hence be used also for beams with a hole placed in position where loading is dominated by shear force action, using the analogies indicated in Figure 2.19. A rectangular hole is assumed to correspond to a right-angled notch while a circular hole is assumed to correspond to a 1:1 tapered notch. The design method for end-notched beams is based on a Linear elastic fracture mechanics analysis of beams with right angled notches derived in [41]. The design criterion formally reads as a comparison of shear stress τ and shear strength f_v. The decisive material parameters from the fracture mechanics approach are however fracture energy in tension perpendicular to grain, the stiffness in the beam length direction and the shear stiffness. These parameters enter the design equations via the factor 6.5, present in the expression for the reduction factor k_v, based on assumptions of their relation with the shear strength. The following criterion should be fulfilled

$$\tau = \frac{3}{2}\frac{V_i}{Bh_i} \leq k_v f_v \tag{2.52}$$

where index i refer to either the upper ($i = u$) or the lower ($i = l$) part of the beam. The shear force may here be assumed to be divided between the upper and lower parts in proportion to their respective stiffness. The reduction factor k_v is given by

$$k_v = \min \begin{cases} 1.0 \\ \dfrac{6.5\left(1 + \dfrac{1.1 j^{1.5}}{\sqrt{h}}\right)}{\sqrt{h}\left(\sqrt{\alpha - \alpha^2} + 0.8\dfrac{e}{h}\sqrt{\dfrac{1}{\alpha} - \alpha^2}\right)} \end{cases} \tag{2.53}$$

where

$$\alpha = h_i/h \tag{2.54}$$

$$h = \begin{cases} h_i + b/2 & \text{for rectangular hole, } h \text{ in mm} \\ h_i + \phi/2 & \text{for circular hole, } h \text{ in mm} \end{cases} \tag{2.55}$$

$$j = \begin{cases} 0 & \text{for rectangular hole} \\ 1.0 & \text{for circular hole} \end{cases} \tag{2.56}$$

$$e = \begin{cases} a/2 & \text{for rectangular hole} \\ 0 & \text{for circular hole} \end{cases} \tag{2.57}$$

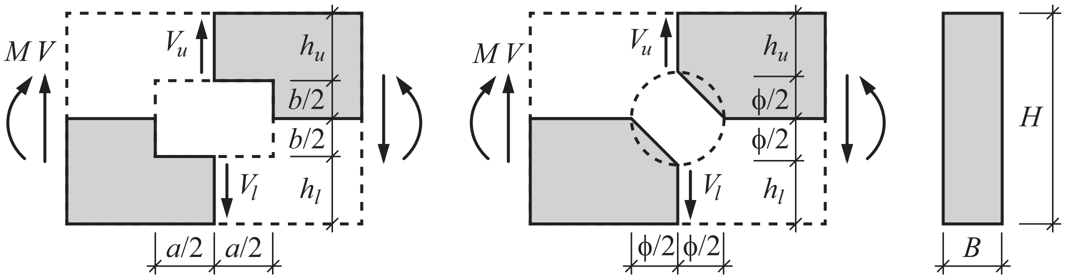

Figure 2.19: Design of beams with a hole using the end-notched beam analogy.

German National Annex to Eurocode 5 - DIN EN 1995-1-1/NA

A design method for beams with a hole is given in the German National Annex to Eurocode 5, DIN EN 1995-1-1/NA [26]. This design approach is rather different from the end-notch beam analogy approach present in the Swedish Glulam handbook. The German method is based on linear elastic stress analysis and equilibrium considerations. It originates from work presented in [54], although simplifications and empirical modifications have been added.

The design criterion is formulated such that the beam strength should be verified with respect to cracking along grain at assumed potential crack planes as indicated in Figure 2.20. Crack planes 1 and 2 are relevant for shear force dominated loading and crack planes 1 and 3 are relevant for loading dominated by (positive) bending moment. Perpendicular to grain tensile stress, having a triangular distribution, is assumed to act along these crack planes. The stress magnitude is determined by a perpendicular to grain force resultant $F_{t,90}$ which in turn is determined based on contributions from the shear force V and bending moment M. The contribution $F_{t,90,V}$ from the shear force is assumed to be statically equivalent to the integral of the beam theory shear stresses from beam mid-axis to the potential crack plane for a beam with a centrically placed hole, as illustrated schematically in Figure 2.20. The contribution $F_{t,90,M}$ from the bending moment is empirically based.

The design criterion may be expressed as a comparison of the maximum perpendicular to grain tensile stress $\sigma_{t,90}$ with the corresponding strength $f_{t,90}$ according to

$$\sigma_{t,90} = \frac{F_{t,90}}{0.5 l_{t,90} B} \leq k_{t,90} f_{t,90} \tag{2.58}$$

The perpendicular to grain force resultant $F_{t,90}$ should be determined as

$$F_{t,90} = F_{t,90,V} + F_{t,90,M} = \frac{Vd}{4H}\left(3 - \frac{d^2}{H^2}\right) + 0.008\frac{M}{h_r} \tag{2.59}$$

where for rectangular holes $d = b$ and for circular holes $d = 0.7\phi$ and further

$$\begin{aligned} h_r &= \min\begin{cases} h_u \\ h_l \end{cases} && \text{for rectangular holes} \\ h_r &= \min\begin{cases} h_u + 0.15\phi \\ h_l + 0.15\phi \end{cases} && \text{for circular holes} \end{aligned} \tag{2.60}$$

The length $l_{t,90}$ of the triangular shaped perpendicular to grain stress distribution is given by

$$\begin{aligned} l_{t,90} &= 0.5(b + H) && \text{for rectangular holes} \\ l_{t,90} &= 0.353\phi + 0.5H && \text{for circular holes} \end{aligned} \tag{2.61}$$

The strength reduction factor related to beam height is given by

$$k_{t,90} = \min\begin{cases} 1 \\ (450/H)^{0.5} \end{cases} \quad \text{with } H \text{ in mm} \tag{2.62}$$

The above given design approach was included in (at least) two previous versions of the German code DIN 1052. In DIN 1052:2004 [24], the influence of beam depth according to $k_{t,90}$ was however not present. The design recommendations for beams with a rectangular hole were withdrawn during 2007, reportedly due to general safety and reliability concerns. The design approach presented above, including the beam height factor $k_{t,90}$ later reappeared in DIN 1052:2008 [25], however with considerably stricter rules for maximum allowed hole size.

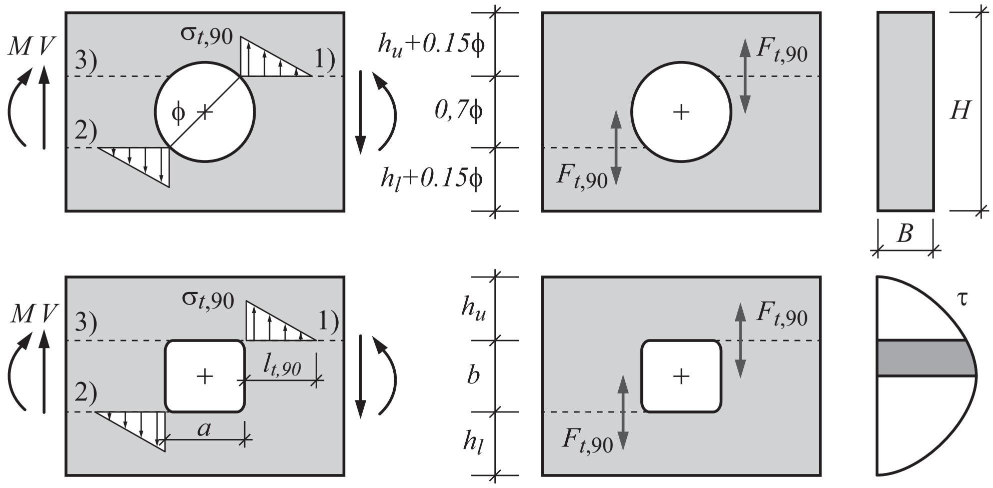

Figure 2.20: Design of beams with a hole according to German National Annex to Eurocode 5.

Design proposal by Aicher, Höfflin and Reinhardt

A design proposal for straight and curved glulam beams with a circular hole is presented [8], based on work also presented in [6], [7] and [51]. The design approach is based on Weibull theory and includes considerations of the size of the stressed volume and the level of heterogeneity in stress distribution. The magnitude and distribution of the perpendicular to grain tensile stress field around the hole was studied for various beam geometries and loading conditions, using 2D and 3D linear elastic FE-analysis. Based on this analysis and calibration to experimental tests, a design criterion was proposed involving strength modification factors relating to the size of the stressed volume and the level of heterogeneity in the stress distribution. Considering straight beams only, the design criterion is expressed as a comparison of the maximum perpendicular to grain tensile stress $\sigma_{t,90}$ and the perpendicular to grain tensile strength $f_{t,90}$ according to

$$\sigma_{t,90} \leq k_{dis} k_{vol} k_{cal} f_{t,90} \tag{2.63}$$

where the perpendicular to grain tensile stress is approximated by

$$\sigma_{t,90} = \left[\frac{3}{2} \frac{V}{BH} \left(1.23 + 0.82 \frac{\phi}{H} \right) + 0.1 \frac{6M}{BH^2} \frac{\phi}{H} \right] \chi \tag{2.64}$$

where $\chi = 1.0$ for a pure bending load case with $M/(VH) = \infty$ and $\chi = 0.9$ for all other load cases. The stress distribution factor is given by

$$k_{dis} = \begin{cases} 1.79 & \text{for} \quad 0 \leq M/(VH) \leq 2 \\ 1.83 & \text{for} \quad M/(VH) \approx 5 \\ 1.88 & \text{for} \quad M/(VH) \approx 10 \\ 2.04 & \text{for} \quad M/(VH) = \infty \end{cases} \tag{2.65}$$

The stressed volume factor is given by

$$k_{vol} = (\Omega_{ref}/\Omega)^{1/5} \qquad \text{where } \Omega = \frac{\phi}{2} \left(\frac{\phi}{2} \cos 20^\circ - \frac{\phi}{2} \cos 80^\circ \right) B = 0.19 \phi^2 B \tag{2.66}$$

with beam and hole dimensions in mm and the reference volume $\Omega_{ref} = 10^7$ mm^3. The calibration factor is determined to $k_{cal} = 1.03$, based on comparison of characteristic strength values and characteristic beam capacity of experimental tests regarding crack initiation across the beam width at the hole.

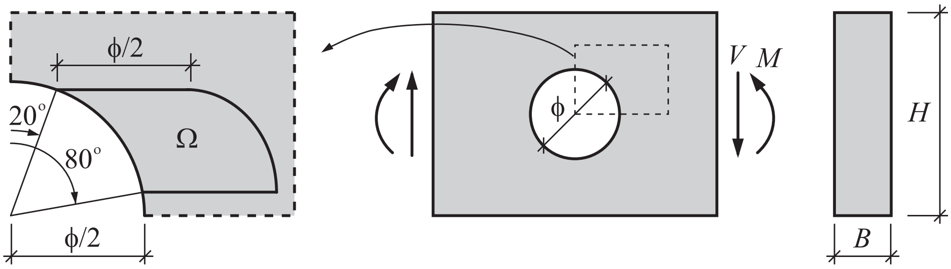

Figure 2.21: Design of beams with a circular hole according to proposal by Aicher et al.

2.3.2 Dowel connections loaded perpendicular to grain

Dowel connections loaded at an angle to grain, as illustrated in Figure 2.22, induce perpendicular to grain tensile stress in the wood member. The connection capacity with respect to cracking along grain should hence be verified in design. The design criterion in Eurocode 5 [32] seems to originate from a LEFM approach, e.g. as presented by van der Put and Leijten [70]. The connection capacity with respect to cracking along grain is according to this LEFM approach given by the critical value V_c of the shear force on either side of the dowel according to

$$V_c = \sqrt{\frac{GG_c}{0.6}} b \sqrt{\frac{h_e}{1 - h_e/h}} \tag{2.67}$$

where G is the shear modulus, G_c is the fracture energy (or critical energy release rate), b and h are beam cross section width and height respectively and h_e is the effective beam height (i.e. dowel-to-loaded-edge distance). This expression is based on assumptions of a single, infinitely stiff dowel which is symmetrically loaded with respect to the wood member width. The above given equation was in [70] suggested to be used for design with respect to cracking along grain and then assumed to be valid for $h_e < 0.7h$. The factor $\sqrt{GG_c/0.6} = 15.5$ N/mm$^{1.5}$ was found to correspond well with strength according to experimental tests at the mean value level. Based on this, the factor $\sqrt{GG_c/0.6} = 15.5 \cdot 2/3 \approx 10$ N/mm$^{1.5}$ was suggested to be used for the code design criterion at the characteristic level.

The design equations in Eurocode 5 [32] for a row of connectors loaded at an angle to grain are given below. For the types of connections in Figure 2.22, the following criterion should be fulfilled

$$F_{v,Ed} \leq F_{90,Rd} \quad \text{with} \quad F_{v,Ed} = \max \begin{cases} F_{v,Ed,1} \\ F_{v,Ed,2} \end{cases} \tag{2.68}$$

where $F_{v,Ed,1}$ and $F_{v,Ed,2}$ are the design shear forces on either side of the connection and $F_{90,Rd}$ is the design splitting capacity of the beam at the connection. The design capacity is found from the characteristic capacity $F_{90,Rk}$ by conventional modifications considering partial factors for material properties and for duration of load and moisture content effects. The characteristic splitting capacity $F_{90,Rk}$ for a connection with metal dowel-type fasteners and a beam element of softwood is given by

$$F_{90,Rk} = 14b \sqrt{\frac{h_e}{1 - h_e/h}} \tag{2.69}$$

where h_e is the distance from the loaded edge to the center of the most distant fastener (the effective beam depth) and where h and b are the wood member height and width respectively, with the capacity in N and all dimensions in mm. The design capacity does hence not explicitly depend on any material parameters such as strength, stiffness or fracture energy. The only parameters influencing the capacity are instead geometrical parameters although capacity according to the underlying fracture mechanics approach is determined by the shear stiffness and the fracture energy, in addition to the geometrical influence. The discrepancy regarding the value of the factor $\sqrt{GG_c/0.6}$ should be noted, a value of 10 N/mm$^{1.5}$ is in [70] suggested to be used at the characteristic level while the corresponding value is 14 N/mm$^{1.5}$ in Eurocode 5.

The LEFM approach underlying the design equations in Eurocode 5 is based on assumption of an infinitely stiff fastener and considers only the case of symmetric loading. The loading situation may however also be such that the dowel load is eccentric, as illustrated in Figure 2.23. Such a loading situation is believed to yield a lower connection capacity compared to the case of symmetric loading. An eccentric loading situation may also arise as a result of development of plastic hinges in the dowel, shifting the mode of failure from a ductile dowel failure to a potentially brittle wood failure by cracking along grain.

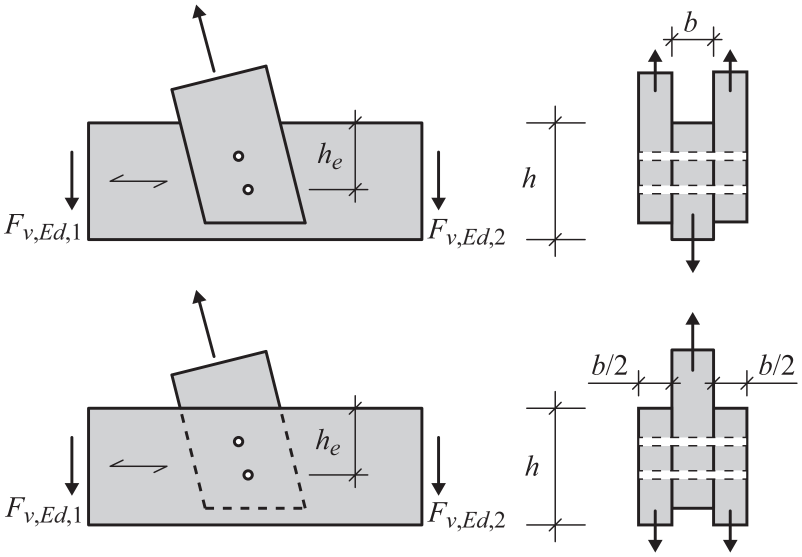

Figure 2.22: Design of dowel connection loaded perpendicular to grain according to Eurocode 5.

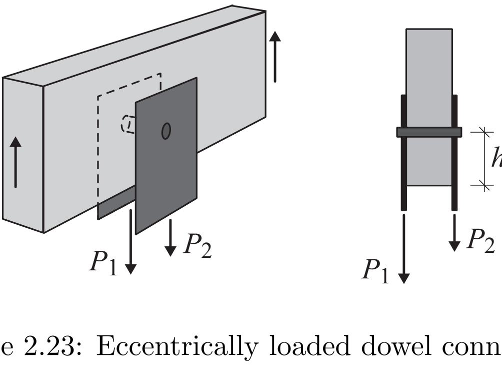

Figure 2.23: Eccentrically loaded dowel connection.

3 Overview of present work

This chapter gives an overview of the work presented in the Papers A-F found in Part III of this thesis. The presentation is here divided into three sections. The first section deals with experimental tests of glulam beams with a hole and is in essence a short summary of Papers A and B. The two latter sections deal with strength analysis approaches for perpendicular to grain fracture in wood. Two different approaches are presented, a probabilistic fracture mechanics method and a cohesive zone model. The work related to these strength analysis approaches takes it start in the theory presented in Chapter 2.

The probabilistic fracture mechanics method (PFM) is based on a combination of Weibull theory and a mean stress method, which is a generalization of Linear elastic fracture mechanics. This strength analysis method is presented in Paper C and there also applied to analysis of glulam beams with a hole.

The second strength analysis approach is a Nonlinear fracture mechanics approach, a 3D cohesive zone model (CZM), which is formulated using theory of plasticity. This model is presented in Paper D and there also applied to analysis of a double cantilever beam and end-notched beams. The model is further applied to analysis of glulam beams with a hole in Paper E and dowel-type connections loaded perpendicular to grain in Paper F. The numerical implementation in terms of solution approaches for global equations of equilibrium and integration of constitutive relations is treated in the attachment found in Part II of this thesis.

3.1 Strength tests of glulam beams with a hole

There are numerous experimental investigations found in the literature concerning the strength of glulam beams with holes. Experimental tests of beams with rectangular or circular holes from eight different sources and a total of 182 individual tests are reviewed in [21] and a compilation of results is also presented in Paper B. Although the experimental tests found in literature all in all represent much work, the review revealed that important parameters such as mode of loading, beam size and hole placement with respect to beam height have often been varied only within a very limit range. It seems for example that all beams tested have had a hole centrically placed with respect to beam height.

With the aim of widening the experimental data base, tests of beams with quadratic holes were carried out and these are reported in Paper A. The test program consisted of nine test series with four nominally equal tests in each series. Four design parameters were investigated; material strength class, bending moment to shear force ratio, beam size and the previously overlooked design parameter of hole placement with respect to beam height. Test setups and hole placements according to Figure 3.1 were used. Beams with cross sections $B \times H = 115{\times}630$ and $115{\times}180$ mm^2 were tested. All holes were quadratic with side length $a = b = H/3$ and rounded corners with $r \approx H/25$. The tests were carried out as short-term static ramp load tests.

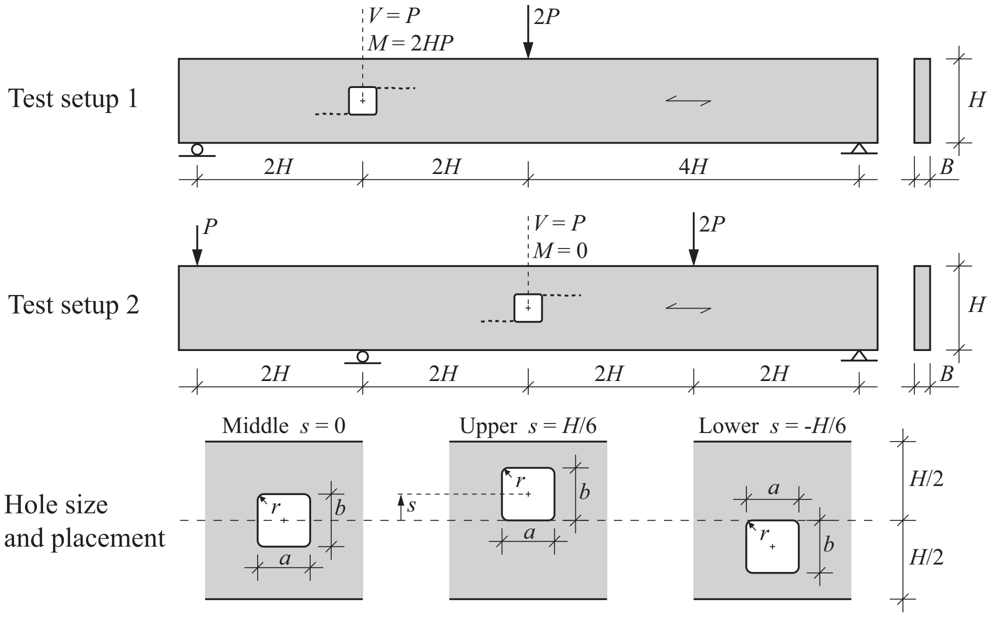

Figure 3.1: Test setups, hole size and placements with respect to beam height.

During loading, cracks appeared at two diagonal corners of the holes exposed to perpendicular to grain tensile stress. The most commonly found crack scenario was that crack initiation occurred at beam mid-width, followed by crack propagation in the beam width direction and eventually crack propagation in the beam length direction. Beams with a hole placed in the upper part of the beam showed the most brittle fracture behavior, with crack initiation followed by unstable crack propagation all the way to the end of the beam.

The test results showed a strong beam size effect on the strength. Increasing the beam size by a factor 3.5 gave about 35% reduction of nominal capacity. This strong beam size effect is in-line with the results of comprehensive experimental test programs of beams with circular holes presented in [6] and [51].

3.2 A probabilistic fracture mechanics method

The probabilistic fracture mechanics method (PFM) considered here is a combination of Weibull theory and a mean stress method which is a generalization of Linear elastic fracture mechanics. Combining these two methods means that the calculated strength is determined considering the stochastic nature of material properties, finite material strength and nonzero fracture energy. A proposal for such a method is briefly outlined in [43] and [83]. This proposal is in Paper C further developed, implemented based on linear elastic plane stress FE-analysis and applied to strength analysis of glulam beams with a hole.

The starting point for PFM is the reformulation of Weibull theory in Section 2.2.2. Based on analysis of different volumes and stress distributions with equal probability of failure, a global effective dimensionless stress parameter α_{global} was there introduced as

$$\alpha_{global} = \left(\frac{1}{\Omega_{ref}} \int_{\Omega} \alpha^{m}(x,y,z)\ \mathrm{d}\Omega \right)^{1/m} \tag{3.1}$$

where α is an effective dimensionless stress field based on one or more stress components and the corresponding strength values. Furthermore is Ω_{ref} the reference volume for which the mentioned strength values are valid and m is the Weibull shape parameter related to the scatter in material strength. Choosing the effective dimensionless stress field α such that the constant value of $\alpha = 1.0$ in Ω_{ref} represents the statistical mean failure state of stress, the value $\alpha_{global} = 1.0$ will correspond to the statistical mean value for global failure of the volume Ω.

To account for nonzero fracture energy, the effective dimensionless stress field is chosen in accordance with the mean stress method reviewed in Section 2.2.4. This mean stress method utilizes a failure criterion based on mean stresses within what is here referred to as a *potential fracture area*. For cracking along grain, the most damage relevant stress components are assumed to be the perpendicular to grain tensile stress and the shear stress (here and in Paper C simply referred to as σ and τ respectively). The size of this potential fracture area is derived such that strength predictions will be consistent with LEFM for the case of a large crack in a large body. Strength predictions will further be consistent with conventional stress based failure analysis for a body in a homogeneous state of stress. The size of the potential fracture area is here assumed to be valid also for all intermediate stress gradients between the two extreme cases of the square root stress singularity gradient and the zero gradient for homogeneous stress. The dimensionless effective stress field used for the plane stress analysis is hence chosen as

$$\alpha(x,y) \quad = \quad \left[\left(\frac{\bar{\sigma}(x,y)}{f_\sigma} \right)^2 + \left(\frac{\bar{\tau}(x,y)}{f_\tau} \right)^2 \right]^{1/2} \tag{3.2}$$

where $\bar{\sigma}$ and $\bar{\tau}$ are mean stresses acting within a potential fracture area. The size of the potential fracture area is based on the length a_{ms}, given in Equation (2.49) as

$$a_{ms} = \frac{2}{\pi} \frac{E_I G_{Ic}}{f_\sigma^2} \frac{E_x}{E_y} \left(\frac{G_{IIc}}{G_{Ic}} \right)^2 \frac{1}{4k^4} \left(\sqrt{1 + 4k^2 \sqrt{\frac{E_y}{E_x}} \frac{G_{Ic}}{G_{IIc}}} - 1 \right)^2 \left(1 + k^2 \frac{f_\sigma^2}{f_\tau^2} \right) \tag{3.3}$$

where $k = \bar{\tau}/\bar{\sigma}$ is the mixed mode ratio and where E_I, E_x, E_y, G_{Ic}, G_{IIc}, f_σ and f_τ are material parameters related to stiffness, fracture energy and material strength which are defined in Sections 2.2.3 and 2.2.4.

The physical interpretation of the method is that all points in the body are considered as potentially weak points where fracture initiation may occur. The material is, due to nonzero fracture energy and ductility, assumed to have the ability to distribute stresses over a potential fracture area and it is hence the mean stresses acting within this area that are considered. In accordance with Weibull theory, the resistance to fracture is not homogeneous but viewed as a stochastic property. Since fracture may start from any point in the body, all possible points need to be considered. The strength prediction of PFM depends, among other parameters, on the value of the Weibull shape parameter m and the fracture energy parameters G_{Ic} and G_{IIc}. For certain choices of these parameters, PFM will break down to Weibull theory, the mean stress method or conventional stress analysis with a stress based failure criterion as special cases as illustrated in Figure 3.2

Application to glulam beams with a hole

The probabilistic fracture mechanics method is in Paper C applied to analysis of beams with a hole. The FE-software ABAQUS [1] was used for the plane stress analysis. The stress fields $\sigma(x,y)$ and $\tau(x,y)$ were determined within a part of the beam as illustrated in Figure 3.3, using a linear elastic and transversely isotropic material model. Based on nodal point stress values,

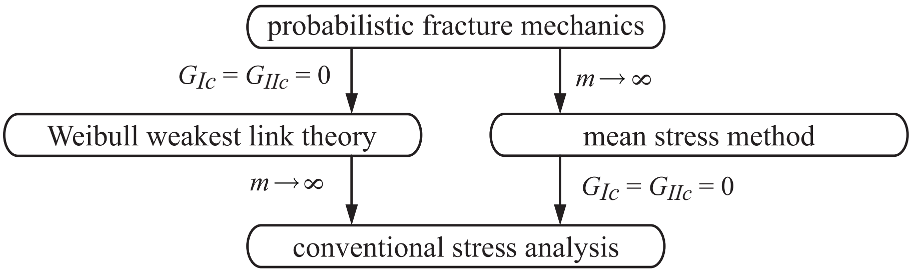

Figure 3.2: Relation between methods for strength analysis.

the stress components σ and τ were interpolated to a fine and structured grid of reference points using MATLAB [61]. The dimensionless effective stress field α was determined at all reference points based on the mean stresses $\bar{\sigma}$ and $\bar{\tau}$ acting within potential fracture areas associated with the respective points. The global dimensionless effective stress parameter α_{global} was determined based on numerical integration of Equation (3.1) according to

$$\alpha_{global} = \left(\frac{B a_{rp}^2}{\Omega_{ref}} \sum_{i=1}^{n} \alpha^m(x_i, y_i) \right)^{1/m} \tag{3.4}$$

where B is the plane stress width, a_{rp} is the distance between the evenly distributed reference points, n is the number of reference points, $\alpha(x_i, y_i)$ is the value of the effective dimensionless stress field for reference point i and m is the Weibull shape parameter. Since $\alpha_{global} = 1.0$ corresponds to the statistical mean failure state of the volume Ω, the predicted mean value of the shear force at failure is finally given by

$$V_{failure} = \frac{1}{\alpha_{global}} V_{FE} \tag{3.5}$$

where V_{FE} is the shear force applied in the FE-analysis and α_{global} is the value obtained from Equation (3.4) for this shear force.

A numerical parameter study of the influence on the global beam strength was carried out considering the following parameters; bending moment to shear force ratio, beam size, hole shape, hole placement with respect to beam height and relative hole size with respect to beam height. Among these parameters and within the considered limits, beam size was found to be the most influential parameter. Theoretical strength predictions were further compared to the strength of experimental tests of beams with quadratic holes, presented in the previous section, and beams of height $H = 450$ and 900 mm containing circular holes presented in [6] and [51]. Results in terms of ratio between theoretical capacity and experimental capacity are presented in Figure 3.4, for the general methods considering mean values and for the code design methods considering characteristic values. The results of the special cases of Weibull theory, the mean stress method (MSM) and conventional stress analysis (CSA) are presented along with the results of the code design methods reviewed in Section 2.3.1.

The probabilistic fracture mechanics method seems to have good ability to predict strength of beams with a hole, with the exception of small beams ($H = 180$ mm) where the strength was overestimated. Good general features of the method include its generality, making it applicable to analysis of bodies including both low and high stress gradients and even singular stress points. The method further acknowledges the material properties assumed to be of importance for perpendicular to grain fracture; material strength, stiffness, fracture energy and heterogeneity.

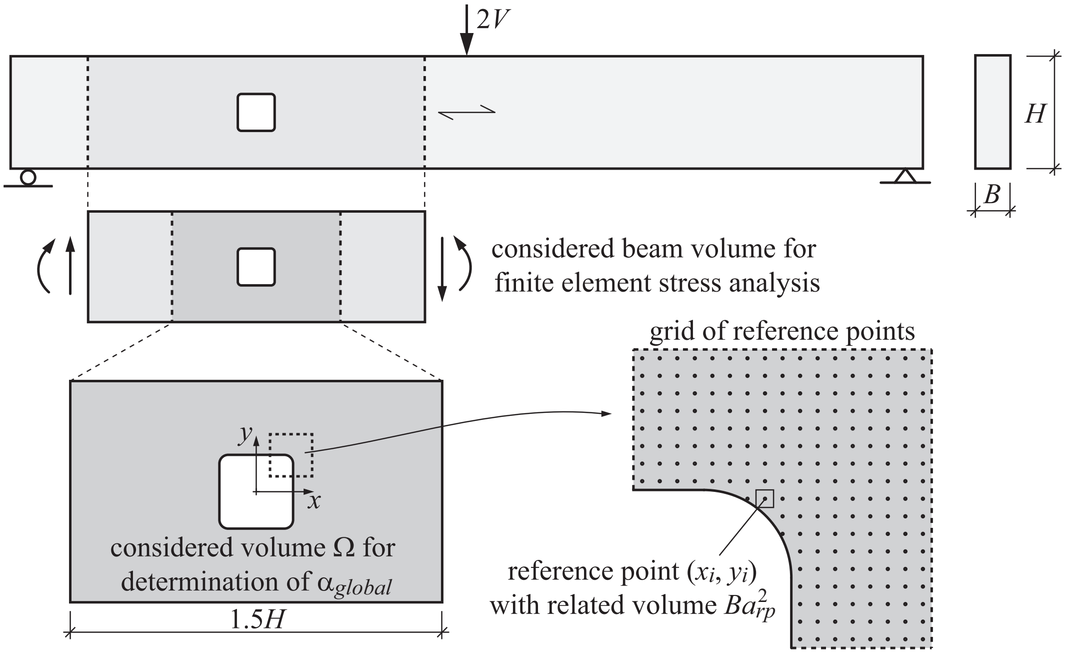
2V
H
B
considered beam volume for
finite element stress analysis
grid of reference points
y
x
considered volume Ω for
determination of α_global
1.5H
reference point (x_i, y_i)
with related volume Ba_rp^2

Figure 3.3: Considered beam parts for stress analysis and calculation of α_{global}.

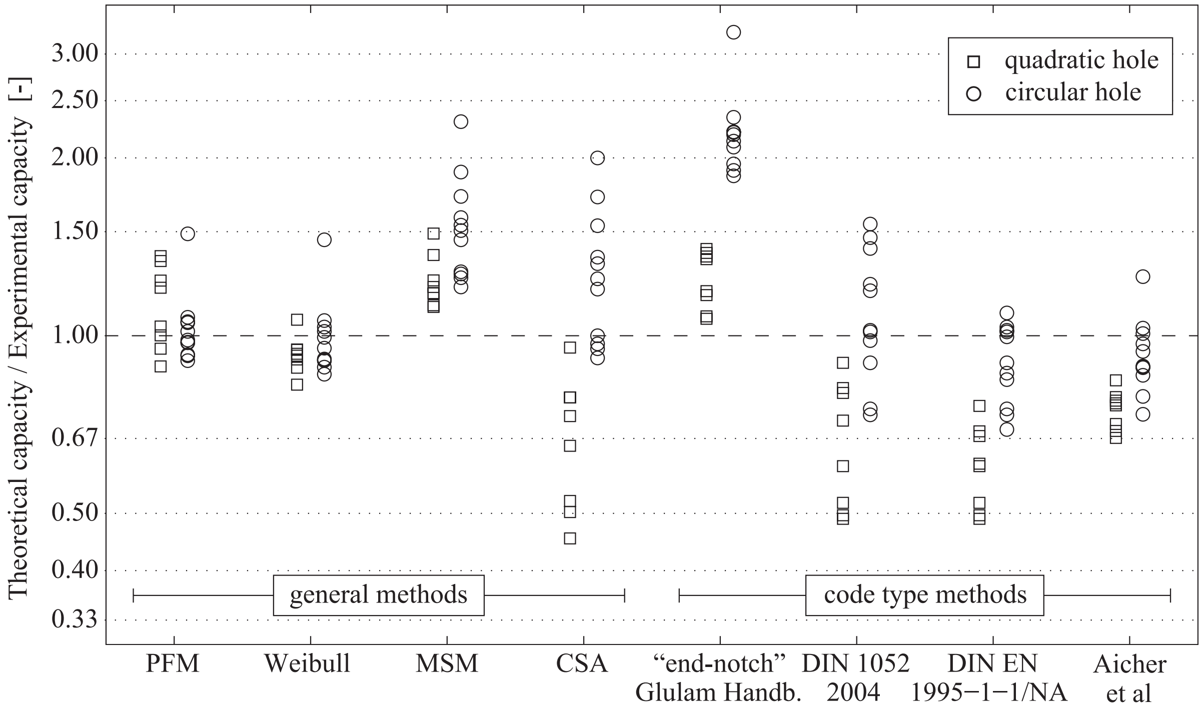

Figure 3.4: Comparison of strength found from experimental tests and predicted strengths according to different general methods and code design methods for strength analysis.

3.3 A cohesive zone model based on plasticity theory

A cohesive zone model for perpendicular to grain fracture analysis is presented in Paper D, based on the Nonlinear fracture mechanics concept of cohesive zone modeling as introduced by Hillerborg et al [48] and here reviewed in Section 2.2.5. The model is derived within the framework of plasticity theory and based on a 3D macro scale continuum representation. Orthotropic material properties are taken into account since distinction is made concerning material strength and stiffness in all three material principal directions and also concerning fracture energy for the different modes of deformation. The material is assumed to be homogeneous in the sense that knots and other defects are disregarded. Small strain assumptions and additive decomposition of elastic and plastic strains are used.

The cohesive zone model is applied to a predefined potential crack plane, within which a fracture process zone may initiate and evolve. The predefined potential crack plane is assumed to be oriented as the global xz-plane and is given a small, but nonzero, height h in the out-of-plane y-direction as depicted in Figure 3.5. The global x-direction is further assumed to coincide with the material longitudinal direction. The wood bulk material is for all applications considered here modeled as a linearly elastic orthotropic material.

Material model

The Tsai-Wu criterion [89] according to Equation (2.14) is used as criterion for initiation of yielding, i.e. the formation of a fracture process zone and initiation of softening. An initial yield function F is hence defined according to

$$F(\bar{\boldsymbol{\sigma}}) = \bar{\boldsymbol{\sigma}}^T\bar{\mathbf{q}} + \bar{\boldsymbol{\sigma}}^T\bar{\mathbf{P}}\bar{\boldsymbol{\sigma}} - 1 \quad \text{where} \begin{cases} F < 0 & \text{elastic response} \\ F = 0 & \text{initiation of softening} \end{cases} \tag{3.6}$$

where $\bar{\mathbf{q}}$ and $\bar{\mathbf{P}}$ are given by material strength properties according to Equations (2.15) and (2.16) and where $\bar{\boldsymbol{\sigma}}$ is the stress given in material directions according to Equation (2.3). Initiation of softening is hence allowed to depend on all six stress components.

The material performance after the instant of initiation of softening changes drastically and is here described by a stress vs. relative displacement relation. The relative displacements assumed to be of importance for the subsequent softening performance are the three out-of-plane relative displacements. These are here expressed as plastic deformations and denoted δ_{yy}, δ_{xy} and δ_{yz}. These plastic deformations do in a sense correspond to the fracture mechanics modes of deformation I, II and III (see Figure 2.7) although no actual distinction can be made between modes II and III for the present model. The subsequent softening performance is further assumed to be governed only by the three out-of-plane stress components and an updated yield function

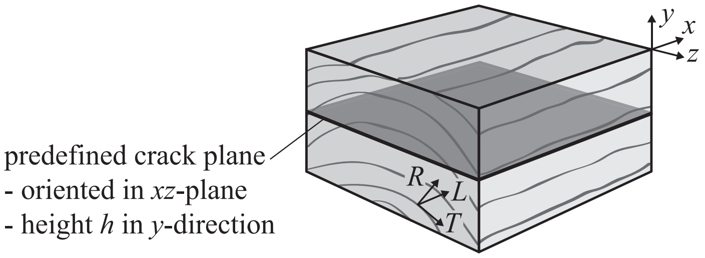

Figure 3.5: Orientation of predefined crack plane with respect to global directions xyz.

is hence defined as

$$f(\boldsymbol{\sigma}, K) = \sigma_{yy}^2 F_{yyyy} + \tau_{xy}^2 F_{xyxy} + \tau_{yz}^2 F_{yzyz} - K^2 \quad \text{where} \begin{cases} f < 0 & \text{elastic response} \\ f = 0 & \text{elasto-plastic response} \end{cases} \tag{3.7}$$

where σ_{yy}, τ_{xy} and τ_{yz} are components of the stress $\boldsymbol{\sigma}$ related to global directions xyz. Further are F_{yyyy}, F_{xyxy} and F_{yzyz} fictitious strength parameters determined from the stress state at initiation of softening and K is a softening parameter. An associated (with respect to the updated yield function f) plastic flow rule is adopted according to

$$\dot{\boldsymbol{\varepsilon}}^p = \dot{\lambda}\frac{\partial f}{\partial \boldsymbol{\sigma}} \qquad \text{with } \dot{\lambda} \geq 0 \text{ and where} \begin{cases} \dot{\lambda} = 0 & \text{elastic strains only} \\ \dot{\lambda} > 0 & \text{plastic strains} \end{cases} \tag{3.8}$$

where $\dot{\lambda}$ is the plastic multiplier.

The change in size of the yield surface is described by the softening parameter K which is a function an internal variable denoted the effective dimensionless deformation δ_{eff}. The softening behavior is defined such that states before initiation of softening are characterized by $\delta_{eff} = 0$ and $K = 1$ while the final state of zero stress transferring capacity and creation of new traction-free crack surfaces is given by $\delta_{eff} = 1.0$ and $K = 0$. Within the work presented here, two different softening functions have been adopted according to

$$K_D = \begin{cases} (1 - \delta_{eff} + c^{1/m}\delta_{eff})^m & \text{for} \quad \delta_{eff} < 1 \\ 0 & \qquad\quad \delta_{eff} \geq 1 \end{cases} \tag{3.9}$$

$$K_{EF} = \begin{cases} \exp(\ln(c)\delta_{eff}^m) & \text{for} \quad \delta_{eff} < 1 \\ 0 & \qquad\quad \delta_{eff} \geq 1 \end{cases} \tag{3.10}$$

where m is a model parameter determining the shape of the softening curve and where c is a small, but nonzero, number. A softening law with $K = K_D$ is used in Paper D and $K = K_{EF}$ is used in Papers E and F. The slightly modified softening function used in Papers E and F was adopted since it was believed to enhance the numerical performance due to the somewhat less abrupt change in stiffness at initiation of softening. Illustrations of the two softening behaviors are found in Figure 3.6 based on model parameters $c = 0.01$, $m_D = 5$ and $m_{EF} = 1.5$ and material properties $f_{Rt} = 3$ MPa and $G_{f,yy} = 300$ J/m^2.

The evolution law for the effective dimensionless deformation δ_{eff} is defined as

$$\dot{\delta}_{eff} = \left[\left(\frac{\dot{\delta}_{yy}}{A_{yy}} \right)^n + \left(\frac{\dot{\delta}_{xy}}{A_{xy}} \right)^n + \left(\frac{\dot{\delta}_{yz}}{A_{yz}} \right)^n \right]^{1/n} \tag{3.11}$$

where the value $n = 2$ has been used for all analyses presented in this thesis. The incremental plastic deformations are given by $\dot{\delta}_{yy} = h\dot{\varepsilon}_{yy}^p$, $\dot{\delta}_{xy} = h\dot{\gamma}_{xy}^p$ and $\dot{\delta}_{yz} = h\dot{\gamma}_{yz}^p$ by assuming constant plastic strains over the small out-of-plane (y-direction) height h of the predefined crack plane. A_{yy}, A_{xy} and A_{yz} are scaling parameters of dimension length which are determined such that the energy required for complete separation at uniaxial loading in any of the three modes of deformation equals the corresponding fracture energies $G_{f,yy}$, $G_{f,xy}$ and $G_{f,yz}$.

The energy required to create a unit traction-free crack in a general mixed mode of deformation is for the present model not explicitly given by a mixed mode energy interaction criterion. The required energy is instead implicitly given by the general formulation of the model and is in particular affected by the choice of the parameter n in Equation (3.11). The fracture energy for a general mixed mode of loading is path dependent and hence also affected by material strength and stiffness properties, in addition to the pure mode fracture energies $G_{f,yy}$, $G_{f,xy}$ and $G_{f,yz}$.

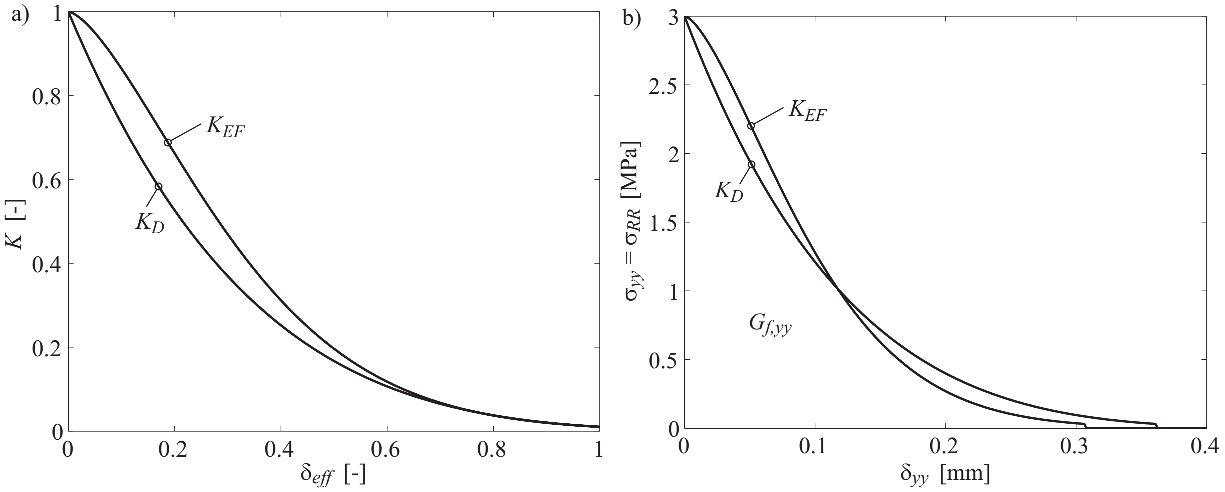

Figure 3.6: Softening functions (a) and stress vs. deformation relationships for uniaxial tension in the radial direction (b).

The energy required for complete separation at monotonic loading for different mixed mode loading situations of combined opening and shearing is illustrated in Figure 3.7a). The illustration is based on analysis of a single finite element loaded by prescribed displacements as depicted in the figure and using model and material parameters according to Paper F, including $G_{f,yy} = 300$ J/m^2 and $G_{f,xy} = 900$ J/m^2. The shape of the curve resembles the mixed mode interaction given in Figure 2.9b), based on experimental test of small-scale notched specimens of Norway spruce [87] and Scots pine [92] loaded in a similar fashion.

The in-plane stress components σ_{xx}, σ_{zz} and τ_{xz} are for the present model allowed to influence the response within the potential crack plane and hence also the global response. Figure 3.7b) shows how the value of σ_{yy} at initiation of softening is affected by the parallel to grain stress component σ_{xx}, based on parameters used in Paper F. The marks represent analysis of a single finite element loaded in a biaxial σ_{yy} and σ_{xx} state of stress and the solid line gives the Tsai-

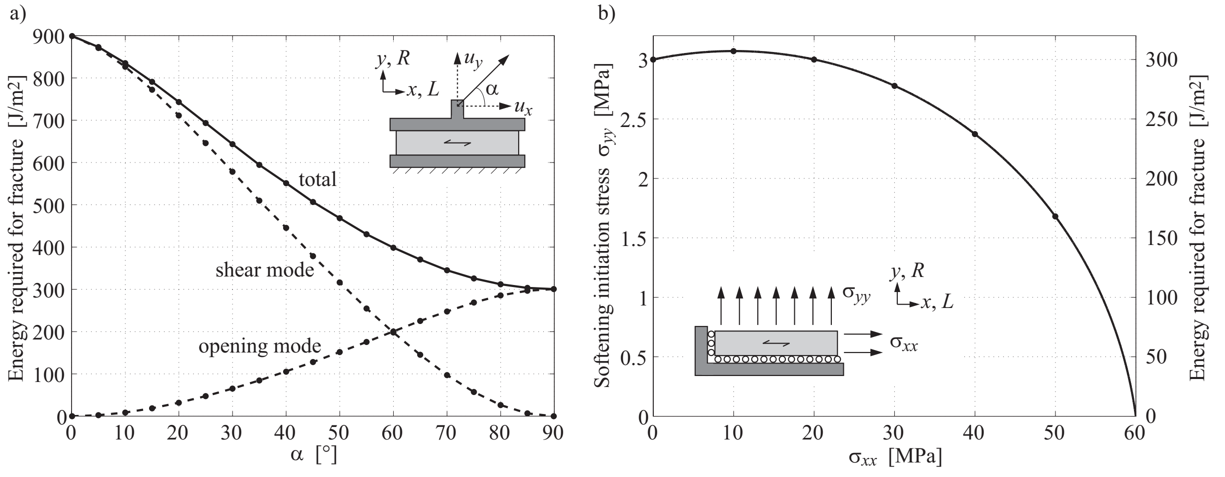

Figure 3.7: Mixed mode interaction for combined opening σ_{yy} and shearing τ_{xy} (a) and interaction between at biaxial stress state σ_{yy} and σ_{xx} (b).

Wu initial yield surface for the considered loading situation. The energy required to bring the material to complete fracture is scaled according to the ratio between the softening initiation stress σ_{yy} and the corresponding uniaxial tensile strength, here being 3 MPa.

Numerical implementation

The material model is implemented for FE-analysis in MATLAB [61] using supplementary routines from the toolboox CALFEM [11]. It is in Paper D applied to analysis of a double cantilever beam and end-notched beams, in Paper E applied to glulam beams with a hole and in Paper F to dowel-type connections loaded perpendicular to grain. The often highly nonlinear global response is solved in an incremental-iterative fashion using either Newton-Raphson methods or arc-length type of path following methods. Issues relating to the formulation of nonlinear finite element method, the solution of global equations of equilibrium and integration of constitutive relations are treated in the attachment found in Part II of this thesis.

Comments regarding the analyses of the respective applications are given below.

Application to a double cantilever beam - Paper D

The purpose of the double cantilever beam (DCB) specimen analysis was two-fold; it served as a verification of the numerical implementation and also served as a base for a small parameter study. The parameter study aimed at illustrating the influence of some material parameters and parameters related to the numerical implementation. The parameter study showed that the tensile strength in the longitudinal direction had a considerable influence on the response of the DCB specimen. This influence comes from using the Tsai-Wu criterion as criterion for initiation of softening and the formation of a fracture process zone. Disregarding whether the considered set of material parameters are representative or not, it is interesting that the material model incorporates, in contrast to most interface-based cohesive zone models, a possible influence of all six stress components on the initiation of softening and hence also on the global response.

Application to end-notched beams - Paper D

End-notched beams were analyzed with respect influence of varying material principal directions on calculated beam strength and development of the fracture process zone. Different heterogeneous and homogeneous growth ring patterns were considered for beams of two different sizes. The development of the fracture process zone and its extension at maximum load differed between the considered growth ring patterns while however only small differences (about 5%) were found regarding calculated strengths.

The results in terms of beam strength were also compared to experimental tests presented in [42]. Beams with a total height of 48 mm and 192 mm were considered. The influence of beam size on the strength was predicted reasonably well by the numerical analyses, although the absolute values of calculated strength are about 10-25% greater than found from the tests.

The global solution approach, using an arc-length type of path following method, was able to capture the nonlinear global response including the snap-back response following maximum load. For all considered beam geometries and growth ring patterns, maximum load was reached before the fracture process zone was fully developed. Rapid extension of the fracture process zone and crack propagation then occurred during snap-back following maximum load.

Application to glulam beams with a hole - Paper E

Strength and fracture course analysis of glulam beams with a hole were carried out. Six out of the nine test series of beams with a hole presented in Paper A were used as a base for verification of the material model. Three different hole placements with respect to beam height and beams of two different heights, $H = 180$ and 630 mm, were represented within these six test series. The experimentally found beam size influence on the strength was captured well by the numerical analyses and also the absolute values of the calculated strengths did further agree well with the experimental results.

A parameter study relating to the combined influence of beam width and lamination growth ring pattern was further performed. The results indicate decreasing nominal strength at increasing beam width. The level of strength reduction depends on the growth ring pattern and is hence related to the orthotropic properties within the plane perpendicular to the direction of grain. The beam width influence is further related to the Poisson effect to some extent, since a small influence of beam width was also found for a homogeneous orientation of material principal directions with nonzero Poisson's ratios but not for analysis with $\nu_{RL} = \nu_{TL} = \nu_{TR} = 0$.

The influence of initial cracks, imitating for example drying cracks, was also studied. This was done by introducing cracks of different extension in the beam length and beam width directions. Among the considered types of initial cracks, an asymmetric crack pattern with an initial crack along one side of the beam forwarded the greatest beam strength reduction.

The FE-analyses of beams with a hole, containing two potential crack planes, showed to be numerically challenging. Numerical problems were encountered for analysis of the large beams ($H = 630$ mm) when considering simultaneous softening within two crack planes. Problems typically occurred shortly after reaching a maximum load or at a load level close to the expected maximum load and were manifested as lack of convergence for the numerical integration of the constitutive relations. The reason is believed to be related to either simultaneous unloading within one fracture process zone and crack propagation within the other or alternatively related to very unstable crack propagation. For the small beams ($H = 180$ mm), simultaneous crack growth at the two crack planes gave no numerical problems.

Application to dowel-type connections loaded perpendicular to grain - Paper F

The fracture performance of dowel-type connections was analyzed for two types of geometries, a plate type of geometry loaded in tension and a simply supported beam loaded in bending. A numerical parameter study regarding the influence of dowel-to-loaded-edge distance and the influence of dowel load eccentricity was performed. Numerical results were further compared to results of experimental tests of LVL plates and beams exposed to centric loading, showing overall good agreement.

Results regarding the influence of dowel-to-loaded-edge distance on strength were for the beam geometry compared to the LEFM-based design approach present in Eurocode 5 [32], valid for softwoods. The two approaches yield consistent results regarding the relative influence of the dowel-to-loaded-edge distance. Based on the present FE-analysis and tests of LVL, the Eurocode 5 design criterion do however seem to give strength predictions on the unsafe side.

The numerical results further showed that load eccentricity may affect the strength to a great extent. A simple and approximate method to account for load eccentricity, suitable for use in a practical design context, was proposed. The influence of load eccentricity given by the approximate method agreed well with the results of the FE-analysis for the plate type of geometry and agreed to a somewhat lesser extent for the beam type of geometry.

4 Conclusions

The most important conclusions drawn from the work presented in this thesis regarding the experimental and theoretical parts in terms of developed models and applications are given below. Following these conclusions are proposals for future work.

4.1 Strength of glulam beams with a hole

Experimental tests

Short term strength tests of glulam beams with a hole were carried out. These tests are presented in Papers A and B and are in Papers C and E used as base for verification of strength analysis models. All beams had quadratic holes with rounded corners and a side length of $H/3$, where H denotes the beam height. The tests included investigations of the influence of beam size, hole placement with respect to beam height, bending moment to shear force ratio and material strength class. Results regarding influence of eccentric hole placement appear not to have been reported before. Conclusions from these tests include:

- The beam size has a strong influence on the nominal strength. For constant beam width, an increase in beam height and length by a factor of 3.5 gave a nominal strength reduction of about 35%.
- About 5-15% lower mean values of beam strength were found for beams with eccentric hole placement with $s = \pm H/6$ compared to beams with centrically placed holes with $s = 0$, where s denotes the distance from the beam central axis to hole center. These results relate to a loading situation with a bending moment to shear force ratio of $M/(VH) = 2$.

Design methods in codes of practice

The comparisons in Papers B and C regarding test results and strength predictions according to design approaches in European codes of practice and handbooks reveal strong discrepancies. Conclusions from these comparisons include:

- The end-notched beam analogy approach, in the form present in the Swedish Glulam handbook [18], should not be used in relation to design of beams with a hole since it seems to strongly overestimate the beam capacity.
- The addition of an empirical beam height reduction factor in DIN 1052:2008 [25] and in the German National Annex to Eurocode 5 [26], compared to original approach presented in [54], is well motivated.

4.2 Fracture analysis models and applications

Probabilistic fracture mechanics method

A Probabilistic fracture mechanics method (PFM) is presented in Paper C. The PFM formulation is based on a combination of Weibull theory and a mean stress method, which is a generalization of Linear elastic fracture mechanics. This combination of approaches means that global strength predictions with respect to perpendicular to grain fracture are obtained based on considerations of fracture energy, material strength and the stochastic nature of the material properties. Based on the analysis of glulam beams with holes and comparison to experimental tests presented in Paper C, the following conclusions are drawn:

- The method appears able to yield accurate results in terms of absolute beam strength and influence of beam size for medium-sized and large beams, while the strength of small beams is overestimated by the considered method.
- The influence of hole eccentricity with respect to beam height is closely related to the mode of loading in terms of bending moment to shear force ratio and large strength reductions are predicted for eccentric hole placement in pure bending loading situations.
- The simplicity of the method, being based on linear elastic stress analysis, makes it suitable for numerical parameter studies relating to influence of various parameters important in practical design.

Cohesive zone model based on plasticity theory

A 3D cohesive zone model is presented in Paper D. The model is formulated using theory of plasticity, accounts for orthotropic material behavior and uses the Tsai-Wu criterion as base for initiation of softening and creation of a fracture process zone. The material model is formulated such that all six stress components are allowed to influence the softening performance and hence the global strength prediction with respect to perpendicular to grain fracture.

The model is in Paper E applied to analysis of glulam beams with a hole and in Paper F to analysis of dowel connections loaded perpendicular to grain. Based on comparison to experimental tests of beams with quadratic holes, the cohesive zone model appears to have an overall good ability to predict the absolute beam strength, beam size influence on beam strength and the general characteristics of the fracture course. The predictions of global strength for dowel connections appear also to agree well with results of experimental tests of steel dowels in LVL. Assuming the model to describe the material fracture performance correctly and to yield accurate results in terms of global strength, some conclusion may be drawn from the numerical analyses of beams with a hole and dowel type connections respectively.

Glulam beams with a hole:

- The extension of the fracture process zone at maximum load is affected by the orientation of the material principal directions, i.e. the growth ring pattern.
- Beam width affects the nominal strength and this influence is in turn affected by the growth ring pattern and by the Poisson effect.
- Presence and extensions of initial cracks influence the beam strength.

Dowels loaded perpendicular to grain:

- The predicted relative influence of the effective beam height on strength agrees well with design strength predictions in Eurocode 5. The code strength predictions, valid for softwoods, do however appear to be unconservative when applied to LVL.
- Dowel load eccentricity has a strong influence on the global strength of dowel connections. This influence is not accounted for in Eurocode 5.
- The proposed approximate method for simple consideration of dowel load eccentricity was found to agree reasonably well with numerical results for a dowel in a plate and agree to a lesser extent, on the conservative side, regarding numerical results for a dowel in a beam.

4.3 Proposals for future work

Proposals for future work, related to the general limitations of the work presented here, include considerations of long term effects and climate effects such as moisture and temperature. Changes in moisture content and moisture gradients are of interest for wood behavior in general and of specific interest in relation the work presented here since moisture induced stress in normal service conditions may give significant contributions to the fracture relevant perpendicular to grain tensile stress.

Another aspect which should be considered in future work is development of simple calculation methods for the case of beams with a hole, suitable for use in design codes of practice. Such work should preferably be aimed at considerations based on fracture mechanics and possibly also include consideration of material heterogeneity by some type of statistical measure. This task is however believed to be a great challenge, which is exemplified by the many load- and geometry parameters affecting the fracture behavior.

Below are some further proposals for possible future work given, which are more closely related to the present work.

Experimental work

Fracture energy and material strengths with respect to tension perpendicular to grain and shear are important properties for strength predictions using the fracture mechanics based models considered within this thesis. Test results for these properties are to a large extent present in the literature, specifically regarding pure mode I loading with the direction of stress within the RT-plane and also regarding longitudinal shear loading, i.e. τ_{LR} and τ_{TL}. Test results regarding strength and fracture energy for rolling shear loading, τ_{RT}, do however appear to be scarce. This mode of loading is believed to be limited for the applications presented here but may be relevant for other applications.

An interesting finding from the numerical analysis of dowel-connections presented in Paper F is the strong influence on the connection capacity of load eccentricity with respect to the wood member width. This finding has however not been experimentally verified since all tests found in the literature seems to have been performed using symmetric loading conditions. Experimental testing of dowels loaded perpendicular to grain should hence preferably be performed, considering both symmetric and asymmetric loading conditions.

Probabilistic fracture mechanics method

Good general features of the probabilistic fracture mechanics method include the possibility to analyze structural elements of arbitrary shape and its inherent simplicity in the sense that it is based on 2D linear elastic stress analysis. Drawbacks of the considered method include its inability to accurately predict strength of small structural elements. A possible remedy may include some kind of modification of the size of the potential fracture area, used for determination of mean stresses, aimed at improving the strength prediction capacity also for small structural elements.

Further possible developments include consideration of the stress component in the parallel to grain direction and a general extension of the method to make it valid also for the full 3D case. Such modifications are probably possible although neither of them appear to be simple and straightforward to include in a manner consistent with the present approach.

Cohesive zone model based on plasticity theory

Possible extensions of the work relating to the presented 3D cohesive zone model include considerations of the natural heterogeneity of material properties. A possible approach for such investigations is the use of Monte Carlo type simulations. Such simulations are feasible although requiring a great deal of computer resources since each single analysis is rather demanding.

The assumption of linear elastic material behavior of the material outside the fracture process zone may in further modeling be abandoned. For example may plastic hardening in compression perpendicular to grain be relevant to include in analysis of dowels loaded perpendicular to grain and for other applications.

The model is also in its current form believed to be a useful tool for further investigations of applications where perpendicular to grain fracture is of importance. An example of possible further work, closely related to the work presented in this thesis regarding wood fracture at a dowel, is investigations of the influence of dowel placement along a simply supported beam and a cantilever beam.

Bibliography

[1] Abaqus, Dassault Systèmes.

[2] Aicher S (1994) Bruchenergien, kritische Energiefreisetzungsraten und Bruchzähigkeiten von Fichte bei Zugbeanspruchung senkrecht zur Faserrichtung. Holz als Roh- und Werkstoff, 52:361-370.

[3] Aicher S, Dill-Langer G, Klöck W (2002) Evaluation of different size effect models for tension perpendicular to grain. CIB-W18/35-6-1, Kyoto, Japan.

[4] Aicher S, Dill-Langer G (2005) Effect of lamination anisotropy and lay-up in glued-laminated timbers. Journal of Structural Engineering, 131:1095-1103.

[5] Aicher S, Gustafsson PJ, Haller P, Petersson H (2002) Fracture mechanics models for strength analysis of timber beams with a hole or a notch – a report of Rilem TC-133. Report TVSM-7134, Division of Structural Mechanics, Lund University, Sweden.

[6] Aicher S, Höfflin L (2006) Tragfähigkeit und Bemessung von Brettschichtholzträgern mit runden Durchbrüchen – Sicherheitsrelevante Modifikationen der Bemessungsverfahren nach Eurocode 5 und DIN 1052. MPA Otto-Graf-Institute, University of Stuttgart, Germany.

[7] Aicher S, Höfflin L (2001) Runde Durchbrüche in Biegeträgern aus Brettschichtholz – Teil 1: Berechnung. Bautechnik 78, Heft 10, 706-715.

[8] Aicher S, Höfflin L, Reinhardt HW (2007) Runde Durchbrüche in Biegeträgern aus Brettschichtholz – Teil 2: Tragfähigkeit und Bemessung. Bautechnik 84, Heft 12, 867-880.

[9] Aicher S, Schmidt J, Brunold S (1995) Desgin of timber beams with holes by means of fracture mechanics. CIB-W18/28-19-4, Copenhagen, Denmark.

[10] Astrup T, Clorius CO, Damkilde L, Hoffmeyer P (2007) Size effect of glulam beams in tension perpendicular to grain. Wood Science and Technology, 41:361-372.

[11] Austrell PE, Dahlblom O, Lindemann J et al (2004) CALFEM – A finite element toolbox. Version 3.4, Division of Structural Mechanics, Lund University, Sweden.

[12] Barenblatt GI (1962) The mathematical theory of equilibrium cracks in brittle fracture. Advances in applied mechanics, 7:55-129.

[13] Bažant ZP, Oh BH (1983) Crack band theory for fracture of concrete. Materials and Structures, 16:155-177.

[14] Berbom Dahl K (2009) Mechanical properties of clear wood from Norway spruce. Doctoral thesis, Department of Structural Engineering, Norwegian University of Science and Technology, Norway.

[15] Bodig J, Jayne BA (1982) Mechanics of wood and wood composites. Van Nostrand Reinhold Company, New York, USA.

[16] Boström L (1992) Method for determination of the softening behaviour of wood and the applicability of a nonlinear fracture mechanics model. Doctoral thesis, Report TVBM-1012, Division of Building Materials, Lund University, Sweden.

[17] Boström L (1994) The stress-displacement relation of wood perpendicular to the grain – Part 1. Experimental determination of the stress-displacement relation. Wood Science and Technology, 28:309-317.

[18] Carling O (2001) Limträhandbok (Glulam handbook). Svenskt Limträ AB, Print & Media Center i Sundsvall AB, Sweden.

[19] Carrington H (1923) The elastic constants of spruce. Philosophical Magazine Series 6, 45:1055-1057.

[20] Damkilde L, Hoffmeyer P, Pedersen TN (1998) Compression strength perpendicular to grain of structural timber and glulam. CIB-W18/31-6-4, Savonlinna, Finland.

[21] Danielsson H (2007) The strength of glulam beams with holes – A survey of tests and calculations methods. Report TVSM-3068, Division of Structural Mechanics, Lund University, Sweden.

[22] Danielsson H (2010) Design and perpendicular to grain tensile stress in double-tapered glulam beams. Report TVSM-7159, Division of Structural Mechanics, Lund University, Sweden.

[23] Daudeville L (1999) Fracture in spruce: experiment and numerical analysis by linear and non linear fracture mechanics. Holz als Roh- und Werkstoff, 57:425-432.

[24] DIN 1052:2004-08 Design of timber structures - General rules and rules for buildings

[25] DIN 1052:2008-12 Design of timber structures - General rules and rules for buildings

[26] DIN EN 1995-1-1/NA:2010-12 National Annex – Nationally determined parameters – Eurocode 5: Design of timber structures – Part 1-1: General – Common rules and rules for buildings

[27] Dinwoodie JM (2000) Timber – Its nature and behaviour. 2nd Edition, E & FN SPON, London.

[28] Dugdale DS (1960) Yielding of steel sheets containing slits. Journal of the Mechanics and Physics of Solids, 8:100-104.

[29] Eberhardsteiner J (2002) Mechanisches Verhalten von Fichtenholz – Experimentelle Bestimmung der biaxialen Festigkeitseigenschaften. Springer, Vienna, Austria.

[30] EN 338:2009 Structural timber – Strength classes

[31] EN 1194:1999 Glued laminated timber – Strength classes and determination of characteristic values

[32] EN 1995-1-1:2004 Eurocode 5: Design of timber structures – Part 1-1: General – Common rules and rules for buildings

[33] prEN 1995-1-1 Eurocode 5: Design of timber structures – Part 1-1: General – Common rules and rules for buildings, Final Draft 2002-10-09

[34] Fleischmann M, Krenn H, Eberhardsteiner J, Schickhofer G (2007) Numerische Berechnung von Holzkonstruktionen unter Verwendung eines orthotropen elasto-plastischen Werkstoffmodells. Holz als Roh- und Werkstoff, 65:301-313.

[35] Frese H, Blaß HJ (2011) Statistics of damages to timber structures in Germany. Engineering Structures, 33:2969-2977

[36] Frühmann K, Reiterer A, Tschegg EK, Stanzl-Tschegg SS (2002) Fracture characteristics of wood under mode I, mode II and mode III loading. Philosophical Magazine A, 82:3289-3298.

[37] Frühwald Hansson E (2011) Analysis of structural failure in timber structures: Typical causes for failure and failure modes. Engineering Structures, 33:2978-2982.

[38] Frühwald E, Serrano E, Toratti T, Emilsson A, Thelandersson S (2007) Design of safe timber structures – How can we learn from structural failures in concrete, steel and timber? Report TVBK-3053, Division of Structural Engineering, Lund University, Sweden.

[39] Griffith AA (1921) The phenomena of rupture and flow in solids. Philosophical Transactions of the Royal Society of London, 221:163-198.

[40] Gustafsson PJ (1985) Fracture mechanics studies of non-yielding materials like concrete – Modelling of tensile fracture and applied strength analyses. Doctoral thesis, Report TVBM-1007, Division of Building Materials, Lund University, Sweden.

[41] Gustafsson PJ (1988) A study of strength of notched beams. CIB-W18A/21-10-1, Parksville, Vancouver Island, Canada.

[42] Gustafsson PJ, Enquist B (1988) Träbalks hållfasthet vid rätvinklig urtagning (Strength of wooden beam at right angle notch). Report TVSM-7042, Division of Structural Mechanics, Lund University, Sweden.

[43] Gustafsson PJ, Serrano E (1999) Fracture mechanics in timber engineering – Some methods and applications. Proceedings of 1st International RILEM Symposium on Timber Engineering, Stockholm, Sweden.

[44] Gustafsson PJ (2003) Fracture perpendicular to grain – Structural applications. Chapter 7 in: Thelandersson S, Larsen HJ (eds) Timber engineering. John Wiley & Sons Ltd, Chichester, England.

[45] Gustafsson PJ, Danielsson H (2013) Perpendicular to grain stiffness of timber cross sections as affected by growth ring pattern, size and shape. European Journal of Wood and Wood Products, 71:111-119.

[46] Hearmon RFS (1948) The elasticity of wood and plywood. Forest Products Research, Department of Scientific and Industrial Research, Special Report No. 7, London.

[47] Hemmer K (1985) Versagensarten des Holzes der Weißtanne (Abies alba) unter mehrachsiger Beanspruchung. Dissertation, 4. Folge - Heft 11, Berichte der Versuchsanstalt für Stahl, Holz und Steine der Universität Fridericiana in Karlsruhe, Germany.

[48] Hillerborg A, Modéer M, Petersson PE (1976) Analysis of crack formation and crack growth in concrete by means of fracture mechanics and finite elements. Cement and Concrete Research, 6:773-782.

[49] Hillerborg A (1991) Application of the fictitious crack model to different types of materials. International Journal of Fracture, 51:95-102.

[50] Hofstetter K, Gamstedt EK (2009) Hierarchical modelling of microstructural effects on mechanical properties of wood. A review. Holzforschung, 63:130-138.

[51] Höfflin L (2005) Runde Durchbrüche in Brettschichtholzträgern – Experimentelle und theoretische Untersuchungen. Doctoral thesis, MPA Otto-Graf-Institute, University of Stuttgart, Germany.

[52] Holmberg S (1998) A numerical and experimental study of initial defibration of wood. Doctoral thesis, Report TVSM-1010, Division of Structural Mechanics, Lund University, Sweden.

[53] Holmberg S, Persson K, Petersson H (1999) Nonlinear mechanical behaviour and analysis of wood and fibre materials. Computers and Structures, 72:459-480.

[54] Kolb H, Epple A (1985) Verstärkung von durchbrochenen Brettschichtholzbindern. Vorschungsvorhaben I.4-34810, Forschungs- und Materialprüfungsanstalt Baden-Württemberg, Stuttgart, Germany.

[55] Kollmann FFP, Côté WA (1968) Principles of wood science and technology – Solid wood. Springer-Verlag, Berlin, Germany.

[56] Landis E, Navi P (2009) Modeling crack propagation in wood and wood composites. A review. Holzforschung, 63:150-156.

[57] Larsen HJ, Gustafsson PJ (1990) The fracture energy of wood in tension perpendicular to grain – Results from a joint testing project. CIB-W18A/23-19-2, Lisbon, Portugal.

[58] Leicester RH (1971) Some aspects of stress fields at sharp notches in orthotropic materials. Division of Forest Products Technological Paper No. 57, CSIRO, Australia.

[59] Mackenzie-Helnwein P, Eberhardsteiner J, Mang HA (2003) A multi-surface plasticity model for clear wood and its application to the finite element analysis of structural details. Computational Mechanics, 31:204-218.

[60] Mackenzie-Helnwein P, Müllner HW, Eberhardsteiner J, Mang HA (2005) Analysis of layered wooden shells using a orthotropic elasto-plastic model for multi-axial loading of clear spruce wood. Computer methods in applied mechanics and engineering, 194:2661-2685.

[61] Matlab. The Mathworks, Inc.

[62] Mishnaevsky Jr L, Qing H (2008) Micromechanical modelling of mechanical behaviour and strength of wood: State-of-the-art review. Computational Materials Science, 44:363-370.

[63] Nairn JA (2007) Material point method simulations of transverse fracture in wood with realistic morphologies. Holzforschung, 61:375-381.

[64] Nairn JA (2007) A numerical study of the transverse modulus of wood as a function of grain orientation and properties. Holzforschung, 61:406-413.

[65] Niemz P (1993) Physik des Holzes und der Holzwerkstoffe. DRW-Verlag, Leinfelden-Echterdingen.

[66] Nilsson F (2001) Fracture mechanics – From theory to applications. Department of Solid Mechanics, Royal Institute of Technology, Stockholm, Sweden.

[67] Norris CB (1962) Strength of orthotropic materials subjected to combined stresses. Report No. 1816, Forest Products Laboratory, Madison, Wisconsin, USA.

[68] Paris PC, Sih GC, Irwin GR (1965) On cracks in rectilinearly anisotropic bodies. International Journal of Fracture Mechanics, 1:189-203.

[69] Persson K (2000) Micromechanical modelling of wood and fibre properties. Doctoral thesis, Report TVSM-1013, Division of Structural Mechanics, Lund University, Sweden.

[70] van der Put TACM, Leijten AJM (2000) Evaluation of perpendicular to grain failure of beams caused by concentrated loads of joints. CIB-W18/33-7-7, Delft, The Netherlands.

[71] Reiterer A, Sinn G, Stanzl-Tschegg SE (2002) Fracture characteristics of different wood species under mode I loading perpendicular to grain. Materials Science and Engineering, A332, 29-36.

[72] Resch E, Kaliske M (2010) Three-dimensional numerical analyses of load-bearing behavior and failure of multiple double-shear dowel-type connections in timber engineering. Computers and Structures, 88:165-177.

[73] Riberholt H, Enquist B, Gustafsson PJ, Jensen RB (1992) Timber beams notched at the support. Report TVSM-7071, Division of Structural Mechanics, Lund University, Sweden.

[74] Riipola K (1995) Timber beams with holes: fracture mechanics approach. Journal of Structural Engineering, 121:225-239.

[75] Scheer C, Haase K (2000) Durchbrüche in Brettschichtholzträgern – Teil 2: Bruchmechanische Untersuchungen. Holz als Roh- und Werkstoff, 58:217-228.

[76] Schmidt J, Kaliske M (2006) Zur dreidimensionalen Materialmodellierung von Fichtenholz mittels eines Mehrflächen-Plastizitätsmodells. Holz als Roh- und Werkstoff, 64:393-402.

[77] Schmidt J, Kaliske M (2007) Simulation of cracks in wood using a coupled material model for interface elements. Holzforschung, 61:382-389.

[78] Schmidt J, Kaliske M (2009) Models for numerical failure analysis of wooden structures. Engineering Structures, 31:571-579.

[79] Schoenmakers JCM (2010) Fracture and failure mechanism in timber loaded perpendicular to grain by mechanical connections. Doctoral thesis, Eindhoven University of Technology, The Netherlands.

[80] Serrano E (2000) Adhesive joints in timber engineering – Modelling and testing of fracture performance. Doctoral thesis, Report TVSM-1012, Division of Structural Mechanics, Lund University, Sweden.

[81] Serrano E, Gustafsson PJ, Larsen HJ (2001) Modeling of finger-joint failure in glued-laminated timber beams. Journal of Structural Engineering, 127:914-921.

[82] Serrano E (2004) A numerical study of the shear-strength-predicting capabilities of test specimens for wood-adhesive bonds. International Journal of Adhesion & Adhesives, 24:23-35.

[83] Serrano E, Gustafsson PJ (2006) Fracture mechanics in timber engineering – Strength analysis of components and joints. Materials and Structures, 40:87-96.

[84] SIA 265:2012 Holzbau (Timber structures). Schweizerischer Ingenieur- und Architektverein, Zürich, Switzerland.

[85] Sjödin J, Serrano E (2008) A numerical study of methods to predict the capacity of multiple steel-timber dowel joints. Holz als Roh- und Werkstoff, 66:447-454.

[86] Smith I, Landis E, Gong M (2003) Fracture and fatigue in wood. John Wiley & Sons Ltd, Chicester, England.

[87] Stefansson F (2001) Fracture analysis of orthotropic beams – Linear elastic and non-linear methods. Licentiate thesis, Report TVSM-3029, Division of Structural Mechanics, Lund University, Sweden.

[88] Thelandersson S (2003) Introduction: Wood as a construction material. Chapter 2 in: Thelandersson S, Larsen HJ (eds) Timber engineering. John Wiley & Sons Ltd, Chichester, England.

[89] Tsai SW, Wu EM (1971) A general theory of the strength of anisotropic materials. Journal of Composite Materials, 5:58-80.

[90] Weibull W (1939) A statistical theory of the strength of materials. Proceedings nr 151, The Royal Swedish Institute for Engineering Research, Stockholm, Sweden.

[91] Weibull W (1939) The phenomenon of rupture in solids. Proceedings nr 153, The Royal Swedish Institute for Engineering Research, Stockholm, Sweden.

[92] Wernersson H (1994) Fracture characterization of wood adhesive joints. Doctoral thesis, Report TVSM-1006, Division of Structural Mechanics, Lund University, Sweden.

[93] Wu EM (1967) Application of fracture mechanics to anisotropic plates. Journal of Applied Mechanics, 34:967-974.

[94] Xu S, Reinhardt HW, Gappoev M (1996) Mode II fracture testing of highly orthotropic materials like wood. International Journal of Fracture, 75:185-214.

Part II

Attachment

Attachment

Path following solution approaches and integration of constitutive relations for a 3D wood cohesive zone model

Henrik Danielsson

Report TVSM-7160, Division of Structural Mechanics, Lund University, 2013

Path following solution approaches and integration of constitutive relations for a 3D wood cohesive zone model

Henrik Danielsson

Report TVSM-7160, Division of Structural Mechanics, Lund University, 2013

Abstract

A nonlinear finite element formulation for material nonlinearity is presented based on assumptions of small strains and neglecting geometrically nonlinear effects. The Euler forward approach, the Newton-Raphson approach and a path-following approach for solving the global nonlinear equations are presented. The considered path-following approach is the arc-length method, for which different types of constraint equations found in the literature are presented. A method for determining the stress based on numerical integration of incremental constitutive relations for an elasto-plastic material is also presented. The considered material model is a 3D cohesive zone model, developed to enable perpendicular to grain fracture analysis of wood.

Contents

1 Introduction **2**

2 Equations of motion - strong and weak forms **2**

3 Finite element formulation **4**

4 Solution of nonlinear equations of equilibrium **5**
  4.1 Euler forward solution scheme 5
  4.2 Newton-Raphson solution scheme 6
  4.3 Path following solution schemes – arc-length methods 8

5 Integration of constitutive relations **12**
  5.1 A 3D wood cohesive zone model based on plasticity theory 13
  5.2 Numerical integration of constitutive relations 14

6 Some comments regarding numerical implementation **16**
  6.1 Arc-length method with a conventional constraint equation 18
  6.2 Arc-length method with a dissipation based constraint equation 19

References **20**

1 Introduction

The theory presented here relates to nonlinear finite element formulation with respect to material nonlinearity, some different procedures for solving the nonlinear equations of equilibrium and a procedure to determine current stress state based on numerical integration of incremental constitutive relations. The aim of the presentation is to give the relevant theoretical background regarding the numerical implementation of a 3D wood cohesive zone model based on theory of plasticity, presented in [4]. The material model is implemented for finite element analysis in MATLAB [7] using supplementary routines from the toolbox CALFEM [1] and is in [4], [5] and [6] used for perpendicular to grain fracture analysis of various wooden structural elements.

The theory presented in Sections 2, 3 and 4 regarding nonlinear finite element formulation and solution approaches does not represent original research carried out by the author but represents common text book approaches regarding the considered areas and is based on [3], [8], [9] and [10]. In Section 5, the cohesive zone model presented in [4] is briefly reviewed and considered with respect to numerical integrations of the incremental constitutive relations. The considered method for the numerical integrations is according to [9]. The notation used here is partly changed with respect to the above given references. In the following presentation, geometrical nonlinear effects are neglected and the assumption of small strains is used.

2 Equations of motion - strong and weak forms

Consider a body, or an arbitrary part of a body, of volume Ω with boundary S and an outward unit normal vector $\mathbf{n}$ according to Figure 1. The forces acting on this body are given by the traction vector $\mathbf{t}$ acting on the surface S and the body forces $\mathbf{b}$ per unit volume in Ω. The displacement is denoted $\mathbf{u}$ and the acceleration is represented by $\ddot{\mathbf{u}}$, i.e. the second derivative of $\mathbf{u}$ with respect to time. Newton's second law of motion states that

$$\int_S \mathbf{t}\ \mathrm{d}S + \int_\Omega \mathbf{b}\ \mathrm{d}\Omega = \int_\Omega \rho\ddot{\mathbf{u}}\ \mathrm{d}\Omega \qquad \text{where} \quad \mathbf{t} = \begin{bmatrix} t_x \\ t_y \\ t_z \end{bmatrix} \ , \quad \mathbf{b} = \begin{bmatrix} b_x \\ b_y \\ b_z \end{bmatrix} \ , \quad \mathbf{u} = \begin{bmatrix} u_x \\ u_y \\ u_z \end{bmatrix} \tag{1}$$

and where ρ is the mass density. The traction vector $\mathbf{t}$ for a surface with an outward normal vector $\mathbf{n}$ is related to the stress tensor $\mathbf{S}$ according to

$$\mathbf{t} = \mathbf{S}\mathbf{n} \qquad \text{where} \quad \mathbf{S} = \begin{bmatrix} \sigma_{xx} & \tau_{xy} & \tau_{xz} \\ \tau_{yx} & \sigma_{yy} & \tau_{yz} \\ \tau_{zx} & \tau_{zy} & \sigma_{zz} \end{bmatrix} \ , \quad \mathbf{n} = \begin{bmatrix} n_x \\ n_y \\ n_z \end{bmatrix} \tag{2}$$

and where $\mathbf{S}$ is symmetric, i.e. $\mathbf{S} = \mathbf{S}^T$, since $\tau_{xy} = \tau_{yx}$, $\tau_{xz} = \tau_{zx}$ and $\tau_{yz} = \tau_{zy}$ due to rotational equilibrium reasons.

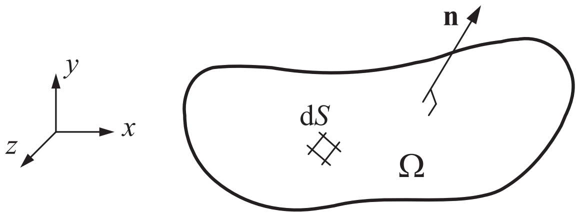

Figure 1: Body of volume Ω with surface S.

The stress vector $\boldsymbol{\sigma}$ and the matrix differential operator $\tilde{\nabla}$ are further introduced according to

$$\boldsymbol{\sigma} = \begin{bmatrix} \sigma_{xx} \\ \sigma_{yy} \\ \sigma_{zz} \\ \tau_{xy} \\ \tau_{xz} \\ \tau_{yz} \end{bmatrix} \qquad \text{and} \qquad \tilde{\nabla} = \begin{bmatrix} \frac{\partial}{\partial x} & 0 & 0 \\ 0 & \frac{\partial}{\partial y} & 0 \\ 0 & 0 & \frac{\partial}{\partial z} \\ \frac{\partial}{\partial y} & \frac{\partial}{\partial x} & 0 \\ \frac{\partial}{\partial z} & 0 & \frac{\partial}{\partial x} \\ 0 & \frac{\partial}{\partial z} & \frac{\partial}{\partial y} \end{bmatrix} \tag{3}$$

Using the divergence theorem of Gauss, Newton's second law of motion according to Equation (1) may then be expressed as

$$\int_\Omega \left(\tilde{\nabla}^T \boldsymbol{\sigma} + \mathbf{b} - \rho \ddot{\mathbf{u}} \right) \, \mathrm{d}\Omega = 0 \tag{4}$$

from which the *strong form* of the equations of motion may be found as

$$\tilde{\nabla}^T \boldsymbol{\sigma} + \mathbf{b} = \rho \ddot{\mathbf{u}} \tag{5}$$

since the considered volume Ω is arbitrary. An arbitrary vector $\mathbf{v}$ - the weight vector - is introduced to arrive at the weak form. Multiplying Equation (5) with $\mathbf{v}$, integrating over the volume Ω and using the divergence theorem of Gauss the *weak form* of the equations of motion may be obtained as

$$\int_\Omega \rho \mathbf{v}^T \ddot{\mathbf{u}} \, \mathrm{d}\Omega + \int_\Omega (\tilde{\nabla}\mathbf{v})^T \boldsymbol{\sigma} \, \mathrm{d}\Omega = \int_S \mathbf{v}^T \mathbf{t} \, \mathrm{d}S + \int_\Omega \mathbf{v}^T \mathbf{b} \, \mathrm{d}\Omega \qquad \text{where} \quad \mathbf{v} = \begin{bmatrix} v_x \\ v_y \\ v_z \end{bmatrix} \tag{6}$$

The weak form may be modified for further preparations for the finite element formulation. A quantity $\boldsymbol{\varepsilon}^v$ is defined, related to the weight vector $\mathbf{v}$ in the same manner as the small strain vector $\boldsymbol{\varepsilon}$ is related to the displacement vector $\mathbf{u}$, i.e. according to the kinematic relation

$$\boldsymbol{\varepsilon} = \begin{bmatrix} \varepsilon_{xx} & \varepsilon_{yy} & \varepsilon_{zz} & \gamma_{xy} & \gamma_{xz} & \gamma_{yz} \end{bmatrix}^T = \tilde{\nabla}\mathbf{u} \qquad \text{and} \qquad \boldsymbol{\varepsilon}^v = \tilde{\nabla}\mathbf{v} \tag{7}$$

with the matrix differential operator $\tilde{\nabla}$ defined in Equation (3). The weak form may hence be expressed as

$$\int_\Omega \rho \mathbf{v}^T \ddot{\mathbf{u}} \, \mathrm{d}\Omega + \int_\Omega (\boldsymbol{\varepsilon}^v)^T \boldsymbol{\sigma} \, \mathrm{d}\Omega = \int_S \mathbf{v}^T \mathbf{t} \, \mathrm{d}S + \int_\Omega \mathbf{v}^T \mathbf{b} \, \mathrm{d}\Omega \tag{8}$$

Interpretation of the weight vector $\mathbf{v}$ as a virtual displacement and hence $\boldsymbol{\varepsilon}^v$ as the related virtual strain, Equation (8) may be referred to as the *principle of virtual work* where the right hand side represents the external work during a virtual displacement $\mathbf{v}$. The strong and weak forms of the equations of motion are derivable from one another. An advantage in favor of the weak form is that it includes no derivatives of the stress tensor, which makes it suitable as a base for finite element formulations.

Both the strong and the weak form of the equations of motion hold for all constitutive relations. In order to solve a specific boundary value problem also the boundary conditions are needed with $\mathbf{u}$ given along the boundary S_u and $\mathbf{t}$ given along the boundary S_t.

3 Finite element formulation

The finite element formulation will be presented for static conditions only, i.e. $\ddot{\mathbf{u}} = 0$. With this restriction, the weak form of the equations of motion in Equation (8) turns to the weak form of the equations of equilibrium according to

$$\int_\Omega (\boldsymbol{\varepsilon}^v)^T \boldsymbol{\sigma} \, \mathrm{d}\Omega = \int_S \mathbf{v}^T \mathbf{t} \, \mathrm{d}S + \int_\Omega \mathbf{v}^T \mathbf{b} \, \mathrm{d}\Omega \tag{9}$$

In the finite element formulation, the displacement vector $\mathbf{u}$ is throughout the body approximated by the nodal displacements and shape functions according to

$$\mathbf{u} \approx \mathbf{N}\mathbf{a} \tag{10}$$

where $\mathbf{N}$ is the global shape function matrix and $\mathbf{a}$ is the nodal displacement vector containing n_{dof} nodal displacements. The strains $\boldsymbol{\varepsilon}$ are then given by the following strain-nodal displacement relationship

$$\boldsymbol{\varepsilon} = \mathbf{B}\mathbf{a} \qquad \text{where} \quad \mathbf{B} = \tilde{\nabla}\mathbf{N} \tag{11}$$

The fundamental issue of the standard finite element method is that the arbitrary weight vector $\mathbf{v}$ is chosen according to Galerkin's method, i.e. according to

$$\mathbf{v} = \mathbf{N}\mathbf{c} \tag{12}$$

where since $\mathbf{v}$ is arbitrary, also $\mathbf{c}$ is arbitrary. The quantity $\boldsymbol{\varepsilon}^v$, related to the weight vector $\mathbf{v}$ as the strain $\boldsymbol{\varepsilon}$ is related to the displacement $\mathbf{u}$, is hence given by

$$\boldsymbol{\varepsilon}^v = \mathbf{B}\mathbf{c} \tag{13}$$

Use of Equations (12) and (13) in the weak form of the equations of equilibrium given in Equation (9) yields

$$\int_\Omega \mathbf{c}^T \mathbf{B}^T \boldsymbol{\sigma} \, \mathrm{d}\Omega = \int_S \mathbf{c}^T \mathbf{N}^T \mathbf{t} \, \mathrm{d}S + \int_\Omega \mathbf{c}^T \mathbf{N}^T \mathbf{b} \, \mathrm{d}\Omega \tag{14}$$

and since the vector $\mathbf{c}$ is independent of position in the body and arbitrary we may finally obtain

$$\int_\Omega \mathbf{B}^T \boldsymbol{\sigma} \, \mathrm{d}\Omega - \int_S \mathbf{N}^T \mathbf{t} \, \mathrm{d}S - \int_\Omega \mathbf{N}^T \mathbf{b} \, \mathrm{d}\Omega = \mathbf{0} \tag{15}$$

The finite element formulation of the equations of equilibrium may hence be expressed as

$$\mathbf{G} = \mathbf{f}_{int} - \mathbf{f}_{ext} = \mathbf{0} \tag{16}$$

where $\mathbf{G}$ is the residual force vector (or the out-of-balance force vector) and where the internal force vector $\mathbf{f}_{int}$ and the external force vector $\mathbf{f}_{ext}$ are given by

$$\mathbf{f}_{int} = \int_\Omega \mathbf{B}^T \boldsymbol{\sigma} \, \mathrm{d}\Omega \tag{17}$$

$$\mathbf{f}_{ext} = \int_S \mathbf{N}^T \mathbf{t} \, \mathrm{d}S + \int_\Omega \mathbf{N}^T \mathbf{b} \, \mathrm{d}\Omega \tag{18}$$

and hence expresses that the internal and external forces must balance each other. The above equations of equilibrium hold irrespective of the constitutive relation. However, to solve a specific boundary value problem, a constitutive relation needs to be defined and also boundary conditions need to be specified. For linear elasticity with a constitutive relation defined by Hooke's law we have with Equation (11) that

$$\boldsymbol{\sigma} = \mathbf{D}\boldsymbol{\varepsilon} = \mathbf{DBa} \tag{19}$$

and the linear equations of equilibrium are given by

$$\mathbf{Ka} = \mathbf{f}_{ext} \qquad \text{where} \quad \mathbf{K} = \int_{\Omega} \mathbf{B}^T\mathbf{DB}\ \mathrm{d}\Omega \tag{20}$$

where the linear elastic stiffness matrix $\mathbf{K}$ is constant.

4 Solution of nonlinear equations of equilibrium

The solution procedure for nonlinear material behavior is more complex compared to that of linear elasticity, since the current stress is generally not possible to obtain directly from the current strain. For many types of material nonlinearity, including plasticity, the constitutive relation is given in an incremental form and the current stress needs to be found by integration of this incremental constitutive relation along the load path. There are hence two sets of nonlinear equations to be dealt with: one related to the global equations of equilibrium and one related to the local constitutive relation at the material point level.

Considering elasto-plasticity, the incremental constitutive relation may be described as

$$\dot{\boldsymbol{\sigma}} = \mathbf{D}_t\dot{\boldsymbol{\varepsilon}} \qquad \text{where} \quad \mathbf{D}_t = \begin{cases} \mathbf{D} & \text{for elastic response} \\ \mathbf{D}^{ep} & \text{for elasto-plastic response} \end{cases} \tag{21}$$

where $(\dot{*})$ denotes incremental quantities and $\mathbf{D}_t$ is the tangential material stiffness matrix, equal to the linear elastic stiffness matrix $\mathbf{D}$ if the response is purely elastic or else equal to the elasto-plastic tangential stiffness matrix $\mathbf{D}^{ep}$.

The nature of this type of problems requires an incremental solution technique, where the response is tracked by applying the external loading in small steps. The demand on the solution procedures for both sets of nonlinear equations is that it should be sufficiently accurate and efficient. Solution techniques for the global equations of equilibrium will be dealt with in this section whereas the a procedure for solving the local equations, i.e. the integration of constitutive relations, will be dealt with in Section 5.

4.1 Euler forward solution scheme

For solving the global equations of equilibrium in an incremental fashion, the *Euler forward* scheme is one of the simplest schemes at hand. The Euler forward scheme is based on the assumption that the tangent stiffness between a known point n on the load path and the next sought point $n+1$ may be approximated by the tangent stiffness at n. To obtain the formulation of the Euler forward scheme, the global equations of equilibrium according to Equation (16) are differentiated yielding

$$\dot{\mathbf{f}}_{int} - \dot{\mathbf{f}}_{ext} = \mathbf{0} \tag{22}$$

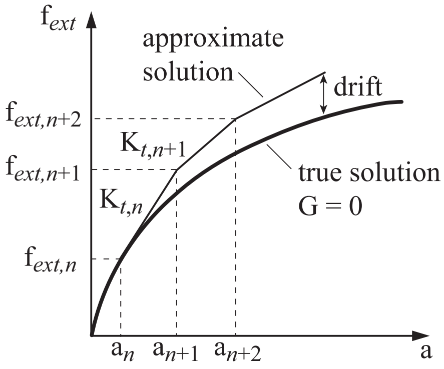

Figure 2: Illustration of Euler forward solution scheme.

where

$$\dot{\mathbf{f}}_{int} = \int_\Omega \mathbf{B}^T \dot{\boldsymbol{\sigma}} \, \mathrm{d}\Omega \qquad \text{and} \qquad \dot{\mathbf{f}}_{ext} = \int_S \mathbf{N}^T \dot{\mathbf{t}} \, \mathrm{d}S + \int_\Omega \mathbf{N}^T \dot{\mathbf{b}} \, \mathrm{d}\Omega \tag{23}$$

Using the incremental constitutive relation according to Equation (21) and the finite element approximation of the strain-nodal displacement relation according to Equation (11) yields

$$\dot{\boldsymbol{\sigma}} = \mathbf{D}_t \dot{\boldsymbol{\varepsilon}} = \mathbf{D}_t \mathbf{B} \dot{\mathbf{a}} \tag{24}$$

and the global equations of equilibrium may hence be expressed in incremental form as

$$\mathbf{K}_t \dot{\mathbf{a}} = \dot{\mathbf{f}}_{ext} \qquad \text{where} \quad \mathbf{K}_t = \int_\Omega \mathbf{B}^T \mathbf{D}_t \mathbf{B} \, \mathrm{d}\Omega \tag{25}$$

where $\mathbf{K}_t$ represent the current tangential stiffness. All quantities are assumed to be known at state n, and the quantities at the next state $n+1$ are sought. Assuming that the tangential stiffness $\mathbf{K}_t$ is constant between these two states, approximations of the sought quantities may be found by first integrating Equation (25) from state n to state $n+1$ yielding

$$\mathbf{K}_{t,n}(\mathbf{a}_{n+1} - \mathbf{a}_n) = \mathbf{f}_{ext,n+1} - \mathbf{f}_{ext,n} \qquad \text{where} \quad \mathbf{K}_{t,n} = \int_\Omega \mathbf{B}^T \mathbf{D}_{t,n} \mathbf{B} \, \mathrm{d}\Omega \tag{26}$$

and solving the sought nodal displacements $\mathbf{a}_{n+1}$ for the load $\mathbf{f}_{ext,n+1}$, considering the essential boundary conditions. This in turn allows for determination of the strains $\boldsymbol{\varepsilon}_{n+1}$, the stresses $\boldsymbol{\sigma}_{n+1}$ and the internal forces $\mathbf{f}_{int}$ that these stresses give rise to. The calculated internal forces $\mathbf{f}_{int}$ do not necessarily balance the external forces $\mathbf{f}_{ext}$ when the Euler forward scheme is used, meaning that the out-of-balance force vector $\mathbf{G}$ may be nonzero and equilibrium hence not fulfilled. This imbalance may introduce a drift of the approximate solution from the true solution, as is illustrated in Figure 2.

The Euler forward scheme does however have the positive features of being simple and robust. Using a formulation where loading is applied as prescribed displacements, a possible post peak-load softening part of the load path may also be followed.

4.2 Newton-Raphson solution scheme

Among the incremental-iterative solution schemes, the *Newton-Raphson* scheme is one of the most widely used when it comes to nonlinear finite element analysis. In contrast to the Euler forward schemes, where global equilibrium is not necessarily fulfilled, the Newton-Raphson procedure aims at fulfilling the global equilibrium equations. The basic concept of the Newton-Raphson scheme is to linearize the nonlinear equations of equilibrium about a given point on the load path. The nonlinear equations are approximated by a Taylor expansion, where terms higher than the linear ones are ignored.

The nonlinear global equations of equilibrium according to Equation (16) may for a fixed external loading be expressed as

$$\mathbf{G}(\mathbf{a}) = \mathbf{f}_{int}(\mathbf{a}) - \mathbf{f}_{ext} = \mathbf{0} \tag{27}$$

since the external forces $\mathbf{f}_{ext}$ are known and fixed and since the internal forces depend on the stresses $\boldsymbol{\sigma}$ which in turn depend on the nodal displacements $\mathbf{a}$. Assuming that an approximate solution $\mathbf{a}^{i-1}$ to the true solution $\mathbf{a}$ has been established, the truncated Taylor expansion of $\mathbf{G}$ about $\mathbf{a}^{i-1}$ yields

$$\mathbf{G}(\mathbf{a}^i) = \mathbf{G}(\mathbf{a}^{i-1}) + \left(\frac{\partial \mathbf{G}}{\partial \mathbf{a}}\right)^{i-1} (\mathbf{a}^i - \mathbf{a}^{i-1}) \tag{28}$$

where the derivative $\partial \mathbf{G}/\partial \mathbf{a}$ is found to be

$$\frac{\partial \mathbf{G}}{\partial \mathbf{a}} = \frac{\partial \mathbf{f}_{int}}{\partial \mathbf{a}} = \int_{\Omega} \mathbf{B}^T \frac{\mathrm{d}\boldsymbol{\sigma}}{\mathrm{d}\mathbf{a}} \, \mathrm{d}\Omega = \int_{\Omega} \mathbf{B}^T \mathbf{D}_t \mathbf{B} \, \mathrm{d}\Omega \tag{29}$$

since $\mathrm{d}\boldsymbol{\sigma} = \mathbf{D}_t \mathrm{d}\boldsymbol{\varepsilon} = \mathbf{D}_t \mathbf{B} \mathrm{d}\mathbf{a}$ and since the external forces $\mathbf{f}_{ext}$ are known and fixed. The derivative $\partial \mathbf{G}/\partial \mathbf{a}$ is hence the tangential stiffness matrix which also emerged in the Euler forward scheme, see Equation (25). Enforcing $\mathbf{G}(\mathbf{a}^i) = \mathbf{0}$, the Newton-Raphson iteration scheme may hence from Equation (28) be expressed as

$$\mathbf{K}_t^{i-1}(\mathbf{a}^i - \mathbf{a}^{i-1}) = -\mathbf{G}(\mathbf{a}^{i-1}) \qquad \text{where} \quad \mathbf{K}_t^{i-1} = \int_{\Omega} \mathbf{B}^T \mathbf{D}_t^{i-1} \mathbf{B} \, \mathrm{d}\Omega \tag{30}$$

where $(*)^{i-1}$ refer to known quantities and the sought nodal displacements $\mathbf{a}^i$ may be solved for, considering the essential boundary conditions. Assuming that n is a known equilibrium state with known nodal displacements $\mathbf{a}_n$, stresses $\boldsymbol{\sigma}_n$ and external forces $\mathbf{f}_{ext,n}$ the aim of the iteration procedure is to find the corresponding quantities for the next state $n+1$, fulfilling the equations of equilibrium. Since the external forces at state $n+1$ are fixed and given by $\mathbf{f}_{ext,n+1}$, the out-of-balance forces $\mathbf{G}(\mathbf{a}^{i-1})$ are given by

$$\mathbf{G}(\mathbf{a}^{i-1}) = \int_{\Omega} \mathbf{B}^T \boldsymbol{\sigma}^{i-1} \, \mathrm{d}\Omega - \mathbf{f}_{ext,n+1} \tag{31}$$

For the first iteration in a load step, when $i = 1$, the starting values are taken as the last known values at equilibrium according to

$$\mathbf{a}^0 = \mathbf{a}_n \ , \qquad \boldsymbol{\varepsilon}^0 = \boldsymbol{\varepsilon}_n \ , \qquad \boldsymbol{\sigma}^0 = \boldsymbol{\sigma}_n \ , \qquad \mathbf{K}_t^0 = \mathbf{K}_{t,n} \tag{32}$$

and the iteration procedure continues until the difference between the external forces $\mathbf{f}_{ext}$ and the internal forces $\mathbf{f}_{int}$ is sufficiently small, i.e. until some norm of the out-of-balance forces $\mathbf{G}(\mathbf{a})$ fulfills a user specified convergence criterion. When equilibrium is reached with sufficient accuracy, the updated equilibrium quantities are accepted as converged equilibrium quantities.

There are variations of the conventional Newton-Raphson scheme (often denoted the *Full Newton-Raphson* scheme) presented above and illustrated in Figure 3. Such variations include

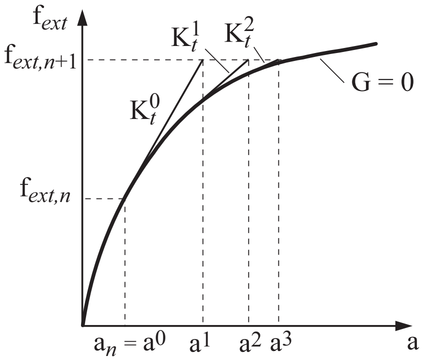

Figure 3: Illustration Newton-Raphson solution scheme.

the *Initial stiffness method*, where the initial linear elastic stiffness is used instead of the tangential stiffness, and the *Modified Newton-Raphson* method, where the tangential stiffness is updated not in every iteration but only once in each load step.

The Newton-Raphson scheme does in general provide a fast convergence and works well in both loading and unloading [9]. Using a formulation where loading is applied as prescribed displacements, a possible post peak-load softening part of the load path may also be followed. The Newton-Raphson scheme does however not manage snap-back behavior of the load path.

4.3 Path following solution schemes – arc-length methods

For the case when the load path includes snap-back, which cannot be followed using a Newton-Raphson scheme, a path following scheme such as the *arc-length method* needs to be employed. The procedure presented here is based on the theory presented in [3] and [10].

The equations of equilibrium that should be solved may be expressed as

$$\mathbf{G}(\mathbf{a}) = \mathbf{f}_{int}(\mathbf{a}) - \mathbf{f}_{ext} = \mathbf{0} \tag{33}$$

where $\mathbf{G}$ is the residual force vector (or out-of-balance force vector) and $\mathbf{f}_{int}$ is the internal force vector which both depend on the n_{dof} nodal displacements $\mathbf{a}$. If constant body forces are neglected, the external forces $\mathbf{f}_{ext}$ may be expressed as

$$\mathbf{f}_{ext} = \lambda \mathbf{f} \tag{34}$$

where $\mathbf{f}$ is a fixed load pattern and where λ is a variable load factor. The equations of equilibrium may then be expressed as

$$\mathbf{G}(\mathbf{a}, \lambda) = \mathbf{f}_{int}(\mathbf{a}) - \lambda \mathbf{f} = \mathbf{0} \tag{35}$$

which represents n_{dof} equations and $n_{dof} + 1$ unknowns; the n_{dof} nodal displacements and the load factor λ. To solve the above system of equations, some further relation is needed in addition to considering the essential boundary conditions. This additional relation, the constraint equation g, is in [3] suggested as

$$g(\mathbf{a}, \lambda) = \Delta\mathbf{a}^T \Delta\mathbf{a} + \psi \Delta\lambda^2 \mathbf{f}^T \mathbf{f} - L^2 = 0 \tag{36}$$

where $\Delta(*)$ refers to a difference between the next sought state and the previous equilibrium state, ψ is a load influence factor and L is the path step length. The constraint equation g is

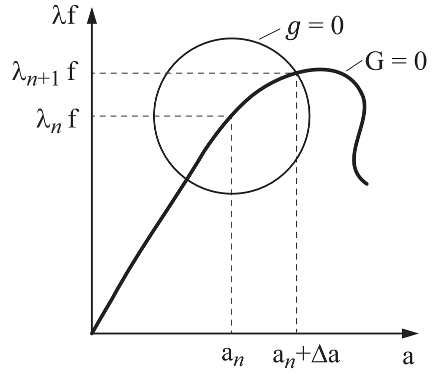

Figure 4: Illustration of constraint equation g with $\psi = 1$ for a single degree of freedom system.

illustrated in Figure 4 for a single degree of freedom system. Setting $\psi = 0$ reduces some of the computational costs and does according to [10] not influence the convergence rate. An approach with $\psi = 0$ is called a cylindrical arc-length method and an approach with $\psi \neq 0$ is called a spherical arc-length method.

In analogy with the derivation of the Newton-Raphson scheme, a truncated Taylor expansion of $\mathbf{G}$ around an approximate solution $(\mathbf{a}^{i-1}, \lambda^{i-1})$ to the true solution $(\mathbf{a}, \lambda)$ yields

$$\mathbf{G}(\mathbf{a}^i, \lambda^i) = \mathbf{G}(\mathbf{a}^{i-1}, \lambda^{i-1}) + \left(\frac{\partial \mathbf{G}}{\partial \mathbf{a}}\right)^{i-1} (\mathbf{a}^i - \mathbf{a}^{i-1}) + \left(\frac{\partial \mathbf{G}}{\partial \lambda}\right)^{i-1} (\lambda^i - \lambda^{i-1}) \tag{37}$$

where the derivatives $\partial \mathbf{G}/\partial \mathbf{a} = \mathbf{K}_t$ and $\partial \mathbf{G}/\partial \lambda = -\mathrm{d}\lambda \mathbf{f}$. Enforcing equilibrium to be fulfilled according to $\mathbf{G}(\mathbf{a}^i, \lambda^i) = \mathbf{0}$ and using the notation $\mathrm{d}\mathbf{a} = \mathbf{a}^i - \mathbf{a}^{i-1}$ and $\mathrm{d}\lambda = \lambda^i - \lambda^{i-1}$ yields

$$\mathbf{K}_t^{i-1} \mathrm{d}\mathbf{a} - \mathrm{d}\lambda \mathbf{f} = -\mathbf{G}(\mathbf{a}^{i-1}, \lambda^{i-1}) \qquad \text{where} \quad \mathbf{K}_t^{i-1} = \int_\Omega \mathbf{B}^T \mathbf{D}_t^{i-1} \mathbf{B} \; \mathrm{d}\Omega \tag{38}$$

In addition to the above given equations of equilibrium, also the constraint equation should be fulfilled. There are at least two available approaches regarding this issue [10]. The constraint equation may be linearized in the same manner as the equations of equilibrium and the solution will then be forced to fulfill the constraint equation only as the solution has converged. Another approach is to enforce fulfillment of the constraint equation in every iteration, i.e. to fulfill

$$g(\mathbf{a}, \lambda) = (\Delta \mathbf{a}^i)^T \Delta \mathbf{a}^i + \psi (\Delta \lambda^i)^2 \mathbf{f}^T \mathbf{f} - L^2 = 0 \tag{39}$$

where

$$\Delta \mathbf{a}^i = \Delta \mathbf{a}^{i-1} + \mathrm{d}\mathbf{a} \tag{40}$$

$$\Delta \lambda^i = \Delta \lambda^{i-1} + \mathrm{d}\lambda \tag{41}$$

where $\Delta \mathbf{a}^i$ and $\Delta \lambda^i$ are the sought increments between the next state i and the last known equilibrium state n and where $\Delta \mathbf{a}^{i-1}$ and $\Delta \lambda^{i-1}$ hence are the known increments between the current state $i-1$ and the last known equilibrium state n. Equations (38) and (39) may be solved in the following manner. Equation (38) is multiplied from the left side by the inverse of the tangential stiffness matrix $\mathbf{K}_t$ and the term related to the load factor $\mathrm{d}\lambda$ is moved to the right side to obtain

$$\mathrm{d}\mathbf{a} = -\left(\mathbf{K}_t^{i-1}\right)^{-1} \mathbf{G}(\mathbf{a}^{i-1}, \lambda^{i-1}) + \mathrm{d}\lambda \left(\mathbf{K}_t^{i-1}\right)^{-1} \mathbf{f} \tag{42}$$

which may be written as

$$\mathrm{d}\mathbf{a} = \mathrm{d}\mathbf{a}_{\mathbf{G}} + \mathrm{d}\lambda \mathrm{d}\mathbf{a}_{\mathbf{f}} \tag{43}$$

and where $\mathrm{d}\mathbf{a}_{\mathbf{f}}$ and $\mathrm{d}\mathbf{a}_{\mathbf{G}}$ are solved from

$$\begin{align} \left(\mathbf{K}_t^{i-1}\right) \mathrm{d}\mathbf{a}_{\mathbf{f}} &= \mathbf{f} \tag{44} \\ \left(\mathbf{K}_t^{i-1}\right) \mathrm{d}\mathbf{a}_{\mathbf{G}} &= -\mathbf{G}(\mathbf{a}^{i-1}, \lambda^{i-1}) \tag{45} \end{align}$$

Using $\mathrm{d}\mathbf{a}$ from Equation (43) and Equations (41) and (40) in Equation (39), the only unknown quantity is the increment in load factor $\mathrm{d}\lambda$ which can be found from

$$a_1 \mathrm{d}\lambda^2 + a_2 \mathrm{d}\lambda + a_3 = 0 \tag{46}$$

where

$$\begin{align} a_1 &= \mathrm{d}\mathbf{a}_{\mathbf{f}}^T \mathrm{d}\mathbf{a}_{\mathbf{f}} + \psi \mathbf{f}^T \mathbf{f} \tag{47} \\ a_2 &= 2\mathrm{d}\mathbf{a}_{\mathbf{f}}^T (\Delta\mathbf{a}^{i-1} + \mathrm{d}\mathbf{a}_{\mathbf{G}}) + 2\psi \Delta\lambda^{i-1} \mathbf{f}^T \mathbf{f} \tag{48} \\ a_3 &= (\Delta\mathbf{a}^{i-1} + \mathrm{d}\mathbf{a}_{\mathbf{G}})^T (\Delta\mathbf{a}^{i-1} + \mathrm{d}\mathbf{a}_{\mathbf{G}}) + \psi (\Delta\lambda^{i-1})^2 \mathbf{f}^T \mathbf{f} - L^2 \tag{49} \end{align}$$

Since Equation (46) is quadratic, two real roots or complex roots may be found. When complex roots are found, the remedy proposed in [3] and [10] is to decrease the path step length L and restart the iteration procedure from a known equilibrium point. Equation (46) may give two real solutions $\mathrm{d}\lambda^{(j)}$ $(j = 1, 2)$ and the solution should then be chosen such that doubling back and following the load path already found is avoided. This can be ensured by choosing the solution j which minimizes the angle between $\Delta\mathbf{a}^{i-1}$ and $\Delta\mathbf{a}^{i}$. This solution is the one which maximizes

$$a_4 + a_5 \mathrm{d}\lambda^{(j)} \qquad \text{where } j = 1, 2 \tag{50}$$

where

$$\begin{align} a_4 &= (\Delta\mathbf{a}^{i-1})^T (\Delta\mathbf{a}^{i-1} + \mathrm{d}\mathbf{a}_{\mathbf{G}}) \tag{51} \\ a_5 &= (\Delta\mathbf{a}^{i-1})^T \mathrm{d}\mathbf{a}_{\mathbf{f}} \tag{52} \end{align}$$

In addition to the cases when complex or two real roots of Equation (46) are found, special attention is also needed for the first iteration in every path step. For the fist iteration is $\Delta\lambda^{i-1} = 0$, $\Delta\mathbf{a}^{i-1} = \mathbf{0}$ and $\mathbf{G}^{i-1} = \mathbf{0}$ which gives $a_2 = 0$ according to Equation (48). Two real solutions of Equation (46) then exists and the solution is then for the general case chosen in accordance with Equations (50)-(52). For the first iteration however, this procedure offers no help since $a_4 = a_5 = 0$. The solution offered in [10] is then to apply the same general principle of minimizing the angle between two previous solutions of the nodal displacements, although now these solutions are two previous accepted equilibrium solutions and not $\Delta\mathbf{a}^{i-1}$ and $\Delta\mathbf{a}^{i}$ as used above. The increment in the load factor $\mathrm{d}\lambda$ is in the first iteration hence determined according to

$$\mathrm{d}\lambda = s \frac{L}{\sqrt{\mathrm{d}\mathbf{a}_{\mathbf{f}}^T \mathrm{d}\mathbf{a}_{\mathbf{f}} + \psi \mathbf{f}^T \mathbf{f}}} \qquad \text{where} \quad s = \mathrm{sign}(\Delta\mathbf{a}_n^T \mathrm{d}\mathbf{a}_{\mathbf{f}}) \tag{53}$$

where $\Delta\mathbf{a}_n$ is taken as the increment in nodal displacements between the two last converged equilibrium points, i.e. $\Delta\mathbf{a}_n = \mathbf{a}_n - \mathbf{a}_{n-1}$.

Conventional arc-length approaches, with a constraint equation according to Equation (36), seems to be well suited for geometrically nonlinear problems but have been reported to work less satisfactory for applications including material instabilities giving localized fracture process zones [12]. Examples of such applications are fracture analyses of concrete or wooden structural elements using cohesive zone models, where the material nonlinearity commonly is confined to only a small volume of the considered body. The global solution path may for such applications include very sharp snap-backs and a constraint equation based on all nodal displacements seems for some reason insufficient to capture this phenomenon correctly. There are numerous suggestions found in the literature regarding the choice of constraint equation, two of these are presented below.

Constraint equation based on only certain degrees of freedom

A constraint equation based on only certain degrees of freedom is in [2] suggested to be used for nonlinear fracture analysis of concrete. The constraint equation is very similar to the one given in Equation (36) with $\psi = 0$ and reads

$$g(\mathbf{a}, \lambda) = \Delta\tilde{\mathbf{a}}^T \Delta\tilde{\mathbf{a}} - L^2 = 0 \tag{54}$$

where $\tilde{\mathbf{a}}$ are the nodal displacements related to elements with material nonlinearity only. This type of approach is straightforward to implement for applications with a known, predefined volume within which the material nonlinearity is present.

Constraint equation based on plastic energy dissipation

A rather different approach for formulation of the constraint equation is presented in [12]. The main idea of this approach is to find the equilibrium path by considering energy dissipation. For an application with strain-softening plasticity in a predefined potential fracture zone (volume) and linear elasticity for the bulk material, the formulation presented in [12] is restated below.

The rate of energy dissipation G may be expressed as

$$G = P - \dot{U}_e \tag{55}$$

where $P = \dot{\mathbf{a}}^T \mathbf{f}_{ext} = \lambda \dot{\mathbf{a}}^T \mathbf{f}$ is the exerted power and $\dot{U}_e$ is the rate of elastic strain energy. The elastic energy stored in a body of volume Ω is given by

$$U_e = \frac{1}{2} \int_\Omega (\boldsymbol{\varepsilon}^e)^T \boldsymbol{\sigma} \, \mathrm{d}\Omega = \frac{1}{2} \int_\Omega \boldsymbol{\sigma}^T \mathbf{D}^{-1} \boldsymbol{\sigma} \, \mathrm{d}\Omega \tag{56}$$

where $\boldsymbol{\varepsilon}^e$ is the elastic part of the total strain $\boldsymbol{\varepsilon} = \boldsymbol{\varepsilon}^e + \boldsymbol{\varepsilon}^p$ and $\boldsymbol{\sigma} = \mathbf{D}\boldsymbol{\varepsilon}^e$ where $\mathbf{D}$ is the linear elastic material stiffness matrix. The rate of the elastic strain energy is then given by

$$\dot{U}_e = \int_\Omega \dot{\boldsymbol{\sigma}}^T \mathbf{D}^{-1} \boldsymbol{\sigma} \, \mathrm{d}\Omega = \int_\Omega \dot{\boldsymbol{\varepsilon}}^T (\mathbf{D}^{ep})^T \mathbf{D}^{-1} \boldsymbol{\sigma} \, \mathrm{d}\Omega \tag{57}$$

where $\mathbf{D}^{ep}$ is the elasto-plastic stiffness matrix which for plastic straining relates the increment in total strain to the increment in stress according to $\dot{\boldsymbol{\sigma}} = \mathbf{D}^{ep}\dot{\boldsymbol{\varepsilon}}$. Using the strain-nodal displacement relation according to Equation (11) then yields

$$\dot{U}_e = \dot{\mathbf{a}}^T \mathbf{f}^* \qquad \text{where} \qquad \mathbf{f}^* = \int_\Omega \mathbf{B}^T (\mathbf{D}^{ep})^T \mathbf{D}^{-1} \boldsymbol{\sigma} \, \mathrm{d}\Omega \tag{58}$$

The energy release rate (or rate of energy dissipation) then follows as

$$G = P - \dot{U}_e = \dot{\mathbf{a}}^T(\lambda \mathbf{f} - \mathbf{f}^*) \tag{59}$$

which is used to formulate the following constraint equation

$$g(\mathbf{a}, \lambda) = \Delta \mathbf{a}^T(\lambda_n \mathbf{f} - \mathbf{f}_n^*) - L = 0 \tag{60}$$

where λ_n and $\mathbf{f}_n^*$ refer to converged quantities from the last equilibrium state. The solution procedure for direct consideration of the dissipation-based constraint equation is the same as for the conventional arc-length approach presented above: Equations (40) - (45) are used and the constraint equation is enforced to be fulfilled in every iteration according to

$$g(\mathbf{a}, \lambda) = (\Delta \mathbf{a}^i)^T(\lambda_n \mathbf{f} - \mathbf{f}_n^*) - L = 0 \tag{61}$$

and the increment in the load factor $\mathrm{d}\lambda$ may then be determined from

$$\mathrm{d}\lambda = \frac{L - (\Delta \mathbf{a}^{i-1} + \mathrm{d}\mathbf{a}_{\mathbf{G}})^T(\lambda_n \mathbf{f} - \mathbf{f}_n^*)}{\mathrm{d}\mathbf{a}_{\mathbf{f}}^T(\lambda_n \mathbf{f} - \mathbf{f}_n^*)} \tag{62}$$

Use of a constraint equation based on energy dissipation will for natural reasons not work properly for non-dissipative parts of the load path, i.e. before any plastic straining has taken place since then $\lambda_n \mathbf{f} = \mathbf{f}_n^*$. Implementation of a solution approach including a dissipation based constraint equation hence needs to be accompanied by an alternative solution approach, such as a conventional arc-length approach or a conventional Newton-Raphson approach, and an appropriate switching criterion.

5 Integration of constitutive relations

The above considered approaches for solution of the nonlinear equations of equilibrium are based on the assumption that the current stress may be determined in some way for all states along the load path. For a general elasto-plastic material, with a constitutive relation expressed in incremental form, the stress is determined by integration of the constitutive relation along the load path. Depending on the specific material model, the constitutive relation may be possible to integrate exactly but approximate solutions based on numerical integration are commonly needed. As for the solution of the global equations of equilibrium, there are several strategies available for numerical integration of incremental constitutive relations.

When solving the global equations of equilibrium in an iterative manner, the internal force vector $\mathbf{f}_{int}$ and hence also the current stresses need to be established in every iteration. From the solution of the global equations, the nodal displacements $\mathbf{a}$ are known and hence also the total strain $\boldsymbol{\varepsilon}$. What remains to determine is how much of the total strain that is elastic and how much is plastic. The following presentation is based on theory presented in [9], where methods are presented for general elasto-plastic material models. The application considered here is to a specific elasto-plastic material model for cohesive perpendicular to grain fracture of wood presented in [4]. All quantities are here expressed in a global xyz coordinate system and additive decomposition of strains is assumed according to

$$\boldsymbol{\varepsilon} = \boldsymbol{\varepsilon}^e + \boldsymbol{\epsilon}^p \tag{63}$$

where $\boldsymbol{\varepsilon}$ is the total strain while $\boldsymbol{\varepsilon}^e$ and $\boldsymbol{\varepsilon}^p$ are the elastic and plastic strains respectively. Hooke's law states that

$$\boldsymbol{\sigma} = \mathbf{D}\boldsymbol{\varepsilon}^e \qquad \text{or} \qquad \dot{\boldsymbol{\sigma}} = \mathbf{D}\dot{\boldsymbol{\varepsilon}}^e \tag{64}$$

where $\mathbf{D}$ is the elastic stiffness matrix and where

$$\boldsymbol{\sigma} = \left[\begin{array}{cccccc} \sigma_{xx} & \sigma_{yy} & \sigma_{zz} & \tau_{xy} & \tau_{xz} & \tau_{yz} \end{array} \right]^T \tag{65}$$

$$\boldsymbol{\varepsilon} = \left[\begin{array}{cccccc} \varepsilon_{xx} & \varepsilon_{yy} & \varepsilon_{zz} & \gamma_{xy} & \gamma_{xz} & \gamma_{yz} \end{array} \right]^T \tag{66}$$

5.1 A 3D wood cohesive zone model based on plasticity theory

The material model presented in [4] is aimed at describing the material behavior within a fracture process zone, from start of strain softening at initiation of plastic straining to the creation of new traction-free surfaces. It is indented to be used within a predefined potential crack plane, which in the current implementation is forced to be oriented in the xz-plane and having a small height h in the y-direction as illustrated in Figure 5. In the FE-discretization, the predefined crack plane consists of one layer of elements.

The Tsai-Wu criterion [11] is used as criterion for initiation of yielding, i.e. the formation of a fracture process zone and initiation of softening. An initial yield function F is hence defined according to

$$F(\boldsymbol{\sigma}) = \boldsymbol{\sigma}^T\mathbf{q} + \boldsymbol{\sigma}^T\mathbf{P}\boldsymbol{\sigma} - 1 \quad \text{where} \begin{cases} F < 0 & \text{elastic response} \\ F = 0 & \text{initiation of softening} \end{cases} \tag{67}$$

where $\mathbf{q}$ and $\mathbf{P}$ are given by material strength properties. The post softening-initiation performance is assumed to be governed by the three out-of-fracture plane stress and plastic deformation components. As softening has initiated, the yield function is changed accordingly and an updated yield function is defined as

$$f(\boldsymbol{\sigma}, K) = \sigma_{yy}^2 F_{yyyy} + \tau_{xy}^2 F_{xyxy} + \tau_{yz}^2 F_{yzyz} - K^2 \quad \text{where} \begin{cases} f < 0 & \text{elastic response} \\ f = 0 & \text{elasto-plastic response} \end{cases} \tag{68}$$

where F_{yyyy}, F_{xyxy} and F_{yzyz} are yield parameters determined from the stress state at initiation of softening and K is a softening parameter. Using matrix notation, the updated yield function may also be expressed as

$$f(\boldsymbol{\sigma}, K) = \boldsymbol{\sigma}^T\mathbf{R}\boldsymbol{\sigma} - K^2 \tag{69}$$

where $\mathbf{R}$ is a 6×6 matrix with $R_{22} = F_{yyyy}$, $R_{44} = F_{xyxy}$ and $R_{66} = F_{yzyz}$ and all other components equal to zero. A plastic flow rule is adopted according to

$$\dot{\boldsymbol{\varepsilon}}^p = \dot{\lambda}\frac{\partial g}{\partial \boldsymbol{\sigma}} = \dot{\lambda}\frac{\partial f}{\partial \boldsymbol{\sigma}} \qquad \text{with } \dot{\lambda} \geq 0 \text{ and where} \begin{cases} \dot{\lambda} = 0 & \text{elastic strains only} \\ \dot{\lambda} > 0 & \text{plastic strains} \end{cases} \tag{70}$$

where $\dot{\lambda}$ is the plastic multiplier and where $g = f$, meaning that the flow rule is associated with respect to the updated yield function f.

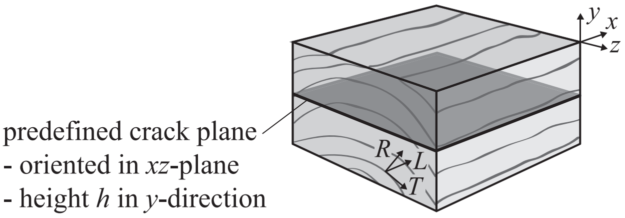

Figure 5: Orientation of predefined crack plane.

The change in size of the yield surface is described by the softening parameter K which is a function of an internal variable denoted the effective dimensionless deformation δ_{eff}. The following softening function is adopted in [4]

$$K = \begin{cases} (1 - \delta_{eff} + c^{1/m}\delta_{eff})^m & \text{for} \quad \delta_{eff} < 1 \\ 0 & \qquad\quad\; \delta_{eff} \geq 1 \end{cases} \tag{71}$$

where m and c are model parameters and where $K = 0$ corresponds to zero stress transferring capacity and the creation of new traction-free surfaces. A slightly different softening function is adopted for the numerical analyses in [5] and [6]. The effective dimensionless deformation δ_{eff} is expressed in plastic deformations δ_{yy}, δ_{xy} and δ_{yz} and the evolution law for the internal variable is defined as

$$\dot{\delta}_{eff} = \sqrt{\left(\frac{\dot{\delta}_{yy}}{A_{yy}}\right)^2 + \left(\frac{\dot{\delta}_{xy}}{A_{xy}}\right)^2 + \left(\frac{\dot{\delta}_{yz}}{A_{yz}}\right)^2} \tag{72}$$

where A_{yy}, A_{xy} and A_{yz} are scaling parameters of dimension length related to the fracture energies in the three corresponding modes of deformation. The increments in plastic deformation are determined according to $\dot{\delta}_{yy} = h\dot{\varepsilon}^p_{yy}$, $\dot{\delta}_{xy} = h\dot{\gamma}^p_{xy}$ and $\dot{\delta}_{yz} = h\dot{\gamma}^p_{yz}$ by assuming constant plastic strains over the small out-of-plane (y-direction) height h of the predefined crack plane. Using Equation (70), the evolution law for the internal variable δ_{eff} may then be expressed as

$$\dot{\delta}_{eff} = \dot{\lambda}k \quad \text{where} \quad k = 2h\sqrt{\left(\frac{\sigma_{yy}F_{yyyy}}{A_{yy}}\right)^2 + \left(\frac{\tau_{xy}F_{xyxy}}{A_{xy}}\right)^2 + \left(\frac{\tau_{yz}F_{yzyz}}{A_{yz}}\right)^2} \tag{73}$$

where k is the evolution function for the internal variable.

5.2 Numerical integration of constitutive relations

With the relevant relations of the material model defined above, attention will now be paid to the process of determining the stress state along the load path. In the following description, the previous equilibrium state where all quantities are known will be denoted state 1 while the updated state for which the stress is sought will be denoted state 2. Accordingly, quantities related to the two states are denoted $(*)_1$ and $(*)_2$ respectively. While all quantities are known at state 1, only the nodal displacements and hence the total strain $\boldsymbol{\varepsilon}_2$ are known at the state 2. Using Equations (63) and (64), the stress at state 1 and state 2 may be expressed as

$$\boldsymbol{\sigma}_1 = \mathbf{D}\left(\boldsymbol{\varepsilon}_1 - \boldsymbol{\varepsilon}^p_1\right) \tag{74}$$

$$\boldsymbol{\sigma}_2 = \mathbf{D}\left(\boldsymbol{\varepsilon}_2 - \boldsymbol{\varepsilon}^p_2\right) \tag{75}$$

which by subtraction, rearrangement and expressing the difference in total strain and in plastic strain as $\Delta\boldsymbol{\varepsilon} = \boldsymbol{\varepsilon}_2 - \boldsymbol{\varepsilon}_1$ and $\Delta\boldsymbol{\varepsilon}^p = \boldsymbol{\varepsilon}^p_2 - \boldsymbol{\varepsilon}^p_1$ respectively yields

$$\boldsymbol{\sigma}_2 = \boldsymbol{\sigma}_1 + \mathbf{D}\Delta\boldsymbol{\varepsilon} - \mathbf{D}\Delta\boldsymbol{\varepsilon}^p \tag{76}$$

where $\Delta\boldsymbol{\varepsilon}^p$ is to be determined by some type of integration of Equation (70) in order to find $\boldsymbol{\sigma}_2$. For further elaboration it is convenient to define a trial stress $\boldsymbol{\sigma}_t$ according to

$$\boldsymbol{\sigma}_t = \boldsymbol{\sigma}_1 + \mathbf{D}\Delta\boldsymbol{\varepsilon} \tag{77}$$

and hence such that the trial stress equals the sought stress $\boldsymbol{\sigma}_2$ if the change in nodal displacements results in a change of strain that is purely elastic, i.e. $\Delta\boldsymbol{\varepsilon} = \Delta\boldsymbol{\varepsilon}^e$ and $\Delta\boldsymbol{\varepsilon}^p = \mathbf{0}$. The stress state is required to be located inside or on the yield surface in the stress space, i.e. the condition $f(\boldsymbol{\sigma}, K) \leq 0$ must always hold. The *consistency relation* states that during plastic loading accompanied by a change in stress state, also the softening parameters vary in such a way that the stress state always remains on the yield surface [9]. For purely elastic loading however, the softening parameters and hence also the yield surface is unchanged. The trial stress may be used as a tool to check for elasto-plastic response according to

- if $f(\boldsymbol{\sigma}_t, K_1) \leq 0 \quad \Rightarrow \quad \left\{ \begin{array}{l} \text{elastic response:} \\ \boldsymbol{\sigma}_2 = \boldsymbol{\sigma}_t,\ K_2 = K_1,\ \delta_{eff,2} = \delta_{eff,1} \end{array} \right.$

- else $\quad \Rightarrow \quad \left\{ \begin{array}{l} \text{elasto-plastic response:} \\ \boldsymbol{\sigma}_2,\ K_2,\ \delta_{eff,2} \text{ determined by numerical integration} \end{array} \right.$

The method for numerical integration of the incremental constitutive relation considered in this section is the *fully implicit (backward Euler) return method* [9], a so called *direct method* based on the *generalized mid-point rule.* The integration of the flow rule in Equation (70) and the evolution law for the internal variable in Equation (73) is performed in an approximate manner according to

$$\dot{\boldsymbol{\varepsilon}}^p = \dot{\lambda}\frac{\partial g}{\partial \boldsymbol{\sigma}} \qquad \Rightarrow \qquad \Delta\boldsymbol{\varepsilon}^p = \int_{\lambda_1}^{\lambda_1+\Delta\lambda} \frac{\partial g}{\partial \boldsymbol{\sigma}}\, \mathrm{d}\lambda \approx \Delta\lambda \left(\frac{\partial g}{\partial \boldsymbol{\sigma}}\right)_2 \tag{78}$$

$$\dot{\delta}_{eff} = \dot{\lambda} k \qquad \Rightarrow \qquad \Delta\delta_{eff} = \int_{\lambda_1}^{\lambda_1+\Delta\lambda} k\, \mathrm{d}\lambda \approx \Delta\lambda k_2 \tag{79}$$

where index 2 indicates that $\partial g/\partial\boldsymbol{\sigma}$ and k are evaluated at state 2. This results in the following set of 6+1+1 nonlinear equations

$$\begin{aligned} \boldsymbol{\sigma}_2 &= \boldsymbol{\sigma}_t - \mathbf{D}\left(\partial g/\partial\boldsymbol{\sigma}\right)_2 \Delta\lambda && (80)\\ f(\boldsymbol{\sigma}_2, K_2) &= 0 && (81)\\ K_2 &= \Big(1 - (\delta_{eff,1} + \Delta\lambda k_2) + c^{1/m}(\delta_{eff,1} + \Delta\lambda k_2)\Big)^m && (82) \end{aligned}$$

which should be solved for the 8 unknowns: the six stress components of $\boldsymbol{\sigma}$, the softening parameter K and the plastic multiplier $\Delta\lambda$. An iterative solution approach based on the Newton-Raphson method is used. A vector $\mathbf{S}$ containing the sought stress components and the plastic multiplier and a residual vector $\mathbf{V}$ are defined according to

$$\mathbf{S}^i = \left[\begin{array}{c} \boldsymbol{\sigma}^i \\ \Delta\lambda^i \end{array}\right] \quad \text{and} \quad \mathbf{V}^i = \left[\begin{array}{c} \mathbf{V}^i_{\boldsymbol{\sigma}} \\ V^i_f \end{array}\right] = \left[\begin{array}{c} \boldsymbol{\sigma}^i + \Delta\lambda^i\mathbf{D}(\frac{\partial g}{\partial \boldsymbol{\sigma}})^i - \boldsymbol{\sigma}_t \\ f(\boldsymbol{\sigma}^i, K^i) \end{array}\right] \tag{83}$$

where i indicates quantities in iteration i. The sought solution is defined by $\mathbf{V}(\mathbf{S}) = \mathbf{0}$ and is found by an iterative procedure according to

$$\mathbf{S}^i \;=\; \mathbf{S}^{i-1} - \left[\frac{\partial \mathbf{V}}{\partial \mathbf{S}}^{i-1}\right]^{-1} \mathbf{V}^{i-1} \tag{84}$$

where the iteration matrix $\partial\mathbf{V}/\partial\mathbf{S}$ for the present material model may be reduced from the expressions given in [9] for a general plasticity model as

$$\frac{\partial \mathbf{V}}{\partial \mathbf{S}} = \left[\begin{array}{cc} \mathbf{I}_6 + \Delta\lambda\mathbf{D}\frac{\partial^2 g}{\partial\boldsymbol{\sigma}\partial\boldsymbol{\sigma}} & \mathbf{D}\frac{\partial g}{\partial \boldsymbol{\sigma}} \\ \left(\frac{\partial f}{\partial \boldsymbol{\sigma}}\right)^T & 0 \end{array}\right] \tag{85}$$

where $\mathbf{I}_6$ denote a 6 × 6 identity matrix and where

$$\frac{\partial g}{\partial \boldsymbol{\sigma}} = \frac{\partial f}{\partial \boldsymbol{\sigma}} = 2\mathbf{R}\boldsymbol{\sigma} \quad \text{and} \quad \frac{\partial^2 g}{\partial \boldsymbol{\sigma} \partial \boldsymbol{\sigma}} = 2\mathbf{R} \tag{86}$$

For the first iteration ($i = 1$), the starting quantities for the iteration procedure are given by $\boldsymbol{\sigma}^0 = \boldsymbol{\sigma}_t$ and $\Delta\lambda^0 = 0$ yielding

$$\mathbf{S}^0 = \begin{bmatrix} \boldsymbol{\sigma}_t \\ 0 \end{bmatrix} \quad \text{and} \quad \mathbf{V}^0 = \begin{bmatrix} \mathbf{0} \\ f(\boldsymbol{\sigma}_t, K_1) \end{bmatrix} \tag{87}$$

The softening parameter K is in every iteration i determined according to

$$K^i \quad = \quad \left(1 - \delta^i_{eff} + c^{1/m}\delta^i_{eff}\right)^m \qquad \text{where } \delta^i_{eff} = \delta_{eff,1} + \Delta\delta^i_{eff} = \delta_{eff,1} + \Delta\lambda^i k^i \tag{88}$$

where the index i indicates that $\Delta\lambda^i$ is obtained from Equation (84) in iteration i and that k is evaluated using the stress $\boldsymbol{\sigma}^i$ obtained in the same manner.

Due to the change from the initial yield function F to the updated yield function f and the nature of the incremental solution, special attention needs to be paid to the integration of constitutive relations at initiation of yielding. The issue concerns the parameters F_{yyyy}, F_{xyxy} and F_{yzyz} which define the updated yield function f and which are unknown in the beginning of the load step where plastic straining is first initiated. This may be solved by approximating these parameters at initiation of yielding according to

$$F_{yyyy} \approx P_{22} \ , \quad F_{xyxy} \approx P_{44} \ , \quad F_{yzyz} \approx P_{66} \tag{89}$$

where P_{ii} ($i = 2, 4, 6$) denotes three diagonal components of the matrix $\mathbf{P}$. The derivate $\partial f / \partial \boldsymbol{\sigma}$ in Equation (85) is however taken as $\partial F / \partial \boldsymbol{\sigma}$ since the stress should be bound to the initial yield surface F. The parameters F_{yyyy}, F_{xyxy} and F_{yzyz} used for subsequent computations are then determined such that the two yield surfaces f and F intersect at the accepted equilibrium stress state $\boldsymbol{\sigma}_c$ at which softening is initialized according to

$$F(\boldsymbol{\sigma}_c) = f(\boldsymbol{\sigma}_c, K = 1) = 0 \tag{90}$$

and the considered parameters may then be determined according to

$$\begin{aligned}
F_{yyyy} &= P_{22}/\left(\sigma^2_{c,yy}P_{22} + \tau^2_{c,xy}P_{44} + \tau^2_{c,yz}P_{66}\right) && (91)\\
F_{xyxy} &= P_{44}/\left(\sigma^2_{c,yy}P_{22} + \tau^2_{c,xy}P_{44} + \tau^2_{c,yz}P_{66}\right) && (92)\\
F_{yzyz} &= P_{66}/\left(\sigma^2_{c,yy}P_{22} + \tau^2_{c,xy}P_{44} + \tau^2_{c,yz}P_{66}\right) && (93)
\end{aligned}$$

The flow rule is hence actually non-associated in the load step were plastic straining is initiated and a small error, related to the path step length, may be introduced. Some further comments on this matter are found in [4].

6 Some comments regarding numerical implementation

The cohesive zone model briefly presented in Section 5, and more thoroughly presented in [4], has been implemented for nonlinear finite element analysis using solution approaches presented in Sections 4 and 5. The implementation was carried out in Matlab [7] using supplementary routines from the toolbox Calfem [1]. The material model has been applied to analysis of double cantilever beam specimens and end-notched beams using a cylindrical arc-length approach with a conventional constraint equation [4] and analysis of glulam beams with a hole using an arc-length approach with a constraint equation based on energy dissipation [5]. Further analyses include studies of dowel-type connections, using a Newton-Raphson approach and using a cylindrical arc-length approach with a constraint equation considering only certain degrees of freedom [6]. Pseudo codes for the arc-length method are given in Section 6.1 for a conventional type of constraint equation and in Section 6.2 for an energy dissipation based constraint equation.

For the applications of the material model presented in [4], [5] and [6], the nonlinear softening performance is restricted to a predefined potential crack plane and linear elastic behavior is assumed for the bulk material. This allows for some simple but rather efficient ways to reduce the computational cost. Since the stiffness contributions from the linear elastic elements to the global tangential stiffness matrix are constant, these contributions need to be determined and assembled only once for each analysis. The residual force vector will furthermore only have non-zero components for the degrees of freedom associated with elements showing nonlinear behavior, i.e. the degrees of freedom associated with the predefined crack plane. If the major interest is some global load vs. displacement relation, determination of stresses is hence only necessary for the elements within the predefined crack plane and for linear elastic elements sharing nodes with the elements within the crack plane.

The conventional formulation of the arc-length method suffers from the drawback that complex solutions may be found when solving Equation (46) to find the increment in load factor $\mathrm{d}\lambda$. The remedy for this problem proposed in [3] and [10] is to restart the iteration procedure from the last know equilibrium point using a smaller value of the prescribed path step length L. This does however not guarantee that real roots and convergence are eventually found. There are also more complex strategies for avoiding the complex roots suggested in the literature. Numerical problems may also be manifested by divergence of the procedure for the numerical integration of constitutive relations according to Equation (84).

The experience from the work presented in [4], [5] and [6] is that numerical problems sometimes can be avoided be restarting the iteration process not from the last equilibrium state, but from a few states back and temporarily adjusting the tolerance limit for the convergence criteria and/or adjusting the path step length. Also simply increasing the path step length L temporarily has been found to solve the problem of finding complex roots for the increment in load factor $\mathrm{d}\lambda$. The solution should however be checked such that the obtained loading path does not deviate from the expected loading path, i.e. such that an equilibrium path with elastic unloading is followed when the sought equilibrium path should correspond to continuous crack propagation.

For analyses of glulam beams loaded in bending and containing a hole, numerical problems were for large beams sometimes encountered when considered softening within two separate crack planes. These problems are believed to be related to simultaneous unloading (crack closure) within one crack plane and crack propagation within the other. See [5] for further comments regarding this matter.

Criteria for acceptance of global equilibrium and convergence are of importance for nonlinear analyses. Within the numerical work relating to the considered cohesive zone model has the following convergence criterion been used

$$\sqrt{\mathbf{G}^T\mathbf{G}} < \epsilon_G F_{tot} \tag{94}$$

where $\mathbf{G}$ is the residual force vector (the out-of-balance force vector), F_{tot} is the total applied external load and ε_G is the tolerance limit. For the analyses presented in [4], [5] and [6], values of ε_G between 10^{-3} and 10^{-5} have been used.

6.1 Arc-length method with a conventional constraint equation

A pseudo code for the arc-length method with a conventional constraint equation is outlined in the box below. The pseudo code is valid also for a constraint equation based on only a limited number of degrees of freedom, whereby all quantities related to the nodal displacements in the constraint equation are determined from the reduced vector $\tilde{\mathbf{a}}$ instead of the full vector $\mathbf{a}$.

Arc-length method with a conventional constraint equation

```
For path step $n = 1, 2, 3, \dots, n_{max}$
  • Initiate iteration quantities from accepted equilibrium quantities
    $\mathbf{a}^0 = \mathbf{a}_{n-1}$ , $\lambda^0 = \lambda_{n-1}$ , $\boldsymbol{\sigma}_1 = \boldsymbol{\sigma}_2$ , $K_1 = K_2$ , $\delta_{eff,1} = \delta_{eff,2}$
  • Equilibrium iterations $i = 1, 2, \dots$ while $\|\mathbf{G}\| >$ tolerance
      · calculate elasto-plastic stiffness and assemble global tangential stiffness
        $\mathbf{D}^{ep}, \mathbf{K}_t \Leftarrow (\boldsymbol{\sigma}_2, K_2, \delta_{eff,2}, \mathbf{D}, \mathbf{q}, \mathbf{P}, \mathbf{R},$ mesh geometry and topology$)$
      · calculate pseudo displacements from
        $\mathbf{K}_t \mathrm{d}\mathbf{a}_\mathbf{f} = \mathbf{f}$ and $\mathbf{K}_t \mathrm{d}\mathbf{a}_\mathbf{G} = -\mathbf{G}$
      · calculate load factor
        if $i = 1$
          $\mathrm{d}\lambda = sL/\sqrt{\mathrm{d}\mathbf{a}_\mathbf{f}^T \mathrm{d}\mathbf{a}_\mathbf{f} + \psi \mathbf{f}^T \mathbf{f}}$   where $s = \mathrm{sign}(\Delta \mathbf{a}_n^T \mathrm{d}\mathbf{a}_\mathbf{f})$
        else
          determine $a_1$, $a_2$, $a_3$ and solve $\mathrm{d}\lambda$ from $a_1 \mathrm{d}\lambda^2 + a_2 \mathrm{d}\lambda + a_3 = 0$
            if two real solutions, take special care
            if complex solutions, restart iteration
        $\lambda^i = \lambda^{i-1} + \mathrm{d}\lambda$
      · calculate nodal displacements
        $\mathrm{d}\mathbf{a} = \mathrm{d}\mathbf{a}_\mathbf{G} + \mathrm{d}\lambda \mathrm{d}\mathbf{a}_\mathbf{f}$
        $\mathbf{a}^i = \mathbf{a}^{i-1} + \mathrm{d}\mathbf{a}$
      · calculate element strains
        $\Delta \boldsymbol{\varepsilon} = \mathbf{B}(\mathbf{a}^i - \mathbf{a}^0)$
      · calculate element stresses according to Section 5
        $\boldsymbol{\sigma}_2, K_2, \delta_{eff,2} \Leftarrow (\Delta \boldsymbol{\varepsilon}, \boldsymbol{\sigma}_1, K_1, \delta_{eff,1}, \mathbf{D}, \mathbf{q}, \mathbf{P}, \mathbf{R})$
      · calculate residual force vector from internal and external force vectors
        $\mathbf{G} = \mathbf{f}_{int} - \mathbf{f}_{ext}$ where $\mathbf{f}_{int} = \int_\Omega \mathbf{B}^T \boldsymbol{\sigma}_2 \, \mathrm{d}\Omega$ and $\mathbf{f}_{ext} = \lambda^i \mathbf{f}$
          restart iteration if global or local divergence
  • For elements with initialization of softening during path step $n$ :
    switch from initial to updated yield function
    $\mathbf{R} \Leftarrow (K_2, K_1, \boldsymbol{\sigma}_2, \mathbf{q}, \mathbf{P})$
  • Accept iteration quantities
    $\lambda_n = \lambda^i$ , $\mathbf{a}_n = \mathbf{a}^i$
```

6.2 Arc-length method with a dissipation based constraint equation

A pseudo code for the arc-length method with a constraint equation based on energy dissipation is outlined in the box below. Due to the nature of the constraint equation, being based on consideration of energy dissipation by plastic straining, the method is only applicable once plastic straining of the material has taken place. The pseudo code below takes it start in the accepted equilibrium quantities of path step n_{dis}, during which plastic straining is first initialized.

Arc-length method with a dissipation based constraint equation

```
For path step $n = n_{dis} + 1, n_{dis} + 2, \ \dots \ , n_{max}$
  • Initiate iteration quantities from accepted equilibrium quantities
    $\mathbf{a}^0 = \mathbf{a}_{n-1} \ , \ \ \lambda^0 = \lambda_{n-1} \ , \ \ \boldsymbol{\sigma}_1 = \boldsymbol{\sigma}_2 \ , \ \ K_1 = K_2 \ , \ \ \delta_{eff,1} = \delta_{eff,2}$
  • Calculate pseudo force vector
    $\mathbf{f}_n^* = \int_\Omega \mathbf{B}^T (\mathbf{D}^{ep})^T \mathbf{D}^{-1} \boldsymbol{\sigma}_2 \ \mathrm{d}\Omega$
  • Equilibrium iterations $i = 1, 2, \ \dots$ while $\|\mathbf{G}\| >$ tolerance
      · calculate elasto-plastic stiffness and assemble global tangential stiffness
        $\mathbf{D}^{ep}, \mathbf{K}_t \quad \Leftarrow \quad (\boldsymbol{\sigma}_2, K_2, \delta_{eff,2}, \mathbf{D}, \mathbf{q}, \mathbf{P}, \mathbf{R}, \text{mesh geometry and topology})$
      · calculate pseudo displacements from
        $\mathbf{K}_t \mathrm{d}\mathbf{a}_\mathbf{f} = \mathbf{f} \quad \text{and} \quad \mathbf{K}_t \mathrm{d}\mathbf{a}_\mathbf{G} = -\mathbf{G}$
      · calculate load factor
        $\mathrm{d}\lambda = \dfrac{L - (\Delta\mathbf{a}^{i-1} + \mathrm{d}\mathbf{a}_\mathbf{G})^T (\lambda^0 \mathbf{f} - \mathbf{f}_n^*)}{\mathrm{d}\mathbf{a}_\mathbf{f}^T (\lambda^0 \mathbf{f} - \mathbf{f}_n^*)} \qquad \text{where} \ \ \Delta\mathbf{a}^{i-1} = \mathbf{a}^{i-1} - \mathbf{a}^0$
        $\lambda^i = \lambda^{i-1} + \mathrm{d}\lambda$
      · calculate nodal displacements
        $\mathrm{d}\mathbf{a} = \mathrm{d}\mathbf{a}_\mathbf{G} + \mathrm{d}\lambda \mathrm{d}\mathbf{a}_\mathbf{f}$
        $\mathbf{a}^i = \mathbf{a}^{i-1} + \mathrm{d}\mathbf{a}$
      · calculate element strains
        $\Delta\boldsymbol{\varepsilon} = \mathbf{B}(\mathbf{a}^i - \mathbf{a}^0)$
      · calculate element stresses according to Section 5
        $\boldsymbol{\sigma}_2, K_2, \delta_{eff,2} \quad \Leftarrow \quad (\Delta\boldsymbol{\varepsilon}, \boldsymbol{\sigma}_1, K_1, \delta_{eff,1}, \mathbf{D}, \mathbf{q}, \mathbf{P}, \mathbf{R})$
      · calculate residual force vector from internal and external force vectors
        $\mathbf{G} = \mathbf{f}_{int} - \mathbf{f}_{ext} \quad \text{where} \ \ \mathbf{f}_{int} = \int_\Omega \mathbf{B}^T \boldsymbol{\sigma}_2 \ \mathrm{d}\Omega \ \ \text{and} \ \ \mathbf{f}_{ext} = \lambda^i \mathbf{f}$
            restart iteration if global or local divergence
  • For elements with initialization of softening during path step $n$ :
    switch from initial to updated yield function
    $\mathbf{R} \quad \Leftarrow \quad (K_2, K_1, \boldsymbol{\sigma}_2, \mathbf{q}, \mathbf{P})$
  • Accept iteration quantities
    $\lambda_n = \lambda^i \ , \ \ \mathbf{a}_n = \mathbf{a}^i$
```

References

[1] Austrell PE, Dahlblom O, Lindemann J et al. (2004) CALFEM – A finite element toolbox. Version 3.4, Division of Structural Mechanics, Lund University, Sweden.

[2] de Borst R (1987) Computation of post-bifurcation and post-failure behavior of strain-softening solids. Computers and Structures, 25:221-224.

[3] Crisfield MA (1991) Nonlinear finite element analysis of solids and structures – Volume 1. John Wiley & Sons Ltd, Chichester, Great Britain.

[4] Danielsson H, Gustafsson PJ (2013) A three dimensional plasticity model for perpendicular to grain cohesive fracture in wood. Engineering Fracture Mechanics, 98:137-152.

[5] Danielsson H, Gustafsson PJ. Fracture analysis of glulam beams with a hole using a 3D cohesive zone model.
Submitted for publication

[6] Danielsson H, Gustafsson PJ. Fracture analysis of perpendicular to grain loaded dowel-type connections using a 3D cohesive zone model.
Submitted for publication

[7] Matlab. The Mathworks, Inc.

[8] Ottosen NS, Petersson H (1992) Introduction to the finite element method. Prentice Hall, Great Britain.

[9] Ottosen NS, Ristinmaa M (2005) The mechanics of constitutive modeling. Elsevier, Great Britain.

[10] Ristinmaa M, Ljung C (1998) An introduction to stability analysis. Division of Solid Mechanics, Lund University, Sweden.

[11] Tsai SW, Wu EM (1971) A general theory of the strength of anisotropic materials. Journal of Composite Materials, 5:58-80.

[12] Verhoosel CV, Remmers JJC, Gutiérrez MA (2009) A dissipation based arc-length method for robust simulation of brittle and ductile failure. International Journal for Numerical Methods in Engineering, 77:1290-1321.

Part III

Appended papers

Paper A

Strength tests of glulam beams with quadratic holes – Test report

Henrik Danielsson

Report TVSM-7153, Division of Structural Mechanics, Lund University, 2008

Abstract

This report deals with strength tests of glulam beams with quadratic holes with rounded corners. A total of 36 individual tests were carried out, divided into nine test series with four nominally equal tests in each test series. There were four parameters varied within these test series: beam size, bending moment to shear force ratio, material strength class and also hole placement with respect to the height of the beam. The latter parameter seems to never have been investigated before since all previously performed tests found in the literature have been carried out on beams with holes placed centrically in the beam height direction. The test results indicate a strong size effect. The influence of eccentric placement of the hole on the crack load was found to be small.

Keywords: glulam, hole, strength, test, size effect, eccentric hole.

Acknowledgements

The work presented in this report was carried out at the Division of Structural Mechanics at Lund University during the winter of 2007/2008. The financial support through collaboration with Ulf Arne Girhammar at Umeå University within the project *Multi-story timber frame buildings* (The European Union's Structural Funds – Regional Fund: Goal 1) and from *Formas* through grant 24.3/2003-0711 is greatly appreciated. I would also like to acknowledge *Svenskt Limträ AB* for assisting the project by supplying all glulam beams. I would furthermore like to give special thanks to my supervisor Per Johan Gustafsson, Roberto Crocetti at Moelven Töreboda AB and research engineers Per-Olof Rosenkvist and Thord Lundgren for valuable contributions during the work with this project.

Lund, February 2008

Henrik Danielsson

Contents

1 Introduction **3**

2 Test series **4**

3 Materials **9**

4 Results **12**

5 Concluding remarks **25**

References **26**

1 Introduction

The tests presented in this report deals with the strength of glulam beams with holes. A total of 36 individual tests were carried out, divided into nine test series with four nominally equal tests in each test series. All holes were quadratic with rounded corners and with a side length equal to one third of the beam height. The study comprises investigations of primarily two interesting and potentially important design variables: *beam size effect* and *hole placement with respect to beam height.* Two other design parameters are also studied to some extent: *material strength class* and *bending moment to shear force ratio* at hole center.

Beam size
: Two different beam cross section sizes were used within the test series, 115×180 mm^2 and 115×630 mm^2, in order to investigate the size dependence of the strength.

Hole placement with respect to beam height
: Three different hole placements with respect to the height of the beam were tested, centrically placed holes and holes placed with its center in the upper or lower part of the beam respectively.

Material Strength Class
: Two different material strength classes were used, homogeneous glulam of lamination strength class LS22 and combined glulam of lamination strength classes LS22 and LS15.

Bending moment to shear force ratio
: Two different test setups were used concerning the bending moment to shear force ratio, one with the hole center placed in a position (in the length direction of the beam) with a combined state of shear force and bending moment and another setup where the hole is placed with its center at a point of zero bending moment.

Different hole placements with respect to the beam height seems to never have been investigated before since all previously performed tests found in the literature have been carried out on beams with holes placed centrically with respect to the beam height [1].

The report is organized in the following way. The nine test series and the different test setups, test procedures, recorded measures and other characteristics of the tests are presented in Section 2. The glulam beams are described concerning material strength class, lamellae size, density, moisture content and other material properties in Section 3. The results of the strength tests are presented in Section 4 and some concluding remarks on the results are given in Section 5.

2 Test series

The test series are in Table 1 described concerning name, number of tests, test setup, hole placement, strength class type, beam size and hole size. The geometric properties and the bending moment to shear force ratios at hole center for Test Setup 1 and Test Setup 2 are illustrated in Figure 1. The names of the test series consist of a three letter combination. All tests with the same first letter (A, B, C, D) have the same test setup and geometry with the exception of the hole placement which is described by the second letter (M=Middle, U=Upper, L=Lower) according to Figure 1. The last letter of the combination tells whether the beams are strength class homogeneous (h) or strength class combined (c).

Table 1: *Test series.*

Test series	Number of tests	Test setup	Hole placement	Strength class type	Beam size $T \times H$ [mm^2]	Hole size $a \times b$ [mm^2]	r [mm]
AMh	4	1	Middle	homogeneous	115 × 630	210 × 210	25
AMc	4	1	Middle	combined	115 × 630	210 × 210	25
AUh	4	1	Upper	homogeneous	115 × 630	210 × 210	25
ALh	4	1	Lower	homogeneous	115 × 630	210 × 210	25
BMh	4	2	Middle	homogeneous	115 × 630	210 × 210	25
CMh	4	1	Middle	homogeneous	115 × 180	60 × 60	7
CUh	4	1	Upper	homogeneous	115 × 180	60 × 60	7
CLh	4	1	Lower	homogeneous	115 × 180	60 × 60	7
DMh	4	2	Middle	homogeneous	115 × 180	60 × 60	7

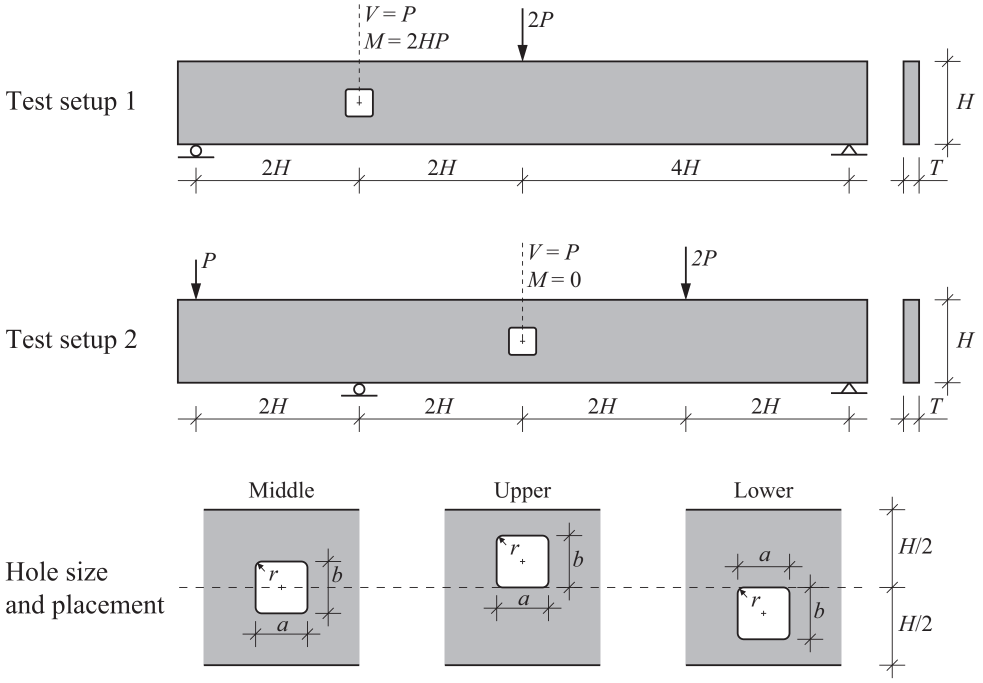

Figure 1: *Test setups and hole placements.*

All tests were run in deformation control. The rate of total deformation was 0.02 mm/s for test series AMh (except AMh-1 were the rate was 0.05 mm/s), AMc, AUh, ALh and BMh while the rate of total deformation was 0.007 mm/s for test series CMh, CUh, CLh and DMh. These rates resulted in a test duration of approximately 20-30 minutes. The rate of total deformation referred to is the rate of the actuator in the testing machine. These rates of total deformations allowed careful observations of the two corners of the holes where cracks were expected during the loading procedure which enabled a careful investigation of the initiation and propagation of the cracks.

The following variables were recorded for all tests: the total deformation, applied load P, beam deflection δ and also vertical deformations d in the beam at the two failing corners of the hole. Four LVDT sensors were used to measure these deformations, one on each side of the beam at the two failing corners of the hole. A fifth LVDT sensor was used to measure the beam deflection δ. The placement of these sensors, glulam beam sizes and sizes of steel beams and support plates are shown in Figures 2 and 3.

For test series AMh, AMc, AUh, ALh, CMh, CUh and CLh the glulam beams were delivered with a total length which was longer than the span length of the test setup and there where two holes in each beam as shown in Figure 3. Hence, two test were performed on the same beam. For these test series, tests 1 and 2 and tests 3 and 4 were performed on the same beam. The larger beams ($H = 630$ mm) were by means of a roller type of support stabilized in the weak direction at three points along the beam length. Photos of the hole and the LVDT sensors are for some tests shown in Figure 4. Photos of the test setups used for the nine different test series are shown in Figure 5.

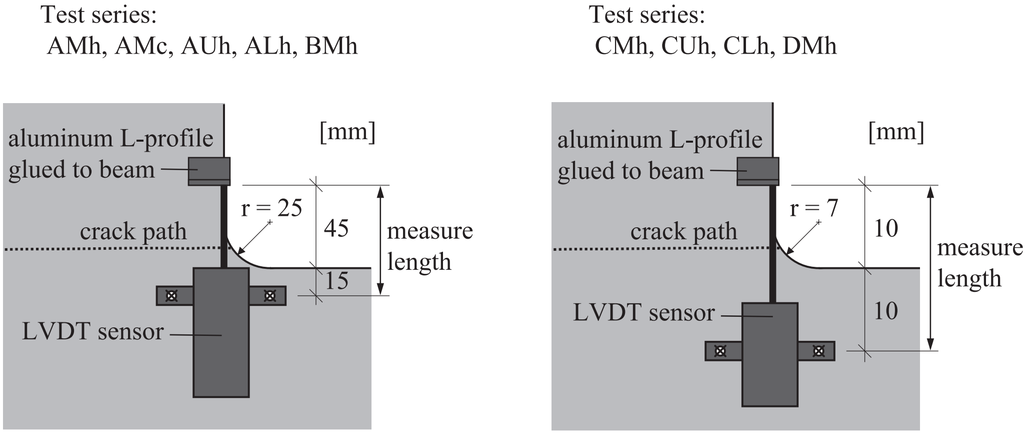
Test series:
AMh, AMc, AUh, ALh, BMh
aluminum L-profile glued to beam
[mm]
r = 25
45
measure length
crack path
15
LVDT sensor
Test series:
CMh, CUh, CLh, DMh
aluminum L-profile glued to beam
[mm]
r = 7
10
measure length
crack path
10
LVDT sensor

Figure 2: *Placement of LVDT sensors for measurement of deformation d.*

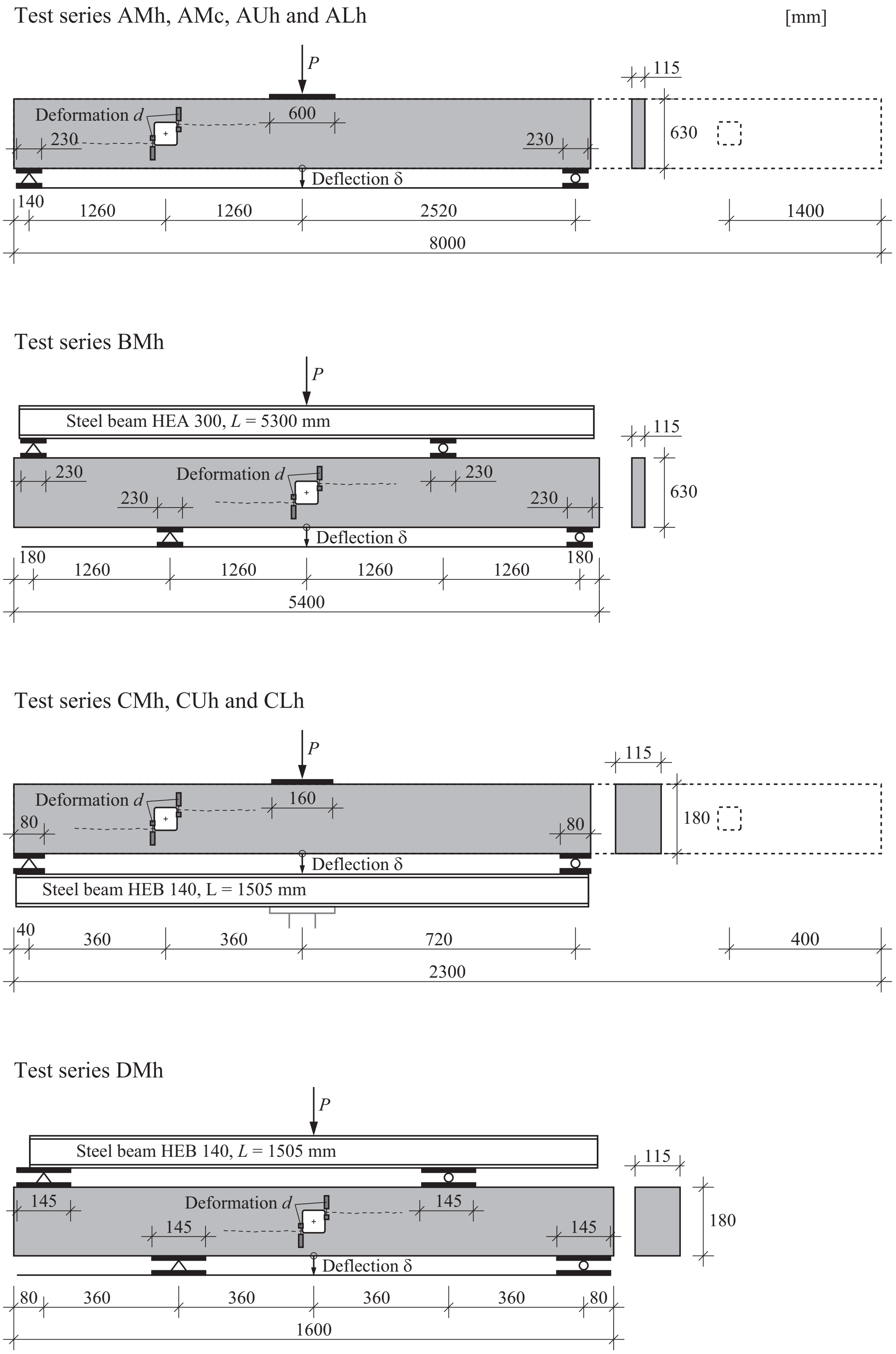
Test series AMh, AMc, AUh and ALh

Test series BMh

Test series CMh, CUh and CLh

Test series DMh

[mm]
P
Deformation d
600
230
230
115
630
Deflection δ
140
1260
1260
2520
1400
8000
Steel beam HEA 300, L = 5300 mm
115
230
Deformation d
230
230
230
630
Deflection δ
180
1260
1260
1260
1260
180
5400
160
80
80
115
180
Steel beam HEB 140, L = 1505 mm
40
360
360
720
400
2300
Steel beam HEB 140, L = 1505 mm
145
145
145
145
80
360
360
360
360
80
1600

Figure 3: *Test setups with dimensions of glulam beams and steel parts.*

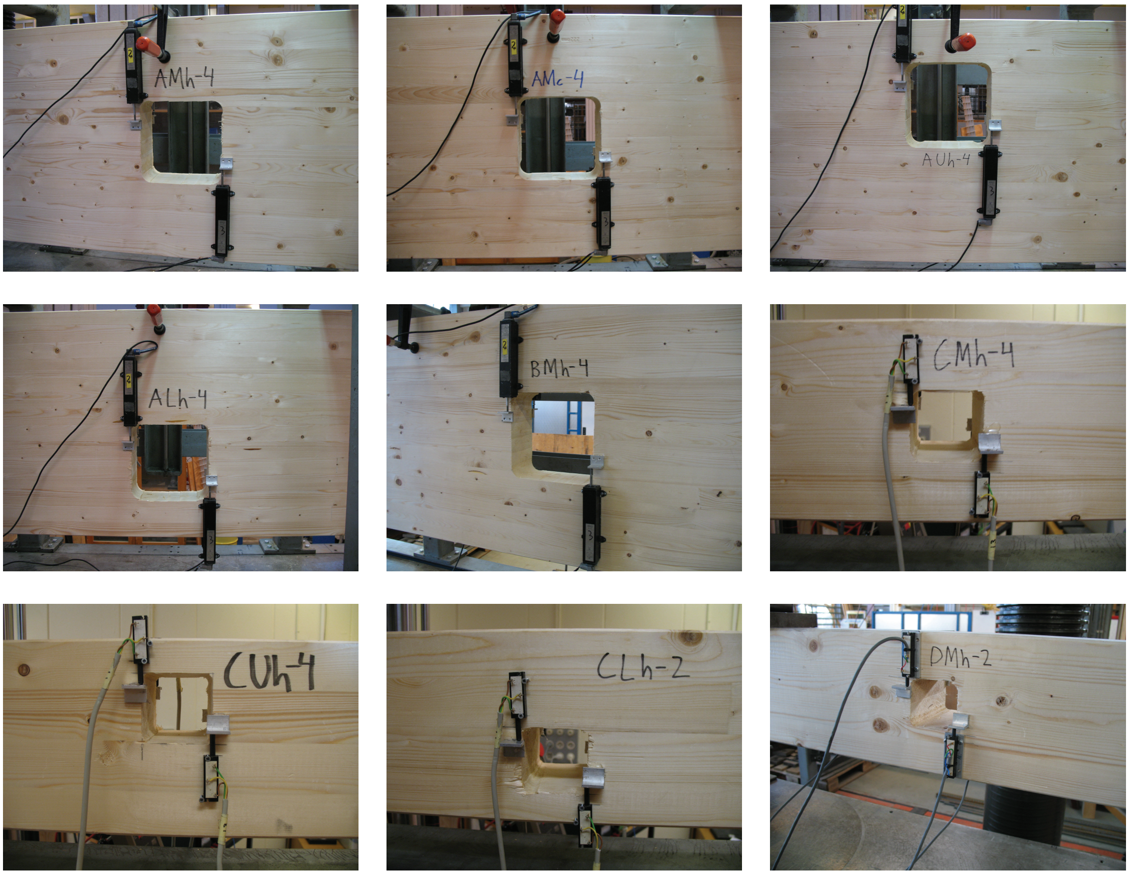
AMh-4
AMc-4
AUh-4
ALh-4
BMh-4
CMh-4
CUh-4
CLh-2
DMh-2

Figure 4: *Photos of the holes and LVDT sensors from test series: AMh, AMc and AUh (top); ALh, BMh and CMh (middle); CUh, CLh and DMh (bottom).*

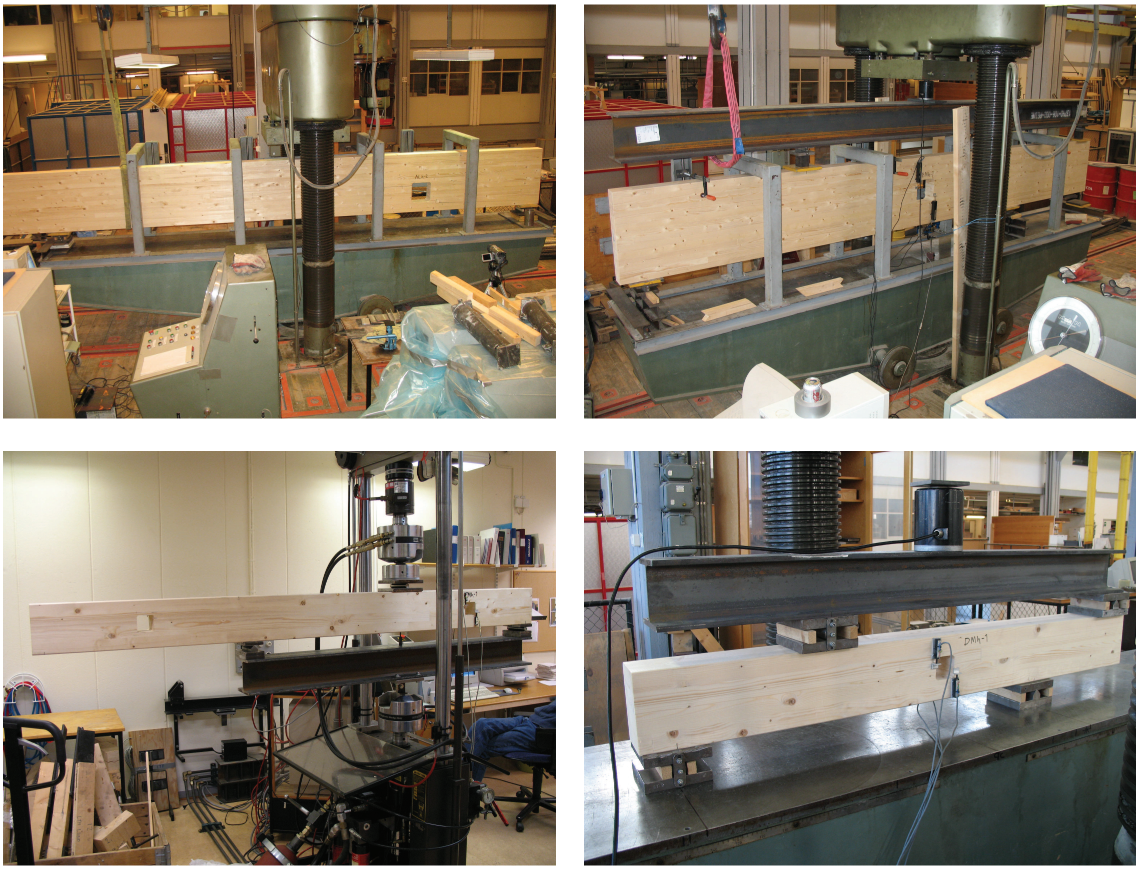

Figure 5: *Photos of test setups used for test series AMh, AMc, AUh and ALh (top left); BMh (top right); CMh, CUh and CLh (bottom left) and DMh (bottom right).*

3 Materials

All glulam beams were produced and delivered by Töreboda Moelven AB. The beams were made of spruce (Lat. *Picea Abies*), glued with melamine-urea-formaldehyde (MUF) resin and delivered with pre-made holes. The lamella thickness was consistently 45 mm which means that there were 4 lamellae in the small beams (115×180 mm^2) and 14 lamellae in the large beams (115×630 mm^2). All small glulam beams were strength class homogeneous while both strength class homogeneous glulam and strength class combined glulam were represented among the large beams. The strength class combined glulam beams were produced with the three outmost lamellae on each side of lamination strength class LS22 and the remaining eight of lamination strength class LS15. The strength class homogeneous glulam beams were produced with lamination strength class LS22 throughout the entire beam cross section. The lamellae compositions of the cross sections are illustrated in Figure 6 and the material properties for these lamination strength classes are presented in Table 2. These material properties correspond to the requirements of lamella material properties for the different glulam strength classes in SS-EN 1194 [4]. There were no obvious differences in the average width of the growth rings, in the number of knots or any other visually observable property between the two lamination strength classes.

Table 2: *Material properties for lamination strength classes according to [3].*

		LS15	LS22
Characteristic tensile strength	[MPa]	14.5	22
Mean tensile Young's modulus	[MPa]	11 000	13 000
Density, 5^{th} percentile	[kg/m^3]	350	390

The strength class homogeneous glulam beams correspond to glulam strength class GL32h according to SS-EN 1194 [4]. The strength class combined glulam beams correspond to the glulam strength class L40 according to Swedish BKR [2] and this class is usually considered to correspond to GL32c although this class should be composed of LS22 and LS18 according to SS-EN 1194.

The nominal beam cross section sizes 115×180 mm^2 and 115×630 mm^2 are used throughout this report although the real cross section sizes were measured to 114×178 mm^2 and 114×628 mm^2 respectively at moisture content corresponding to the moisture content at the time of testing. Figure 6 shows the arrangement and relative growth ring orientation of the lamellae in the cross sections and also the location of the holes in relation to the location of the glue lines. The placement of the holes and the direction of load was random with respect to the orientation of the growth rings. The holes were not perfectly shaped according to the dimensions in Table 1 although there were no major discrepancies. The corners of the holes in the small beams were however not ideally quarter circular in shape. The hole surfaces were not smoothed in any way.

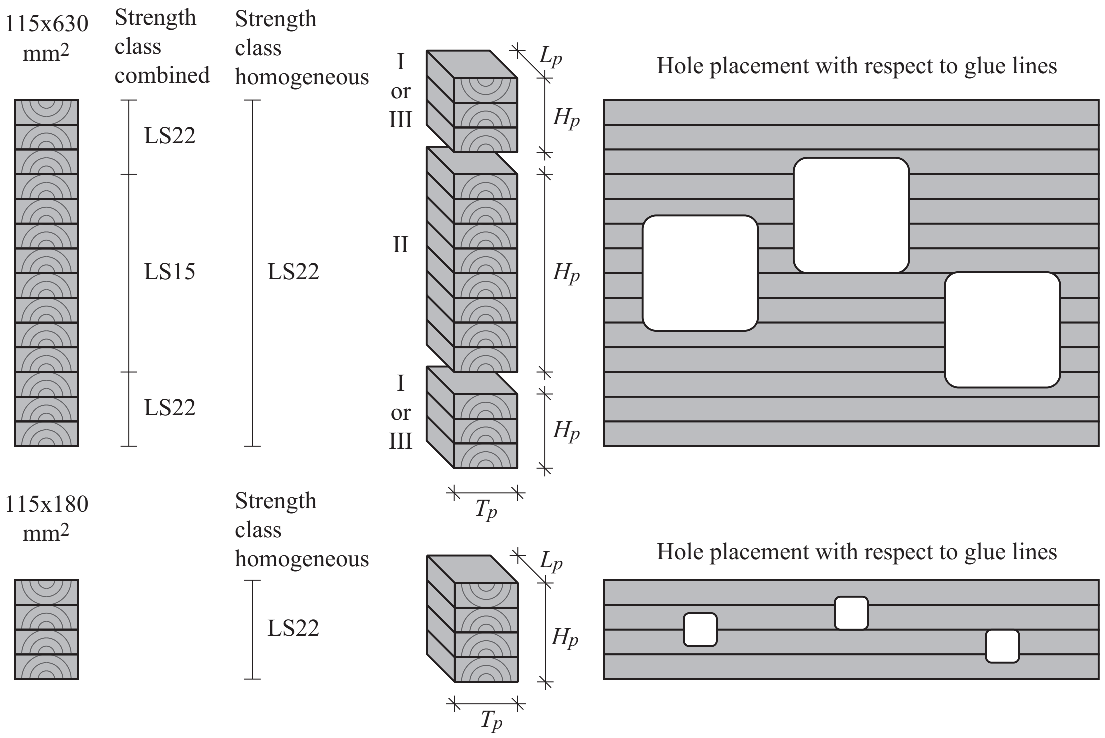
115x630 mm2
Strength class combined
Strength class homogeneous
LS22
LS15
LS22
LS22
I or III
II
I or III
Lp
Hp
Hp
Hp
Tp
Hole placement with respect to glue lines
115x180 mm2
Strength class homogeneous
LS22
Lp
Hp
Tp
Hole placement with respect to glue lines

Figure 6: *Illustration of beam cross section composition and hole placement.*

The beams were delivered wrapped in plastic cover and with a moisture content believed to be approximately 12 %. From the time of delivery to the time of testing the beams were kept indoors in a climate of about 20 °C and 35 % RH. The beams were kept in the plastic covers until about ten minutes before testing in order to reduce the risk of any drying and development of any moisture gradient in the material. The moisture content u at time of testing and the density ρ were determined from samples of the tested beams. This was carried out by cutting a piece of length about 100 mm from the beam cross section. The pieces from the large beams where then cut into smaller pieces denoted I, II and III according to Figure 6. The volume V_{test} was determined by measuring the side lengths T_p, H_p and L_p and the mass at time of testing m_{test} was also determined. The pieces were then left to dry in a temperature of 105 °C until the mass was constant and the moisture content was considered to be zero. The moisture content u were for the individual parts determined according to Equation (1) and the mean value according to the same equation with the masses m_{test} and m_{dry} replaced by $\sum m_{test}$ and $\sum m_{dry}$ respectively. The density was determined in the same manner according to Equation (2). The measured data, the moisture content u and the density ρ are presented in Table 3.

$$u = \frac{m_{test} - m_{dry}}{m_{dry}} \qquad [\text{kg/kg}] \text{ or } [\%] \tag{1}$$

$$\rho = \frac{m_{test}}{V_{test}} \qquad [\text{kg/m}^3] \tag{2}$$

Table 3: *Measured data, density ρ and moisture content u at time of testing.*

Test series	no.	piece	T_p [mm]	H_p [mm]	L_p [mm]	m_{test} [g]	m_{dry} [g]	u [%]	ρ [kg/m^3]	
AMh	1,2	I	114	134	100	714.7	638.4	11.95	467.9	
		II	114	359	100	1850.4	1656.7	11.69	452.1	
		III	114	132	99	655.4	593.8	10.37	439.9	
AMh	3,4	I	114	132	100	625.2	565.6	10.54	415.5	
		II	114	359	102	1914.6	1719.3	11.36	458.6	
		III	114	133	101	641.2	579.7	10.61	418.7	
AMc	1,2	I	114	133	99	665.3	595.1	11.80	443.2	
		II	114	360	99	1802.2	1610.5	11.90		443.6^*
		III	114	132	99	640.4	571.8	12.00	429.9	
AMc	3,4	I	114	134	98	711.2	633.6	12.25	475.1	
		II	114	360	99	1803.2	1607.1	12.20		443.8^*
		III	114	131	100	681.9	610.3	11.73	456.6	
AUh	1,2	I	114	133	101	649.2	586.5	10.69	423.9	
		II	114	359	100	1889.3	1687.7	11.95	461.6	
		III	114	132	101	693.3	620.8	11.68	456.2	
AUh	3,4	I	114	133	102	722.6	649.7	11.22	467.2	
		II	114	360	102	1954.1	1751.5	11.57	466.8	
		III	114	132	101	721.5	648.8	11.21	474.7	
ALh	1,2	I	114	131	92	638.6	574.6	11.14	464.8	
		II	114	359	95	1857.7	1663.1	11.70	477.8	
		III	114	134	99	787.9	704.1	11.90	521.0	
ALh	3,4	I	114	130	94	671.6	601.3	11.69	482.1	
		II	114	359	96	1816.6	1629.5	11.48	462.4	
		III	114	134	99	797.8	709.5	12.45	527.5	
BMh	1	I	114	132	100	768.4	694.5	10.64	510.6	
		II	114	360	100	1876.6	1682.1	11.56	457.3	
		III	114	133	100	735.7	663.1	10.95	485.2	
BMh	2	I	114	133	98	702.2	631.8	11.14	472.6	
		II	114	359	99	1882.2	1675.9	12.31	464.5	
		III	114	132	99	704.6	633.2	11.28	473.0	
BMh	3	I	114	133	99	717.2	641.9	11.73	477.8	
		II	114	359	99	1781.6	1598.9	11.43	439.7	
		III	114	132	99	623.4	564.3	10.47	418.5	
BMh	4	I	114	133	101	765.0	686.1	11.50	499.6	
		II	114	360	99	1883.8	1688.8	11.55	463.7	
		III	114	131	99	749.4	668.4	12.12	506.9	
CMh	1,2		114	178	100	1021.2	908.7	12.38	503.3	
CMh	3,4		114	178	99	944.9	842.3	12.18	470.4	
CUh	1,2		114	178	99	987.6	879.7	12.27	491.6	
CUh	3,4		114	178	101	1065.9	946.9	12.57	520.1	
CLh	1,2		114	178	99	980.4	871.9	12.44	488.0	
CLh	3,4		114	178	100	1029.4	916.8	12.28	507.3	
DMh	1		114	178	99	948.0	845.3	12.15	471.9	
DMh	2		114	178	99	945.6	841.9	12.32	470.7	
DMh	3		114	178	99	960.3	854.6	12.37	478.0	
DMh	4		114	178	100	986.8	879.1	12.25	486.3	
mean								11.73	468.8	443.7^*

* = lamination strength class LS15.

4 Results

Three different load levels are used to present and compare the test results:

Crack initiation shear force V_{c0}
Shear force at first crack development visually observable by the naked eye.

Crack shear force V_c
Shear force at the instant of crack development across the entire beam width.

Maximum shear force V_f
Shear force at instant of either a sudden crack propagation or a step-wise stable/unstable crack growth to the end of the beam.

The crack patterns for these load levels are illustrated in Figure 7 and some examples from the tests are given in Figures 8, 9 and 10 where dashed lines have been drawn under the cracks to emphasize their length and location.

The shear forces corresponding to the three definitions above are for all tests presented in Table 4 and Figures 11 and 12. The exact values of the presented shear forces were determined from visual observations during the testing with aid from the recorded beam deflection δ and the deformations d at the cracked corners of the hole. The crack initiation shear force V_{c0} is only given in the cases when there was a visually observable crack in the cross section before there was a crack spreading across the entire beam width at the given corner. The crack shear force V_c is given for both corner B and corner T for all tests. The length of the crack (in the beam length direction) at this level varies between the tests. For some tests, the crack was only one to a few centimeters in the length direction at this load level while other tests showed an instant crack propagation all the way to the end of the beam at this load level. The maximum shear force V_f is not given for test series BMh and DMh since the test setup for these test series is such that this load level is irrelevant. All forces refer to the shear force at hole center due to the externally applied load. The dead weights of the glulam beams are hence not taken into account. The dead weights of the steel beams used in test series BMh and DMh are however included in the presented loads.

The shear force V is plotted vs the beam deflection δ and the deformations d respectively in Figures 13 to 21 for all individual tests. The crack shear forces V_{cB} and V_{cT} for the individual tests are in these figures indicated in by dotted lines. The deformation d_B corresponds to the measurements from the LVDT sensors at corner B and d_T corresponds to measurements at corner T. Some plots lack deformations from one or more of the LVDT sensors at the corners of the holes due to technical problems. The beam deflections δ for test series CMh, CUh and CLh are presented as measured and is hence not compensated for the deflection in the steel beam (approximately 1 mm at $V = 30$ kN) used in the test setup.

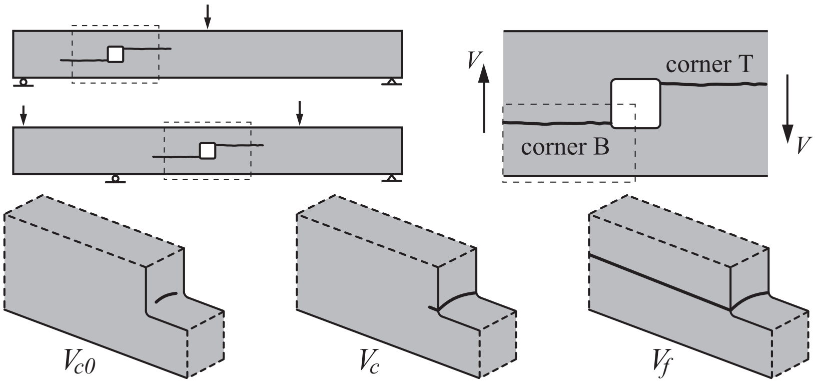
V
corner T
corner B
V
V_{c0}
V_c
V_f

Figure 7: *Illustration of crack patterns for defined load levels.*

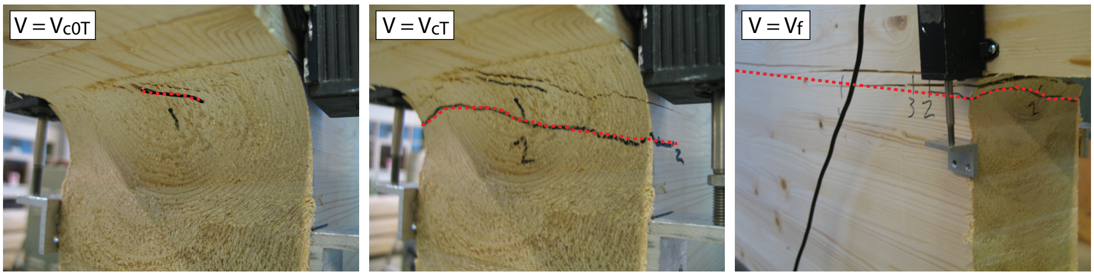
V = Vc0T
V = VcT
V = Vf

Figure 8: *Photos of crack patterns for corner T of ALh-4.*

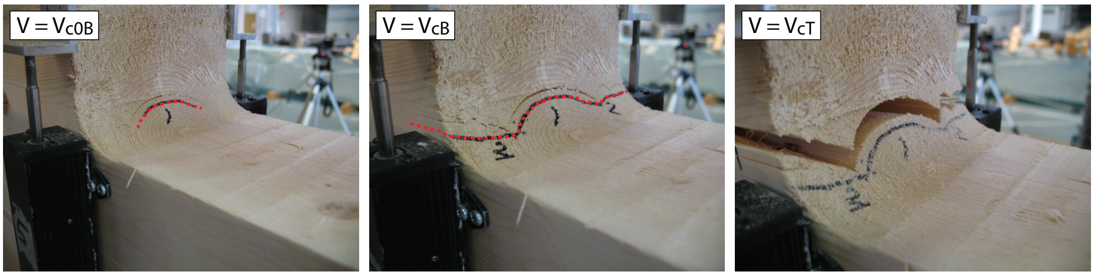
V = Vc0B
V = VcB
V = VcT

Figure 9: *Photos of crack patterns for corner B of BMh-4.*

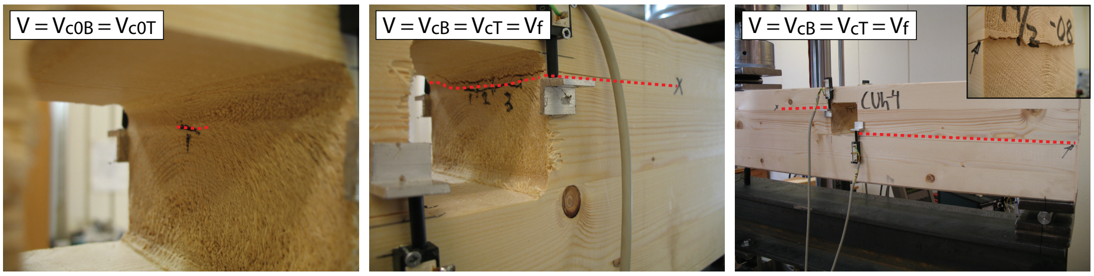
V = Vc0B = Vc0T
V = VcB = VcT = Vf
V = VcB = VcT = Vf
CUh4

Figure 10: *Photos of crack patterns for CUh-4.*

Table 4: *Shear forces V for all test series.*

		V_{c0} [kN]				V_c [kN]				V_f [kN]	
		V_{c0B}	V_{c0T}	min		V_{cB}	V_{cT}	min			
AMh	1					47.6	45.7	45.7		52.1	
	2	47.5	47.5	47.5		71.4	64.4	64.4		71.4	
	3		42.0	42.0		58.4	58.4	58.4		58.4	
	4					60.5	60.5	60.5		60.5	
	mean (std)			44.8	(3.9)			57.3	(8.1)	60.6	(8.0)
AMc	1	61.0		61.0		64.3	64.3	64.3		64.3	
	2	48.0	44.4	44.4		49.7	51.3	49.7		63.6	
	3	45.0	40.0	40.0		51.2	51.2	51.2		52.8	
	4					49.1	47.7	47.7		54.4	
	mean (std)			48.5	(11.1)			53.2	(7.5)	58.8	(6.0)
AUh	1		28.6	28.6		59.2	57.6	57.6		59.2	
	2					51.6	59.0	51.6		60.5	
	3		55.1	55.1		56.2	56.2	56.2		56.2	
	4	47.5	54.6	47.5		57.4	57.4	57.4		57.4	
	mean (std)			43.7	(13.6)			55.7	(2.8)	58.3	(1.9)
ALh	1	50.2	41.5	41.5		53.9	50.2	50.2		58.9	
	2		43.7	43.7		54.5	52.1	52.1		69.6	
	3		40.0	40.0		64.8	53.2	53.2		64.8	
	4		39.5	39.5		57.0	44.6	44.6		69.8	
	mean (std)			41.2	(1.9)			50.0	(3.8)	65.8	(5.1)
BMh	1		51.9	51.9		61.3	61.3	61.3		-	
	2	59.4	49.0	49.0		65.7	65.7	65.7		-	
	3	61.4	56.0	56.0		62.1	62.1	62.1		-	
	4	48.5		48.5		59.7	68.7	59.7		-	
	mean (std)			51.4	(3.4)			62.2	(2.5)		
CMh	1	20.6	20.6	20.6		27.3	27.3	27.3		27.3	
	2	24.1	23.3	23.3		24.9	24.9	24.9		29.5	
	3	23.1	17.9	17.9		24.4	23.1	23.1		25.3	
	4	24.4	24.4	24.4		27.0	27.0	27.0		27.0	
	mean (std)			21.6	(2.9)			25.6	(2.0)	27.3	(1.7)
CUh	1	24.0	18.8	18.8		25.3	25.3	25.3		25.3	
	2		19.0	19.0		23.2	22.5	22.5		25.3	
	3	20.5	20.5	20.5		23.3	23.3	23.3		23.3	
	4	16.7	16.7	16.7		22.3	22.3	22.3		22.3	
	mean (std)			18.8	(1.6)			23.4	(1.4)	23.6	(2.2)
CLh	1		17.5	17.5		23.1	22.3	22.3		26.9	
	2	19.2	19.2	19.2		23.7	23.7	23.7		29.5	
	3	21.8	23.4	21.8		24.3	24.3	24.3		25.5	
	4					21.8	21.8	21.8		24.5	
	mean (std)			19.5	(2.2)			23.0	(1.2)	26.6	(2.2)
DMh	1	26.0	26.0	26.0		29.1	29.1	29.1		-	
	2					25.3	25.3	25.3		-	
	3	23.3		23.3		25.3	25.3	25.3		-	
	4	25.4	22.6	22.6		26.7	28.1	26.7		-	
	mean (std)			24.0	(1.8)			26.6	(1.8)		

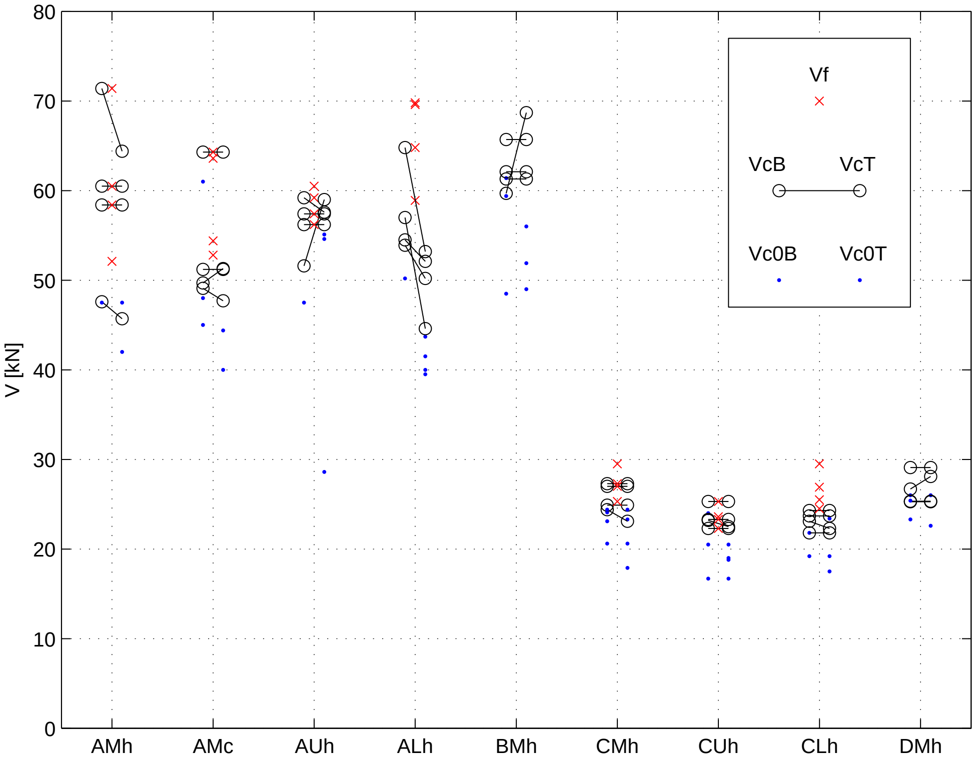

Figure 11: *Shear force V for all test series.*

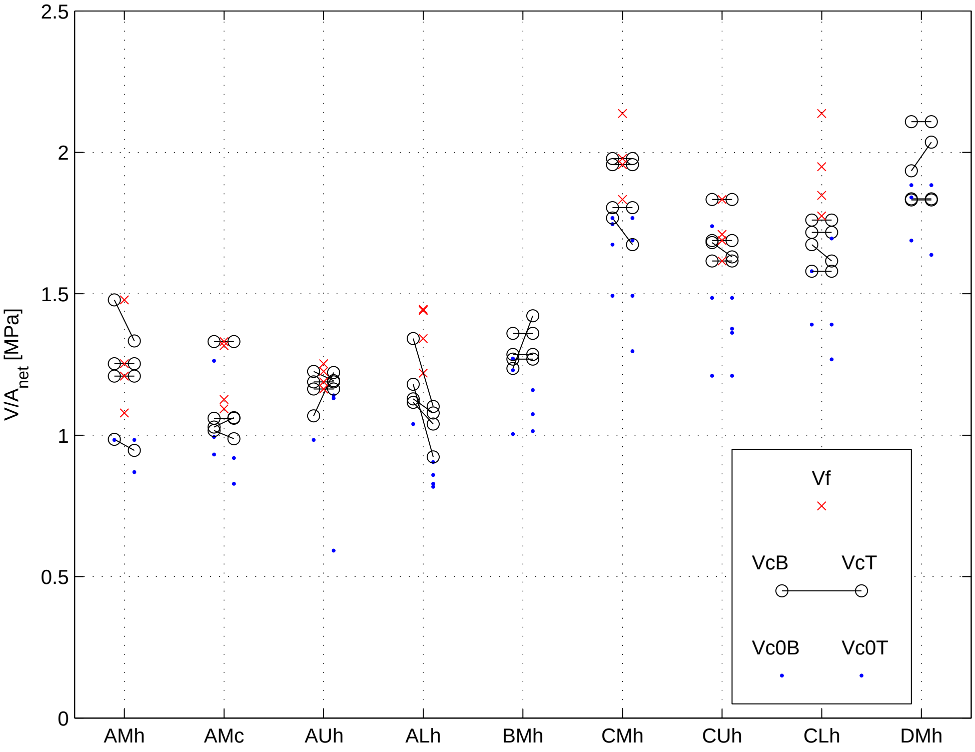

Figure 12: *Mean shear stress $\tau = V/A_{net} = V/((H-b)T)$ for all test series.*

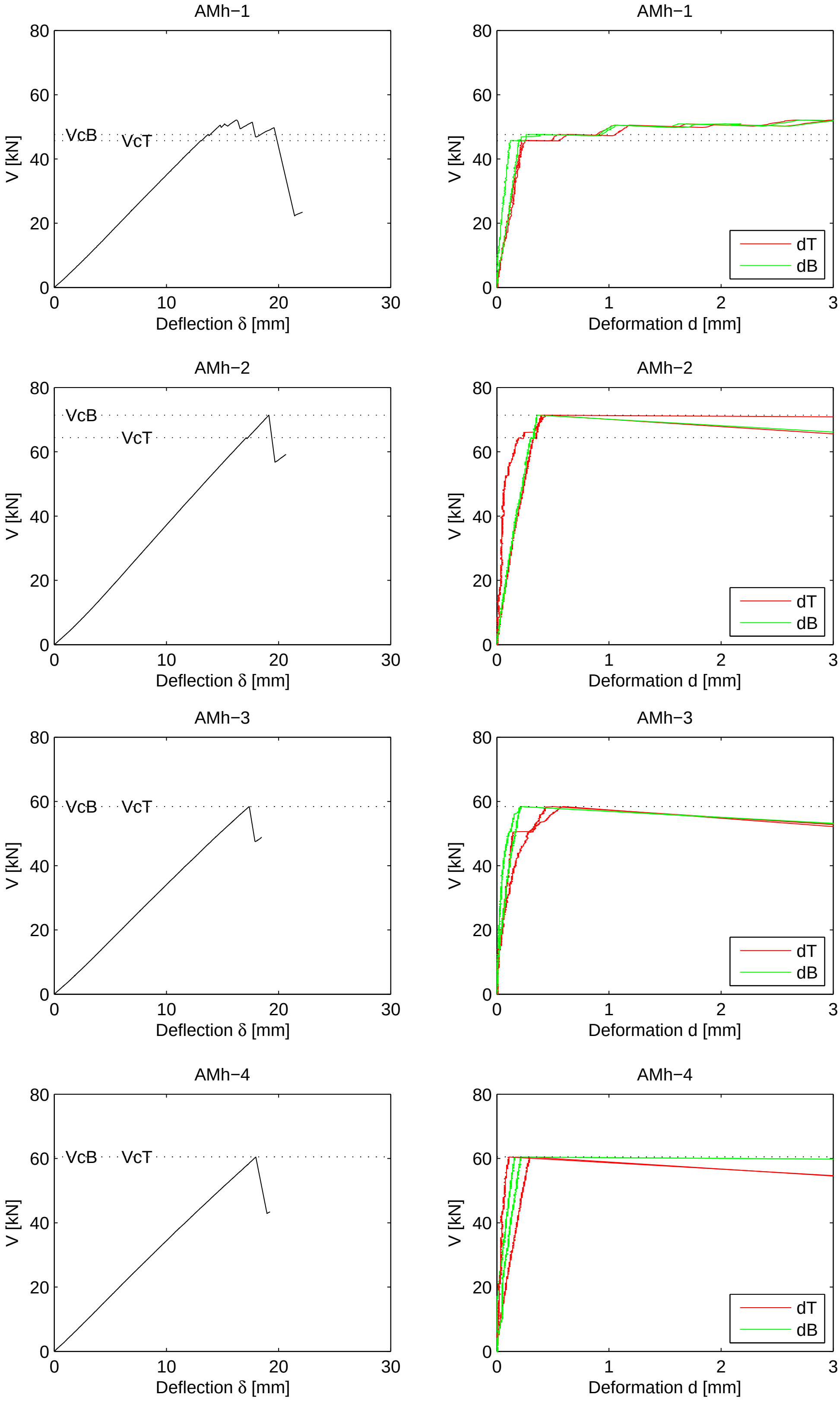

Figure 13: *Deflection δ and deformations d for test series AMh.*

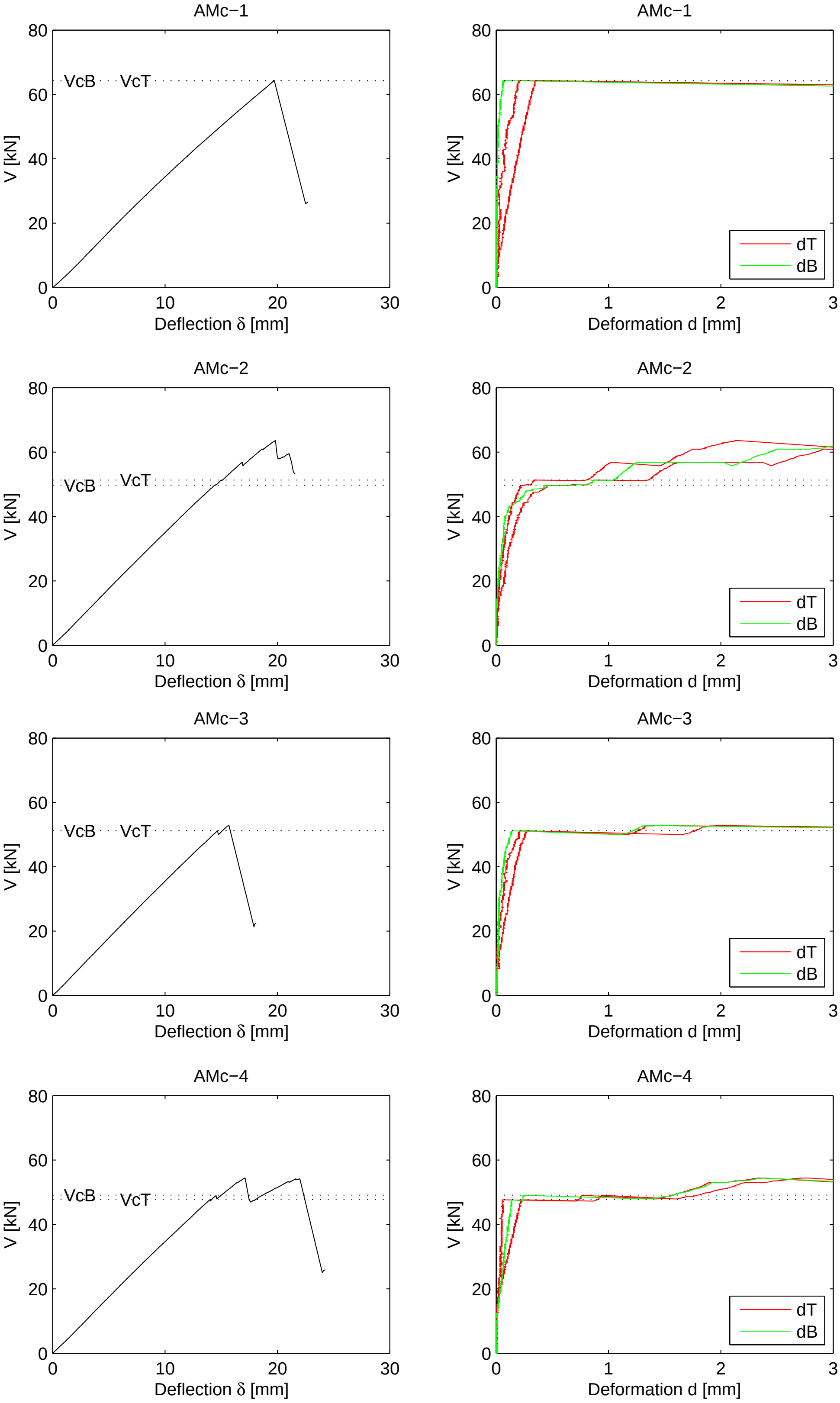

Figure 14: *Deflection* δ *and deformations* d *for test series AMc.*

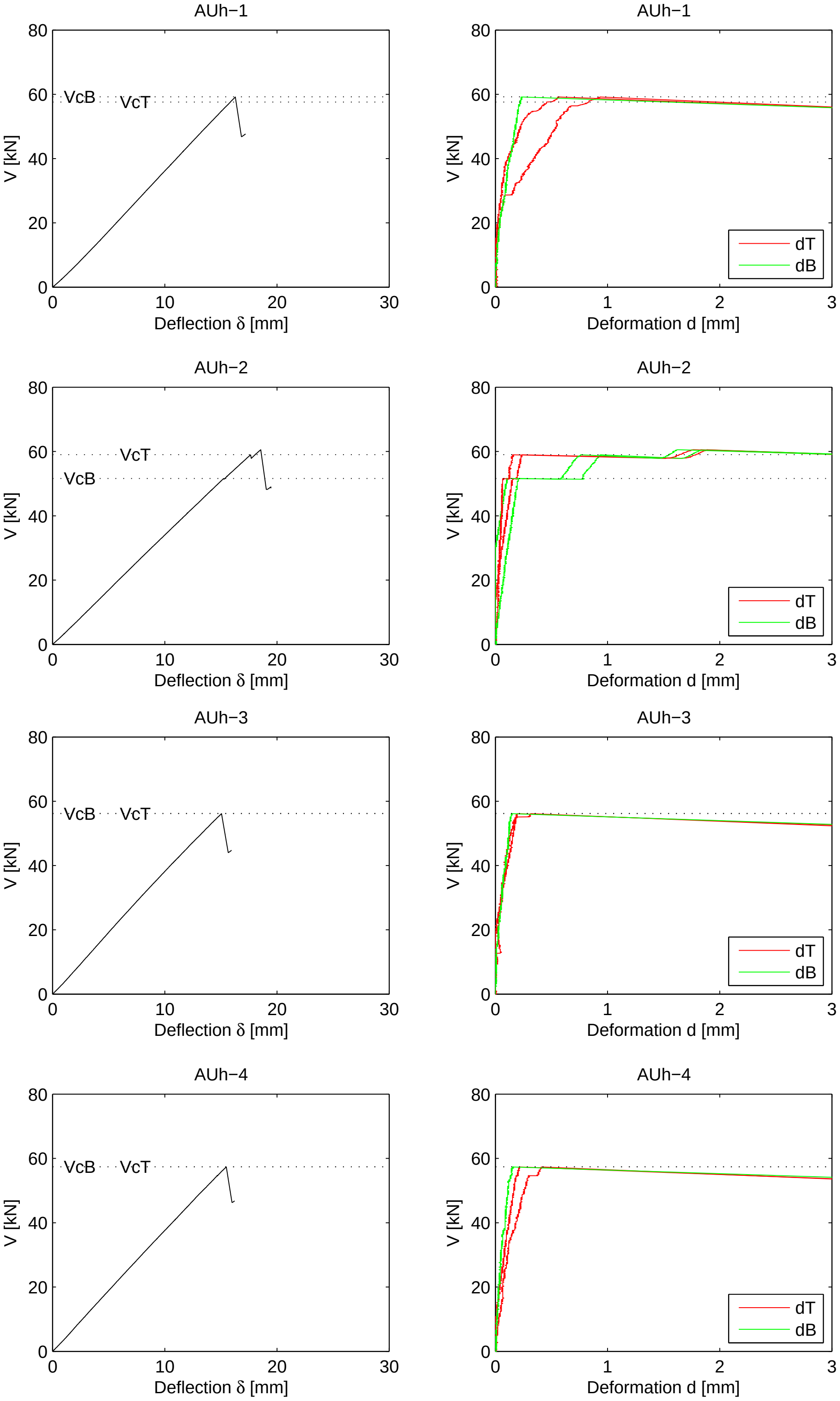

Figure 15: *Deflection δ and deformations d for test series AUh.*

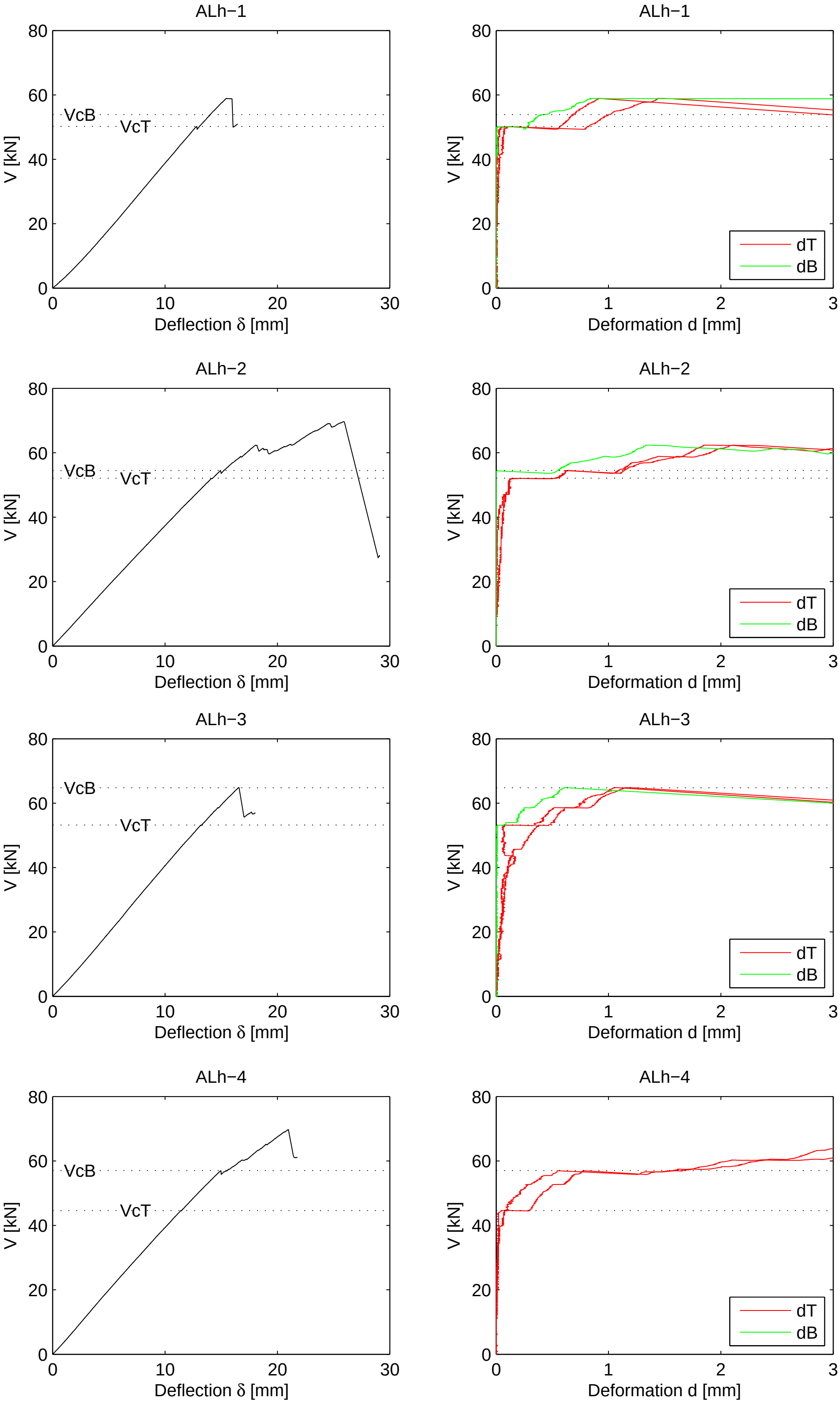

Figure 16: *Deflection δ and deformations d for test series ALh.*

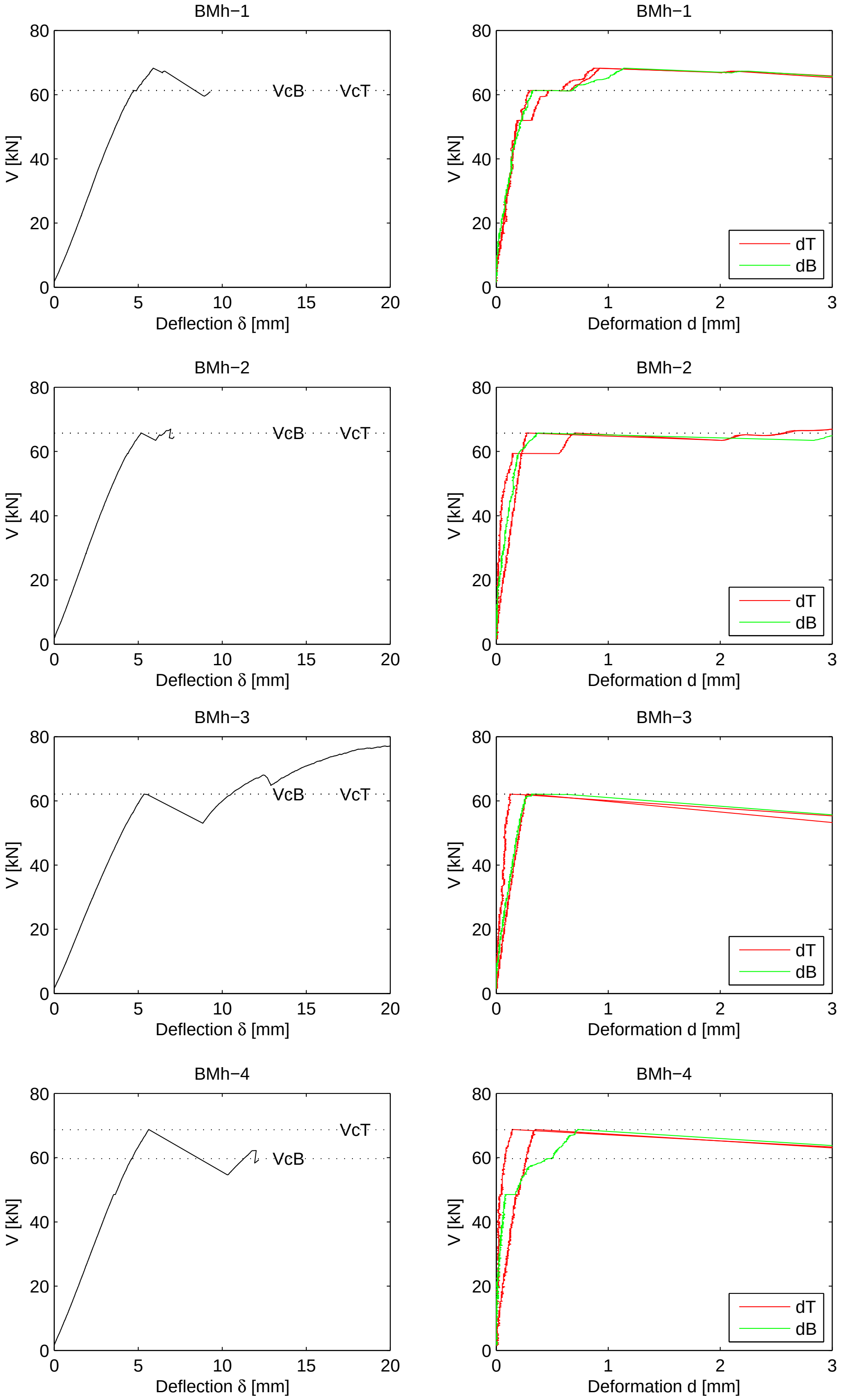
BMh−1

BMh−1

BMh−2

BMh−2

BMh−3

BMh−3

BMh−4

BMh−4

Figure 17: *Deflection δ and deformations d for test series BMh.*

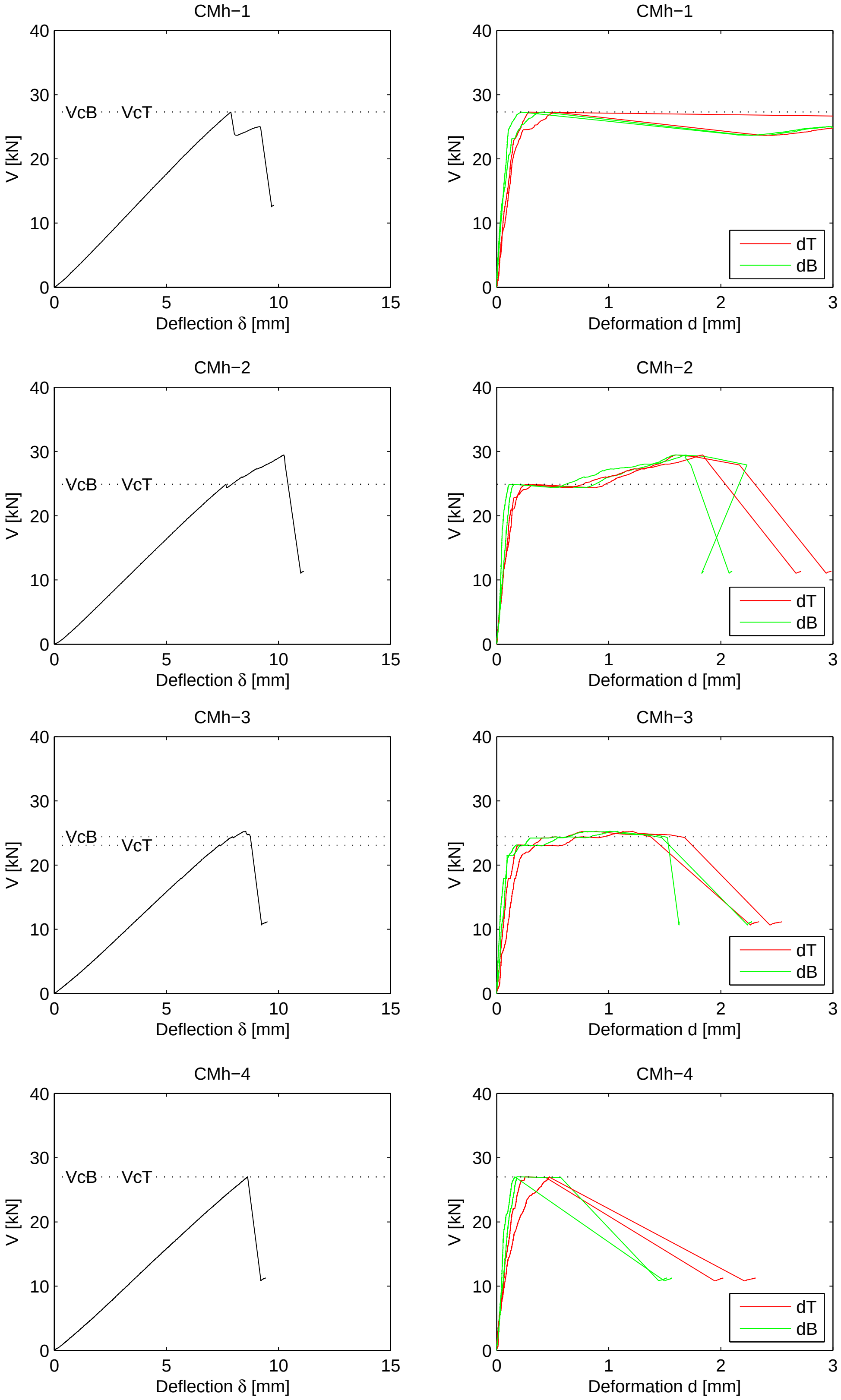

Figure 18: *Deflection δ and deformations d for test series CMh.*

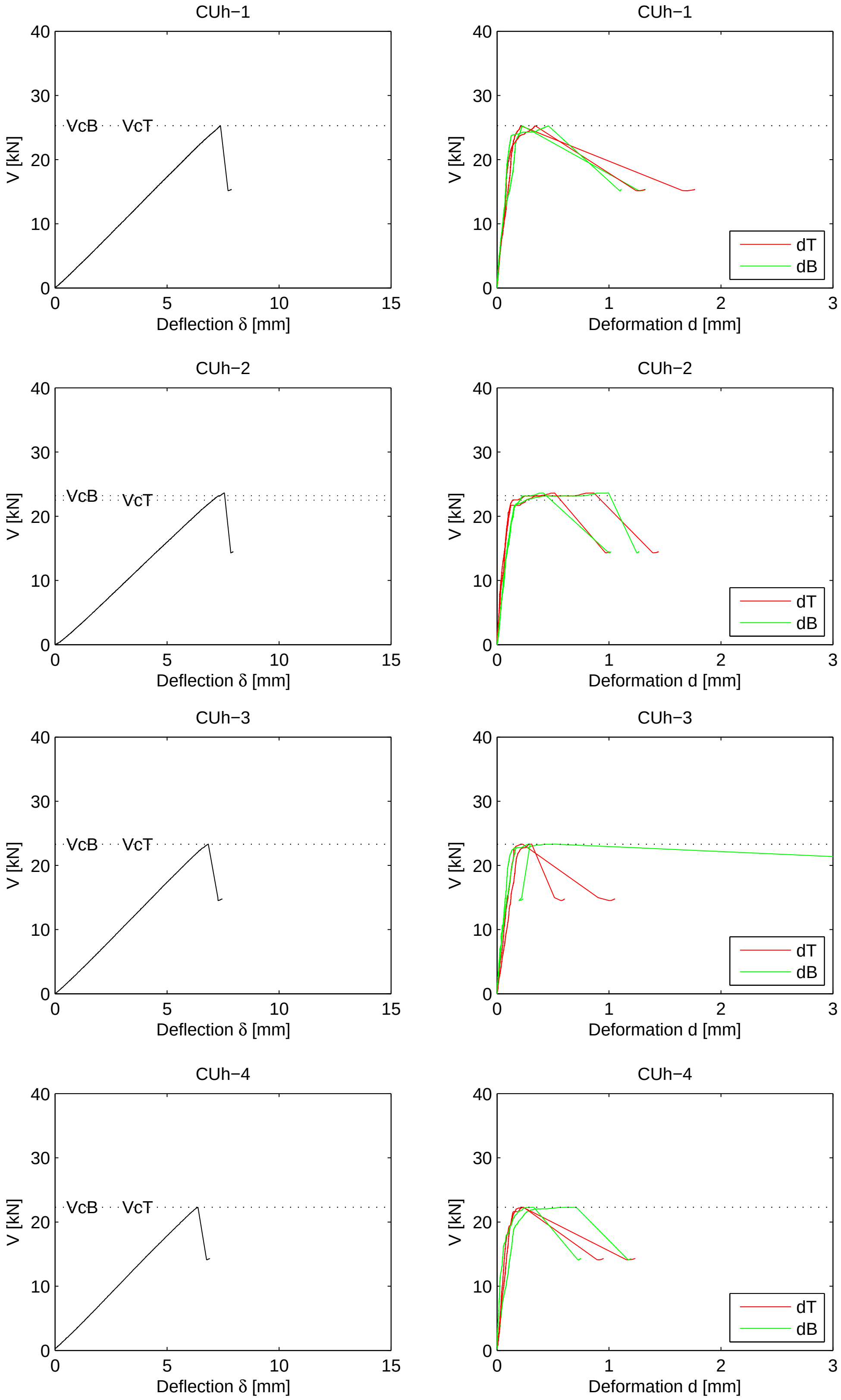

Figure 19: *Deflection δ and deformations d for test series CUh.*

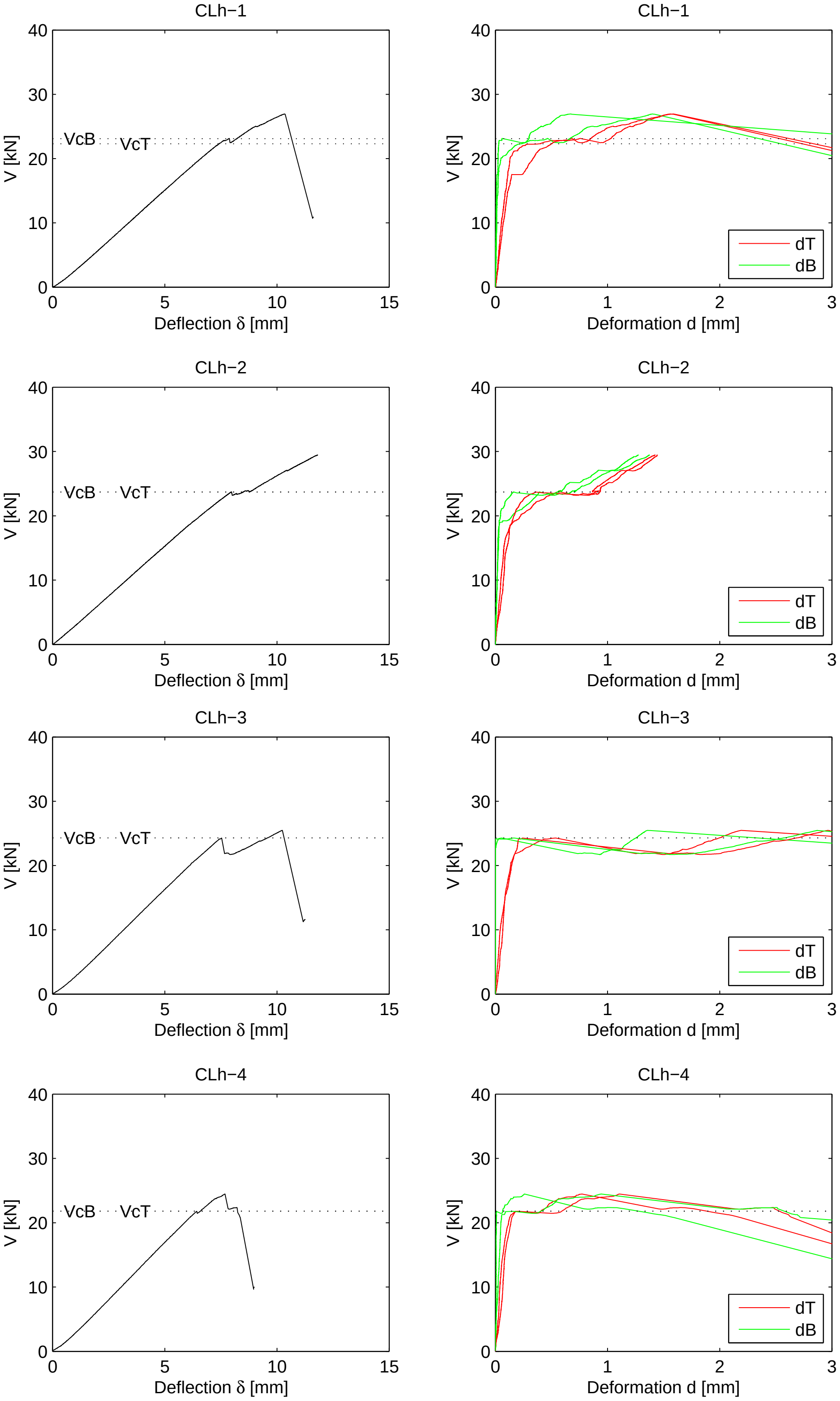

Figure 20: *Deflection δ and deformations d for test series CLh.*

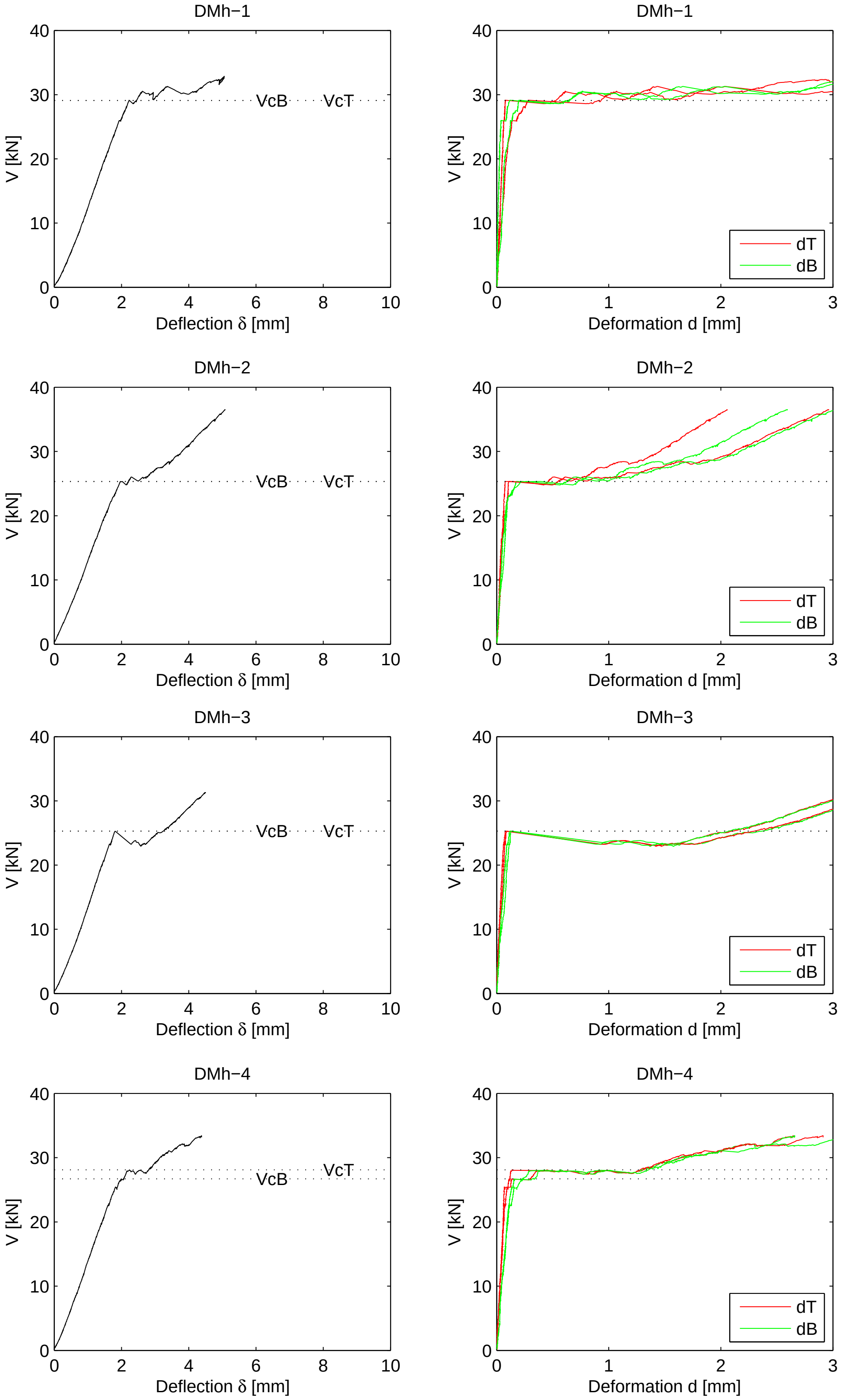

Figure 21: *Deflection δ and deformations d for test series DMh.*

5 Concluding remarks

Some comments on the test results concerning the influence of the four investigated design parameters are listed below.

Beam size

The test results indicate a strong beam size effect on the relative strength as can be seen in Figure 12. Increasing the beam size by a factor 3.5 gave about 30-35 % reduction in nominal shear stress V/A_{net} at the instant of crack development across the entire beam width.

Hole placement with respect to beam height

Slightly lower (approximately 5-15 % considering mean values) crack shear forces V_c were found for the beams with eccentrically placed holes compared to the beams with centrically placed holes. There is furthermore another interesting difference concerning the beams with eccentrically placed holes. Both among the large and the small beams the tests generally showed a more sudden crack propagation all the way to the end of beam for the beams with the hole placed in the upper part of the beam (test series AUh and CUh) compared to the beams with the hole placed in the lower part of the beam (test series ALh and CLh).

Material Strength Class

There was no significant difference in the behavior between the material strength class homogeneous beams of test series AMh and the strength class combined beams of test series AMc. The results of these two test series are however comparatively scattered.

Bending moment to shear force ratio

For beams with centrically placed holes, two different bending moment to shear force ratios were investigated. The beams with holes placed in a position of zero bending moment (test series BMh and DMh) shows on average slightly higher (approximately 5-10 % considering mean values) crack shear forces V_c compared to the beams with holes placed in a position of combined bending moment and shear force (test series AMh and CMh).

The scatter in the strength between nominally equal tests within a test series is not very large, the coefficient of variation of V_c being from 4 % to 14 % with an average of 8 %.

The test results furthermore show that it is more frequent with crack development across the entire beam width (V_c) at the upper corner T before the lower corner B than the other way around. The most frequent scenario is however that cracks develop simultaneously at both corners. The most common place for crack initiation (V_{c0}) is in the middle of the beam width although some tests showed a crack initiation all the way to one side of the beam width.

References

[1] Danielsson H.
The Strength of Glulam Beams with Holes – A Survey of Tests and Calculation Methods
Report TVSM-3068, Division of Structural Mechanics, LTH, Lund University, 2007.

[2] Boverket
(The National Board of Housing, Building and Planning)
Regelsamling för konstruktion – Boverkets konstruktionsregler BKR.
(Design Regulations)
Elanders Gotab, Vällingby, 2003.

[3] SP Sveriges Provnings- och Forskningsinstitut
(SP Swedish National Testing and Research Institute)
Lamination strength classes for glued laminated timber according to EN 1194.
PM, 2002-06-14.

[4] SS-EN 1194:1999
Träkonstruktioner – Limträ – Hållfasthetsklasser och bestämning av karakteristiska värden.
(Glued laminated timber – Strength classes and determination of characteristic values.)
SIS Förlag, Stockholm, 2000.

Paper B

Strength of glulam beams with holes – Tests of quadratic holes and literature test result compilation

Henrik Danielsson and Per Johan Gustafsson

CIB-W18/41-12-4, St Andrews, Canada, 2008

CIB-W18/41-12-4

**INTERNATIONAL COUNCIL FOR RESEARCH AND INNOVATION
IN BUILDING AND CONSTRUCTION**

WORKING COMMISSION W18 - TIMBER STRUCTURES

STRENGTH OF GLULAM BEAMS WITH HOLES – TESTS OF QUADRATIC HOLES AND LITERATURE TEST RESULT COMPILATION

H Danielsson
P J Gustafsson
Division of Structural Mechanics, Lund University

SWEDEN

MEETING FORTY ONE

ST. ANDREWS

CANADA

AUGUST 2008

Strength of Glulam Beams with Holes – Tests of Quadratic Holes and Literature Test Result Compilation

Henrik Danielsson and Per Johan Gustafsson

Division of Structural Mechanics, Lund University, Sweden

1 Background

Looking at design recommendations for glulam beams with holes in European timber engineering codes over the last decades, it can be seen that the strength design has been treated in many different ways. The theoretical backgrounds on which the recommendations are based shows fundamental differences and there are major discrepancies between the strength estimations according to the different codes as well as between tests and estimations according to codes [5]. The contemporary version of Eurocode 5 [7] does not state any equations concerning design of glulam beams with holes and the recommendations in the German code DIN 1052 [3] concerning rectangular holes were withdrawn during the fall of 2007. The absence of design recommendations indicates a need for further investigations of the subject. There are, however, several tests found in the literature concerning the strength of glulam beams with holes. Two of the most recent and more comprehensive studies were presented by Höfflin in 2005 [10] and by Aicher and Höfflin in 2006 [1]. These studies dealt exclusively with beams with circular holes. Although the test results found in literature all in all represent much work, important parameters such as mode of loading, beam size and hole placement have often been varied only within a very limit range. Among other limitations, it seems that all available test results relate to glulam beams with holes that are centrically placed with respect to the beam height [5].

2 Strength tests of glulam beams with quadratic holes

2.1 Test series and test setups

Experimental tests of the strength of glulam beams with quadratic holes have been carried out at the Division of Structural Mechanics at Lund University and they are in detail reported in [6]. The study comprised investigations of four design variables: *bending moment to shear force ratio at hole center*, *material strength class*, *beam size effect* and the previously overlooked design variable of *hole placement with respect to beam height*. Two different test setups were used to investigate the influence of bending moment to shear force ratio. Three different hole placements were used for one of the test setups to investigate the influence of hole placement with respect to beam height. The size effect was investigated for each combination of test setup and hole placement by using two test series with a scale factor of 3.5 for the length and height dimensions while the width was kept constant. All holes had rounded corners and a side length equal to 1/3 of the beam height. Altogether, the study consists of nine separate test series with four nominally equal tests in each series according to Table 1 and Figure 1.

Table 1: *Description of test series.*

Test series	Number of tests	Test setup	Hole placement	Strength class type	Beam size $T \times H$ [mm]	Hole size $a \times b$ [mm]	r [mm]
AMh	4	1	Middle	homogeneous	115 × 630	210 × 210	25
AMc	4	1	Middle	combined	115 × 630	210 × 210	25
AUh	4	1	Upper	homogeneous	115 × 630	210 × 210	25
ALh	4	1	Lower	homogeneous	115 × 630	210 × 210	25
BMh	4	2	Middle	homogeneous	115 × 630	210 × 210	25
CMh	4	1	Middle	homogeneous	115 × 180	60 × 60	7
CUh	4	1	Upper	homogeneous	115 × 180	60 × 60	7
CLh	4	1	Lower	homogeneous	115 × 180	60 × 60	7
DMh	4	2	Middle	homogeneous	115 × 180	60 × 60	7

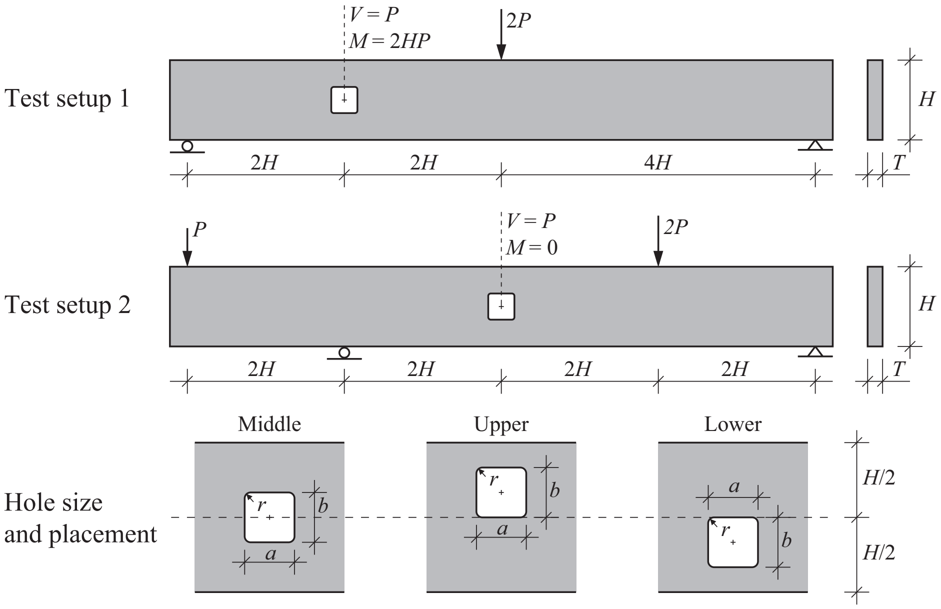

Figure 1: *Test setups and hole placements.*

2.2 Materials

The beams were all made of spruce (Lat. *Picea Abies*) and glued with melamine-urea-formaldehyde (MUF) resin. The lamella thickness was consistently 45 mm. All beams except the beams of test series AMc were of strength class homogeneous glulam. The strength class combined beams of test series AMc were composed of lamination strength class LS22 in the three outmost lamellae on each side and of lamination strength class LS15 in the remaining eight lamellae. The strength class homogeneous glulam beams were composed of lamination strength class LS22 throughout the entire beam height. The requirements on the two lamination strength classes are stated in [15] as: characteristic tensile strength, 14.5 and 22 MPa; mean tensile Young's modulus, 11 000 and 13 000 MPa and density (5^{th} percentile), 350 and 390 kg/m^3 for LS15 and LS22, respectively. The homogeneous beams correspond to the requirements in SS-EN 1194 [16] for glulam strength class GL 32h. The strength class combined beams correspond to the Swedish strength class L40. The mean value of the moisture content at the time of testing was measured to 11.7 % and the mean densities for the two different lamination strength classes was measured to 444 kg/m^3 and 469 kg/m^3 for LS15 and LS22, respectively.

2.3 Test Results

Three different load levels are used to present and compare the test results according to the definitions in Figure 2. The test results are presented in Figure 3 and in Table 2. The crack initiation shear force V_{c0} is only given in the cases when there was a visually observable crack in the cross section before there was a crack spreading across the entire beam width at the given corner. The crack shear force V_c is given for both corner B and corner T for all tests. The maximum shear force V_f is not given for test series BMh and DMh since the test setup for these test series is such that this load level is irrelevant.

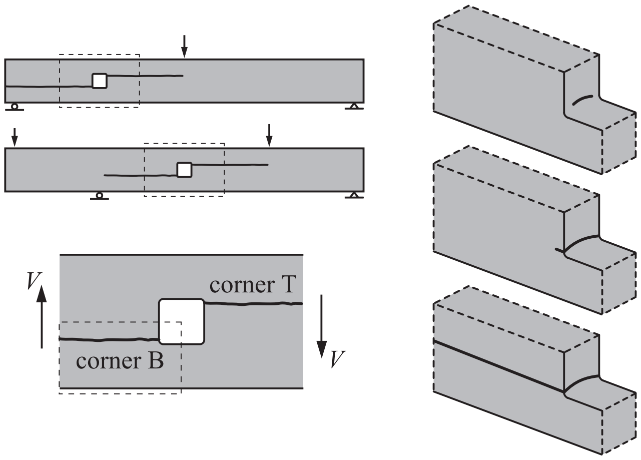

Crack initiation shear force V_{c0}
Shear force at first crack development visually observable by the naked eye.

Crack shear force V_c
Shear force at the instant of crack development across the entire beam width.

Maximum shear force V_f
Shear force at instant of either a sudden crack propagation or a step-wise stable/unstable crack growth to the end of the beam.

Figure 2: *Definitions and illustrations of load levels.*

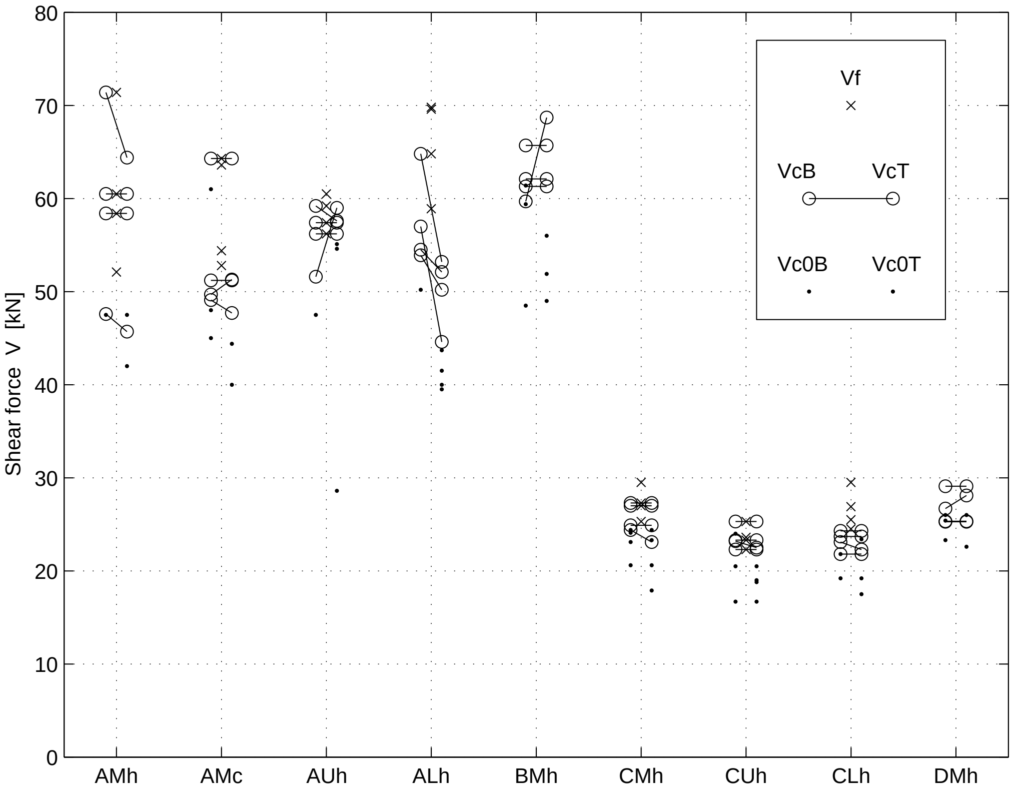

Figure 3: *Shear forces V for the three load levels and all tests in all nine test series.*

Table 2: *Beam cross section, hole size, hole placement, bending moment to shear force ratio and test results for the three defined load levels for all tests in all nine test series.*

Test series	$T \times H$	$a \times b$	r	hole placement	$\frac{M}{VH}$		V_{c0}			V_c			V_f
							V_{c0B}	V_{c0T}	min	V_{cB}	V_{cT}	min	
	[mm]	[mm]	[mm]		[-]		[kN]	[kN]	[kN]	[kN]	[kN]	[kN]	[kN]
AMh	115 × 630	210 × 210	25	middle	2.0	1				47.6	45.7	45.7	52.1
						2	47.5	47.5	47.5	71.4	64.4	64.4	71.4
						3		42.0	42.0	58.4	58.4	58.4	58.4
						4				60.5	60.5	60.5	60.5
						mean			44.8			57.3	60.6
						(std)			(3.9)			(8.1)	(8.0)
AMc	115 × 630	210 × 210	25	middle	2.0	1	61.0		61.0	64.3	64.3	64.3	64.3
						2	48.0	44.4	44.4	49.7	51.3	49.7	63.6
						3	45.0	40.0	40.0	51.2	51.2	51.2	52.8
						4				49.1	47.7	47.7	54.4
						mean			48.5			53.2	58.8
						(std)			(11.1)			(7.5)	(6.0)
AUh	115 × 630	210 × 210	25	upper	2.0	1		28.6	28.6	59.2	57.6	57.6	59.2
						2				51.6	59.0	51.6	60.5
						3		55.1	55.1	56.2	56.2	56.2	56.2
						4	47.5	54.6	47.5	57.4	57.4	57.4	57.4
						mean			43.7			55.7	58.3
						(std)			(13.6)			(2.8)	(1.9)
ALh	115 × 630	210 × 210	25	lower	2.0	1	50.2	41.5	41.5	53.9	50.2	50.2	58.9
						2		43.7	43.7	54.5	52.1	52.1	69.6
						3		40.0	40.0	64.8	53.2	53.2	64.8
						4		39.5	39.5	57.0	44.6	44.6	69.8
						mean			41.2			50.0	65.8
						(std)			(1.9)			(3.8)	(5.1)
BMh	115 × 630	210 × 210	25	middle	0.0	1		51.9	51.9	61.3	61.3	61.3	-
						2	59.4	49.0	49.0	65.7	65.7	65.7	-
						3	61.4	56.0	56.0	62.1	62.1	62.1	-
						4	48.5		48.5	59.7	68.7	59.7	-
						mean			51.4			62.2	
						(std)			(3.4)			(2.5)	
CMh	115 × 180	60 × 60	7	middle	2.0	1	20.6	20.6	20.6	27.3	27.3	27.3	27.3
						2	24.1	23.3	23.3	24.9	24.9	24.9	29.5
						3	23.1	17.9	17.9	24.4	23.1	23.1	25.3
						4	24.4	24.4	24.4	27.0	27.0	27.0	27.0
						mean			21.6			25.6	27.3
						(std)			(2.9)			(2.0)	(1.7)
CUh	115 × 180	60 × 60	7	upper	2.0	1	24.0	18.8	18.8	25.3	25.3	25.3	25.3
						2		19.0	19.0	23.2	22.5	22.5	25.3
						3	20.5	20.5	20.5	23.3	23.3	23.3	23.3
						4	16.7	16.7	16.7	22.3	22.3	22.3	22.3
						mean			18.8			23.4	23.6
						(std)			(1.6)			(1.4)	(2.2)
CLh	115 × 180	60 × 60	7	lower	2.0	1		17.5	17.5	23.1	22.3	22.3	26.9
						2	19.2	19.2	19.2	23.7	23.7	23.7	29.5
						3	21.8	23.4	21.8	24.3	24.3	24.3	25.5
						4				21.8	21.8	21.8	24.5
						mean			19.5			23.0	26.6
						(std)			(2.2)			(1.2)	(2.2)
DMh	115 × 180	60 × 60	7	middle	0.0	1	26.0	26.0	26.0	29.1	29.1	29.1	-
						2				25.3	25.3	25.3	-
						3	23.3		23.3	25.3	25.3	25.3	-
						4	25.4	22.6	22.6	26.7	28.1	26.7	-
						mean			24.0			26.6	
						(std)			(1.8)			(1.8)	

2.4 Comments concerning test results

The scatter in the strength between nominally equal tests within a test series is not very large, the coefficient of variation of $V_{c,min}$ being from 4 % to 14 % with an average of 8 %. The test results furthermore show that it was more frequent with crack development across the entire beam width at the upper corner T before the lower corner B than the other way around. The most frequent scenario was, however, that cracks developed simultaneously at both corners. The most common place for crack initiation was in the middle of the beam width although some tests showed a crack initiation all the way to one side of the beam width. Some further comments on the test results concerning the influence of the four investigated design parameters are listed below. When nothing else is stated, the crack shear force V_c refers to the minimum of V_{cB} and V_{cT}.

Bending moment to shear force ratio: For beams with centrically placed holes, two different bending moment to shear force ratios were investigated. The beams with holes placed in a position of zero bending moment (test series BMh and DMh) shows on average slightly higher (approximately 5-10 % considering mean values) crack shear forces V_c compared to the beams with holes placed in a position of combined bending moment and shear force (test series AMh and CMh).

Material Strength Class: There was no significant difference in the behavior between the material strength class homogeneous beams of test series AMh and the strength class combined beams of test series AMc. The results of these two test series are, however, comparatively scattered.

Beam size: The test results indicate a strong beam size effect on the strength. Increasing the beam size by a factor 3.5 gave about 30-35 % reduction in nominal shear stress V_c/A_{net}.

Hole placement with respect to beam height: Slightly lower (approximately 5-15 % considering mean values) crack shear forces V_c were found for the beams with eccentrically placed holes compared to the beams with centrically placed holes. There is furthermore another interesting difference concerning the beams with eccentrically placed holes. Both among the large and the small beams the tests generally showed a more sudden crack propagation all the way to the end of beam for the beams with the hole placed in the upper part of the beam (test series AUh and CUh) compared to the beams with the hole placed in the lower part of the beam (test series ALh and CLh).

3 Previous tests of glulam beams with holes

3.1 Compilation of test results in literature

A compilation of previously performed tests of glulam beams with holes from various sources is presented in Table 3. The tests are described concerning beam cross section, hole design, bending moment to shear force ratio, number of tests and results corresponding to the three load levels defined in Figure 2. All holes were centrically placed with respect to beam height. Load levels V_{c0} and V_c refers to the minimum of the values for the two corners, if values for both corners are given in the original source. A more comprehensive compilation including further details such as material strength class, moisture content, how well the definition of load levels correspond with the ones found in the original sources, etc. is found in [5].

Table 3: *Compilation of test results of glulam beams with holes.* n = *number of tests.*

Reference	$T \times H$ [mm]	$\square : a \times b$ $\bigcirc : \phi$ [mm]	r	$\frac{M}{VH}$ [-]	n [-]	V_{c0} mean [kN]	V_{c0} (std) [kN]	V_c mean [kN]	V_c (std) [kN]	V_f mean [kN]	V_f (std) [kN]
Bengtsson & Dahl [2]	90 × 500	300 × 150	0	1.20	2					39.0	(0.3)
	90 × 500	200 × 100	0	1.20	2					49.6	(1.1)
Kolb & Frech [12]	80 × 550	250 × 250	?	0.91	2					32.7	(2.1)
	80 × 550	250 × 150	?	0.91	2					44.0	(2.8)
	80 × 550	250 × 250	?	1.82	2					33.8	(1.1)
	80 × 550	250 × 150	?	1.82	2					35.4	(4.0)
Penttala [13]	90 × 500	200 × 200	?	1.60	1					33.8	
	90 × 500	400 × 200	?	1.60	1	25.0				31.3	
	90 × 500	600 × 200	?	1.60	1	20.8				30.0	
	115 × 800	400 × 200	?	1.25	1					69.1	
	115 × 800	200 × 200	?	1.25	1	52.5				84.4	
Johannesson [11]	90 × 500	250 × 250	25	1.30	2			26.8	(0.5)	28.5	(2.8)
	90 × 500	250 × 250	25	2.80	2			22.2	(2.3)	25.6	(0.6)
	140 × 400	600 × 200	25	2.25	1			30.0		37.0	
	88 × 495	125 × 125	25	2.53	4			40.4	(11.1)		
	88 × 495	375 × 125	25	2.53	4			37.7	(6.4)		
	88 × 495	370 × 370	25	2.53	4			9.1	(2.1)		
	88 × 495	735 × 245	25	2.53	4			12.8	(1.1)		
	88 × 495	1100 × 370	25	2.53	4			4.2	(0.3)		
Pizio [14]	120 × 400	180 × 180	0	1.05	2	24.1	(12.4)	30.6	(3.1)	63.7	(4.6)
	120 × 400	180 × 90	0	1.05	2	37.2	(15.4)	54.9	(3.4)	75.5	(1.6)
	120 × 400	180 × 10	0	1.05	2	92.5	(26.3)	103.3	(14.8)	103.3	(14.8)
	120 × 400	180 × 90	0	1.05	1	56.6		71.0		84.5	
	120 × 400	180 × 10	0	1.05	1	110.1		110.1		110.1	
	120 × 400	360 × 180	0	1.75	2	21.7	(2.3)	23.3	(0.0)	24.8	(2.1)
	120 × 400	10 × 180	0	1.75	1	34.0		34.0		34.0	
	120 × 400	360 × 180	0	1.75	1	19.2		21.1		28.8	
	120 × 400	10 × 180	0	1.75	2	30.0	(1.1)	33.8	(0.0)	33.8	(0.0)
	120 × 400	180 × 90	0	1.75	3	45.8	(11.2)	54.2	(7.0)	54.2	(0.7)
	120 × 400	180 × 180	0	1.05	2	20.6	(4.9)	26.8	(3.8)	70.0	(11.2)
Hallström [9]	90 × 315	400 × 150	25	2.78	5			11.9	(1.5)		
	90 × 315	400 × 150	0	2.78	5			12.2	(1.1)		
	90 × 315	400 × 150	25	2.78	5			12.2	(0.5)		
	90 × 315	400 × 150	25	?	1			12.2			
	165 × 585	600 × 295	25	?	4			27.1	(1.9)		
Bengtsson & Dahl [2]	90 × 500	ϕ250		1.20	2					38.4	(1.2)
	90 × 500	ϕ150		1.20	1					52.5	
Penttala [13]	90 × 500	ϕ255		1.20	1					33.8	
	90 × 500	ϕ250		2.10	1					31.6	
	90 × 500	ϕ150		1.20	1					51.3	
	115 × 800	ϕ400		1.03	1	57.1				65.9	
	115 × 800	ϕ300		2.00	1					89.5	
Johannesson [11]	90 × 500	ϕ250		1.30	2			29.6	(5.4)	36.5	(4.3)
	90 × 500	ϕ250		2.80	2			33.2	(2.6)	37.5	(3.5)
	90 × 500	ϕ250		0.60	2			33.8	(7.1)	41.7	(4.1)
	90 × 500	ϕ125		0.60	2			-		40.1	(0.1)
	88 × 495	ϕ125		2.53	4			51.9	(4.6)		
	88 × 495	ϕ396		2.53	4			16.1	(1.5)		
Hallström [9]	90 × 315	ϕ150		2.78	5			24.5	(3.5)		
Höfflin H1	120 × 900	ϕ180		1.50	5	69.2	(23.2)	106.4	(27.8)	128.1	(19.2)
[10] H2	120 × 900	ϕ270		1.50	6	65.3	(22.1)	96.4	(11.7)	108.7	(6.7)
H3	120 × 900	ϕ360		1.50	5	48.0	(8.4)	69.2	(9.0)	88.6	(15.6)
H4	120 × 900	ϕ270		5.00	5	43.1	(8.3)	55.1	(8.6)	84.2	(18.0)
H5	120 × 450	ϕ90		1.50	5	62.8	(15.6)	76.8	(13.8)	82.1	(7.6)
H6	120 × 450	ϕ135		1.50	6	38.8	(6.0)	65.5	(7.6)	67.9	(7.0)
H7	120 × 450	ϕ180		1.50	4	34.6	(7.4)	47.6	(8.5)	51.8	(5.9)
H8	120 × 450	ϕ135		5.00	5	34.7	(18.2)	58.0	(7.1)	63.4	(6.5)
Aicher & Höfflin A1	120 × 900	ϕ180		5.00	4	66.4	(21.5)	106.4	(15.0)	111.6	(13.1)
[1] A2	120 × 900	ϕ360		5.00	5	46.7	(15.3)	61.6	(15.0)	79.9	(3.2)
A3	120 × 450	ϕ180		5.00	6	42.4	(9.6)	48.8	(7.7)	53.7	(8.0)
	120 × 450*	ϕ180		5.00	3	15.4	(3.1)	37.9	(6.8)	44.8	(2.5)
	120 × 900*	ϕ360		5.00	3	33.5	(13.6)	49.6	(17.4)	66.6	(6.9)

* = curved beam, radius of curvature = $H/0.03$

3.2 Influence of bending moment to shear force ratio

Figure 4 illustrates the influence of the bending moment to shear force ratio on the strength. The results indicate a only a small influence of the bending moment on the crack shear force V_c. There is however one exception: The test series with $T \times H = 120 \times 900$ mm^2 and $\phi = 270$ mm shows a 43 % reduction in the crack shear force V_c for $M/(VH) = 5.0$ compared to $M/(VH) = 1.5$. It is worth pointing out that the mean value of the crack shear force is lower for the test series with $T \times H = 120 \times 900$ mm^2, $M/(VH) = 5.0$ and $\phi = 270$ mm than it is for the test series with equal cross section and bending moment to shear force ratio but with a larger hole, $\phi = 360$ mm, as can be seen in Figure 4 and in Table 3.

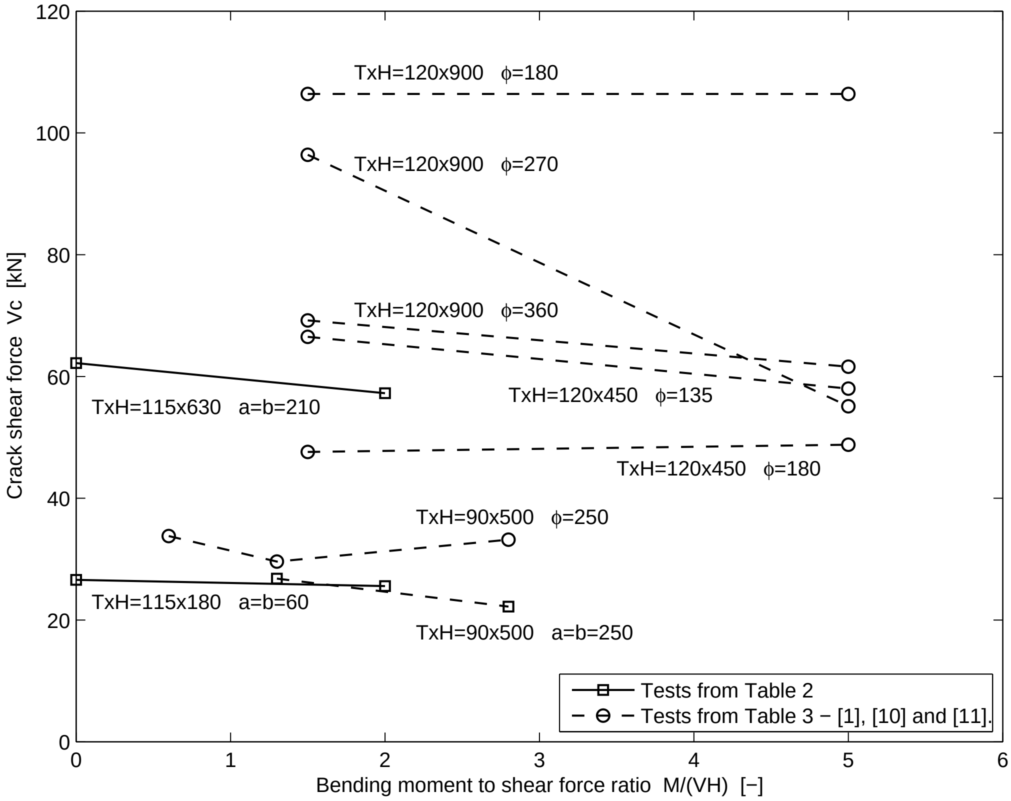

Figure 4: *Influence on strength of bending moment to shear force ratio for nominally equal tests concerning beam cross section, material strength class, hole size and hole placement.*

3.3 Influence of beam size

The present tests of glulam beams with quadratic holes indicated a strong beam size effect. Figure 5 shows the test series mean of the nominal shear stress V_c/A_{net} vs. beam height H for these tests and tests presented in [1] and [10]. Test results connected with lines represent test series which are equal concerning bending moment to shear force ratio, material strength class, beam width and hole size to beam height ratio but with different beam height H. The beam size effect can be expressed according to $V_c/A_{net} \sim H^{-m}$ where the parameter m describing the beam size effect can be determined from two test series of different size scale. The values of m are for the nine pair of test series given in Figure 5. It can be seen that the tests from [1] and [10] and relating to circular holes indicate a stronger beam size effect than the tests relating to quadratic holes presented in Section 2. The value of the parameter

$m = 1.07$ for test series with $M/(VH) = 5.0$ and $\phi = 0.3H$ is substantially higher than the value for the other eight pair of test series. This deviating result is due to the test series with $T \times H$ = 120×900 mm^2, $M/(VH)$ = 5.0 and ϕ = 270 mm. The result of that series gave also the deviating result with respect to influence of bending moment according to Figure 4 and showed lower strength than the corresponding beam with a larger hole, ϕ = 360 mm.

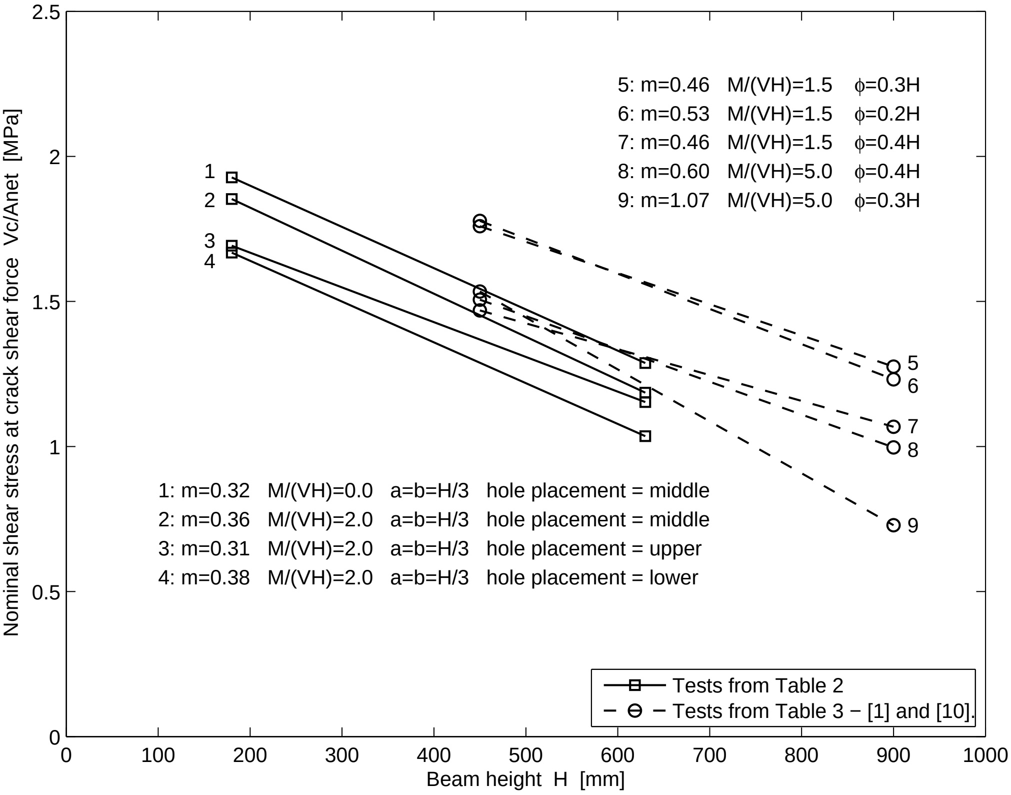

Figure 5: *Influence on strength of beam size (beam height, beam length and hole size uniformly scaled) for otherwise nominally equal tests.*

4 Comparison of design codes and test results

In order to make a simple evaluation of some of the proposed design recommendations, a comparison between test results and the shear force capacities according to codes is presented. The characteristic shear force capacities according to the following three methods are used in the comparison; (1) the empirically based method found in Swedish code of practise *Limträhandbok* [4], (2) The "end-notched beam analogy"-method found in a previous version of Eurocode 5 (prEN 1995-1-1 [8]) and also found in *Limträhandbok* and (3) the design method found in the German code DIN 1052 [3] (recently withdrawn for rectangular holes). The present results of beams with quadratic holes and test results of straight beams with circular holes presented in [1] and [10] are used in the comparison. The beams of test series AMc are considered to correspond to strength class GL 32c while the material strength class of all other beams is GL 32h. The following strength values (taken from SS-EN 1194 [16]) are used when determining characteristic capacities according to codes; $f_{v,k}$ = 3.8 MPa and $f_{t,90,k}$ = 0.5 MPa for GL 32h and $f_{v,k}$ = 3.2 MPa and $f_{t,90,k}$ = 0.45 MPa for GL 32c. Characteristic values for the beam test results $V_{i,k}$ and the coefficient of variation *cov* are determined according to Equations (1) and (2)

$$V_{i,k} = \bar{V}_i \cdot (1 - 1.645 \cdot cov) \tag{1}$$

$$cov = \sqrt{\frac{1}{n_{tot} - 1} \sum_{i=1}^{n_i} \sum_{j=1}^{n_j} \left(\frac{\bar{V}_i - V_{ij}}{\bar{V}_i} \right)^2} \tag{2}$$

where n_{tot} is the total number of individual tests, n_i is the number of test series, n_j is the number of individual tests within the test series, $\bar{V}_i$ is the mean value of the crack shear force V_c for test series i and V_{ij} is the individual value of the crack shear force V_c for test j in test series i. For the beams with quadratic holes, the minimum crack shear force $V_c = \min\,(V_{cB}, V_{cT})$ of the test results according to Table 2 and the overall coefficient of variation $cov = 7.55$ % based on these 36 test is used to determine the characteristic values $V_{i,k}$. For the beams with circular holes, the crack shear force V_c according to Table 3 and the overall coefficient of variation $cov = 15.3$ % based on these 56 tests is used to determine the characteristic values $V_{i,k}$. The comparison between tests and codes is presented in Table 4 and in Figure 6 for the quadratic holes and in Figure 7 for the circular holes. The test series notations for circular holes (H1-H8 and A1-A3) refer to notations in Table 3.

Comparing the characteristic values $V_{i,k}$ based on the test results and the characteristic strength values V_{code} according to codes, some observations are worth pointing out. *Limträhandbok* and DIN 1052 underestimates the capacity of all test series with quadratic holes. This underestimation is more severe for the test series with small beams since the beam size effect is not taken into account in any way in these two codes. The test results of beams with quadratic holes do however not indicate the strong size effect suggested by Eurocode 5. This code is on the unsafe side for all test series with quadratic and circular holes, but shows a fairly good ability to predict relative influence of the various parameters.

Table 4: *Test results and characteristic shear force capacities according to codes in kN.*

Test series	Test results		Characteristic shear force capacities V_{code} according to codes		
	mean	characteristic	*Limträhandbok*	Eurocode 5	DIN 1052
	$\bar{V}_i$	$V_{i,k}$	empirical method	prEN 1995-1-1	
AMh	57.3	50.1	36.6	60.1	41.8
AMc	53.2	46.6	30.8	50.6	37.6
AUh	55.7	48.8	36.6	53.3*	35.9*
ALh	50.0	43.8	36.6	53.3*	35.9*
BMh	62.2	54.5	36.6	60.1	50.2
CMh	25.6	22.4	10.5	32.1	11.9
CUh	23.4	20.5	10.5	28.5*	10.2*
CLh	23.0	20.2	10.5	28.5*	10.2*
DMh	26.6	23.3	10.5	32.1	14.3
H1	106.4	79.6	83.7	176.4	116.5
H2	96.4	72.2	66.4	134.7	88.2
H3	69.2	51.8	51.9	108.0	72.8
A1	106.4	79.6	83.7	176.4	78.1
H4	55.1	41.3	66.4	134.7	63.8
A2	61.6	46.1	51.9	108.0	54.9
H5	76.8	57.5	41.8	109.4	58.3
H6	65.5	49.0	33.2	95.8	44.1
H7	47.6	35.6	25.9	77.9	36.4
H8	58.0	43.4	33.2	95.8	31.9
A3	48.8	36.5	25.9	77.9	27.4

* = Hole placement with respect to beam height not according to regulations in code.

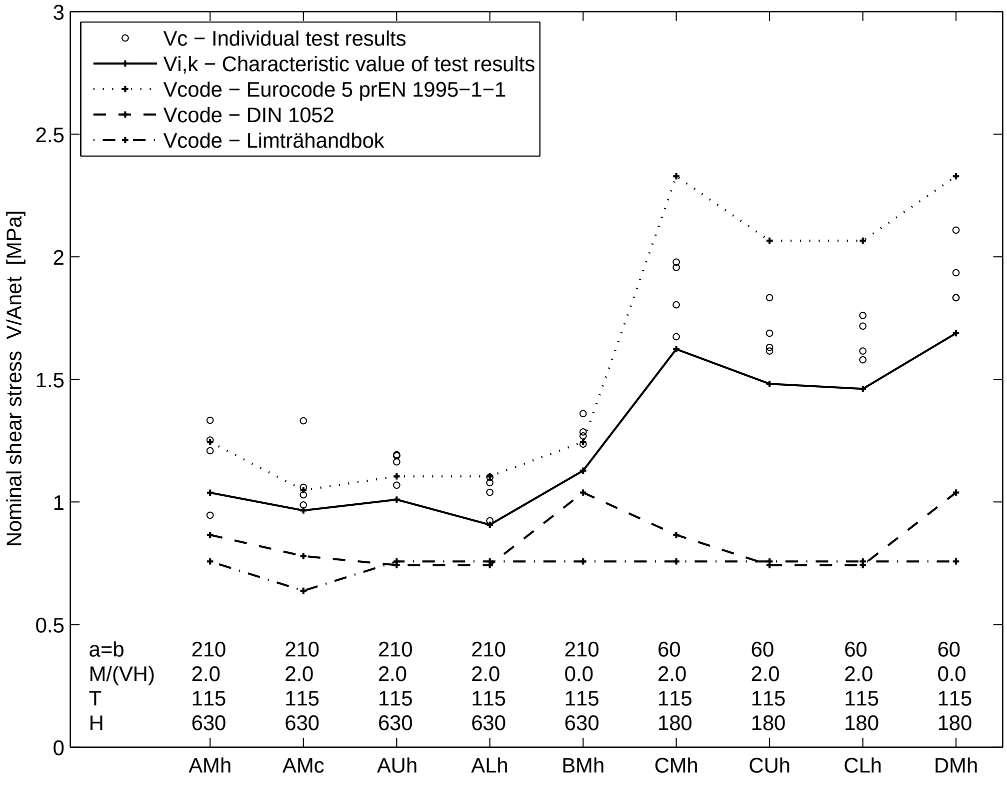

Figure 6: *Comparison of codes and test results for quadratic holes.*

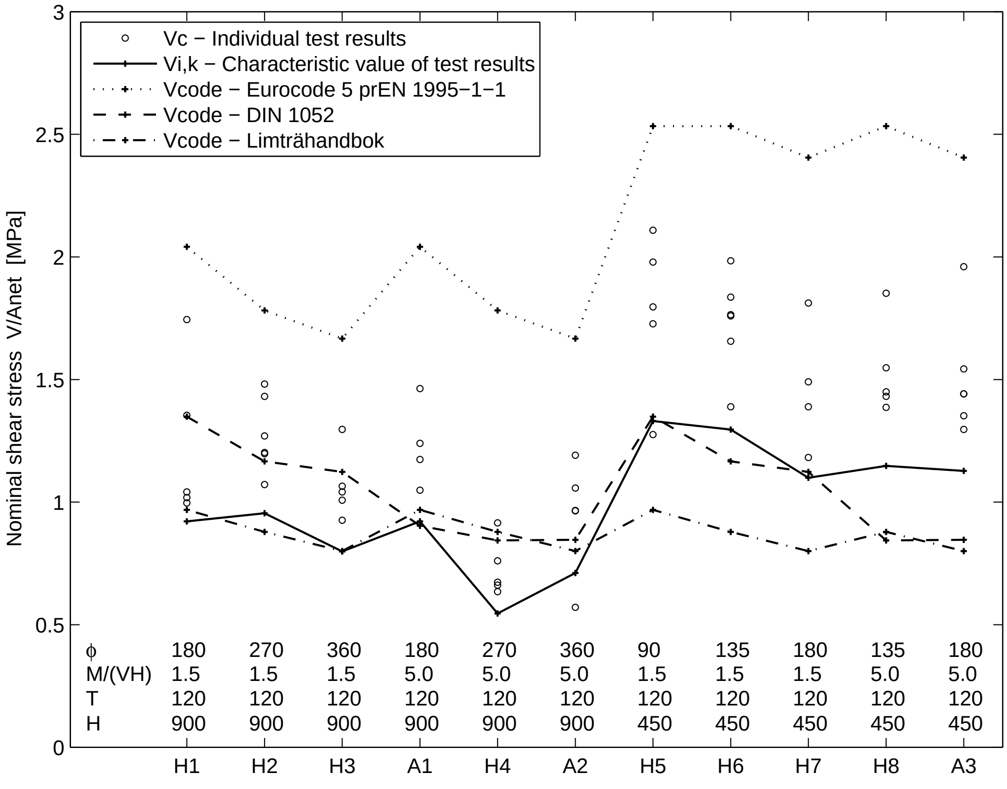

Figure 7: *Comparison of codes and test results for circular holes.*

References

[1] Aicher S., Höfflin L.
Tragfähigkeit und Bemessung von Brettschichtholzträgern mit runden Durchbrüchen – Sicherheitsrelevante Modifikationen der Bemessungsverfahren nach Eurocode 5 und DIN 1052
MPA Otto-Graf-Institute, University of Stuttgart, 2006.

[2] Bengtsson S., Dahl G.
Inverkan av hål nära upplag på hållfastheten hos limträbalkar
Master's Thesis, Byggnadsteknik II, Lund University, 1971.

[3] Blaß H.J., Ehlbeck J., Kreuzinger H., Steck G.
Erläuterungen zu DIN 1052:2004-08 – Entwurf, Berechnung und Bemessung von Holzbauwerken
2nd Edition including original text. DGfH innovations- und Service GmbH, München, 2005.

[4] Carling O.
Limträhandbok
Svenskt Limträ AB, Print & Media Center i Sundsvall AB, 2001.

[5] Danielsson H.
The Strength of Glulam Beams with Holes – A Survey of Tests and Calculation Methods
Report TVSM-3068, Division of Structural Mechanics, Lund University, 2007.
(available for download at: www.byggmek.lth.se/english/publications/)

[6] Danielsson H.
Strength Tests of Glulam Beams with Quadratic Holes – Test Report
Report TVSM-7153, Division of Structural Mechanics, Lund University, 2008.
(available for download at: www.byggmek.lth.se/english/publications/)

[7] *Eurocode 5: Design of timber structures - Part 1-1: General - Common rules and rules for buildings*
EN 1995-1-1:2004 (E).

[8] *Eurocode 5: Design of timber structures - Part 1-1: General Rules-General rules and rules for buildings*
prEN 1995-1-1: Final Draft 2002-10-09.

[9] Hallström S.
Glass fibre reinforcemed laminated timber beams with holes
Report 95-12, Department of Lightweight Structures, Royal Institute of Technology, Stockholm, 1995.

[10] Höfflin L.
Runde Durchbrüche in Brettschichtholzträger – Experimentelle und theoretische Untersuchungen
Dissertation, MPA Otto-Graf-Institute, University of Stuttgart, 2005.

[11] Johannesson B.
Design problems for glulam beams with holes
Dissertation, Div. of Steel and Timber structures, Chalmers University of Technology, Göteborg, 1983.

[12] Kolb H., Frech P.
Untersuchungen an durchbrochenen Bindern aus Brettschichtholz
Holz als Roh- und Werkstoff 35, p. 125-134, 1977.

[13] Penttala V.
Reiällinen liimapuupalkki
Publication 33, Division of Structural Engineering, Helsinki Univeristy of Technology, Otaniemi, 1980.

[14] Pizio S.
Die Anwendung der Bruchmechanik zur Bemessung von Holzbauteilen, untersucht am durchbrochen und am ausgeklinkten Träger
Publication 91:1, Dissertation, Baustatik und Stahlbau, ETH, Zürich, 1991.

[15] SP – Sveriges Provnings- och Forskningsinstitut
Lamination strength classes for glued laminated timber according to EN 1194
PM, 2002-06-14.

[16] SS-EN 1194:1999
Träkonstruktioner – Limträ – Hållfasthetsklasser och bestämning av karakteristiska värden
SIS Förlag, Stockholm, 2000.

Paper C

A probabilistic fracture mechanics method for strength analysis of glulam beams with holes

Henrik Danielsson and Per Johan Gustafsson

European Journal of Wood and Wood Products 69:407-419, 2011

Article excluded from this PDF version of the thesis due to copyright reasons.
Article available at http://dx.doi.org/10.1007/s00107-010-0475-1

Paper D

A three dimensional plasticity model for perpendicular to grain cohesive fracture in wood

Henrik Danielsson and Per Johan Gustafsson

Engineering Fracture Mechanics 98:137-152, 2013.

Article excluded from this PDF version of the thesis due to copyright reasons.
Article available at http://dx.doi.org/10.1016/j.engfracmech.2012.12.008

Paper E

Fracture analysis of glulam beams with a hole using a 3D cohesive zone model

Henrik Danielsson and Per Johan Gustafsson

submitted for publication

Manuscript submitted for publication

Fracture analysis of glulam beams with a hole using a 3D cohesive zone model

Henrik Danielsson · Per Johan Gustafsson

Abstract Introducing a hole in a glulam beam generally results in a significant decrease in load bearing capacity. For common structural sizes of beams and holes, global strength is most often limited by perpendicular to grain fracture with crack initiation at hole periphery and crack propagation in the grain direction. Strength analysis and design is however far from trivial, which is reflected by the lack of design criteria in contemporary timber engineering design codes. This paper presents nonlinear 3D FE-analyses of beams with a hole carried out with the purpose of investigating beam strength and fracture course as influenced by lamella growth ring pattern, beam width and presence of initial cracks. The analyses are performed using a cohesive zone model based on plasticity theory. The considered model is not suitable in a practical engineering design context but may be valuable as a research tool for understanding the influence of various parameters. As a verification of the model, results of numerical analyses are compared to experimental tests showing good agreement. Results of a parameter study relating to beam width and growth ring pattern are presented, showing decreasing nominal beam strength with increasing beam width and that the beam strength is affected by the growth ring pattern. Furthermore are analyses of the influence of different types of initial cracks presented.

Keywords Glulam · Hole · Fracture · Cohesive zone model · Wood · Orthotropy

H. Danielsson · PJ. Gustafsson
Division of Structural Mechanics, Lund University
P.O. Box 118, SE-221 00 Lund, Sweden
Tel.: +46-46-222 46 89
Fax: +46-46-222 44 20
E-mail: henrik.danielsson@construction.lth.se

1 Introduction

Wood is in many aspects a very appealing structural material. It does however possess some unique and complex properties, demanding careful considerations in design in order to utilize the material in a proper way and to its full potential. Among these properties are the strongly orthotropic strength and stiffness properties of great importance. Wood is comparatively weak when loaded in tension perpendicular to grain and in shear and the associated failure type, with cracking along grain, commonly has a brittle course. This type of loading is for timber structures a common cause of damage [21]. A beam with a hole is a typical example of a structural element for which the global strength commonly is limited by perpendicular to grain fracture, with crack initiation at hole periphery and crack propagation along the grain. In spite of the research effort within the area, a lack of knowledge is reflected by the absence of design criteria for beams with a hole in the current European timber engineering design code EN-1995-1-1:2004 [18].

Glulam beams with a hole are in practical design often reinforced, using either internal or external reinforcement. The use of reinforcement appears to be due to the significant strength reduction related to the introduction of a hole in combination with a lack of knowledge and the lack of code design criteria regarding the strength of unreinforced beams. Studies of unreinforced beams with a hole are hence motivated.

The strength of beams with a hole has in several studies been analyzed using 2D linear elastic fracture mechanics (LEFM) approaches by assuming a predefined crack of a certain length at a critical location, see e.g. [1], [2], [28], [29], [30] and [35]. Drawbacks of such approaches include the inherent dependence between crack propagation load and length of the assumed crack. LEFM can furthermore be expected to give accurate results only for large enough structural elements, where the fracture process zone is small compared to the length of the crack and other relevant dimensions.

Strength analysis of beams with a circular hole has also been performed using Weibull theory [4], assuming heterogeneous and stochastically distributed strength properties. A generalized LEFM approach (a mean stress method) is combined with an assumption of a stochastically distributed resistance to fracture based on Weibull theory in [13], yielding a probabilistic fracture mechanics method. Comparison to experimental tests of beams with quadratic or circular holes showed good agreement for fairly large beams while the strength of small beams was overestimated.

Cohesive zone models (CZM), originating from [6], [17] and [23], appear however better suited as base for applied strength and fracture analysis and have been widely used for analyses of wooden structural elements and joints, see e.g. [9], [16], [33], [34] and [38]. A 3D interface CZM is presented in [31] and applied to analysis of beams with a hole considering homogeneous orientation of the material principal directions in [32].

Strain softening models for perpendicular to grain tension and shear have also been derived within the framework of plasticity theory. A 2D plasticity model, based on the Tsai-Wu criterion and including strain softening in tension perpendicular to grain, is presented in [25]. This model is in [20] applied to analysis of beams with a hole, considering homogeneous material properties and accounting for the presence of knots in an approximate way.

In the above mentioned approaches and in timber engineering in general, homogeneous orientation of material principal directions is commonly assumed and the material is modeled as transversely isotropic or rectilinearly orthotropic. The stiffness in the plane perpendicular to grain may however vary considerably with direction of load relative to the annual growth rings, due to the very low rolling shear stiffness and the difference in stiffness between radial and tangential directions [22]. For softwood elements of common structural size with heterogeneous orientation of material principal directions, this may hence induce a very uneven stress distribution in the plane perpendicular to grain as is shown in e.g. [3] and [27].

This paper presents nonlinear 3D FE-analyses of glulam beams with a hole, with the purpose to investigate strength and fracture course as influenced by different parameters. The analyses were performed using a cohesive zone model based on plasticity theory [14], which allows for distinction concerning material properties between all three material principal directions. The analyses relate to short term static and monotonic loading of unreinforced glulam beams with a hole. The presented results relate to global strength and fracture course, including the two dimensional evolution of the fracture process zone during crack initiation and propagation. Influence of possible moisture induced stress is not considered. A verification of the material model is carried out by comparison to results of experimental tests. Parameter studies relating to influence of growth ring pattern, beam width and initial cracks are also presented. The considered analysis approach is not suitable in a practical engineering design context but is believed to be a suitable research tool for perpendicular to grain fracture analysis and identification of parameters important for strength design.

2 Material model and implementation

2.1 Cohesive zone model

The numerical analyses were performed using a cohesive zone model based on plasticity theory, briefly reviewed here and more thoroughly presented in [14].

A 3D macro scale continuum representation is used considering cylindrical orthotropy where distinction is made between the material longitudinal L, radial R and tangential T directions. The material is assumed to be homogeneous in the sense that knots and other possible stochastically distributed heterogeneities are disregarded. Small strain assumptions and additive decomposition of elastic and plastic strains are used. The cohesive zone model is applied to a predefined potential crack plane, within which a fracture process zone may initiate and evolve. This plane is assumed to be oriented as the global xz-plane and has a small height h in the out-of-plane direction, see Fig. 1. The global x-direction is further assumed to coincide with the material longitudinal direction. The wood bulk material is modeled as a linearly elastic orthotropic material.

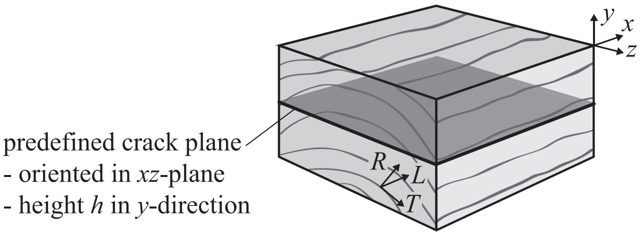

Fig. 1 Orientation of predefined crack plane

The Tsai-Wu criterion [36] is often proposed as a suitable failure criterion for wood since it includes orthotropic strength properties and allows for different tensile and compressive strengths. It is here used as criterion for initiation of yielding, i.e. the formation of a fracture process zone and initiation of softening. An initial yield function F is hence defined according to

$$F(\boldsymbol{\sigma}) = \boldsymbol{\sigma}^T\mathbf{q} + \boldsymbol{\sigma}^T\mathbf{P}\boldsymbol{\sigma} - 1 \tag{1}$$

where $\boldsymbol{\sigma}$ is the stress and where $\mathbf{q}$ and $\mathbf{P}$ are given by the material strengths properties. The post softening initiation performance is assumed to be governed by the three out-of-fracture plane stress and plastic deformation components. As softening has initiated, the yield function is changed accordingly and the updated yield function f is then defined as

$$f(\boldsymbol{\sigma}, K) = \sigma_{yy}^2 F_{yyyy} + \tau_{xy}^2 F_{xyxy} + \tau_{yz}^2 F_{yzyz} - K \tag{2}$$

where F_{yyyy}, F_{xyxy} and F_{yzyz} are fictitious material strength parameters determined from the stress state at initiation of softening and where K is a softening parameter. An associated plastic flow rule is adopted. Since the updated yield function f only depends on the three out-of-fracture plane stress components, plastic strains are obtained only in these three directions corresponding to the fracture mechanics modes of deformation I, II and III. The softening parameter K is a function of an internal variable denoted the effective plastic deformation δ_{eff} and the following softening function is adopted here

$$K = \begin{cases} \exp(\ln(c)\delta_{eff}^m) & \text{for } \delta_{eff} \leq 1 \\ 0 & \delta_{eff} > 1 \end{cases} \tag{3}$$

where m is a model parameter determining the shape of the softening curve and where c should be a small, but nonzero, number. The evolution law for the internal variable is defined as

$$\dot{\delta}_{eff} = \sqrt{\left(\frac{\dot{\delta}_{yy}}{A_{yy}}\right)^2 + \left(\frac{\dot{\delta}_{xy}}{A_{xy}}\right)^2 + \left(\frac{\dot{\delta}_{yz}}{A_{yz}}\right)^2} \tag{4}$$

where the incremental plastic deformations $\dot{\delta}_{yy} = h\dot{\varepsilon}_{yy}^p$, $\dot{\delta}_{xy} = h\dot{\gamma}_{xy}^p$ and $\dot{\delta}_{yz} = h\dot{\gamma}_{yz}^p$ by assuming constant strains over the small out-of-plane height h of the predefined potential crack plane. A_{yy}, A_{xy} and A_{yz} are scaling parameters of dimension length, defined such that the work required for complete separation in any of the three modes of deformation equals the corresponding fracture energy. Normalized stress vs. plastic deformation relationships for uniaxial loading are presented in Fig. 2 for $c = 10^{-2}$ and $m = 1.0$, 1.5 and 2.0, where G_f and f_t refer to fracture energy and material strength respectively and δ refers to the plastic deformation.

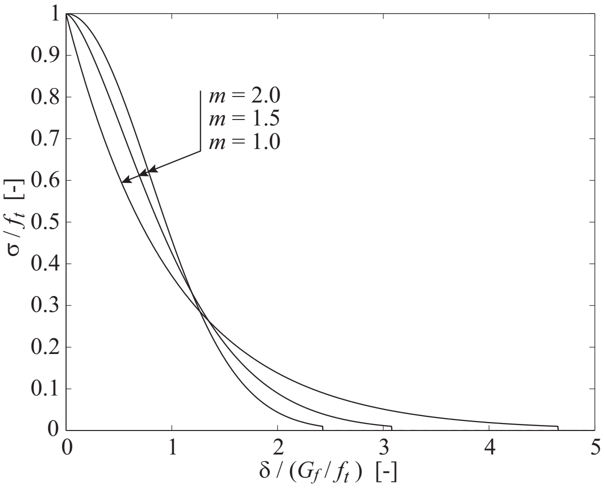

Fig. 2 Normalized stress vs. deformation relationships

2.2 Numerical implementation

The material model is implemented for FE-analysis in Matlab [26], using supplementary routines from the toolbox Calfem [5]. The highly nonlinear global response, often including snap-back, is solved in an incremental-iterative fashion using an arc-length type of path following method, see e.g. [10]. The constraint equation used to determine the increments in displacement and in load is based on an energy dissipation approach presented in [37]. 8-node isoparametric elements with trilinear displacement interpolation and numerical integration are used, with 1 and 8 integration points for the elements within the predefined crack plane and within the linear elastic bulk material respectively. Further information regarding the numerical implementation is given in [14] and [15].

3 Verification of material model

3.1 Experimental tests of glulam beams with a hole

A verification of the material model is carried out by means of comparison to experimental tests of glulam beams with a hole, presented in [11] and [12]. Beam geometry, boundary conditions and loads are presented in Fig. 3 for the test series considered here. Three different hole placements with respect to beam height were tested; centrically placed holes and holes placed in the upper or lower part of the beam respectively. The beam width was consistently $B = 115$ mm while beams of height $H = 630$ mm and $H = 180$ mm were tested for all three hole placements. The holes had a quadratic shape with a side length of $H/3$ and rounded corners with a curvature such that $H/r \approx 25$ where r denotes

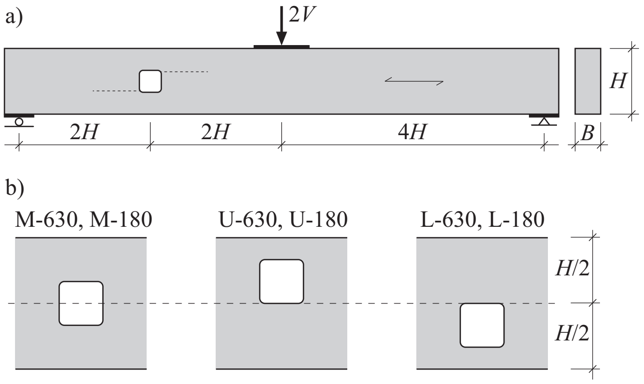

Fig. 3 Experimental test setup (a) and hole placements and test series notation (b)

the hole corner radius. Four nominally equal tests were carried out within each test series.

The beams were produced from Norway spruce (Lat. *Picea Abies*) and were of quality complying to strength class GL 32h according to [19]. The mean density and the mean moisture content at the time of testing were measured to 471 kg/m^3 and 11.7% respectively. The lamellas had a cross section of 115 × 45 mm^2 and were in general cut from a part of the log close to the pith, with location of the pith close to the centre of one of the long sides of the lamella cross section. There were no visible cracks near the holes prior to testing.

Cracks developed at two diagonal hole corners during testing, as indicated in Fig. 3. The beam strength V_c of the experimental tests is defined as the maximum value of the shear force at the instant of, or prior to, crack development across the entire beam width. Since cracks appeared at two corners of the hole, two values of V_c were obtained for each individual test. These values may coincide, meaning that cracks developed simultaneously at both corners, or they may differ. The considered load level V_c was not necessarily associated with onset of unstable crack propagation and global maximum load.

3.2 Finite element mesh and material properties

3D FE-analyses were carried out with geometry and load according to the six test series presented in Fig. 3. Predefined potential crack planes were modeled at the hole corners where cracks appeared in the tests. The exact positions of the crack planes were determined by the location of the maximum Tsai-Wu effective stress $\sigma_{TW} = \boldsymbol{\sigma}^T\mathbf{q} + \boldsymbol{\sigma}^T\mathbf{P}\boldsymbol{\sigma}$, see Eq. (1), along the edge of the hole based on 2D plane stress analysis for the respective beam geometries. In order to reduce model size and calculation cost, the crack planes were not modeled along the complete beam length but were instead only given a length sufficient to enable analysis of crack initiation and beginning of crack propagation. Analyses were performed for the following three cases:

- softening behavior within crack plane CT only
- softening behavior within crack plane CB only
- softening behavior within crack planes CT and CB

with definitions of crack planes CT and CB in Fig. 4. The lamellas were assigned heterogeneous orientation of material directions LRT according to a cylindrical growth ring pattern with the location of pith at the center of the lower boundary of each lamella, i.e. with $(y'_p, z'_p) = (0{,}0)$ according to Fig. 4. This lamella growth ring pattern was believed to resemble the ones of the lamellas of the experimental tests with reasonable accuracy. For the actual tests, the orientation of the lamellas with respect to the direction of load were however random, meaning that location of piths at $(y'_p, z'_p) = (45{,}0)$ would resemble the tests in an equally accurate way. Symmetry was assumed in the beam length direction, although the geometry is not perfectly symmetric due to the hole. Symmetry was also assumed in the beam width direction when the considered growth ring pattern allowed this simplification. Typical FE-meshes are presented in Fig. 5. The meshes consisted of approximately 18-22 000 elements and 65-80 000 degrees of freedom. Each crack plane was modeled by 7 elements in the beam width direction and a minimum of 60 elements in the beam length direction. The thickness h of the predefined crack planes was about $0.0008H$, which based on previous analyses should be sufficiently small to yield results which are independent of h [14].

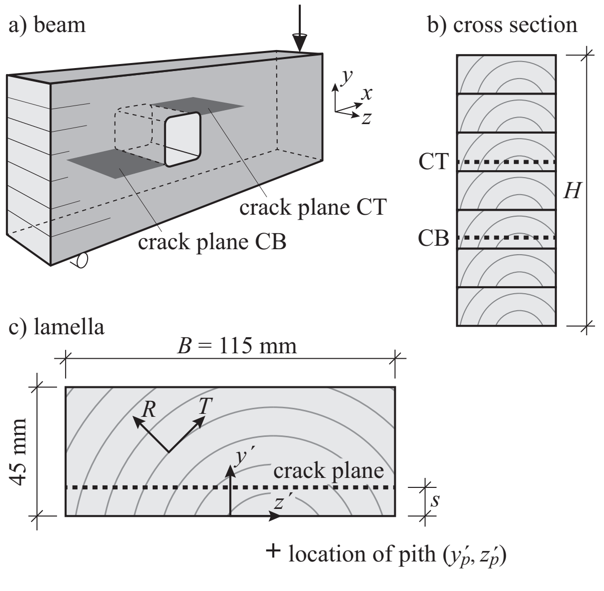

Fig. 4 Definition of crack planes CT and CB in relation to the beam (a), the cross section (b) and a lamella (c)

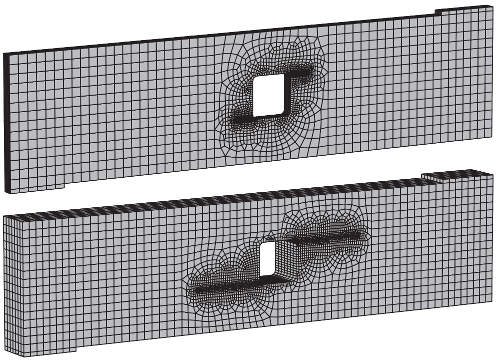

Fig. 5 Typical FE-meshes for beam height $H = 630$ mm (top) and 180 mm (bottom)

Material parameters according to Table 1 were used, which should comply fairly well with mean values found in the literature for Norway spruce grown in Scandinavia, see e.g. [7], [8], [24], [35] and [38]. Fracture energies are assumed to be independent of the direction of deformation with respect to the RT-directions, as suggested by test results in [8] and [24]. The model parameters defining the softening function were set to $m = 1.5$ and $c = 10^{-2}$ corresponding to a curved shape as illustrated in Fig. 2 and roughly as suggested by mode I test results presented in [8], [35] and [38]. With the current set of parameters, creation of traction-free crack surfaces do for mode I loading in the R- or T-direction correspond to a plastic deformation $\delta_{yy} = 0.31$ mm. Steel plates at supports and loads were modeled as linear elastic isotropic with $E = 210$ GPa and $\nu = 0.3$.

3.3 Comparison of experimental and numerical results

A comparison between FE-analyses and tests regarding load vs. deflection and beam strength is presented in Fig. 6 for test series L-630, with a hole placed in the lower (tension) part of the beam and with $H = 630$ mm. The applied load is expressed as nominal shear stress V/A_{net}, where V and $A_{net} = 2HB/3$ refer to the shear force and net cross section area at hole center respectively. The four curves to the left, which are offset for the sake of clarity, represent the four individual experimental tests. Load levels V_{cB} and V_{cT}, corresponding to crack development across the entire beam width at corner CB and CT respectively, are marked with circles. The two curves to the right are based on FE-analyses considering softening behavior within crack plane CB and CT separately. Illustrations of the extensions of fracture process zones are presented in Fig. 7 for points along the load vs. deflection path defined in Fig. 6. For crack plane CB, crack initiation is followed by stable crack propagation at increasing load. For crack plane CT, showing sharp snap-back behavior at a load lower than the crack load for CB, the fracture process zone is far from fully developed at the local maximum load.

Analysis considering simultaneous softening within both crack planes was also performed, showing a very similar response as when considering softening within crack plane CT only. The maximum loads differ only 0.3% between the two analyses and the extensions of the fracture process zones and the stress distributions within the crack planes are almost identical considering equal external load. Also comparing the analyses with double crack planes and the analysis with softening within crack plane CB only, the fracture process zone extensions and stress distributions are also almost identical considering equal external load. Numerical problems were however encountered shortly after passing maximum load when considering softening within both crack planes simultaneously, see further comments below and in Section 5.

For numerical analyses of test series M-630 and U-630, qualitatively similar results as presented above are obtained including numerical problems after reaching a local maximum load when considering softening behavior within the two crack planes simultaneously. The load vs. deflection responses further showed sharp snap-backs for these geometries when considering softening within crack plane CT only and also when considering softening within crack plane CB only.

Table 1 Material parameters used for FE-analysis.

Stiffness			
Modulus of elasticity	E_L	12000	MPa
	E_R	800	MPa
	E_T	500	MPa
Modulus of shear	G_{LR}	700	MPa
	G_{LT}	700	MPa
	G_{RT}	50	MPa
Poisson's ratio	ν_{RL}	0.02	-
	ν_{TL}	0.02	-
	ν_{TR}	0.30	-
Strength			
Tensile strength	f_{Lt}	40	MPa
	f_{Rt}	3.0	MPa
	f_{Tt}	3.0	MPa
Compressive strength	f_{Lc}	40	MPa
	f_{Rc}	4.0	MPa
	f_{Tc}	4.0	MPa
Shear strength	f_{LR}	6.0	MPa
	f_{LT}	6.0	MPa
	f_{RT}	3.0	MPa
Fracture energy			
	$G_{f,yy}$	300	J/m^2
	$G_{f,xy}$	900	J/m^2
	$G_{f,yz}$	900	J/m^2

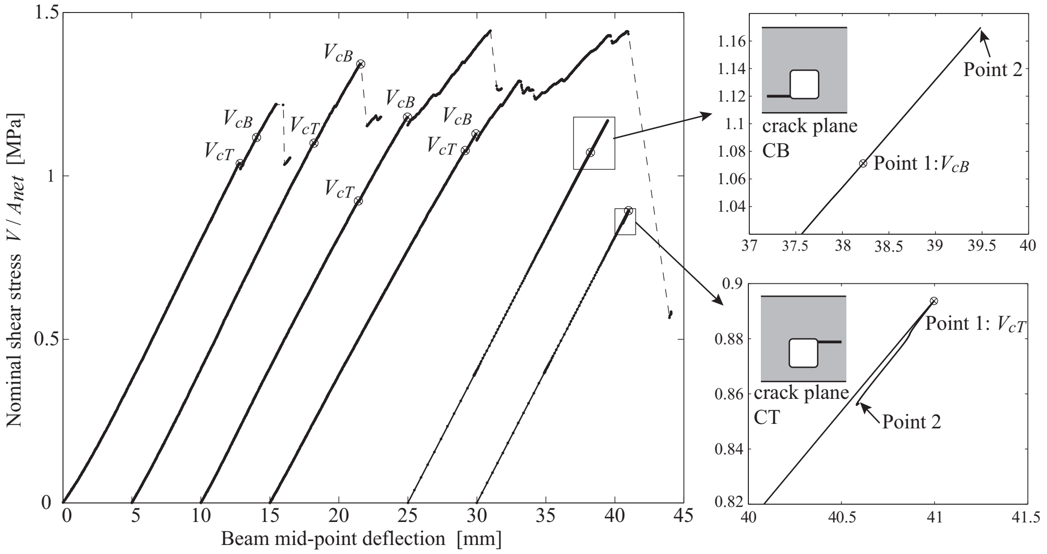

Fig. 6 Experimental [11] and numerical load vs. deflection responses for test series L-630

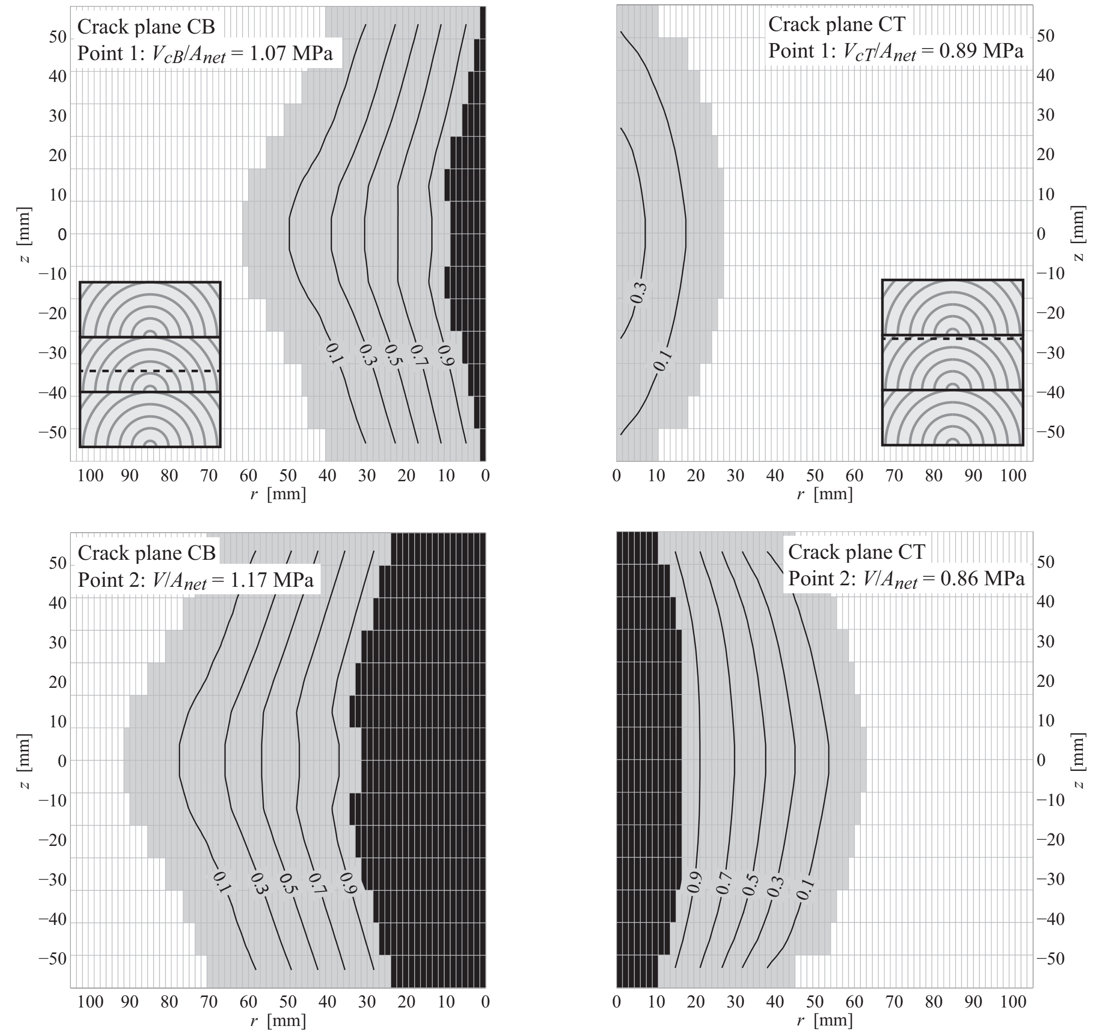

Fig. 7 Extensions of fracture process zones for different load levels for test series L-630: Grey elements represent softening region, black elements represent traction-free crack, iso-lines represent the effective deformation δ_{eff} and r denotes a local coordinate with $r = 0$ at start of crack plane at hole edge

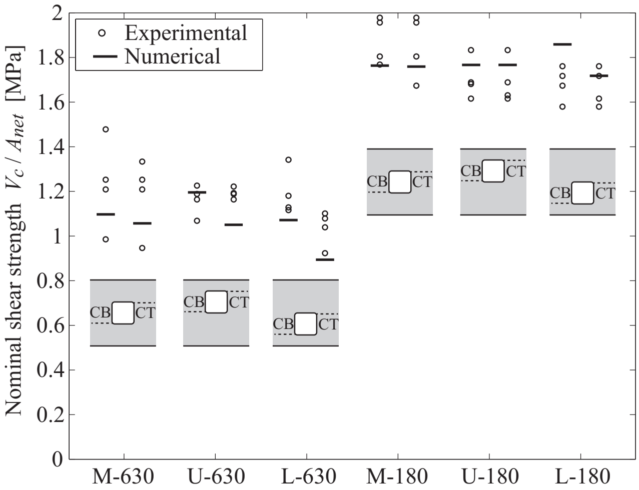

Fig. 8 Test [11] and FE-results for beam strength with respect to cracking at bottom corner (CB) and top corner (CT)

For numerical analyses of test series with $H = 180$ mm, snap-back behavior was only found for test series U-180 while test series M-180 and L-180 showed increasing load also after the instant of crack propagation across the entire beam width. The fracture behavior of the small beams do however, in contrast the large beams, differ much between analyses with softening within a single crack plane only and simultaneous softening within both crack planes. The softening processes in the respective crack planes are hence mutually influenced by one another for the small beams but not for the large beams. No numerical problems were encountered when analyzing the beams with $H = 180$ mm.

A graphical comparison regarding beam strength found by tests and FE-analyses are presented in Fig. 8. The beam strength is for the numerical analyses defined in the same way as for the tests; as the maximum shear force at the instant of, or prior to, crack development such that a traction-free crack spreads across the entire beam width. The presented results are for beams with $H = 630$ mm based on separate analyses of softening at crack planes CB or CT respectively while for beams with $H = 180$ mm results are based on analyses considering softening within both crack planes simultaneously.

4 Parameter study

The tests and FE-analyses presented above relate to variation of two parameters relevant in design; beam height and hole placement with respect to beam height. In this section, parameter studies are presented relating to the influence of beam width, growth ring pattern and initial cracks. Geometry and loading is according to test series M-630, see Fig. 3, with exception of the varied parameters. Softening is considered within crack plane CT only, since such an analysis seems to yield values of V_{cT} equal or lower than the values of V_{cB} found from analysis when considering softening within crack plane CB only. The results relating to test series M-630, U-630 and L-630 further indicate that the values of V_{cT} differ only insignificantly when considering softening within both potential crack planes simultaneously.

4.1 Influence of growth ring pattern and beam width

The influence of beam width on the strength is illustrated in Fig. 9 for cross sections with homogeneous and heterogeneous orientation of the material principal directions. Beam widths B in the range 56-215 mm were analyzed. The results relate to three different cross sections, each with identical growth ring pattern for the individual lamellas within each of considered cross sections. The growth ring patterns may be described by the locations of pith as $(y'_p, z'_p) = (\infty, 0)$, $(0, 0)$ and $(45, 0)$. The beam strengths are normalized with respect to the values of V_{cT}/A_{net} for $B = 56$ mm: 1.11, 1.13 and 1.15 MPa for the three respective cross sections mentioned above. The beam strength is for all presented analyses related to a local load maximum occurring prior to the instant of crack development such that a traction-free crack spreads the entire beam width. The local maximum is followed by snap-back of the load vs. deflection response during which the fracture process zone develops rapidly, much as illustrated in Figs. 6 and 7 for test series L-630 when considering softening within crack plane CT.

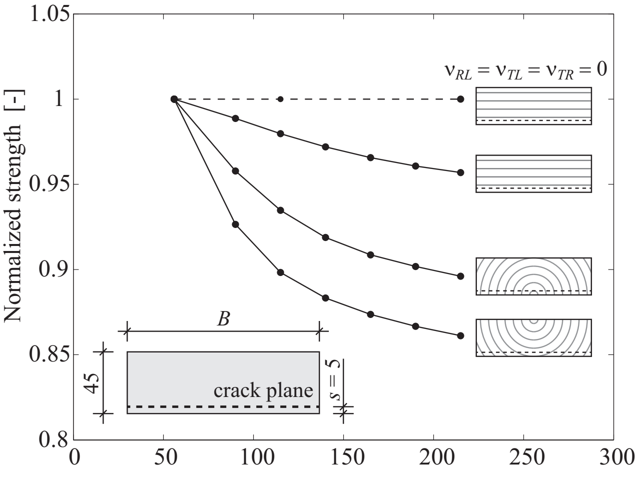

Fig. 9 Influence of beam width and growth ring pattern

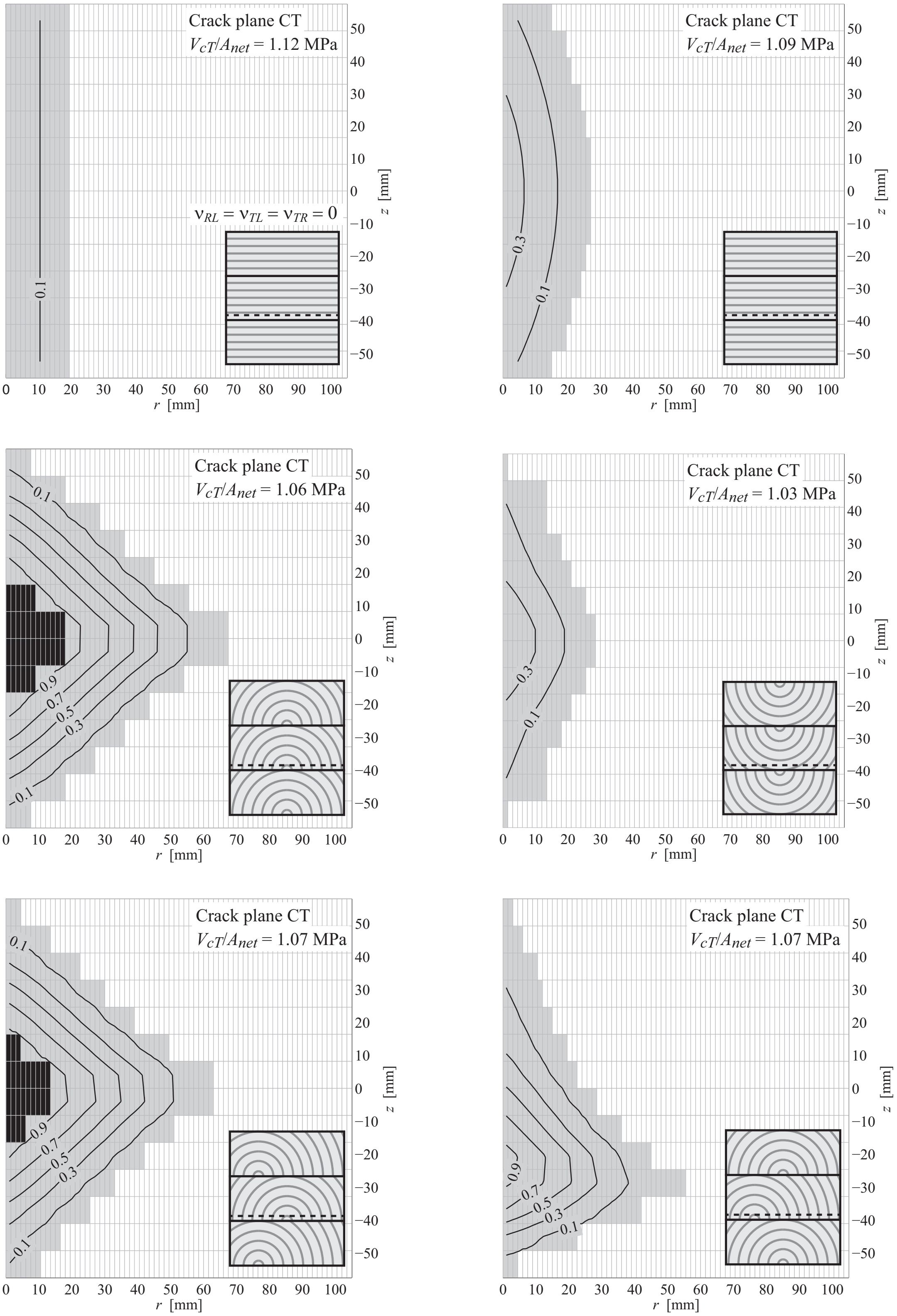

Fig. 10 Extensions of fracture process zones at respective maximum load for different growth ring patterns: Grey elements represent softening region, black elements represent traction-free crack, iso-lines represent the effective deformation δ_{eff} and r denotes a local coordinate with $r = 0$ at start of crack plane at hole edge

The influence of beam width on the calculated beam strength is related to the uneven stress distribution in the beam width direction, induced by the varying material principal directions and the orthotropy within the RT-plane. The decreasing nominal strength at increasing beam width seems further to be influenced by the Poisson effect and the normal stress component σ_{zz} in the beam width direction. For the homogeneous growth ring pattern with $(y'_p, z'_p) = (\infty, 0)$, analyses with Poisson's ratios $\nu_{RL} = \nu_{TL} = \nu_{TR} = 0$ forwarded the same nominal beam strength $V_{cT}/A_{net} = 1.12$ MPa for beam widths $B = 56$, 115 and 215 mm. Illustrations of the fracture process zones at the load level V_{cT}, corresponding to a local maximum load, are presented in Fig. 10 for the growth ring patterns considered in Fig. 9 and beam width $B = 115$ mm. Analyses were also performed using growth ring patterns that are asymmetric with respect to the beam width central axis. The extension of the fracture process zone seems to be closely related to the orientation of the material principal directions within the fracture process zone, and not much affected by the orientation of the material principal directions of the neighboring lamellas.

4.2 Influence of initial cracks

Cracks may appear in structural timber and glulam elements already at zero external load. For example may cracks develop due to variations in temperature and relative humidity, yielding changes in wood moisture content which in turn may lead to cracking due to stresses caused by the orthotropy of wood shrinkage properties. A parameter study of the influence of such initial cracks on the beam strength are presented in this section.

Three types of initial crack geometry according to the illustrations in Fig. 11 were analyzed; cracks spreading the entire beam width (type 1) and cracks with only partial extension in the beam width direction (type 2 and 3). The initial cracks were in the FE-models introduced by omitting elements of the predefined crack plane, corresponding to the geometrical extension of the modeled initial crack. A beam and hole geometry according to test series M-630 was considered, with beam width $B = 115$ mm and height $H = 630$ mm and a growth ring pattern with location of pith at $(y'_p, z'_p) = (0, 0)$. All results are presented as normalized with respect to the numerically found strength of the uncracked geometry, $V_{cT}/A_{net} = 1.06$ MPa.

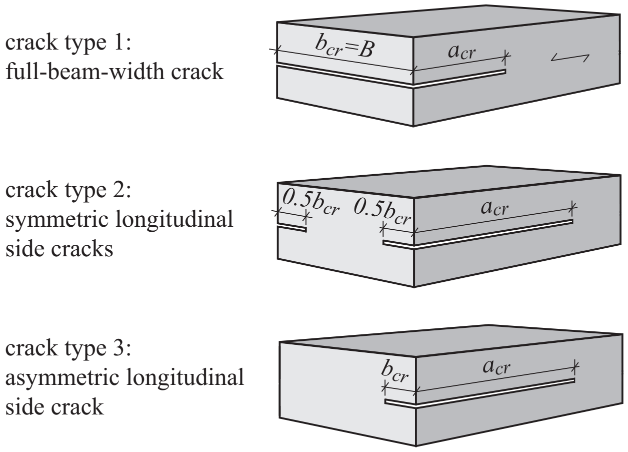

Fig. 11 Considered types of initial cracks

For crack type 1, a full-beam-width crack, are results in terms of beam strength vs. initial crack length a_{cr} presented in Fig. 12. Filled circles represent analyses where V_{cT} was reached due to a local maximum load, with a fracture process zone that is not yet fully developed, followed by crack propagation during snap-back. The unfilled circles relate to analyses where V_{cT} was reached due to creation of new traction-free surfaces spreading the entire beam width and hence propagation of the initial crack at increasing load and increasing beam deflection. For short initial crack lengths may the fracture process zone be considered to be in mixed mode deformation, however dominated by mode I deformation with ratios $\sigma_{yy}/f_{Rt} = \sigma_{yy}/f_{Tt}$ being on average greater than $\tau_{xy}/f_{LR} = \tau_{xy}/f_{LT}$ and considerably greater than τ_{yz}/f_{RT}. For longer initial crack lengths, the mode of deformation is instead more dominated by mode II deformation. This yields a larger size of the fracture process zone and a more even distribution of the softening process across the beam width, since the shear stress τ_{xy} distribution is not much affected by the heterogeneous orientation of material principal directions.

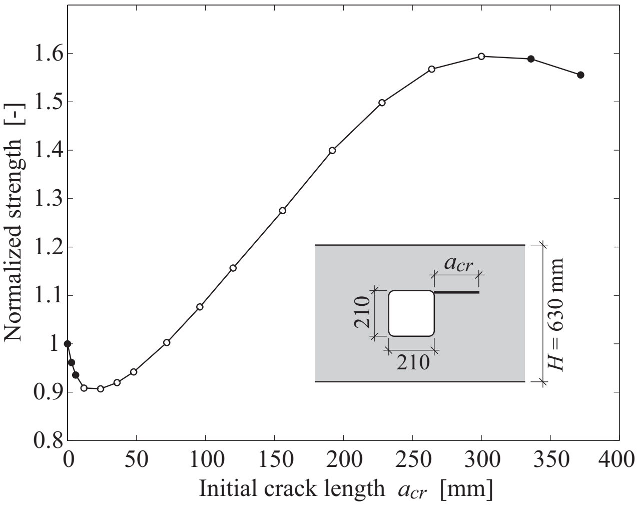

Fig. 12 Influence of initial crack length a_{cr} for crack type 1

For crack types 2 and 3, symmetric and asymmetric longitudinal side cracks respectively, are results in terms of beam strength as influenced by initial crack length a_{cr} and initial crack width b_{cr} presented in Figs. 13 and 14. The results indicate that the asymmetric crack pattern of crack type 3 gives a greater strength reduction than symmetric crack pattern of crack type 2 for equal size of the initial crack surface, i.e. with equal values of a_{cr} and b_{cr}. The numerical analyses suggest a strength reduction due to asymmetric initial cracks that is about equal to, or greater than, the corresponding reduction in stress transferring area, i.e. $V_c \propto 1 - b_{cr}/B$.

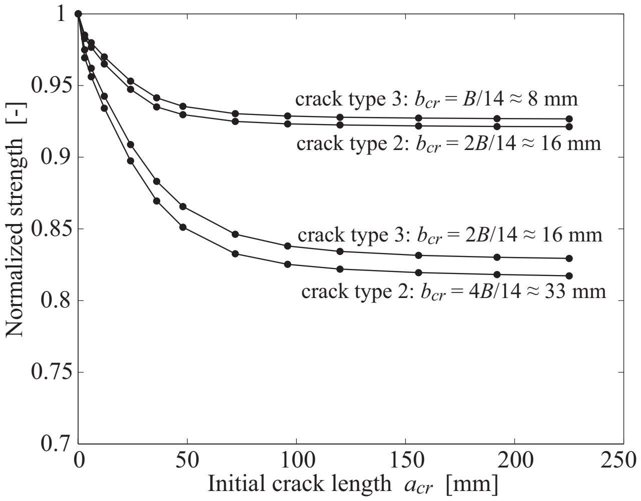

Fig. 13 Influence of initial crack length a_{cr} for crack types 2 and 3, valid for beam width $B = 115$ mm

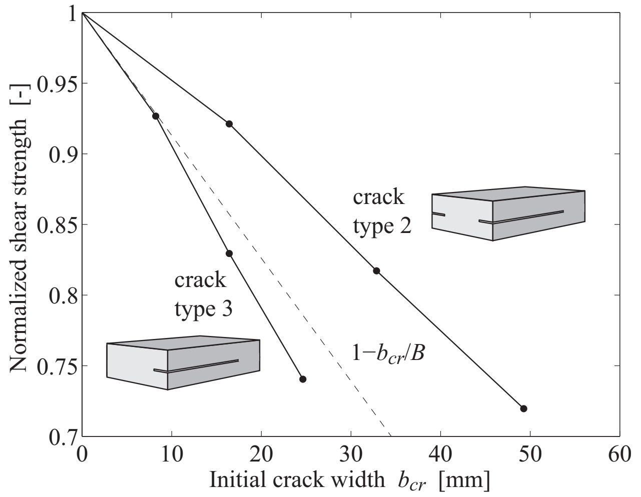

Fig. 14 Influence of initial crack length b_{cr} for crack types 2 and 3, valid for $a_{cr} = 225$ and beam width $B = 115$ mm

5 Results and discussion

Based on the comparison of experimental tests and FE-analyses presented in Fig. 8, the material model seems to capture the beam size influence fairly accurately for an increase in beam height and length dimensions by a factor 3.5 from $H = 180$ to 630 mm. The material model seems further to be fairly accurate also in determining the absolute beam strength. The ratio between calculated strength and mean strength found from experimental tests are between 0.86-0.91 and 0.95-0.104 for the test series with $H = 630$ and 180 mm respectively, considering cracking at the top corner (CT) of the holes.

The FE-analyses of beams with a hole presented in [20] and [32] were compared to results of experimental tests, presented in [20]. These tests were carried out on beams of cross section $B \times H = 120 \times 450$ mm^2 and with circular holes of diameters $\phi/H = 0.2$, 0.3 and 0.4. The ratios between numerically and experimentally found beam strengths for the three test series were between 0.88-1.08 and 1.03-1.33 for analyses presented in [20] and [32] respectively.

Partly different failure behavior was observed for the experimental tests with different hole placement with respect to beam depth presented in [11]. A generally more brittle character was found for holes placed in the upper part of the beam (U-630 and U-180) compared to holes placed in the lower part of the beam (L-630 and L-180). The same general trend was also present in the numerical analyses presented here. Likewise do observations of the location of the first visible traction-free crack in the beam cross section, close to beam width mid-point and hence close to the location of pith, agree well with the experimental observations.

One can in general expect that the absolute size of the fracture process zone at maximum load decreases with decreasing structure size for bodies with an initial sharp crack or notch that give rise to a square root stress singularity. For the particular geometries studied however, without the stress singularity, this relation was to some extent contradicted. For the large beams, a local maximum load was commonly reached before the fracture zone was fully developed. This was however in general not the case for the small beams.

The parameter study relating to growth ring pattern and beam width shows that these parameters may influence the calculated nominal strength, see Fig. 9. For the considered growth ring patterns, an increase in beam width by a factor of about 3.8, from $B = 56$ to 215 mm, gave nominal strength reductions of approximately 5-15%. An influence of growth ring pattern is found although the considered fracture energy properties are assumed independent of the material principal directions and material strength properties are assumed equal in the tangential and radial directions. The influence of growth ring pattern and beam width is related to the orthotropic stiffness properties, i.e. the low rolling shear stiffness and the difference in stiffness between radial and tangential directions. The beam strength is further influenced by the Poisson effect and the normal stress σ_{zz} in the beam width direction. This stress component affects the initiation of softening using the Tsai-Wu based initial yield function given in Eq. (1).

The parameter study relating to initial cracks shows that such may have significant influence on the beam strength. The general influence of the initial crack length a_{cr} for full-beam-width cracks, see Fig. 12, resembles the one obtained from LEFM analysis of a beam with a hole with similar geometry and loading presented in [2]. A longitudinal side crack on one side of the beam seems to induce the greatest reduction of beam strength among the considered types of cracks, according to Figs. 12-14. This is probably related to torsional action due to the asymmetry of the cross section giving an increase in the perpendicular to grain tensile stress at the crack tip in the beam width direction.

For the FE-analyses of large beams, $H = 630$ mm, a local load maximum followed by a sharp snap-back of the load vs. deflection response was commonly found. When considering simultaneous softening within two crack planes, numerical problems were in general encountered shortly after reaching the local maximum. These problems, which were manifested as convergence issues for integration of constitutive relations, are believed to be related to simultaneous elastic unloading within one fracture process zone and crack propagation within the other or alternatively to very unstable crack propagation.

6 Concluding remarks

Strength and fracture course analyses of glulam beams with a hole have been presented, carried out using nonlinear 3D FE-analyses and a cohesive zone model based on plasticity theory. Results of the numerical analyses have been compared to results of experimental tests, showing good agreement both with respect to beam size influence on the strength and overall fracture behavior. Parameter studies relating to influence of growth ring pattern, beam width and different types of initial crack have also been presented.

Cohesive zone modeling has the advantage, compared to conventional LEFM approaches, that both uncracked and cracked geometries can be analyzed. The cohesive zone model used in this paper is very general in the sense that it incorporates the possible influence of all six stress components on the fracture behavior and further takes the orthotropic strength and stiffness properties of wood into account. These features enable full 3D analysis including considerations of heterogeneous orientation of the material principal directions. Although to complex for application in a practical engineering design context, full 3D analysis of the presented type may be a useful research tool for analyzing different applications where perpendicular to grain fracture are of importance, i.e. analysis of shear strength of beams as influenced by drying cracks and different types of steel-timber joints.

References

1. Aicher S, Schmidt J, Brunold S (1995) Design of timber beams with holes by means of fracture mechanics. CIB-W18/28-19-4, Copenhagen, Denmark.
2. Aicher S, Gustafsson PJ (ed), Haller P, Petersson H (2002) Fracture mechanics models for strength analysis of timber beams with a hole or a notch – A report of RILEM TC-133. Report TVSM-7042, Division of Structural Mechanics, Lund University, Sweden.
3. Aicher S, Dill-Langer G (2005) Effect of lamination anisotropy and lay-up in glued-laminated timbers. J Struct Eng 131:1095-103.
4. Aicher S, Höfflin L, Reinhardt HW (2007) Runde Durchbrüche in Biegeträgern aus Brettschichtholz – Teil 2: Tragfähigkeit und Bemessung. Bautechnik 84, Heft 12, 867-880.
5. Austrell PE, Dahlblom O, Lindemann J et al (2004) CALFEM – A finite element toolbox. Version 3.4, Division of Structural Mechanics, Lund University, Sweden.
6. Barenblatt GI (1962) The mathematical theory of equilibrium cracks in brittle fracture. Adv Appl Mech 7:55-129.
7. Berbom Dahl K (2009) Mechanical properties of clear wood from Norway spruce. Doctoral thesis, Department of Structural Engineering, Norwegian University of Science and Technology, Norway.
8. Boström L (1992) Method for determination of the softening behaviour of wood and the applicability of a nonlinear fracture mechanics model. Doctoral thesis, Report TVBM-1012, Division of Building Materials, Lund University, Sweden.
9. Coureau JL, Morel S, Gustafsson PJ, Lespine C (2006) Influence of the fracture softening behaviour of wood on load-COD curve and R-curve. Mat and Struct 40:97-106.
10. Crisfield MA (1991) Nonlinear finite element analysis of solids and structures – Volume 1. John Wiley & Sons Ltd, Chichester, Great Britain.
11. Danielsson H (2008) Strength tests of glulam beams with quadratic holes – Test report. Report TVSM-7153, Division of Structural Mechanics, Lund University, Sweden.
12. Danielsson H, Gustafsson PJ (2008) Strength of glulam beams with holes – Tests of quadratic holes and literature test result compilation. CIB-W18/41-12-4, St Andrews, Canada.
13. Danielsson H, Gustafsson PJ (2011) A probabilistic fracture mechanics method and strength analysis of glulam beams with holes. Eur J Wood Prod 69:407-19.

14. Danielsson H, Gustafsson PJ (2013) A three dimensional plasticity model for perpendicular to grain cohesive fracture in wood. Engng Fract Mech 98:137-52.
15. Danielsson H (2013) Path following solution approaches and integration of constitutive relations for a 3D wood cohesive zone model. Report TVSM-7160, Division of Structural Mechanics, Lund University, Sweden.
16. Dourado N, de Moura MFSF, Morais J (2011) A numerical study of the SEN-TPB test applied to mode I wood fracture characterization. Int J Sol Struct 48:234-42.
17. Dugdale DS (1960) Yielding of steel sheets containing slits. J Mech Phys Solids 8:100-4.
18. EN 1995-1-1:2004 (2004) Eurocode 5: Design of timber structures – Part 1-1: General – common rules and rules for buildings
19. EN 1194:1999 (1999) Glued laminated timber – Strength classes and determination of characteristic values
20. Fleischmann M, Krenn H, Eberhardsteiner J, Schickhofer G (2007) Numerische Berechnung von Holzkonstruktionen unter Verwendung eines orthotropen elasto-plastischen Werkstoffmodells. Holz Roh Werkst 65:301-13.
21. Frühwald Hansson E (2011) Analysis of structural failure in timber structures: Typical causes for failure and failure modes. Eng Struct 33:2978-82.
22. Gustafsson PJ, Danielsson H (2013) Perpendicular to grain stiffness of timber cross sections as affected by growth ring pattern, size and shape. Eur J Wood Prod 71:111-9.
23. Hillerborg A, Modéer M, Peterson PE (1976) Analysis of crack formulation and crack growth in concrete by means of fracture mechanics and finite elements. Cem Concr Res 6:773-82.
24. Larsen HJ, Gustafsson PJ (1990) The fracture energy of wood in tension perpendicular to the grain – Results from a joint testing project. CIB-W18A/23-19-2, Lisbon, Portugal.
25. Mackenzie-Helnwein P, Müllner HW, Eberhardsteiner J, Mang HA (2005) Analysis of layered wood shells using a orthotropic elasto-plastic model for multi-axial loading of clear spruce. Comp Meth Appl Mech Eng 194:2661-85.
26. MATLAB, Version R2011b, The MathWorks, Inc.
27. Pedersen MU, Clorius CO, Damkilde L, Hoffmeyer P (2003) A simple size effect model for tension perpendicular to the grain. Wood Sci Technol 37:125-40.
28. Pizio S (1991) Die Anwendung der Bruchmechanik zur Bemessung von Holzbauteilen, untersucht am durchbrochen und am ausgeklinkten Träger. Publication 91:1, Dissertation, Baustatik und Stahlbau, ETH, Zürich, Switzerland.
29. Riipola K (1995) Timber beams with holes: fracture mechanics approach. J Struct Eng 121:225-40.
30. Scheer C, Haase K (2000) Durchbrüche in Brettschichtholzträgern, Teil 2: Bruchmechanische Untersuchungen. Holz Roh Werkst 58:217-28.
31. Schmidt J, Kaliske M (2007) Simulations of cracks in wood using a coupled material model for interface elements. Holzf 61:382-9.
32. Schmidt J, Kaliske M (2009) Models for numerical failure analysis of wooden structures. Eng Struct 31:571-9.
33. Serrano E (2004) A numerical study of the shear-strength-predicting capabilities of test specimens for wood-adhesive bonds. Int J Adhes Adhes 24:23-35.
34. Serrano E, Gustafsson PJ (2006) Fracture mechanics in timber engineering – Strength analyses of components and joints. Mat Struct 40:87-96.
35. Stefansson F (2001) Fracture analysis of orthotropic beams – linear elastic and non-linear methods. Licentiate thesis, Report TVSM-3029, Division of Structural Mechanics, Lund University, Sweden.
36. Tsai SW, Wu EM (1971) A general theory of the strength of anisotropic materials. J Compos Mater 5:58-80.
37. Verhoosel CV, Remmers JJC, Gutiérrez MA (2009) A dissipation based arc-length method for robust simulation of brittle and ductile failure. Int J Numer Meth Engng 77:1290-321.
38. Wernersson H (1994) Fracture characterization of wood adhesive joints. Doctoral thesis, Report TVSM-1006, Division of Structural Mechanics, Lund University, Sweden.

Paper F

Fracture analysis of perpendicular to grain loaded dowel-type connections using a 3D cohesive zone model

Henrik Danielsson and Per Johan Gustafsson

submitted for publication

Manuscript submitted for publication

Fracture analysis of perpendicular to grain loaded dowel-type connections using a 3D cohesive zone model

Henrik Danielsson · Per Johan Gustafsson

Received: date / Accepted: date

Abstract The strength and fracture behavior of dowel-type connections with stiff dowels loaded perpendicular to grain was studied by nonlinear 3D FE-analysis. A cohesive zone model was used to model the perpendicular to grain fracture of the wood. The influence of load eccentricity and dowel-to-loaded-edge distance was studied for a plate type of geometry loaded in tension and for a simply supported beam loaded in bending. The strength found from the FE-analysis is compared to strength from experimental tests with centric loading, showing overall good agreement. Numerical results for centric loading are further compared to the strength according to Eurocode 5. FE-analysis regarding dowel load eccentricity showed that such loading conditions yield significantly lower strengths. An approximate engineering method to account for the strength reduction due to load eccentricity is furthermore presented.

Keywords cohesive zone model, dowel, eccentricity, LVL, wood

1 Introduction

Wood is in many aspects a very appealing structural material. It does however possess unique and complex properties, demanding careful considerations in design in order to utilize the material in a proper way and to its full potential. Wood is for example weak when loaded in tension perpendicular to grain and the associated failure type, with cracking along grain, may have a very brittle character. This type of loading is a relatively common cause for damage of timber structures [15]. Efforts should hence be made in design such that perpendicular to grain tensile stress is avoided or at least limited. This task is however far from trivial and many technical solutions, with appealing properties, induce the undesired perpendicular to grain tensile stress, i.e. notched beams, beams with holes and curved beams. Also various types of connections induce the undesired stress state, since the direction of load commonly shifts where one structural element is connected to another. A typical example is dowel-type connections with a force component at an angle to grain.

Many studies of the strength of dowel-type connections loaded perpendicular to grain are found in the literature. Experimental tests are for example presented in [2], [3], [12], [16], [17], and [29]. Most of the work seems to relate to influence of connection configuration in terms of number of dowels and dowel spacing, dowel slenderness and loaded-edge distance, i.e. the distance between the wood member surface and the furthest dowel in the direction of the load. The comprehensive compilation of test results presented in [12] relates to dowel and nail connections with multiple fasteners. Among these tests, all connections with a loaded-edge-distance of less than 70% of the wood member height failed due to cracking along grain. Based on the compilation of results, a semi-empirical design approach was proposed which later formed the base for the design equations present in the German design code DIN 1052:2008 [11].

Connection strength with respect to perpendicular to grain fracture in the wood member has been studied using various 2D fracture mechanics approaches. Analytical Linear elastic fracture mechanics (LEFM) approaches are for example used in [18], [21] and [24]

H. Danielsson · PJ. Gustafsson
Division of Structural Mechanics, Lund University
P.O. Box 118, SE-221 00 Lund, Sweden
Tel.: +46-46-222 46 89
Fax: +46-46-222 44 20
E-mail: henrik.danielsson@construction.lth.se

and quasi-nonlinear fracture mechanics approaches are used in [17] and [19]. These methods are simple enough to allow for derivation of design criteria suitable for use in a practical design context. Furthermore are cohesive zone models used for a 2D representation in [14] and for a 3D representation in [25] to model the strain softening material performance within a fracture process zone. General drawbacks of 2D analyses include the inability to study out-of-plane variation of parameters relating to loading, geometry and material properties.

The design criterion in Eurocode 5 [13], which seems to originate from the LEFM approach presented in [24], is reviewed below. For the types of connections in Fig. 1, the following criterion should be fulfilled

$$F_{v,Ed} \leq F_{90,Rd} \quad \text{with} \quad F_{v,Ed} = \max \begin{cases} F_{v,Ed,1} \\ F_{v,Ed,2} \end{cases} \tag{1}$$

where $F_{v,Ed,1}$ and $F_{v,Ed,2}$ are the design shear forces on either side of the connection and $F_{90,Rd}$ is the design splitting capacity of the beam at the connection. $F_{90,Rd}$ is found from the characteristic capacity $F_{90,Rk}$ by conventional modifications accounting for the partial factors for material properties and for duration of load and moisture content effects. The characteristic splitting capacity is for a connection with metal dowel-type fasteners and a beam element of softwood given by

$$F_{90,Rk} = 14b\sqrt{\frac{h_e}{1-h_e/h}} \tag{2}$$

where h_e is the distance from the loaded edge to the center of the most distant fastener (the effective beam height) and where h and b are the wood member height and width respectively, with the capacity in N and all dimensions in mm. The design criterion in Eurocode 5 does not explicitly include any material parameters such as strength, stiffness or fracture energy. The only parameters influencing the capacity are instead the geometrical parameters b, h and h_e.

According to the LEFM approach presented in [24] is the critical shear force given by

$$V_c = \sqrt{\frac{GG_c}{0.6}}\,b\sqrt{\frac{h_e}{1-h_e/h}} \tag{3}$$

where G is the shear modulus and G_c is the fracture energy (or critical energy release rate). The above given equation was suggested to be used for design with respect to cracking along grain and then assumed to be valid for $h_e < 0.7h$. The factor $\sqrt{GG_c/0.6} = 15.5$ N/mm$^{1.5}$ was found to correspond well with strength according to experimental tests at the mean value level. Based on this, the factor $\sqrt{GG_c/0.6} = 15.5 \cdot 2/3 \approx 10$ N/mm$^{1.5}$ was suggested to be used for the code design criterion at the characteristic level.

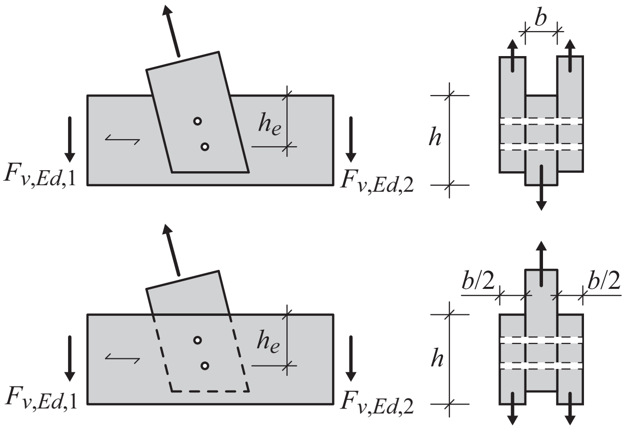

Fig. 1 Dowel connection loaded perpendicular to grain

The Eurocode 5 approach reviewed above has been questioned and there seems to have been disagreement regarding the general reliability of the design equations, see e.g. [4], [14], [19] and [22]. This motivates further studies of the validity of Eqs. (1) and (2).

A parameter which further seems to have been overlooked when it comes to experimental and theoretical studies is dowel load eccentricity. The LEFM approach underlying the design criterion in Eurocode 5 is based on assumptions of an infinitely stiff fastener and centric loading conditions. The loading may however also be applied eccentrically, as illustrated in Fig. 2.

This paper presents a numerical parameter study of the strength of dowel-type connections with stiff dowels loaded perpendicular to grain. The influence of load eccentricity and loaded-edge-distance in studied for a plate type of geometry and for a beam geometry. The parameter study is carried out using 3D FE-analysis, where crack initiation and propagation is modeled using a cohesive zone model which simulates the strain softening performance of the wood. Numerical results are compared to results of experimental tests and to predictions according to the LEFM-based strength design criterion given in Eurocode 5. An approximate engineering method which accounts for the influence of load eccentricity on the strength is also presented.

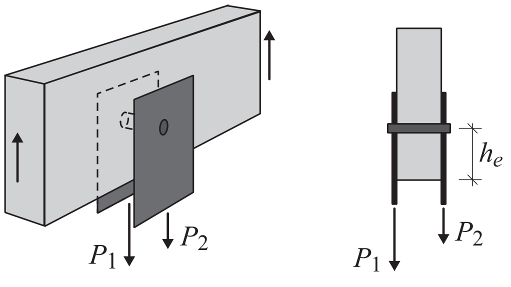

Fig. 2 Eccentric loading of a dowel-type connection

2 Approximate method for load eccentricity

The design approach in Eurocode 5, Eqs. (1) and (2), and most similar analytical approaches are based on assumptions of an infinitely stiff fastener and centric loading conditions with respect to the wood member width b. The effect of load eccentricity may however be accounted for in an approximate manner in the following way.

Consider the centric and eccentric loading conditions illustrated in Fig. 3a) and b) respectively. The centric loading is assumed to give a uniformly distributed load [N/m] over the entire wood member width b. The distributed load intensity at the instant of critical load on the dowel is then $q_c = P_{c,0}/b$ where $P_{c,0}$ denotes the critical value of the dowel load P for centric loading conditions according to for example LEFM or similar approaches. The critical value $P_{c,e}$ of the dowel load for eccentric loading is also assumed to be reached once the distributed load reaches the critical value q_c. At the instant of critical load for eccentric loading conditions, the distributed load is approximated by the plastic distribution given in Fig. 3b) and hence acting upward along a part of the dowel. The critical value $P_{c,e}$ at eccentric loading conditions may then be found from equilibrium considerations as

$$P_{c,e} = k_e P_{c,0} \qquad \text{where} \tag{4}$$

$$k_e = \sqrt{1 + \frac{4e^2}{b^2}} - \frac{2e}{b} \quad \text{and} \quad \frac{e}{b} = \frac{1}{2}\frac{P_1 - P_2}{P_1 + P_2}$$

and where k_e hence describes the decrease in capacity due to a load eccentricity e/b.

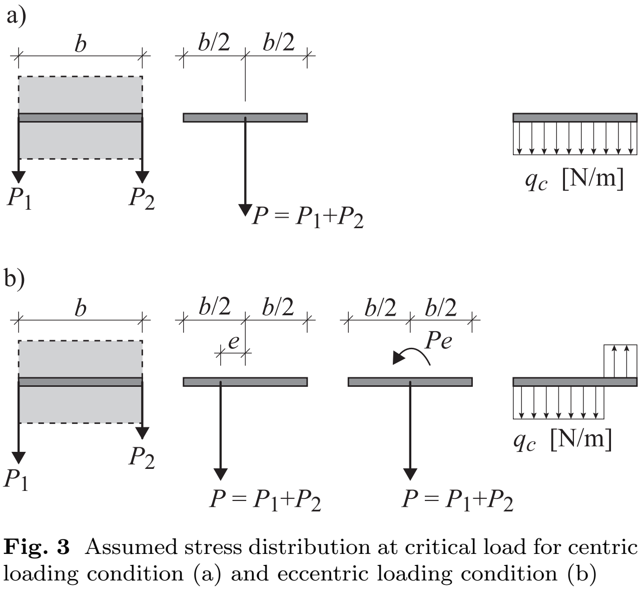

Fig. 3 Assumed stress distribution at critical load for centric loading condition (a) and eccentric loading condition (b)

3 Material model and implementation

3.1 Cohesive zone model

The numerical analyses were performed using a cohesive zone model based on plasticity theory, briefly reviewed here and more thoroughly presented in [9].

The material model is based on a 3D macro scale continuum representation considering cylindrical orthotropy where distinction is made between the material longitudinal L, radial R and tangential T directions. The material is assumed to be homogeneous in the sense that knots and other possible stochastically distributed heterogeneities are disregarded. Small strain assumptions and additive decomposition of elastic and plastic strains are used. The cohesive zone model is applied to a predefined potential crack plane, within which a fracture process zone may initiate and evolve. This plane is assumed to be oriented as the global xz-plane and has a small, but nonzero, height in the out-of-plane direction. The global x-direction is further assumed to coincide with the material longitudinal direction, see Fig. 4.

The Tsai-Wu criterion [27] is often proposed as a suitable failure criterion for wood since it includes orthotropic strength properties and allows for different tensile and compressive strengths. It is here used as criterion for initiation of yielding, i.e. the formation of a fracture process zone and initiation of softening. An initial yield function F is hence defined according to

$$F(\boldsymbol{\sigma}) = \boldsymbol{\sigma}^T \mathbf{q} + \boldsymbol{\sigma}^T \mathbf{P} \boldsymbol{\sigma} - 1 \tag{5}$$

where $\boldsymbol{\sigma}$ is the stress and where $\mathbf{q}$ and $\mathbf{P}$ are given by the material strengths properties. The post softening initiation performance is assumed to be governed by the three out-of-fracture plane stress and plastic deformation components. As softening has initiated, the yield function is changed accordingly and the updated yield function f defined as

$$f(\boldsymbol{\sigma}, K) = \sigma_{yy}^2 F_{yyyy} + \tau_{xy}^2 F_{xyxy} + \tau_{yz}^2 F_{yzyz} - K \tag{6}$$

where F_{yyyy}, F_{xyxy} and F_{yzyz} are fictitious material strength parameters determined from the stress state at initiation of softening and where K is a softening

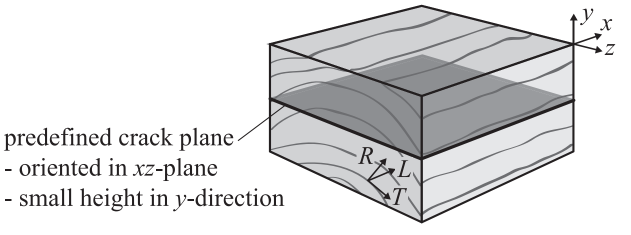

Fig. 4 Orientation of predefined crack plane

parameter. An associated plastic flow rule is adopted. Since the updated yield function f only depends on the three out-of-fracture plane stress components, plastic strains are obtained only in these three directions corresponding to the fracture mechanics modes of deformation I, II and III. The softening parameter K is a function of an internal variable denoted the effective plastic deformation δ_{eff} and the following softening function is adopted here

$$K = \begin{cases} \exp(\ln(c)\delta_{eff}^{m}) & \text{for} \quad \delta_{eff} \leq 1 \\ 0 & \qquad\quad \delta_{eff} > 1 \end{cases} \tag{7}$$

where m is a model parameter determining the shape of the softening curve and where c should be a small, but nonzero, number. The evolution law for the internal variable is defined as

$$\dot{\delta}_{eff} = \sqrt{\left(\frac{\dot{\delta}_{yy}}{A_{yy}}\right)^2 + \left(\frac{\dot{\delta}_{xy}}{A_{xy}}\right)^2 + \left(\frac{\dot{\delta}_{yz}}{A_{yz}}\right)^2} \tag{8}$$

where $\dot{\delta}_{yy}$, $\dot{\delta}_{xy}$ and $\dot{\delta}_{yz}$ denote incremental plastic deformations, determined from the plastic strains by assuming constant strains over the small out-of-plane height of the predefined potential crack plane. A_{yy}, A_{xy} and A_{yz} are scaling parameters of dimension length, defined such that the work required for complete separation in any of the three modes of deformation equals the corresponding fracture energy. Normalized stress vs. plastic deformation relationships for uniaxial loading are presented in Fig. 5 for $c = 10^{-3}$ and $m = 1.0$, 1.5 and 2.0, where G_f and f_t refer to fracture energy and material strength respectively and δ refers to the plastic deformation.

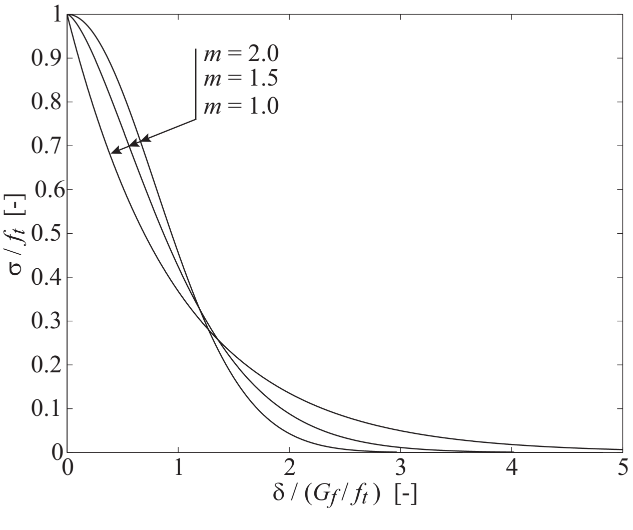

Fig. 5 Normalized stress vs. deformation relationships

3.2 Numerical implementation

The material model was implemented for FE-analysis in MATLAB [23] using supplementary routines from the toolbox CALFEM [1]. The nonlinear global response was solved in an incremental-iterative fashion using either a conventional displacement driven Newton-Raphson method or a cylindrical arc-length type of path following method, see e.g. [8]. Both these approaches are capable of following a softening-unloading part of the global load vs. displacement path, for the arc-length method also when this path includes snap-back. In relation to results presented here, the main difference between the two approaches lies in the application of the external load. The displacement driven Newton-Raphson approach applies the load by prescribed displacements, and the force eccentricity may then vary as softening occur and the material behaves in a nonlinear fashion. In the arc-length method, the external load is instead applied as a fixed load pattern, giving a fixed load eccentricity along the entire loading path.

The implemented arc-length method uses a constraint equation considering the degrees of freedom within the predefined crack plane only, following a proposal in [6] for strain softening materials with localized fracture performance. Further information regarding the numerical implementation is given in [9] and [10].

The contact between the wood and the dowel was modeled in a simplified manner. One layer of 0.5 mm thick linear elastic elements was modeled between the dowel and the wood. These elements were given a stiffness in the, with respect to dowel central axis, radial direction of 800 MPa. This value is equal to the wood material stiffness in the radial direction E_R used for the presented FE-analyses. The moduli of elasticity in the other two directions and the shear moduli were given small values to simulate an almost friction-free load transfer from dowel to the wood. The global solution procedure was further formulated such that only compressive stress was allowed in the, with respect to dowel central axis, radial direction.

4 Results

Two types of geometries were analyzed: a plate type of geometry loaded in tension (Fig. 6) and a simply supported beam loaded in three-point-bending (Fig. 11). Parameter studies relating to influence of load eccentricity and influence of dowel-to-loaded-edge distance for centric loading were carried out for both geometries.

The numerical results are compared to results of experimental tests presented in [16] and [17]. The material used for the experimental tests was Laminated

Veneer Lumber (LVL) made of Spruce and with the same grain orientation for all veneers. The mean density of the tested material was 475 kg/m^3 at a moisture content of 12%. The load was applied in a displacement controlled fashion by the use of steel plates. The load was for all tests applied centrically with respect to the LVL member width direction.

The material parameters used for the FE-analyses relating to strength, stiffness and fracture energy of the LVL are presented in Table 1. These values should comply fairly well with mean values for Spruce grown in Scandinavia, see e.g. [5], [7], [20], [26] and [28]. The model parameters defining the softening function were set to $m = 1.5$ and $c = 10^{-3}$ corresponding to a curved shape as illustrated in Fig. 5 and roughly as suggested by test results for mode I loading presented in [7], [26] and [28]. With the current set of parameters, creation of traction-free crack surfaces do for pure mode I loading in the R- or T-direction correspond to a plastic deformation $\delta_{yy} = 0.40$ mm.

Homogeneous orientation of material principal directions was assumed and the wood bulk material outside the potential crack plane was modeled as a linear elastic orthotropic material. The steel dowels were modeled as a linear elastic isotropic material with $E = 210$ GPa and $\nu = 0.3$.

Table 1 Material parameters used for FE-analysis

Stiffness			
Modulus of elasticity	E_L	12000	MPa
	E_R	800	MPa
	E_T	500	MPa
Modulus of shear	G_{LR}	700	MPa
	G_{LT}	700	MPa
	G_{RT}	50	MPa
Poisson's ratio	ν_{RL}	0.02	-
	ν_{TL}	0.02	-
	ν_{TR}	0.30	-
Strength			
Tensile strength	f_{Lt}	60	MPa
	f_{Rt}	3.0	MPa
	f_{Tt}	3.0	MPa
Compressive strength	f_{Lc}	40	MPa
	f_{Rc}	4.0	MPa
	f_{Tc}	4.0	MPa
Shear strength	f_{LR}	6.0	MPa
	f_{LT}	6.0	MPa
	f_{RT}	3.0	MPa
Fracture energy			
	$G_{f,yy}$	300	J/m^2
	$G_{f,xy}$	900	J/m^2
	$G_{f,yz}$	900	J/m^2

4.1 Plate geometry

Three types of plate geometries according to Fig. 6 were analyzed, with dowel diameter $d = 14$ mm and out-of-plane width is $b = 40$ mm. Since the geometries exhibit double symmetry, only one quarter of the specimens were modeled in the FE-analyses as illustrated in Fig. 7. A predefined crack plane was introduced at the dowel with the greatest distance to the loaded edge. The element size within the crack plane was $3.0 \times 0.5 \times 4.0$ mm^3 in the xyz-directions respectively.

The three plate geometries $n = 1 \times 1$, 1×2 and 1×3 were analyzed using centric load conditions, i.e. $P_1 = P_2 = 0.5P$ and hence $e/b = 0$. The loading was applied by prescribing the dowel displacements, equal for all dowels. The maximum loads found from the FE-analyses are given in Table 2 together with specimen strength found from experimental tests in [16]. The results in terms of total applied load P vs. dowel displacement is presented in Fig. 8.

The influence of load eccentricity was studied for geometry $n = 1 \times 1$. The eccentric loading situation was achieved by prescribing either eccentric dowel displacements or by prescribing the loads directly. The results are presented in Fig. 9 where the strength is normal-

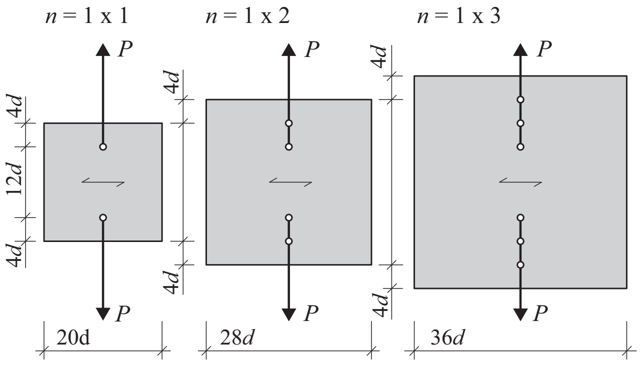

Fig. 6 Plate geometries and loading conditions, $d = 14$ mm

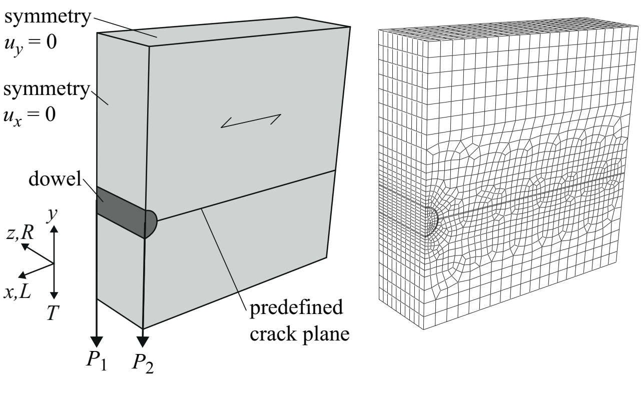

Fig. 7 Loads, boundary conditions and finite element mesh for plate geometry $n = 1 \times 1$

ized with respect to the strength for centric loading, $P_f = 7.56$ kN. The results representing analyses using prescribed displacements are presented by two curves, since the load ratio P_1/P_2 and hence e/b varies along the loading path due to material nonlinearity. The curve representing prescribed loads is almost identical with the curve representing prescribed displacements with the load eccentricity e/b determined from maximum loads. The influence of load eccentricity according to the approximate engineering method given in Eq. (4) is also given in the figure, showing a slightly stronger influence than found from the FE-analyses. The extensions of the fracture process zone at maximum load are illustrated in Fig. 10 for $e/b = 0.00$, 0.25 and 0.50.

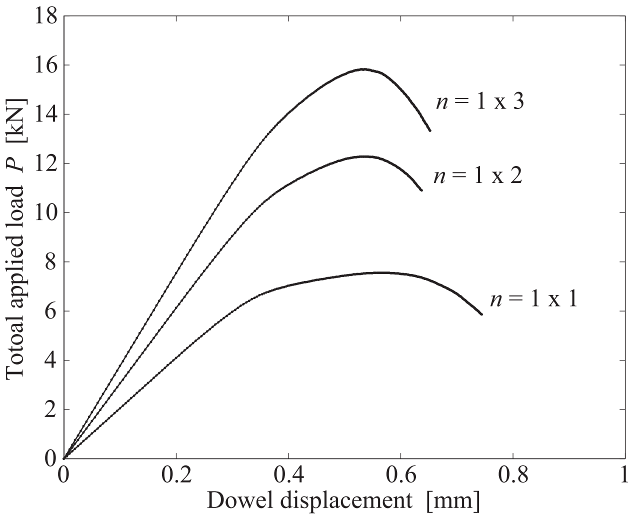

Fig. 8 Total applied load P vs. dowel displacement

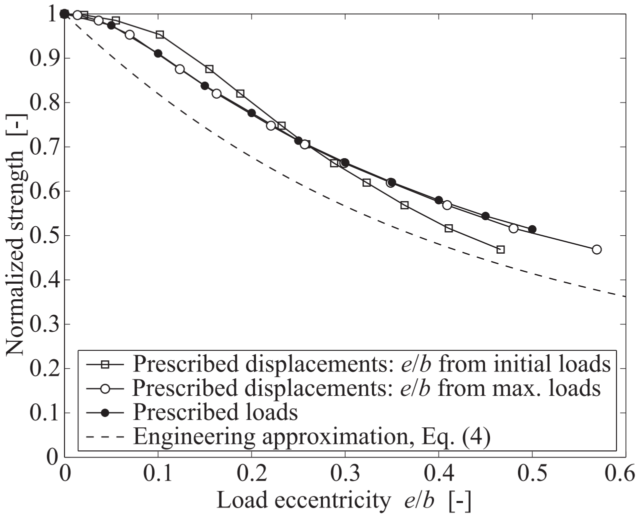

Fig. 9 Strength vs. load eccentricity e/b for $n = 1 \times 1$

Table 2 Strength (mean value±std) in kN from experimental tests [16] and finite element analysis for plate geometries

	$n = 1 \times 1$	$n = 1 \times 2$	$n = 1 \times 3$
$P_{f,exp}$	7.55 ± 0.39	11.05 ± 0.68	14.53 ± 1.14
$P_{f,FE}$	7.56	12.27	15.82

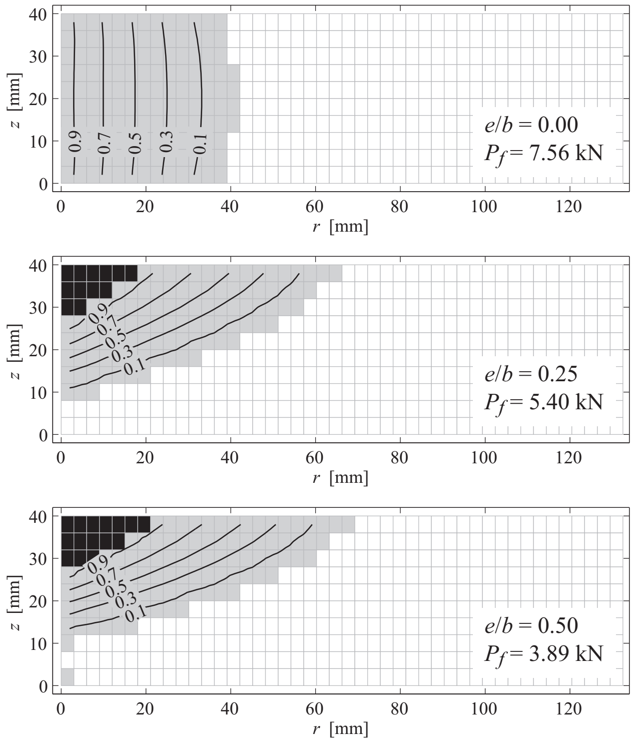

Fig. 10 Extension of fracture process zone at maximum load for plate geometry $n = 1 \times 1$: black elements represent traction-free crack, white elements represent linear elastic behavior, grey elements represent the fracture process zone and isolines represent the effective plastic deformation δ_{eff}

4.2 Beam geometry

A beam loaded by a single dowel and with geometry according to Fig. 11 was analyzed. Presented results relate to dowel diameter $d = 14$ mm and beam cross section $b \times h = 40 \times 200$ mm^2. Experimental tests of beams with equal geometry and effective beam height $h_e = 0.28h$ mm are presented in [17]. Loads, boundary conditions and an example of FE-mesh are given in Fig. 12. Crack planes were modeled at the dowels, with a minimum extension of 120 mm in the beam length direction. The element size within the crack plane was $3.0 \times 0.5 \times 4.0$ mm^3 in the xyz-directions respectively.

For an effective beam height $h_e = 0.28h = 56$ mm, the maximum load found from the FE-analysis was 9.13 kN and the corresponding experimentally found mean value (from 4 individual test) was 10.3 kN [17]. The influence of effective beam height h_e on the strength was studied for centric loading conditions and within the interval $0.07h \leq h_e \leq 0.70h$. The applied load vs. dowel displacement curves are given in Fig. 13.

The applied load vs. traction-free crack length is given in Fig. 14, where the maximum load is indicated by a dot for each curve. The traction-free crack length is determined as the total traction-free crack area divided by the beam width. It should here be noted that a traction-free crack is first formed during unloading after the instant of maximum load for effective beam heights $h_e = 0.07h, 0.14h$ and $0.21h$.

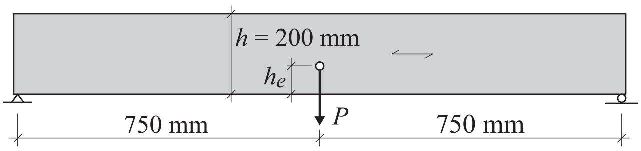

Fig. 11 Beam loaded by dowel in three-point-bending

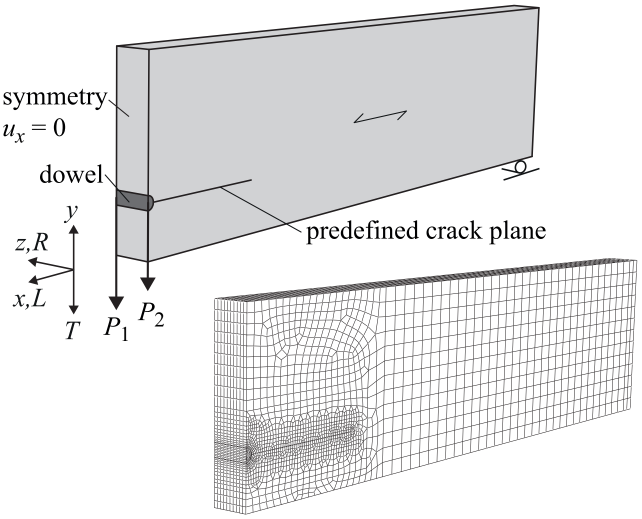

Fig. 12 Loads, boundary conditions and finite element mesh for beam geometry

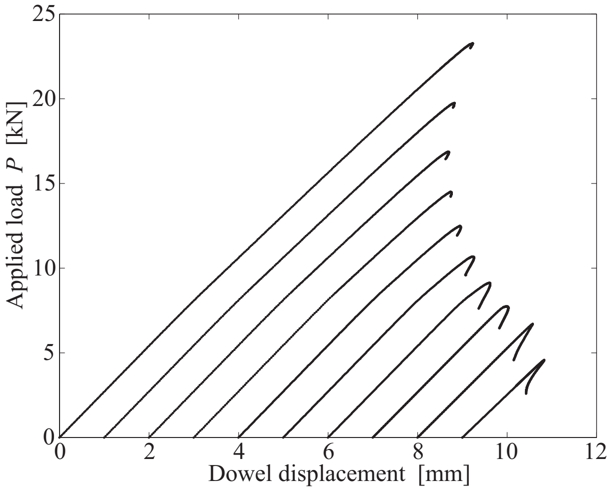

Fig. 13 Total applied load P vs. dowel displacement

The step-shape of the curves in Fig. 14 is related to the mesh density and the extension of the traction-free crack which occur in a discrete manner, corresponding to one row of finite elements in the beam width z-direction.

The beam strength vs. effective beam height h_e is given in Fig. 15 together with the characteristic beam strength according to Eurocode 5 [13], valid for a softwood member with a metal dowel-type fastener. For the present three-point-bending loading case, the characteristic capacity is given by $P_k = 2F_{90,Rk}$ with $F_{90,Rk}$ according to Eq. (2). Numerically found beam strengths, based on assumed mean values of material properties as presented in Table 1, are close to or lower than the characteristic capacity according to Eqs. (1) and (2).

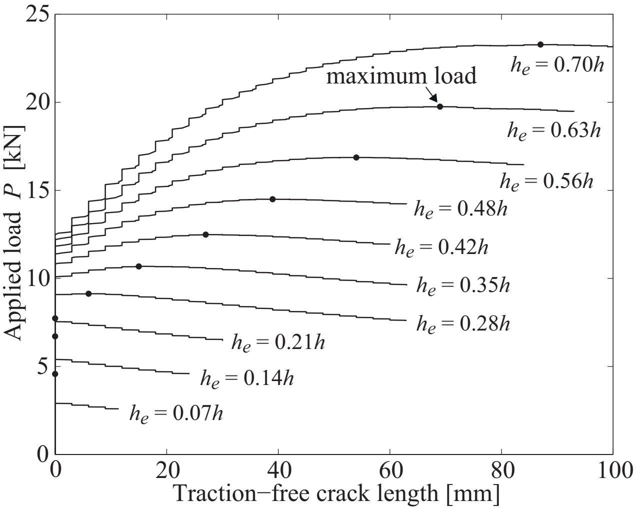

Fig. 14 Total applied load P vs. traction-free crack length

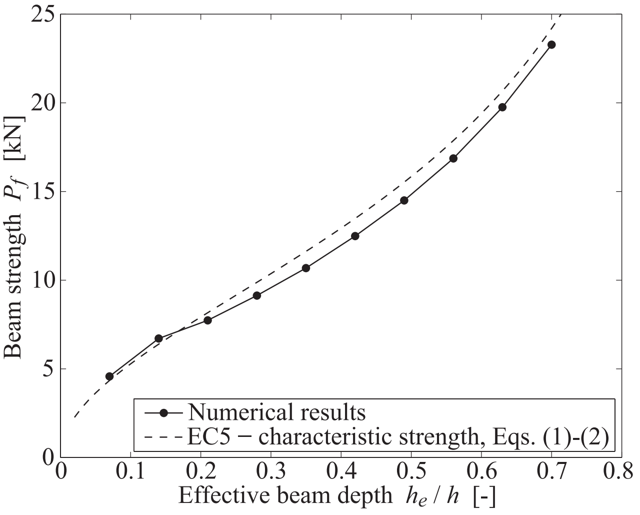

Fig. 15 Beam strength P_f vs. effective beam height h_e

The influence of load eccentricity e/b on the beam strength was studied for $h_e = 0.28h$. The results in terms of beam strength vs. load eccentricity e/b are presented in Fig. 16. The extensions of the fracture process zone at maximum load are illustrated in Fig. 17 for $e/b = 0.00$, 0.25 and 0.50.

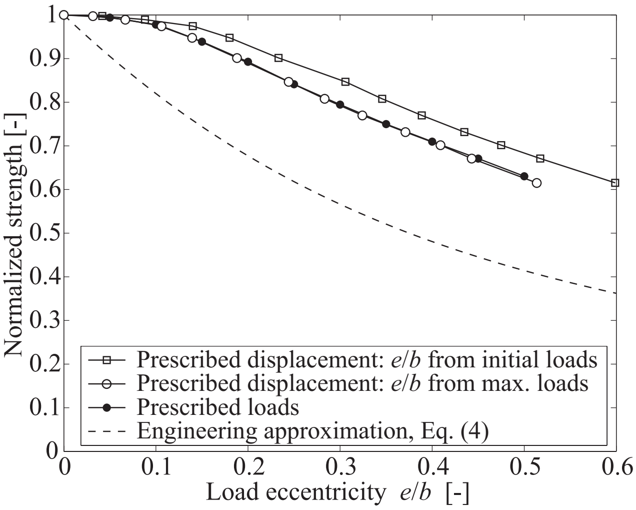

Fig. 16 Beam strength vs. load eccentricity e/b, $h_e = 0.28h$

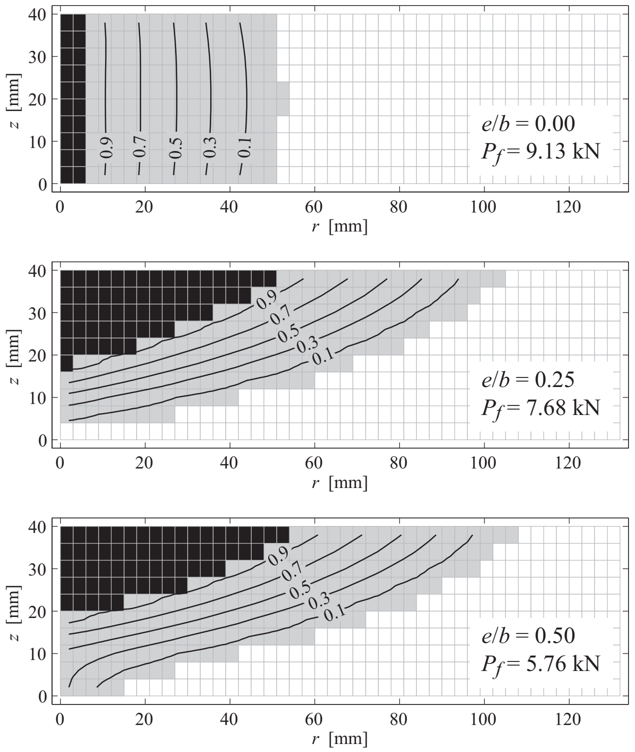

Fig. 17 Extension of fracture process zone at maximum load for beam geometry, $h_e = 0.28h$: black elements represent traction-free crack, white elements represent linear elastic behavior, grey elements represent the fracture process zone and isolines represent the effective plastic deformation δ_{eff}

5 Discussion

The influence of load eccentricity on the strength was studied for one beam geometry and one plate geometry, both showing decreasing strength at increasing load eccentricity however to a somewhat different extent. There seems however to be a lack of experimental test results for corresponding types of loading and experimental verification of the numerical results was therefore not possible. Experimental tests of eccentrically loaded dowel-type connections should hence preferably be performed, as well as FE-analyses of different types of beam geometries such as different beam cross section sizes and effective beam heights.

All results presented above relate solely to strength with respect perpendicular to grain fracture, i.e. cracking along the grain, and other possible failure modes such as embedment failure at the dowel or bending failure of the beam is hence not considered. The risk for other failure modes than cracking along grain is believed to be highest for the beam geometry with large effective beam heights h_e. For example does the failure load with respect to cracking along grain for $h_e = 0.70h$, $P_f = 23.3$ kN, correspond to an embedment stress of $P_f/(bd) = 42$ MPa and a beam theory bending stress of 33 MPa.

It is furthermore worth noting that since the design approach in Eurocode 5 is based on the maximum value of the shear forces on either side of the connection, the design strength varies with placement along the beam length for a simply supported beam. A dowel placed at midspan, where the shear force is half the applied dowel force, gives the greatest design capacity. The design capacity then decreases for dowel placements closer to a support. The design capacity for a cantilever beam is only half that of a beam loaded by a dowel at midspan. This strong influence on the location of the connection along a simply supported beam is according to [19] not correct.

6 Conclusions

A numerical study of the fracture strength of dowel-type connections, by nonlinear 3D FE-analysis using a cohesive zone model to simulate the strain softening performance of the wood, has been presented. The influence of dowel-to-loaded-edge distance and load eccentricity has been studied for a plate type of geometry loaded in tension and for a beam geometry.

Numerical results were compared to results of experimental tests of LVL plates loaded in tension and a LVL beam loaded in bending. For the three considered plate geometries, the ratio between predicted strength and tested strength was $P_{f,FE}/P_{f,exp} = 1.00$, 1.11 and 1.09 and for the beam geometry 0.89.

The influence of dowel-to-loaded-edge distance (effective beam height) on the strength was for the beam geometry also compared to the characteristic strength according to Eurocode 5. The comparison showed an overall good agreement regarding the relative influence of the effective beam height on the strength. The design equation, valid for softwood, seems however to be unconservative since the predicted characteristic strength is very close to or greater than the strength found from FE-analysis, based on assumed mean values of material properties. This statement is supported by the results of the experimental tests of LVL-beams in [17] with $h_e = 0.28h$. The experimentally found mean strength, $P_f = 10.3$ kN, is only 4% greater than the corresponding Eurocode 5 characteristic capacity, $P_k = 9.88$ kN.

Results of the FE-analyses showed that dowel load eccentricity may affect the strength considerably. The ratio between the strength at a load eccentricity of $e/b = 0.50$ and the strength at centric loading was found to be 0.51 and 0.63 for the plate and the beam geometry respectively. An approximate equation proposed for simple consideration of load eccentricity was found to agree reasonably well with the numerical results for a dowel in a plate. For the beam geometry studied, the equation overestimated the influence of load eccentricity.

References

1. Austrell PE, Dahlblom O, Lindemann J, et al (2004) CALFEM – A finite element toolbox. Version 3.4, Division of Structural Mechanics, Lund University, Sweden.
2. Ballerini M (1999) A new set of experimental tests on beams loaded perpendicular-to-grain by dowel-type connections. CIB-W18/32-7-2, Graz, Austria.
3. Ballerini M, Giovanella A (2003) Beams transversally loaded by dowel-type joints: influence on splitting strength of beam thickness and dowel size. CIB-W18/36-7-7, Colorado, USA.
4. Ballerini M (2004) A new prediction formula for the splitting strength of beams loaded by dowel-type connections. CIB-W18/37-7-5, Edinburgh, Scotland.
5. Berbom Dahl K (2009) Mechanical properties of clear wood from Norway spruce. Doctoral thesis, Department of Structural Engineering, Norwegian University of Science and Technology, Norway.
6. de Borst R (1987) Computation of post-bifurcation and post-failure behavior of strain-softening solids. Computers and Structures 25:221-224.
7. Boström L (1992) Method for determination of the softening behaviour of wood and the applicability of a nonlinear fracture mechanics model. Doctoral thesis, Report TVBM-1012, Division of Building Materials, Lund University, Sweden.
8. Crisfield MA (1991) Non-linear finite element analysis of solids and structures. Volume 1, John Wiley & Sons Ltd, Chichester, England.
9. Danielsson H, Gustafsson PJ (2013) A three dimensional plasticity model for perpendicular to grain cohesive fracture in wood. Engineering Fracture Mechanics 98:137-152.
10. Danielsson H (2013) Path following solution approaches and integration of constitutive relations for a 3D wood cohesive zone model. Report TVSM-7160, Division of Structural Mechanics, Lund University, Sweden.
11. DIN 1052:2008-12 Design of timber structures - General rules and rules for buildings.
12. Ehlbeck J, Görlacher R, Werner H (1989) Determination of perpendicular-to-grain tensile stresses in joints with dowel-type fasteners – A draft proposal for design rules. CIB-W18A/22-7-2, Berlin, DDR.
13. EN 1995-1-1:2004 Eurocode 5: Design of timber structures – Part 1-1: General – common rules and rules for buildings
14. Franke B, Quenneville P (2010) Failure behaviour and resistance of dowel-type connections loaded perpendicular to grain. CIB-W18/43-7-6, Nelson, New Zealand.
15. Frühwald Hansson E (2011) Analysis of structural failure in timber structures: Typical causes for failure and failure modes. Engineering Structures 33:2978-2982.
16. Gustafsson PJ, Larsen HJ (2001) Dowel joints loaded perpendicular to grain. Joints in Timber Structures - Proceedings of the International Rilem Symposium, Stuttgart, Germany.
17. Jensen JL, Gustafsson PJ, Larsen HJ (2003) A tensile fracture model for joints with rods or dowels loaded perpendicular to grain. CIB-W18/36-7-9, Colorado, USA.
18. Jensen JL (2003) Splitting strength of beams loaded by connections. CIB-W18/36-7-8, Colorado, USA.
19. Jensen JL, Quenneville P, Girhammar UA, Källsner B (2012) Beams loaded perpendicular to grain by connections – Combined effect of edge and end distances. CIB-W18/45-7-2, Växjö, Sweden.
20. Larsen HJ, Gustafsson PJ (1990) The fracture energy of wood in tension perpendicular to the grain – Results from a joint testing project. CIB-W18A/23-19-2, Lisbon, Portugal.
21. Larsen HJ, Gustafsson PJ (2001) Dowel joints loaded perpendicular to grain. CIB-W18/34-7-3, Venice, Italy.
22. Leijten AJM (2001) Splitting strength of beams loaded by connections, model comparison. CIB-W18/35-7-7, Venice, Italy.
23. MATLAB, Version R2012b. The MathWorks, Inc.
24. van der Put TACM, Leijten AJM (2000) Evaluation of perpendicular to grain failure of beams caused by concentrated loads of joints. CIB-W18/33-7-7, Delft, The Netherlands.
25. Schoenmakers JCM (2010) Fracture and failure mechanisms in timber loaded perpendicular to grain by mechanical connections. Doctoral thesis, Eindhoven University of Technology, The Netherlands.
26. Stefansson F (2001) Fracture analysis of orthotropic beams – linear elastic and non-linear methods. Licentiate thesis, Report TVSM-3029, Division of Structural Mechanics, Lund University, Sweden.
27. Tsai SW, Wu EM (1971) A general theory of the strength of anisotropic materials. Journal of Composite Materials 5:58-80.
28. Wernersson H (1994) Fracture characterization of wood adhesive joints. Doctoral thesis, Report TVSM-1006, Division of Structural Mechanics, Lund University, Sweden.
29. Yasumura M, Daudeville L (1999) Design and analysis of bolted timber joints under lateral force perpendicular to grain. CIB-W18/32-7-3, Graz, Austria.